The Dissertation Committee for Christopher Stanley Combs Certifies that this is the approved version of the following dissertation:

Quantitative Measurements of Ablation-Products Transport in Supersonic Turbulent Flows Using Planar Laser-Induced Fluorescence

Committee:

Noel T. Clemens, Supervisor

Paul M. Danehy

Ofodike A. Ezekoye

Laxminarayan Raja

Philip L. Varghese

Quantitative Measurements of Ablation-Products Transport in Supersonic Turbulent Flows Using Planar Laser-Induced Fluorescence

by

Christopher Stanley Combs, B.S.M.E.

Dissertation

Presented to the Faculty of the Graduate School of

The University of Texas at Austin

in Partial Fulfillment

of the Requirements

for the Degree of

Doctor of Philosophy

The University of Texas at Austin

August 2015

For Casen

Acknowledgements

I would first like to thank my wife, Casen, for being endlessly supportive during this process, after both good experiments and bad. I also would like to thank my parents, Craig and Dorie Combs, for their encouragement along the way. Furthermore, I would not be in this position without the assistance of my advisor, Dr. Noel Clemens. His expertise, advice, and mentorship has helped me to grow as a researcher and achieve my goals at The University of Texas. Dr. Paul Danehy at NASA Langley Research Center deserves a great deal of thanks as well. He served as a sort of co-advisor and provided excellent technical insight, career advice, and was always full of new ideas for the project. Thank you to my dissertation committee, Dr. Ofodike Ezekoye, Dr. Laxminarayan Raja, and Dr. Philip Varghese, for taking the time to be a part of my Ph.D. proposal and dissertation defense. I would also like to thank all the teachers and professors—particularly Ms. Wilson at Model Lab High School—who helped me develop a passion for science and pushed me to be my best.

Dr. Ross Burns was particularly helpful during my time at The University of Texas. Whether it was help with coursework, lasers, setting up experiments, or simply finding things around the lab, he was an invaluable resource. I have to thank Dr. Jeremy Jagodzinski for all his help maintaining the wind tunnel facility at PRC and for sharing his knowledge of lasers and wind tunnel testing. Without his hard work and assistance very little research would get done in our lab. I also want to thank the fellow lab-mates I've enjoyed working with over the past five years, including Bryan Lochman, Dominik Ebi, Benton Greene, Heath Reising, Rakesh Ranjan, Dr. Okjoo Park, Dr. Leon Vastone, Dr. Kevin Marr, Dr. Venkat Narayanaswamy, Dr. Oli Buxton, Dr. Manu Sharma, Jonathan Ashley, Mohammed Saleem, and Tim Haller. I would like to thank Joe Pokluda

and the machine shop staff for their assistance with making parts. Donna Soward and Geetha Rajagopal were extremely helpful as well, assisting with orders and above all, making sure I got paid.

This work was supported by a NASA Office of the Chief Technologist's Space Technology Research Fellowship Grant (#NNX11AN55H). I would also like to thank the Wheeler family and the Temple Foundation for fellowships granted during my time at The University of Texas at Austin.

Quantitative Measurements of Ablation-Products Transport in Supersonic Turbulent Flows Using Planar Laser-Induced Fluorescence

Christopher Stanley Combs, Ph.D.

The University of Texas at Austin, 2015

Supervisor: Noel T. Clemens

A recently-developed experimental technique based on the sublimation of naphthalene, which enables imaging of the dispersion of a passive scalar using planar laser-induced fluorescence (PLIF), is applied to a Mach 5 turbulent boundary layer and a NASA Orion capsule flowfield.

To enable the quantification of naphthalene PLIF images, quantitative fluorescence and quenching measurements were made in a temperature- and pressure-regulated test cell. The test cell measurements were of the naphthalene fluorescence lifetime and integrated fluorescence signal over the temperature range of 100 K to 525 K and pressure range of 1 kPa to 40 kPa in air. These data enabled the calculation of naphthalene fluorescence yield and absorption cross section over the range of temperatures and pressures tested, which were then fit to simple functional forms for use in the calibration of the PLIF images.

Quantitative naphthalene PLIF images in the Mach 5 boundary layer revealed large-scale naphthalene vapor structures that were regularly ejected out to wall distances of approximately $y/\delta = 0.6$ for a field of view that spanned 3δ to 5δ downstream of the trailing edge of the naphthalene insert. The magnitude of the calculated naphthalene mole

fraction in these structures at $y/\delta = 0.2$ ranged from approximately 1-6% of the saturation mole fraction at the wind tunnel recovery temperature and static pressure. An uncertainty analysis showed that the uncertainty in the inferred naphthalene mole fraction measurements was ± 20%. Mean mole fraction profiles collected at different streamwise locations were normalized by the mole fraction measured at the wall and a characteristic height of the scalar boundary layer, causing the profiles to collapse into one "universal" mole fraction profile.

Two-dimensional fields of naphthalene mole fraction were also obtained simultaneously with velocity by using particle image velocimetry (PIV) and PLIF. The images show large-scale naphthalene vapor structures that coincide with regions of relatively low streamwise velocity. The covariance of naphthalene mole fraction with velocity indicates that an ejection mechanism is transporting low-momentum, high-scalar-concentration fluid away from the wall, resulting in the protrusions of naphthalene vapor evident in the instantaneous PLIF images.

Lastly, naphthalene PLIF was used to visualize the dispersion of gas-phase ablation products on a scaled Orion capsule model at four different angles of attack at Mach 5. High concentrations of scalar were imaged in the capsule recirculation region. Additionally, intermittent turbulent structures were visualized on the heat shield surface, particularly for the 12° and 52° AoA cases.

Table of Contents

Nomenclature

Symbols

A	=	Einstein A Coefficient
c	=	Speed of Light
C	=	Experimental Constant
E	=	Laser Fluence
h	=	Planck's Constant
I	=	Light Intensity
k_B	=	Boltzmann Constant
k_{int}	=	Collisionless Non-Radiative De-excitation Rate
k_Q	=	Collisional Quenching Rate
k_{SV}	=	Stern-Volmer Coefficient
l	=	Interaction Path Length
M	=	Mach Number
m	=	Atomic Mass
n	=	Number Density
P	=	Pressure
Pr	=	Prandtl Number
r	=	Recovery Factor
Re	=	Reynolds Number
S	=	Singlet State or Signal
T	=	Triplet State or Temperature
T'	=	Instantaneous Temperature Fluctuation
T_r	=	Recovery Temperature

T_w	=	Wall Temperature
U	=	Streamwise Velocity
u	=	Instantaneous Streamwise Velocity
u'	=	Instantaneous Streamwise Velocity Fluctuation
v	=	Instantaneous Wall-Normal Velocity
v'	=	Instantaneous Wall-Normal Velocity Fluctuation
$\langle v \rangle$	=	Mean Relative Molecular Speed
ΔV	=	Probe Volume
$(.)^+$	=	Normalized Boundary Layer Wall Units

Greek Symbols

δ or δ_{99}	=	Velocity Boundary Layer Thickness
ε	=	Measurement Discrepancy
η	=	Collection Optics Efficiency
λ	=	Light Wavelength or Characteristic Scalar Layer Height
μ	=	Reduced Mass
ν	=	Light Frequency
ρ	=	Covariance
σ	=	Cross Section or Standard Deviation
θ	=	Momentum Thickness
τ	=	Decay Constant
Φ	=	Turbulent Flux
φ	=	Fluorescence Yield
χ	=	Mole Fraction

Subscripts

0	=	Ground State
1	=	First Excited State
2	=	Second Excited State
266	=	266 nm Excitation
283	=	283 nm Excitation
3	=	Third Excited State
a	=	Absorption
aw	=	Adiabatic Wall
eff	=	Effective Fluorescence
D	=	Diameter
i	=	Species or Index
f	=	Fluorescence
Naph	=	Naphthalene
o	=	Initial State
Q	=	Quenching
ref	=	Reference State
rms	=	Root-Mean-Square
sat	=	Saturation
θ	=	Momentum Thickness
∞	=	Freestream

List of Tables

List of Figures

Chapter 1: Introduction

There remains continued interest in the study of ablation owing to the need to develop suitable thermal protection systems (TPS) for spacecraft that undergo planetary entry. Ablation is a complex multi-physics process and codes that predict it require a number of coupled submodels, each of which requires validation (Smits et al., 2009). For example, Reynolds-averaged Navier-Stokes (RANS) and large-eddy simulation (LES) codes require models of the turbulent transport of ablation products under variable compressibility and pressure gradient conditions; however, suitable scalar-velocity data under relevant conditions are very rare (Ho et al., 2007). A technique is being developed that uses planar laser-induced fluorescence (PLIF) of a low-temperature sublimating ablator (naphthalene) to enable visualization of the ablation products in a hypersonic flow. While it is difficult to measure scalar transport in high-enthalpy facilities, low temperature ablation creates a limited physics problem that can be used to simulate the ablation process.

Previous researchers have used NO PLIF to simulate the ablation process by transpiring NO gas through a port on the surface of a capsule model (Inman et al., 2008). For this type of seeding, however, it is possible that the momentum injected into the boundary layer alters the flow. Additionally, since only a finite number of injection ports can be employed this technique is generally limited to the study of ablation from point sources as opposed to simulating ablation occurring over an entire surface. Using sublimating surface material, such as naphthalene, is therefore advantageous in that the turbulent scalar dispersion more closely resembles that from a high-temperature ablating surface.

In the current study, low-temperature ablation is studied by exposing a naphthalene surface to a high-speed flow and imaging the dispersion of the sublimated vapor in the boundary layer. For this technique to be used for quantitative measurements of ablation products transport in supersonic wind tunnel facilities, it is necessary that the PLIF signals be mapped to concentration or mole fraction. However, to do so requires that the fluorescence properties of naphthalene be investigated over a wide range of temperatures and pressures similar to the range of conditions in the wind tunnels of interest. For the boundary layer case, the temperature field in the boundary layer is determined using a mean approximation based on the Crocco-Busemann relation and the mean boundary layer velocity profile while the static pressure is assumed to be constant at the mean value. For the capsule flowfield, CFD predictions of the mean temperature and pressure fields are employed. Then, the resulting calibration of naphthalene fluorescence is applied to the PLIF images of naphthalene, resulting in two-dimensional fields of naphthalene mole fraction. Coupled with simultaneous PIV data, these images provide scalar-velocity data to help better understand the physics of scalar transport in high-speed compressible flows. Furthermore, these experiments may provide needed data on scalar transport necessary to help validate computational models of ablative thermal protection systems for planetary reentry vehicles.

1.1 - LITERATURE SURVEY

In this section, the literature on ablation, sublimation, naphthalene spectroscopy, pertinent laser diagnostics, and related experimental efforts are discussed.

1.1.1 - High-Temperature Ablation

Ablation is a process involving coupled heat and mass transfer that is characterized by the removal of material from a surface by aerodynamic heating. Ablative heat shields have been used to cool and protect space capsules during atmospheric reentry since the earliest days of manned spaceflight (Sietzen, 2005). Ablation can involve many different physical processes such as conduction into the heat shield surface, convection from the freestream to the surface, convection of heat away from the surface due to reaction products, radiation to the surface, re-radiation from the surface, heat transfer due to phase changes, mass transfer, and chemical reactions (Johnston et al., 2013). However, the mechanisms involved in an ablation process can vary depending on the ablator (Steg and Lew, 1962). In their 1962 review, Steg and Lew (1962) identified four different classes of materials with varying ablative characteristics. First, certain plastics such as Teflon depolymerize into a high-vapor-pressure monomer which will then flash directly to the vapor phase. Another class of materials, with graphite being the example, sublimate and then combust at the solid surface upon reacting with dissociated air. Glasses, meanwhile, melt and form a thin liquid layer along the solid surface. This liquid then vaporizes and the resulting gas is injected into the boundary layer. The fourth group of materials identified was reinforced plastics and cast unreinforced resins such as phenolic impregnated carbon ablator (PICA) and Avcoat. These materials pyrolyze, leaving behind a carbonaceous char layer that over time is eroded by aerodynamic forces. The resulting char layer is porous and of a relatively low

density. The char is able to achieve high enough temperatures to reradiate a substantial amount of the heat reaching the heat shield surface and also acts as an insulator to the layer of unpyrolyzed virgin heat shield material. Additionally, pyrolysis gases pass through the porous char layer and are injected into the boundary layer, further reducing heat transfer to the heat shield surface. The many modes of heat transfer resulting from the ablation of this fourth group of materials, as illustrated in Figure 1.1 makes them attractive as potential heat shield materials. Avcoat (a composite of silica fibers in an epoxy-novalic resin that is used to fill a solid honeycomb matrix) was used as the heat shield material for the Apollo capsules and has also been selected as the heat shield material for the Orion MPCV (Garcia, 2013).

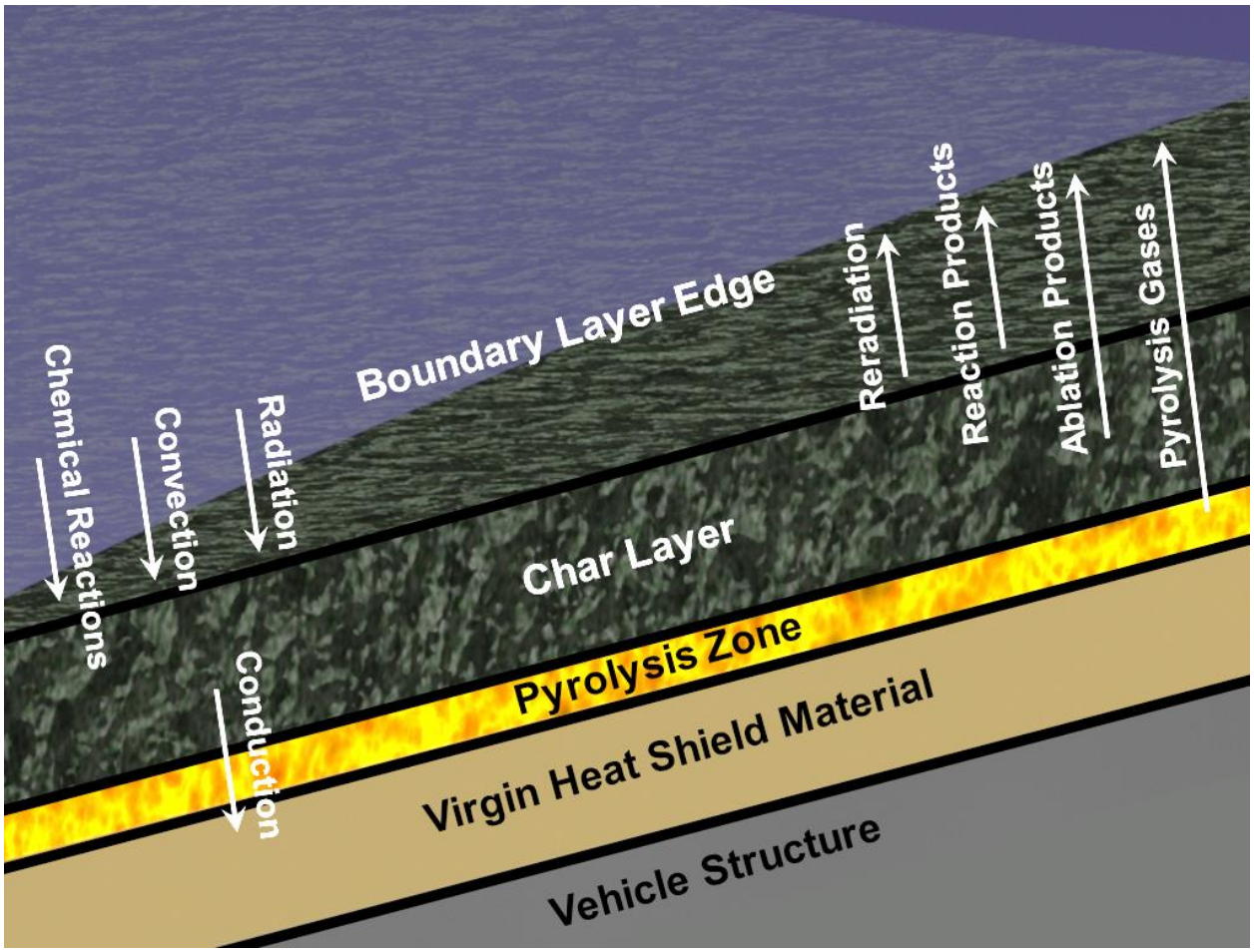

Figure 1.1: Heat and mass transfer mechanisms acting on the surface of an ablating TPS material.

The complex and coupled nature of the ablation process for composite plastics like Avcoat makes simulating the aerothermal environment for space capsules undergoing planetary entry extremely difficult. Relatively simplistic algorithms that generate a flowfield solution and then simulate the ablation process in a post-processing procedure have been developed but were shown to introduce significant errors (Chen and Milos, 2001; Johnston et al., 2013). Therefore, for accurate results, codes aiming to predict ablation require a number of coupled submodels. To date, these codes have

mainly focused on calculating mass transfer rates at the surface, temperature near and at the surface, chemical composition near the surface, and heat transfer rates (Chen and Milos, 2004; Ho et al., 2006; Johnston et al., 2009). These codes require experimental data for validation, however, and there is a deficiency in the experimental databases regarding surface transpiration, ablation, wall-catalysis, and real gas effects (Smits et al., 2009). The absence of good data has made heat shield design difficult, as evidenced by the post-flight analysis of the PICA heat shield used on NASA's Mars Science Laboratory (MSL) which indicated that less than 8% of the heat shield thickness was removed by ablation during atmospheric entry while computations using NASA's FIAT code predicted this much recession to occur in the first thirty seconds of the approximately 275 second duration reentry event (Mahzari et al., 2013).

Experimental investigations of high-temperature ablation have primarily centered on investigating integrated quantities of potential TPS materials, such as surface temperature and recession rate (Ho et al., 2007). The vast majority of these studies have been performed in arc jet facilities owing to their ability to examine the performance of near flight-scale test articles at appropriate enthalpies and Reynolds numbers for simulations of atmospheric entry (Wright and Grinstead, 2007). An experimental study of Avcoat was performed by Schaefer et al. (1967) that involved testing 158 models in an arc jet facility to study ablation at a wide range of lunar return conditions. Three regimes of surface behavior with respect to wall temperature were identified during these tests. While the wall temperature (T_w) was relatively low (< 1600 K) a "scab" of agglomerated silica fibers formed on the heat shield surface. For 1600 K < T_w < 2100 K globules of silica partially covered the surface, with more coverage at lower temperatures, and for T_w > 2100 K there was no longer evidence of liquid silica on the heat shield surface. It

was also determined that for surface pressures greater than 100 kPa, significant surface erosion occurred. Additionally, atmospheric air and pure N_2 flows were found to cause substantial surface erosion, while only slight surface erosion occurred when He was used as the test gas. Lastly, it was found that surface recession rate was independent of run duration.

Covington et al. (2008) analyzed the thermal and ablative performance of PICA in an arc jet facility by varying model size and arc jet conditions. It was found that an endothermic process at low temperatures was resulting in an unexpected delay in internal temperature rise that had not been captured by computer codes. The resulting data were used to iteratively modify the thermophysical properties of PICA used in NASA's FIAT code to generate surface recession rates and maximum internal temperatures that agreed with experimental results.

Spallation—when a chip or fragment is removed from a larger surface—has been observed to occur when carbonaceous heat shields experience extreme heating environments (Davies and Park, 1982). The trajectories of spalled solid particles emanating from a carbonaceous heat shield were investigated by Davies and Park (1982). In their work, a model was developed using the equations for conservation of mass, momentum, and energy to compute the individual trajectories of spalled particles. It was found that significant slip existed between the spalled particles and the surrounding flowfield, often resulting in supersonic flow around the individual particles. Some particles were found to pass through the bow shock upstream of the model before returning to the shock layer and occasionally striking the heat shield surface. It was also determined that a significant fraction of the original particle mass was converted into gaseous carbon and deposited into the flow. A preliminary experimental investigation of

spallation was recently performed by Martin et al. (2015) that employed high speed cameras for the detection of individual spalled particles. Samples of PICA and FiberForm® were tested and over 1000 particles could be identified during a 30 s test run. The particle images were then used to estimate two-dimensional velocity vectors of the spalled particles and an average velocity of 102 m/s was identified with a maximum velocity of nearly 300 m/s (Martin et al., 2015).

Suzuki et al. (2005) studied the pressure forces inside a carbon-fiber-reinforced plastic (CFRP) ablator with an interest in predicting the onset of delamination. Delamination is a process whereby a large sheet of heat shield material is ejected into the boundary layer, occurring when the normal stress due to pressure forces inside the ablator exceeds the bond strength between layers of the material. This can lead to disturbances in the boundary layer, transition to turbulence, and significantly higher heating rates (Suzuki et al., 2005). The study determined that the intermediate region between the char layer and pyrolysis zone is the most likely location for delamination to occur. In this layer, the ablator is partially pyrolyzed but not yet fully charred, resulting in high pyrolysis gas pressure but too low of a porosity to sufficiently exhaust the gases.

A combination of arc jet and ballistic range tests were employed by Reda et al. (2004) to study the effect of ablation on boundary layer turbulent transition. Hemispherical graphite nose tips were first ablated in an arc jet facility to acquire a surface roughness characteristic of atmospheric entry. The ablated models were then launched at hypersonic speeds in a ballistics range and imaged end-on by an intensified CCD (ICCD) camera. By calibrating the ICCD camera with reference blackbody sources, the images could be converted into global surface temperature maps. These temperature distributions indicated the location of turbulent transition in the boundary layer on the

model surface leading to the identification of three different transition regimes based on roughness height.

1.1.2- Low-Temperature Sublimating Ablators

While high temperature ablation is relatively difficult and expensive to recreate in a laboratory environment, low temperature ablation creates a limited physics problem that can be used to study the ablation process. Naphthalene (Charwat, 1968), camphor (Lipfert and Genovese, 1971), wax (Stock and Ginoux, 1971), CO_2 (dry ice; Callaway et al., 2010), water-ice (Silton and Goldstein, 2000), ammonium chloride (McDevitt, 1971), and paradichlorobenzene (Grimes and Casey, 1965)—all low-temperature sublimating ablators—have been used previously to study ablation, with camphor and CO_2 being employed most often. Measuring shape change and determining recession rates of cones, hemispheres, and other projectile-like models has been the focus of the majority of ablation studies performed using low-temperature sublimating ablators (Kohlman and Richardson, 1969).

Charwat (1968) performed extensive studies observing ablation in camphor and naphthalene models in a relatively low-enthalpy Mach 3 flow. Numerous cone-shaped geometries were tested with features such as flat noses, rounded noses, forward-facing cavities, backward-facing cavities, rectangular grooves, and shoulders. The models were machined from sintered blocks of naphthalene and camphor, as the authors determined that this method produced models with twice the shear strength of cast models. Schlieren imaging was used to determine the flowfield surrounding the various models and the dark shadow of the model in the Schlieren images was used to monitor shape change and recession rate. It was observed that the conical models generally achieved a needle point during wind tunnel testing. Grooves and cross-hatching were also found to develop on the

model surface, however, cross-stream grooves tended to be erased by the ablation process whereas the size of streamwise grooves was amplified due to coupling with oscillations in the boundary layer. These surface patterns have been observed by many others in the literature, as well. Stock and Ginoux (1971) used pointed wax and camphor cones to assess the effect of local flow parameters like local Mach number, pressure, and temperature on the cant angle and streamwise spacing of cross-hatch patterns in a Mach 5.3 freestream flow. Photographs of models post-run were captured that clearly illustrate the cross-hatching phenomenon. The cant angle of the cross-hatching was found to decrease with increasing local Mach number. Results also showed that the streamwise spacing of the grooves increased with decreasing local static pressure while the spacing showed a positive linear correlation with the driving temperature ratio (defined as $[T_r - T_w]/T_w$, where T_r is the recovery temperature). No correlation was found between local Mach number and cross-hatch spacing.

Kohlman and Richardson (1969) developed a method for fabricating dry ice models for wind tunnel testing and measured recession rates by comparing photographs of the models taken during wind tunnel runs. This fabrication technique was later used by Callaway et al. (2010), who measured recession rates of dry-ice projectile models using a laser dot projection photogrammetry technique coupled with Schlieren imaging. The experiments compared favorably with CFD predictions and showed that the nose tip recession rate remained effectively constant over the course of a run. Dry ice and camphor models were also used by Lipfert and Genovese (1971), who made measurements of surface pressure, temperature, and recession rate with the goal of calculating blowing rates. The study found that turbulent blowing rates were significantly under-predicted by theory. It was postulated that this may be because theoretical

calculations often predict uniform blowing, whereas the grooves and cross-hatching found on ablating surfaces may represent areas of locally high blowing.

The effect of a forward-facing cavity on the recession rate at the nose tip of a supersonic projectile model was investigated by Silton and Goldstein (2000). The ablator used for these experiments was water-ice reinforced with fiberglass threads. For the baseline case with no cavity, it was observed that recession began at the sides of the model rather than the stagnation point, most likely due to turbulent transition in the boundary layer on the model surface. For the cavity models, ablation began at the cavity lip but little ablation was observed inside the cavity. Models with deeper cavities outperformed shallow-cavity models, however, the baseline case showed less nose tip recession than the cavity models. Since deeper cavities led to lower recession rates, a hypothesis was developed that the cavity depths selected for this study were not sufficient to improve performance when compared to the baseline model. Experimental results were compared to a numerical simulation with good agreement.

Several experiments have also been conducted using low-temperature sublimating ablators to explore the effect of ablation on vehicle stability. Using camphor, ammonium chloride, and Korotherm cones in a Mach 7.4 flow, McDevitt (1971) found that grooves, turbulent wedge erosion, and cross-hatching all induced roll torques on the models. Grimes and Casey (1965) studied the effect of ablation on the damping of oscillatory motion by comparing conical models made of aluminum (non-ablating), porous nickel with nitrogen injection (to simulate blowing), ablating ammonium chloride, and ablating paradichlorobenzene. Coating the entire model or simply the front half of the model (with respect to the center of mass) with an ablator was shown to produce a dynamically stable configuration while only coating the rear half of the model resulted in a dynamically

unstable configuration. Experiments were conducted by Griffith et al. (1977) to determine if mass injection using a transpired gas through a porous surface affected drag in the same manner as mass transfer from an ablating surface. Force balance measurements were made using solid steel cones as a control and were compared to measurements made on porous sintered metal and camphor cones. Three different gases were used for mass injection for the porous cone cases—sulfur hexafluoride, argon, and nitrogen—to test for molecular weight effects. It was found that while both mass injection techniques reduced drag when compared to the baseline case, the ablating cones exhibited lower drag than the cones with a transpiring gas. The authors suggest that this discrepancy is most likely a result of the fact that both the porous gas transpiration and ablation techniques exhibit non-uniform blowing on the surface, however, it is extremely difficult to create a porous surface that can match the blowing distribution on the surface of an ablator.

1.1.3- Naphthalene Sublimation Techniques

Experiments taking advantage of naphthalene sublimation have been used to study boundary layer transition, heat transfer, and mass transfer (Obara, 1988; Goldstein and Cho, 1995). Gray (1944) has been credited with being the first to develop the technique for studying boundary layer transition at the Royal Aircraft Establishment in 1944. When using naphthalene sublimation to study transition to turbulence, models are generally coated with a thin film of naphthalene prior to testing. This thin film rapidly sublimates off the model surface in regions where the boundary layer is turbulent, allowing one to determine the location of transition by visually inspecting the model (Radeztsky et al., 1999). Often to enhance clarity and contrast, a matte black coat of paint is applied to the test surface before application of the white naphthalene crystals.

Additionally, as detailed by Jensen (1991) in his patent of the technique, it is possible to mix colored dyes or paints with naphthalene and paint successive colored layers of naphthalene on a test surface to generate a colored surface map corresponding to the flow quantity of interest.

Obara (1988) provided a detailed overview of the naphthalene sublimation technique for studying transition and included examples where the diagnostic was used to study transition in-flight on various aircraft. The technique is well-suited for large-scale applications like this owing to its simplicity, relatively low cost, and ability to produce a detailed surface map of transition from laminar to turbulent flow on a surface. Radezsky et al. (1999) used the diagnostic to study the effect of micron-sized roughness on transition in a swept wing flow for an NLF(2)-0415 airfoil. The work showed that the location of the roughness elements affected transition Reynolds number and also that increasing the diameter of the roughness elements decreased the transition Reynolds number, as would be expected. Paschal et al. (2012) and White and Saric (2000) also used naphthalene sublimation to identify transition on airfoils.

For making heat and mass transfer measurements, models are typically cast from liquid naphthalene or machined from a block of solid naphthalene (Souza Mendes, 1991). The model can simply be weighed before and after a test or the recession of the naphthalene layer can be measured in order to perform a mass transfer experiment. Using a heat/mass transfer analogy, heat transfer rates can be inferred from these results. This analogy is derived in reviews by both Goldstein and Cho (1995) and Souza Mendes (1991). Goldstein and Cho (1995) note that this technique is difficult to employ in high-speed flows since recovery temperature effects and model shape change must be accounted for. Additionally, Souza Mendes (1991) stresses the difficulty in obtaining

repeatable results with the technique in natural convection experiments due to low sublimation rates and a difficulty in creating a truly quiescent environment.

The naphthalene sublimation technique has been used to study heat transfer in numerous applications including external flows, ducts, channels, fins, heat exchangers, impinging jets, rotating discs, electronics cooling, and natural convection (Souza Mendes, 1991). Christian and Kezios (1959) used a modified lathe and micrometer dial indicator to measure radial shape changes of sharp-edged cylinders exposed to an axisymmetric laminar flow. The data were used to calculate local mass and heat transfer coefficients for the cylinders. The effect of Reynolds number and angle of attack on the heat transfer coefficients for adjacent spheres was investigated by Sparrow and Prieto (1983). The study determined that the interaction between the spheres was most pronounced at zero angle of attack (when the spheres were in line with the flow direction), represented by increased heat transfer relative to the single sphere baseline case. Additionally, Goldstein and Taylor (1982) simulated heat transfer on a film-cooled wall by applying the naphthalene sublimation technique to measure mass transfer coefficients in the vicinity of a row of jets in a crossflow. It was observed that the mass transfer coefficient (and by analogy the heat transfer coefficient) was significantly increased near the jet exits and just downstream of the jet exit centerlines. The technique was also used by Wang et al. (1999) to study the effect of freestream turbulence on heat and mass transfer on gas turbine blades.

1.1.4- Spectroscopic Measurements of Naphthalene

Naphthalene, $C_{10}H_8$, is a polycyclic aromatic hydrocarbon (PAH) and is a byproduct of many combustion processes. Naphthalene is the simplest PAH, an asymmetric top molecule consisting of two fused benzene rings, and is a white crystalline

solid at room temperature with a strong odor of coal tar. Naphthalene has a melting temperature of 353 K and the vapor pressure of the solid phase is large enough that mass loss by sublimation can be significant near room temperature. It should be noted that the addition of naphthalene to an air flow at the conditions of the experiments in this work ($\chi_{Naph} \sim 1 \times 10^{-4}$) results in a change in the properties of the gas mixture (e.g., density, viscosity, molecular weight, and specific gas constant) of less than 0.05%. It can thus be assumed that naphthalene vapor is behaving as a passive scalar in the current work.

Table 1.1 contains some relevant thermo-physical properties of naphthalene.

Table 1.1**:** Physical properties of naphthalene

Molecular Formula	$C_{10}H_8$
Molar Mass	128 kg/mole
Melting Temperature	353 K
Vapor Pressure at 300 K*	13.4 Pa
Vapor Pressure at 350 K*	668.5 Pa
Kinematic Viscosity at 300 K ($\times 10^6$)†	15.7 m^2/s
Mass Diffusion Coefficient in Air at 300 K ($\times 10^6$)†	6.89 m^2/s

*De Kruif et al. (1981), †Goldstein and Cho (1995)

Naphthalene is a relatively large molecule with a complex energy-level structure that is difficult to model computationally owing to a number of entangled vibronic manifolds (Beck et al., 1980). A simplified vibrational-electronic energy-level diagram for vapor-phase naphthalene close to the photon energy of 266 nm (ν = 37,594 cm^{-1}) excitation can be seen in Figure 1.2, since this is the primary excitation frequency used in the current work. In this region, naphthalene has two excited singlet states, S_1 and S_2, located 32,027 cm^{-1} and 35,815 cm^{-1} above the origin S_0, respectively. The singlet states

are each associated with a manifold of tightly-packed vibrational energy levels. The S_1 and S_2 manifolds become tangled and extremely complicated in a 200 cm^{-1} wide region near the S_2 origin due to the close spacing of the two electronic states and an overlapping of the respective vibrational manifolds (Beck et al., 1980).

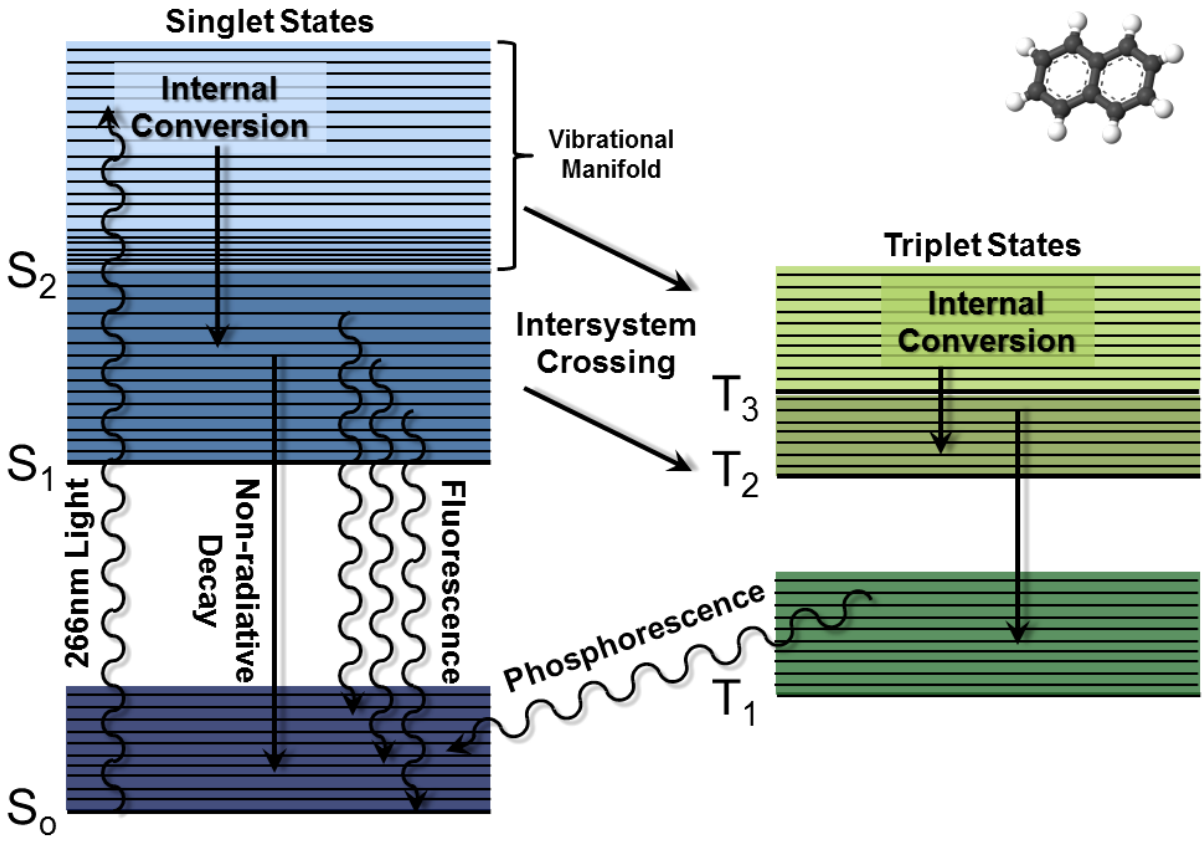

Figure 1.2: Energy-level diagram for naphthalene in the vapor phase. Energy levels are not drawn to scale.

At least two (and as many as four) triplet state manifolds exist with origins below the S_1 origin, with more triplet states existing at higher energies (Behlen and Rice, 1981). Based on schematics presented by Stockburger et al. (1975), three triplet states are

illustrated in Figure 1.2, with T_2 and T_1 below the origin of S_1 and the origin of T_3 having a slightly higher energy than the S_1 origin.

As depicted in Figure 1.2, excitation with 266 nm light results in electrons being elevated to the second excited singlet state, S_2. Many have shown that upon excitation to S_2, almost all excited molecules undergo an internal conversion to S_1 (Watts and Strickler, 1966; Laor and Ludwig, 1971; Beddard et al., 1973). Internal conversion is defined as a radiationless transition from a higher energy level to a lower energy level of the same system (i.e. singlet to singlet or triplet to triplet; Watts and Strickler, 1966). Since almost all molecules excited to the S_2 state undergo this internal conversion and the internal conversion occurs much faster than the fluorescence lifetime of the S_2-S_0 transition, all measurable fluorescence occurs from the S_1 state when pumping to the S_2 state (Watts and Strickler, 1966; Stockburger et al., 1975). This measured fluorescence has been observed to occur between 300 and 400 nm (Watts and Strickler, 1966; Orain et al., 2011). The fluorescence observed in the current work was emitted over this band. A third excited singlet state, S_3, exists at approximately 42,000 cm^{-1} above S_0 (not shown in Figure 1.2), however, it exhibits vastly different fluorescence properties than the first two excited singlet states (Laor and Ludwig, 1971). For example, Laor and Ludwig (1971) demonstrated that the inverse of the fluorescence lifetime had a linear relationship with excitation frequency when exciting the first and second singlet states while excitation to the third singlet state exhibited an exponential trend.

Another de-excitation pathway upon excitation to S_2 involves an intersystem crossing to a triplet state. An intersystem crossing is defined by Watts and Strickler (1966) as a radiationless transition between singlet and triplet states. Given that these processes are quantum mechanically forbidden, they occur at a much lower rate than

most other competing processes and only a small fraction of the molecules in the S_1 and S_2 states make an intersystem crossing to one of the triplet manifolds (Ashpole et al., 1971). Ashpole et al. (1971) describe a typical intersystem crossing from the S_1 state as a crossing from S_1 to T_2 or another higher triplet state followed by an internal conversion to the T_1 state. Avouris et al. (1977) note that intersystem crossing is more prevalent for higher excitation energies since there will be more triplet states below the energy level of the excited singlet. This, in turn, leads to lower fluorescence yields. Upon arrival at the lowest excited triplet state, molecules can undergo collisional de-excitation (quenching) or return to the ground state via emission of a photon. Radiative transitions from T_1 to S_0 occur in the form of relatively long-lived phosphorescence with lifetimes of order milliseconds. However, given that only a small fraction of molecules in the excited singlet states undergo intersystem crossing, observed phosphorescence is dominated by fluorescence from the S_1-S_0 transition. This intersystem crossing has been shown to be strongly dependent on pressure by both Ashpole et al. (1971) and Soep et al. (1973). Both studies found that the triplet yield of naphthalene vanishes as pressure goes to zero, while the fluorescence yield increased (Ashpole et al., 1971; Soep et al., 1973).

Molecules in an excited singlet state can also return directly to the ground state via non-radiative processes, termed quenching. The collisional quenching rate, k_Q, of colliding species *i* can be written as,

$$k_Q = \sum_i n_i \sigma_{Q,i} \langle v \rangle_{i-Naph} \qquad 1.1$$

where n_i is the number density of species *i*, $\sigma_{Q,i}$ is the quenching cross section of species *i*, and $\langle v \rangle_{i-Naph}$, is the mean relative speed between species *i* and naphthalene. This final term can be expressed as,

$$\langle v \rangle_{i-Naph} = \sqrt{\frac{8k_B T}{\pi \mu}} \tag{1.2}$$

where k_B is the Boltzmann constant, T is the temperature of the gas, and μ is the reduced mass between naphthalene and species *i*, written as,

$$\mu = \frac{m_{Naph} m_i}{m_{Naph} + m_i} \tag{1.3}$$

with m_{Naph} representing the atomic mass of naphthalene and m_i representing the atomic mass of species *i*. Assuming a (relatively) short-pulse laser excitation and a fluorescence decay exhibiting an exponential decay with time constant τ_f, the fluorescence lifetime, τ_f, can be related to the quenching rate with the following expression,

$$\tau_f = \frac{1}{A + k_Q + k_{int}} \tag{1.4}$$

where A is the Einstein coefficient for spontaneous emission and k_{int} is the rate of non-radiative de-excitation not due to collisions. The fluorescence lifetime can be measured directly through experimentation; however, naphthalene exhibits a bi-exponential decay due to multiple radiative de-excitation pathways. As a consequence, an effective lifetime, τ_{eff}, can be written in the form (Ossler et al., 2001; Martinez et al., 2004):

$$\tau_{eff} = \frac{I_1 \tau_1 + I_2 \tau_2}{I_1 + I_2} \tag{1.5}$$

where τ_1 and τ_2 are the short and long decay components, respectively, while I_1 and I_2 represent the intensities corresponding to the two lifetime components. This formulation is important when making measurements in pure nitrogen environments as both components contribute to the fluorescence decay. Conversely, at high temperatures and

when oxygen is present, the short decay component becomes negligibly small and the waveform can be treated as a single-exponential decay function (Ossler et al., 2001).

Several studies have been conducted to investigate the effect of the presence of species such as O_2, NO, CO_2, CH_4, H_2O, and noble gases on the collisional quenching of naphthalene fluorescence (Stevens, 1957; Ashpole et al., 1971; Jones and Siegel, 1971; Ossler et al., 2001; Kaiser and Long, 2005; Orain et al., 2011; Faust et al., 2013). Paramagnetic molecules like O_2 and NO have been shown to be the most effective quenchers of naphthalene (Stevens, 1957; Ashpole et al., 1971; Jones and Siegel, 1971; Ossler et al., 2001; Kaiser and Long, 2005; Orain et al., 2011; Faust et al., 2013). Xenon and Krypton have also been shown to quench naphthalene fluorescence (Beddard et al., 1973). Oxygen, though, has been proven to be the most effective quencher and research has shown that in addition to decreasing the fluorescence intensity and fluorescence lifetime of naphthalene vapor, increasing the partial pressure of oxygen results in a red-shift of the fluorescence spectrum and diffuses the fine details of the spectrum (Stevens, 1957; Ashpole et al., 1971; Jones and Siegel, 1971; Soep et al., 1973; Avouris et al., 1977; Ossler et al., 2001; Martineze et al., 2004; Kaiser and Long, 2005; Orain et al., 2011; Faust et al., 2013). Martinez et al. (2004) calculated the quenching rates of O_2 and N_2 at 297 K for varying number densities of the quenching species and found that O_2 quenched twelve times more effectively than N_2. However, the addition of certain inert gases, such as N_2, has been shown to increase the fluorescence yield of naphthalene owing to the fact that the naphthalene vibrational levels do not reach equilibrium until relatively high pressures (Stevens, 1957; Ashpole et al., 1971; Jones and Siegel, 1971; Soep et al., 1973; Avouris et al., 1977; Ossler et al., 2001; Martineze et al., 2004; Kaiser and Long, 2005; Lochman, 2010; Orain et al., 2011; Faust et al., 2013). In

other words, at low pressures the laser pulse excites the molecules to the S_2 vibronic states and the molecules undergo rapid internal transfer to the S_1 vibronic states (at rates of 10^{10} s^{-1}) but a lack of collisions locks the population in these upper vibrational states, whose fluorescence decay times are short (on the order of 50 ns) (Schlag et al. 1971). However, at higher pressure, the upper states are more thermalized, meaning the lower vibrational states are more populated compared to that at lower pressures. These lower vibrational states have a longer radiative decay time constant (on the order of 100 ns) compared to the higher states, evidenced by the increased fluorescence decay time constant at higher pressures (Schlag et al. 1971).

Knowing the quenching rates of various species is an important part of developing an empirical expression for the fluorescence yield of naphthalene. The time-integrated fluorescence signal S_f (units of photons) can be written as,

$$S_f = \frac{E}{hc/\lambda}\eta \Delta V \chi_i n(P,T)\sigma_a(\lambda,T)\varphi(\lambda,T,P,\chi) \qquad 1.6$$

where E is the laser fluence (J/m^2), h is Planck's constant, c is the speed of light, λ is the wavelength of the laser, η is the collection optics collection efficiency, ΔV is the probe volume, χ_i is the species mole fraction, n is the total number density, σ_a is the absorption cross section, φ is the fluorescence yield, P is pressure and T is temperature. The quenching cross section enters this equation through the fluorescence yield term. Using Eq. 1.4 and assuming that the fluorescence results from the S_1 state, that the spontaneous emission rate and electronic quenching rates are the same for all vibronic states in S_1, and assuming a two-level model with broadband detection, the fluorescence yield φ can be written as,

$$\varphi(\lambda, T, P, \chi) = A\tau_f = \frac{A}{A + k_Q + k_{int}} \quad 1.7$$

Measuring the fluorescence lifetime through experimentation therefore provides a means to experimentally determine quenching cross sections and measure fluorescence yield.

In addition to understanding the variation of fluorescence yield with thermodynamic properties, it can be seen from Eq. 1.6 that to make the fluorescence signal quantitative, it is necessary to determine the absorption cross section as a function of temperature. Assuming Stern-Volmer behavior (in the quenching-dominated limit), constant pressure, and taking advantage of a known reference condition, Eq. 1.6 can be reduced to the form,

$$\frac{\sigma_a(T)}{\sigma_a(T_{ref})} = \frac{S_f}{S_{f,ref}} \frac{\sqrt{T}}{\sqrt{T_{ref}}} \frac{\sigma_{q,O_2}(T)}{\sigma_{q,O_2}(T_{ref})} \quad 1.8$$

allowing one to measure a relative absorption cross section with respect to temperature.

Even with an understanding of the behavior of the fluorescence yield and absorption cross section with respect to temperature, pressure, and excitation wavelength, there are still many terms in Eq. 1.6 that are difficult to quantify. To circumvent this issue a further simplification is required to make quantitative PLIF measurements. This can be achieved by dividing the imaged fluorescence signal by a reference image, collected at known conditions. As seen in Eq. 1.9, signals normalized by fluorescence collected from a reference cell containing the species of interest at known conditions while using the same excitation wavelength can eliminate many of the constants in Eq. 1.6:

$$\frac{S_f}{S_{f,ref}} = \frac{\chi_i}{\chi_{i,ref}} \frac{PT_{ref}}{P_{ref}T} \frac{\sigma_a(T)}{\sigma_a(T_{ref})} \frac{\varphi(T, P, \chi)}{\varphi(T_{ref}, P_{ref}, \chi_{ref})} \quad 1.9$$

which can be rearranged to solve for mole fraction:

$$\chi_i = \chi_{i,ref} \frac{S_f}{S_{f,ref}} \frac{P_{ref} T}{P T_{ref}} \frac{\sigma_a(T_{ref})}{\sigma_a(T)} \frac{\varphi(T_{ref}, P_{ref}, \chi_{ref})}{\varphi(T, P, \chi)} \quad 1.10$$

With a relationship for the variation of fluorescence signal with respect to pressure and temperature, it is possible to determine the mole fraction of naphthalene from the fluorescence signal at locations in the flow where pressure and temperature are known. One goal of the current work is to develop a thermometry technique based on naphthalene PLIF to make instantaneous temperature field measurements. Using Eq. 1.5 and taking the ratio of fluorescence signal resulting from excitation at two separate wavelengths, it can be shown that:

$$\frac{S_{f,\lambda_2}}{S_{f,\lambda_1}} \propto \frac{\sigma(\lambda_2, T)\varphi(\lambda_2, T, P, \chi)}{\sigma(\lambda_1, T)\varphi(\lambda_1, T, P, \chi)} = f(T, \lambda_1, \lambda_2) \quad 1.11$$

where λ_1 and λ_2 are the two excitation wavelengths. Assuming the ratio is acquired at constant temperature and pressure conditions, Eq. 1.11 reduces to a function of temperature and the two excitation wavelengths. It is then possible to determine the temperature at any point in the flow by comparing the fluorescence signal resulting from excitation at two different wavelengths (Eckbreth, 1996).

Being a natural byproduct of combustion, many studies have investigated the fluorescence properties of naphthalene for different purposes. However, the majority of the literature on naphthalene fluorescence focuses on understanding naphthalene photophysics (Stevens 1957; Ferguson et al. 1957; Craig et al. 1961; Schlag et al. 1971; Jones and Siegel 1971; Stockburger et al. 1975a; Stockburger et al. 1975b; Beck et al. 1980; Suto et al. 1992). In these previous studies, the naphthalene vapor is generally held at its room-temperature vapor pressure in an evacuated static cell or it is seeded into a cold supersonic jet exhausting into a vacuum. With the temperature and pressure of the

naphthalene vapor held constant, the excitation wavelength is varied. Valuable information about the energy level structure of the naphthalene molecule has been gleaned from these experiments, such as the locations of individual transitions, the shapes of the absorption and fluorescence spectra, and the origins of the vibrational manifolds themselves (Behlen and Rice 1981). Beck et al. (1980) showed that the fluorescence spectra of naphthalene shifts to the red with increasing excitation wavelength. Additionally, Beddard et al. (1973) and Suto et al. (1992) found that the fluorescence yield increases with increasing excitation wavelength. It was also demonstrated that the fluorescence lifetime of naphthalene vapor increases with increasing excitation wavelength (Beddard et al., 1973; Beck et al., 1981).

Few studies on naphthalene vapor fluorescence have been conducted where temperature and pressure are both varied, and even fewer have been conducted over a range of conditions that may be experienced in a hypersonic blowdown wind tunnel environment. However, a small number of relevant studies have been conducted since 2001 that are similar to the investigation that will be required for this project. Ossler et al. (2001) used a flowing cell held at atmospheric pressure to study naphthalene fluorescence while varying the temperature from 400-1200 K and varying the mole fraction of oxygen from 0-10% (N_2 was the primary gas). Excitation was achieved with 266 nm light. A red shift and broadening in the fluorescence spectrum was observed with increasing temperature. Additionally, the fluorescence lifetime decreased exponentially by two orders of magnitude over the temperature range studied and the overall signal was found to decrease as well. Bi-exponential fluorescence decay was observed, which should be expected when exciting multiple transitions in the naphthalene molecule simultaneously (Ossler et al., 2001). A subtle red shift in the fluorescence spectra with increasing oxygen

content was measured. An increase in the mole fraction of oxygen was also found to decrease the fluorescence lifetime and signal. Linear Stern-Volmer behavior was observed at 540 K (Ossler et al., 2001). Lastly, it was shown that the absorption coefficients exhibited a limited temperature dependence (Ossler et al., 2001).

Similarly, Kaiser and Long (2005) used a heated jet setup and 266 nm excitation to study fluorescence of vapor-phase naphthalene with the goal of developing a two-color ratiometric technique for measuring temperature in internal combustion engines. The main finding of the study was that O_2 was confirmed to be the dominant quencher of naphthalene fluorescence. Additionally, it was observed that both increased temperature and increased O_2 concentration induced a red shift and broadening of the fluorescence spectra, with the effect saturating at $\chi_{O2} \approx 0.1$ (Kaiser and Long, 2005). In agreement with the work of Ossler et al., (2001) fluorescence signal was seen to decrease with increasing temperature and linear Stern-Volmer behavior was observed at 500 K and 800 K (Kaiser and Long, 2005). The two Stern-Volmer plots showed that the Stern-Volmer coefficient decreased with increasing temperature.

Lochman (2010) studied the fluorescence of naphthalene vapor excited with 266 nm light in a flowing cell by varying the temperature from 297-525 K while holding the pressure constant at 100 kPa and then varying the pressure from 1-100 kPa while maintaining the temperature at 297 K. Similar to previous work, the fluorescence signal was found to decrease with increasing temperature, increasing O_2 concentration was found to decrease the fluorescence lifetime, and increasing N_2 concentration was found to decrease the fluorescence lifetime. However, unlike Ossler et al. (2001), Lochman (2010) found the absorption cross section to increase non-monotonically with increasing temperature. The study also found Stern-Volmer behavior with increasing oxygen

concentration at room temperature, but it was observed that the slope became non-linear at pressures below 2 kPa, which was suggested to be due to the increased importance of collisionless de-excitation mechanisms at low pressures (Lochman, 2010). Buxton et al. (2012) would later continue the study by Lochman and measure fluorescence lifetime at 4 kPa from 300-475 K and at 4.98 kPa from 175-300 K. It was found that the lifetime of naphthalene in air exhibited a monotonic increase with increasing temperature over the range of 175-300 K at 100 kPa (Buxton et al., 2012).

In another flow cell experiment, Orain et al. (2011) varied the temperature of a flowing naphthalene/undecane/air mixture from 350-900 K, varied pressure from 100 kPa-3 MPa, and varied χ_{O2} from 0 to 0.21 using 266 nm excitation. The work reproduced certain trends observed in previous papers such as a red shift in the fluorescence spectrum with increasing temperature, an order of magnitude decrease in fluorescence signal over the temperature range studied, a red shift and diffusion of fine structure in the fluorescence spectrum with increasing oxygen concentration, a strong oxygen quenching effect, and linear Stern-Volmer behavior (Orain et al., 2011). Stern-Volmer coefficients were seen to decrease exponentially with increasing temperature, agreeing with trends observed by Kaiser and Long (2005). The fluorescence signal was also observed to increase with increasing N_2 pressure and the shape of the normalized fluorescence spectrum was unchanged by changing pressure. Lastly, it was observed that the absorption cross section had a non-monotonic dependence on temperature, contradicting the work of Ossler et al. (2001) but agreeing with the findings of Lochman (2010).

Most recently, Faust et al. (2013) used picosecond 266 nm excitation to study flowing naphthalene vapor over the range of 374-1123 K and 100 kPa-1 MPa. Many of

the same trends found in previous research were found in this work and bi-exponential fluorescence decay was measured. Also in agreement with previous research, linear Stern-Volmer behavior was observed over a wide range of temperatures. In agreement with Ossler et al. (2001), it was found that the Stern-Volmer coefficients decreased exponentially with increasing temperature. The effect of CO_2 concentration was found to be similar to that of N_2, with increasing CO_2 pressure increasing the fluorescence lifetime (Faust et al., 2013). Additionally, a fit for the fluorescence yield of naphthalene vapor was formulated. The fit applied to N_2 gas with naphthalene vapor over the entire range of conditions studied as well as air with naphthalene vapor at 100 kPa (Faust et al., 2013).

A summary of the parameter space covered by the most relevant studies of naphthalene fluorescence in air using 266 nm excitation is provided in Table 1.2 below. As seen in the table, the majority of studies have considered temperatures above 300 K while only Buxton et al. (2012) made measurements at lower temperatures (down to 175 K). Considering that the range of temperatures in the flows to be studied is approximately 60-360 K, there is a need for spectroscopic data at these conditions. Furthermore, the low-temperature measurements made by Buxton et al. (2012) were only at one pressure condition (4.98 kPa). While this is nominally the Mach 5 wind tunnel static pressure in the current work, it is desirable to conduct low-temperature measurements over a range of pressures. First, these measurements are necessary for calculating the quenching cross section of naphthalene fluorescence due to oxygen, which is needed to calculate the absorption cross-section as seen in Eq. 1.8. Furthermore, measuring over a range of pressures will permit the development of empirical fits to the fluorescence data that can then be applied to the capsule flowfield and supersonic flows in other future works.

Table 1.2**:** Parameter space covered by relevant studies of naphthalene fluorescence lifetime and integrated fluorescence signal in air with 266 nm excitation.

Study	Pressure Range	Temperature Range
Ossler et al. (2001)	0-48 kPa	540 & 980 K
Kaiser and Long (2005)	0-130 kPa	500 & 800 K
Lochman et al. (2010)	1-7* & 100 kPa	297-525 K
Orain et al. (2011)	0-100 kPa	450-750 K
Buxton et al. (2012)	4[†] & 4.98[‡] kPa	175-475 K
Faust et al. (2013)	0.1-1 MPa	350-900 K
Mach 5 Boundary Layer in Current Work	4.8-5.1 kPa	60-330 K
Capsule Flowfield in Current Work	5-150 kPa	60-360 K

* 1-7 kPa measurements made only at 297 K

[†] 4 kPa measurements made from 300-475 K

[‡] 4.98 kPa measurements made from 175-300 K

1.1.5 - Planar Laser-Induced Fluorescence of Naphthalene

PLIF is a well-developed non-intrusive flow diagnostic technique that enables imaging of the two-dimensional distribution of a chemical species in a flow (Eckbreth, 1996). PLIF uses a laser sheet to interrogate a slice in the flow containing the species of interest. In the case of naphthalene PLIF, an ultraviolet (UV) laser is used to excite the vapor molecules, resulting in fluorescence that is detected by a digital camera. When factors affecting the fluorescence intensity such as collisional quenching, temperature, and optical collection efficiencies are accounted for, the PLIF signal can be converted into species number density and/or mole fraction (Hanson et al., 1990). Numerous compressible flow fields have been studied using PLIF of species including—but not

limited to—acetone, CH, CO, CO_2, OH, krypton, naphthalene, NO, and toluene (Eckbreth, 1996). PLIF has also been used to investigate various capsule geometries in high speed flows including Apollo capsule designs and variants of the Orion MPCV studied in the current work (Danehy et al., 2006; Alderfer et al., 2007; Danehy et al., 2009; Combs et al., 2015).

Naphthalene PLIF has seen limited use to date and only recently has the technique been used in supersonic turbulent boundary layer (Lochman, 2010; Buxton et al., 2012). The first published use of the technique was by Ni and Melton in 1996. In their work, two-dimensional fluorescence lifetime imaging of hot (298-723 K) turbulent nitrogen jets seeded with naphthalene was performed (Ni and Melton, 1996). The study was conducted in an oxygen-free environment, making the fluorescence lifetime measurements independent of species concentration. To properly calibrate the technique, fluorescence lifetimes of naphthalene vapor seeded into N_2 were measured using a flowing gas cell at the pressure of 100 kPa and over the temperature range of 298 K to 723 K. This study provided an empirical formula relating naphthalene fluorescence lifetime directly to temperature. Two-dimensional fluorescence lifetimes were then calculated by comparing the relative intensities of two images separated 113 ns in time and acquired immediately after excitation of the naphthalene molecules by a frequency-quadrupled Nd:YAG laser. The technique yielded instantaneous two-dimensional temperature fields of the turbulent jets (Ni and Melton, 1996).

In another early work, Gould (1998) used naphthalene PLIF to investigate evaporated gas surrounding droplets. In the study, spheres of solid naphthalene were used to simulate liquid droplets, and the gas-phase (sublimed) naphthalene was visualized using the PLIF technique (Gould, 1998). The images depicted various turbulent structures

emanating from the naphthalene spheres, indicating that an oscillating naphthalene boundary layer could be generating turbulence in the separated flow region behind the spheres.

Kaiser and Long (2005) used naphthalene as a fuel tracer in combustion experiments. Equivalence ratio and temperature were measured in a two dimensional plane by seeding naphthalene vapor into a mesoscale burner. A two-line ratiometric PLIF thermometry technique was developed through calibrations of the naphthalene fluorescence signal as described in Section 1.1.4 (Kaiser and Long, 2005). The naphthalene vapor in the burner was excited by a 266 nm planar laser sheet generated by a frequency-quadrupled Nd:YAG laser. The resulting fluorescence was imaged by an intensified CCD camera and 20 images were averaged to improve the signal-to-noise ratio (SNR). Large-scale features could be distinguished in the images depicting equivalence ratio, however, after converting the images to temperature an SNR of 11 was the best that could be achieved (Kaiser and Long, 2005).

In the precursor to the current work, Lochman (2010) used naphthalene PLIF to study the transport of ablation products in a Mach 5 turbulent boundary layer. A solid naphthalene insert was flush-mounted in the floor of a wind tunnel and 266 nm excitation was used to fluoresce the naphthalene vapor downstream of the insert. This technique provided images of naphthalene vapor in the turbulent boundary layer with excellent SNR, visualizing both large and small-scale turbulent structures. However, while some spectroscopic measurements were made, as described in Section 1.1.4, a temperature correction was only applied to the profile of the naphthalene boundary layer to yield a "corrected" profile and the images presented are qualitative visualizations. Buxton et al. continued this work in 2012, collecting simultaneous PIV and naphthalene PLIF in a

Mach 5 turbulent boundary layer using the same naphthalene insert design as Lochman (2010), providing relative scalar-velocity data of ablation-products transport in the boundary layer. However, naphthalene concentration was not determined from the PLIF images since the PLIF signals were not corrected for temperature effects and the images suffered from poor SNR. Both studies observed that the stagnation temperature of the wind tunnel greatly affected the quality of images collected, owing to the high sensitivity of naphthalene's vapor pressure to temperature. For example, images collected with a stagnation temperature of 360 K were significantly improved when compared to those acquired with a stagnation temperature of 350 K since the vapor pressure of naphthalene nearly doubles over this 10 K temperature increase. Also, use of either a double-pulsing laser or a pulse-stretched laser were shown to increase the SNR of images since the authors claim that naphthalene fluorescence can become saturated at relatively low laser power densities. Lastly, measured fluorescence signal was found to be noticeably reduced on humid days when the air supplied to the wind tunnel had a higher moisture content.

In work by Regert et al. (2013) naphthalene PLIF was employed in a Mach 6 boundary layer to study transition due to roughness elements. Naphthalene was introduced into a laminar boundary layer via a thin coating of the material upstream of the roughness elements. The naphthalene that was introduced into the flow was then imaged using PLIF and revealed flow structures such as streaks, vortices, and wave packets downstream of the roughness elements.

1.1.6 - Particle Image Velocimetry in Supersonic Flows

Particle Image Velocimetry (PIV) is a mature experimental diagnostic for determining velocity fields in two or three dimensions in a fluid flow (Adrian and Westerweel, 2011). To measure velocity, sub-micron scale particles are seeded into the

flow to track fluid motion. These particles are then excited by a double-pulsed light sheet (generally a laser). The scattered light from the particles is then recorded by an imaging device for each laser pulse. The images are then subdivided into interrogation windows and mean particle motion in each subdivision can be determined by cross-correlations performed between the two images, yielding a velocity vector for each window.

While technical challenges related to particle seeding and image acquisition rate initially limited PIV to relatively low speed flows, advances over the past twenty years have extended the use of PIV to supersonic wind tunnel facilities (Scarano, 2008). PIV now sees extensive use in many types of supersonic flows (Scarano, 2008; Adrian and Westerweel, 2011). The following is intended to provide a sampling of some relevant examples of applications of PIV to supersonic flows and is by no means comprehensive.

One of the earliest applications of PIV in a supersonic facility was by Humphreys et al. in 1993 at NASA Langley Research Center. The authors claimed to be the first to use PIV in a Mach 6 flow and made velocimetry measurements for supersonic flow over a wedge (Humphreys et al., 1993). The detrimental effect of particle lag in supersonic flows was illustrated and it was estimated that the 1 μm Al_2O_3 particles recovered 10 mm downstream of the shockwave (Humphreys et al., 1993). Later, Urban et al. (1998) used PIV to study a compressible mixing layer behind a splitter-plate at various compressibility conditions. The authors presented velocity measurements in both the plan-view and side-view planes. The images indicated that instantaneous velocity fields display similar large scale structures to those previously observed in instantaneous scalar visualizations. In a subsequent publication, Urban and Mungal (2001) again investigated a compressible mixing layer using PIV at various compressibility conditions. It was observed that under these conditions peak transverse

vorticity values were confined to thin streamwise sheets. Additionally, it was noted that compressibility was seen to inhibit mixing by interrupting transverse motion. Scarano and Oudheusden (2003) used PIV to study the wake behind a blunt-based two-dimensional body in a Mach 2 freestream. In the subsequent analysis of the velocity data a double-row of counter-rotating vortical structures was identified in the wake. A Mach 7 flow over two-dimensional double compression ramp was investigated by Schrijer et al. (2006) using PIV and Schlieren and the measurements showed good agreement with compressible flow theory.

PIV has been employed often to study shockwave boundary layer interaction. A series of experiments were conducted in the early 2000s to study the relationship between boundary layer fluctuations and separation shock unsteadiness (Unalmis et al., 2000; Beresh et al., 2002; Hou et al., 2003). The researchers used PIV to measure instantaneous, mean, and fluctuating velocity in the streamwise and transverse directions in Mach 2 (Hou et al., 2003) and Mach 5 (Unalmis et al., 2000; Beresh et al., 2002) turbulent boundary layers. Piponniau et al. (2009) and Humble et al. (2009) both used PIV to study this phenomenon in Mach 2 flows. Tomographic PIV was employed in the work by Humble et al. (2009), and the authors identified many three-dimensional coherent structures in the flow such as regions of low and high-speed fluid aligned in the streamwise direction upstream of the shockwave. Elsinga et al. (2010) also used tomographic PIV to measure the velocity field in a Mach 2 turbulent boundary layer. The authors observed coherent structures like hairpin vortices and long low-speed zones, noting similarities between this flow and subsonic turbulent boundary layers.

Ganapathisubramani et al. (2006) made PIV measurements of the turbulent boundary layer in a Mach 2 flow. Velocity measurements were made in the streamwise-

spanwise plane at two different transverse locations that illustrated the presence of strips of low- and high-speed fluid that were coherent over large streamwise distances (Ganapathisubramani et al. 2006). Additionally, Wagner et al. (2009) used PIV to study unstart in an inlet-isolator model at Mach 5, determining instantaneous and mean velocity fields in the streamwise-transverse and streamwise-spanwise planes. In a previous naphthalene PLIF experiment at The University of Texas at Austin, Buxton et al. (2012) conducted PIV simultaneously with naphthalene PLIF in a Mach 5 turbulent boundary layer. PLIF images were captured between the two PIV images to achieve simultaneous acquisition, allowing instantaneous velocity fields to be compared to local PLIF signal. Mean and instantaneous boundary layer profiles of velocity, RMS velocity, and fluorescence signal were determined as well. The results indicated that there was a strong correlation of high fluorescence signal with high velocity wall-normal fluctuations and negative streamwise velocity fluctuations away from the wall (Buxton et al., 2012).

1.1.7- Scalar Transport

Experiments aimed towards developing an improved understanding of the physics of scalar transport have seen interest from researchers for some time. Laser diagnostics, including Rayleigh scattering and LIF, have been used extensively for investigating scalar transport in both water and gas-phase flows. Clemens and Mungal (1992) studied the structure of planar mixing layers using planar laser Mie scattering while Messersmith and Dutton (1992) used NO LIF and Mie scattering of condensed ethanol to investigate mixing in a compressible mixing layer. NO PLIF was also used by Clemens and Paul (1995) to study mixing in the shear layer of a jet seeded with NO. The quantitative fraction of mixed fluid was then determined using the PLIF signal. Rossman et al. (2002) also used NO PLIF to study mixing, investigating the mixing layer downstream of a

splitter plate placed in a shock tunnel. Rossman et al. (2002) corrected the NO PLIF signal for temperature and pressure effects using an analytical model of NO fluorescence and presented mean and instantaneous images of NO mole fraction in the mixing layer for three different imaging planes. Simultaneous measurements of velocity and relative scalar concentration were made by Koochesfahani et al. (2000) and Hjertager et al. (2003) in liquid mixing layers. Koochesfahani et al. (2000) employed fluorescein LIF for measuring scalar and molecular tagging velocimetry (MTV) to determine simultaneous velocity vectors while Hjertager et al. (2003) employed PLIF of rhodamine dye complemented by PIV. These measurements enabled correlations to be made between local velocity and fluorescence signal. For instance, Koochesfahani et al. (2000) found that regions of high vorticity correlated with regions of relatively low fluorescence signal.

Many other studies have been conducted to study scalar transport in low-speed water flows (Hishida and Sakakibara, 2000; Crimaldi and Koseff, 2001; Crimaldi et al., 2002; Wagner et al., 2007; Somandepalli et al., 2010; Sarathi et al., 2012). Each of these works employed PLIF of rhodamine dye seeded into the flow upstream of the measurement region to measure scalar concentration. Additionally, Hishida and Sakakibara (2000), Wagner et al. (2007), Somandepalli et al. (2010), and Sarathi et al. (2012) complimented the PLIF images with simultaneously acquired PIV data which permitted analysis of the scalar-velocity field. Wagner et al. (2007), for example, observed evidence of scalar transport being governed by the presence of roller-like structures that transport regions of fluid with high scalar concentration into the bulk of the flow.

Scalar transport and mixing have also been investigated thoroughly in jet flows. Frank et al. (1996) demonstrated the use of simultaneous biacetyl PLIF and PIV to study

scalar transport in both a non-reacting jet and a flame, reporting a negative correlation between velocity normal to the flame front and reactant concentration. Turbulent water jets were investigated by Lemoine et al. (1996) and Borg et al. (2001) using simultaneous rhodamine LIF and laser Doppler velocimetry (LDV) and simultaneous rhodamine PLIF and PIV, respectively. In these works the profiles of both normal velocity and scalar concentration were approximately Gaussian and showed a strong correlation. Borg et al. (2001) also demonstrated good agreement between the two measurement campaigns. Su and Clemens (1999) employed PLIF and planar Rayleigh scattering to measure scalar and study mixing and scalar dissipation of an acetone-seeded propane jet. Additionally, a non-reacting air jet was studied by Fajardo et al. (2006) with simultaneous biacetyl PLIF and PIV, primarily as a demonstration of the technique.

Despite the abundant literature on scalar transport, there have been relatively few reported studies relating to scalar transport in supersonic flows, with even fewer studying transport in supersonic turbulent boundary layers. Palma et al. (2000) made temperature measurements in a supersonic laminar boundary layer in a shock tube using NO PLIF. The NO was naturally generated in the freestream. Instantaneous two-dimensional temperature fields were not determined but a mean boundary layer temperature profile was presented that compared favorably to computations of the flow. The effect of helium injection on a supersonic (Mach 8) turbulent boundary layer was studied by Auvity et al. (2001) using planar Rayleigh scattering of condensed CO_2 injected upstream of the measurement region. While it was shown that helium injection can significantly alter the structure of the boundary layer, details inside the boundary layer could not be visualized as the condensed CO_2 was primarily present in the cold freestream flow, resulting in extremely low signal inside the boundary layer. Su and Mungal (2004) and

Balakumar et al. (2008) each employed simultaneous acetone PLIF and PIV to study scalar transport in supersonic flows. Su and Mungal (2004) used the diagnostics to study a jet in a supersonic cross-flow while Balakumar et al. (2008) investigated Richtmyer–Meshkov instability growth in a shock tunnel flow. Aside from the previously discussed works by Lochman (2010) and Buxton et al. (2012), however, the only published work that could be found in the literature investigating scalar transport in a supersonic turbulent boundary layer was performed by Lin et al. in 2013. This was primarily a proof-of-concept experiment for a technique where velocity and density could be measured simultaneously with a single laser using nano-particles. The technique, called nano planar laser scattering (NPLS), employs nano-particles that the authors claim can track the flow faithfully enough so that the resultant scattering signal from the particles can be used to measure density. Since NPLS employs discrete particles, a second pulse from the same laser can then be used to obtain simultaneous PIV data. Using this technique, Lin et al. (2013) computed turbulent statistics in a Mach 3 supersonic turbulent boundary layer and presented plots of quantities such as the mean and RMS values of velocity and Reynolds stress components, which all showed good agreement with previous experimental results and computations.

1.2 - Context of Current Work

As illustrated by the reviewed literature, ablation involves many coupled physical mechanisms that have yet to be fully characterized by researchers. While most studies of ablation near reentry conditions have been focused on determining recession and heat transfer rates for given materials, very little work has been conducted to study the turbulent transport of ablation products. Similarly, studies using low-temperature sublimating ablators to simulate the ablation process have generally been motivated by an

interest in investigating blowing rates, recession rates, cross-hatching, and the effect of ablation on stability. Additionally, no known high-temperature ablation studies have investigated a capsule geometry and the research on low-temperature sublimating ablators has almost exclusively involved cones and hemispheres. The current work focuses on acquiring needed scalar-velocity data to better understand the physics of scalar transport through the use of PLIF coupled with PIV in a turbulent supersonic boundary layer and demonstrates the potential of the naphthalene PLIF technique for a reentry capsule model. Furthermore, this work may provide useful data for validation of CFD algorithms predicting ablation.

Neither PLIF nor PIV is a new technique, however there are many challenges involved in this novel application of both diagnostics. First, it is clear from the literature that while PLIF of several common species (e.g., OH, NO, acetone) have been implemented frequently over the past two decades, naphthalene PLIF requires further development to become a viable technique. As discussed in Section 1.1.4, naphthalene fluorescence has been investigated at an assortment of conditions in the available literature. However, a comprehensive study of naphthalene fluorescence at relevant wind tunnel conditions (particularly over a range of low temperatures and pressures) conducted with the intention of making quantitative PLIF measurements has not been conducted, as was show in Table 1.2. Therefore, to enable satisfactory quantitative naphthalene PLIF measurements, a complete study of the fluorescence of naphthalene with varying pressure and temperature is required. Additionally, it is a goal of this work to explore the possibility of using two-line naphthalene PLIF to make temperature measurements in supersonic flows. The fluorescence measurements conducted by Thurber et al. (1998) and Lochman (2010) are used as a model for this portion of the experimental program.

While ablation on a reentry capsule geometry is investigated (Chapter 5), the current work is primarily focused on the application of naphthalene PLIF to study the transport of ablation products in a Mach 5 turbulent boundary layer. First, this simplification aids in the generation of quantitative results since in a boundary layer a constant pressure assumption can be applied and the Crocco-Busemann relation can be used to make a first-order temperature correction in the absence of a simultaneous temperature measurement. Also, being a simpler and more general flowfield than a capsule flow, the findings of the boundary layer research may be more directly applied to the validation of CFD simulations. Another advantage of studying ablation products transport in a boundary layer as opposed to in a capsule flow is that measuring velocity with PIV is much more tractable. While Buxton et al. (2012) demonstrated the feasibility of conducting simultaneous PIV and naphthalene PLIF in a supersonic turbulent boundary layer, the few images presented suffered from poor SNR and were only semi-quantitative, leaving ample room for the current experimental campaign to expand on the research. Moreover, this review of the literature has demonstrated that measurements of scalar transport in supersonic turbulent boundary layers are scarce. Scalar transport has been investigated extensively in low speed flows, and those that have been made in supersonic flows have focused mainly on free shear flows. A clear need for the supersonic turbulent boundary layer scalar-velocity data provided in the current work was revealed in the literature survey.

Chapter 2: Calibration of naphthalene PLIF signal for making quantitative measurements of naphthalene mole fraction

2.1 - INTRODUCTION

As discussed in Chapter 1, spectroscopic data pertaining to naphthalene fluorescence are required in order to convert qualitative naphthalene PLIF images into two-dimensional fields of naphthalene mole fraction. Insufficient data are available in the existing literature at relevant conditions to accomplish this task, therefore studies are conducted to determine the characteristics of the fluorescence signal of naphthalene over a range of temperatures and pressures that could be experienced in the Mach 5 wind tunnel facility at The University of Texas at Austin. Additionally, the effect of varying excitation wavelength on the fluorescence signal is studied over a range of temperatures with the goal of developing a two-line PLIF thermometry technique.

2.2 - EXPERIMENTAL PROGRAM

2.2.1 - Naphthalene Fluorescence Test Cell Measurements

In the Mach 5 wind tunnel facility at The University of Texas at Austin, the stagnation temperature is approximately 350 K ± 4 K with a stagnation pressure of approximately 2.5 MPa ± 15 kPa, resulting in a freestream static temperature and static pressure of approximately 60 K and 5 kPa, respectively. To reproduce these conditions in a well controlled environment, a stainless steel test cell was employed in which temperature and pressure were controlled, to calibrate the fluorescence signal across the specified temperature and pressure ranges. A schematic of the test cell is shown in Figure 2.1, a photograph of the test cell and PMT is shown in Figure 2.2, and the full experimental setup for the fluorescence calibration experiments can be seen in Figures 2.3 and 2.4.

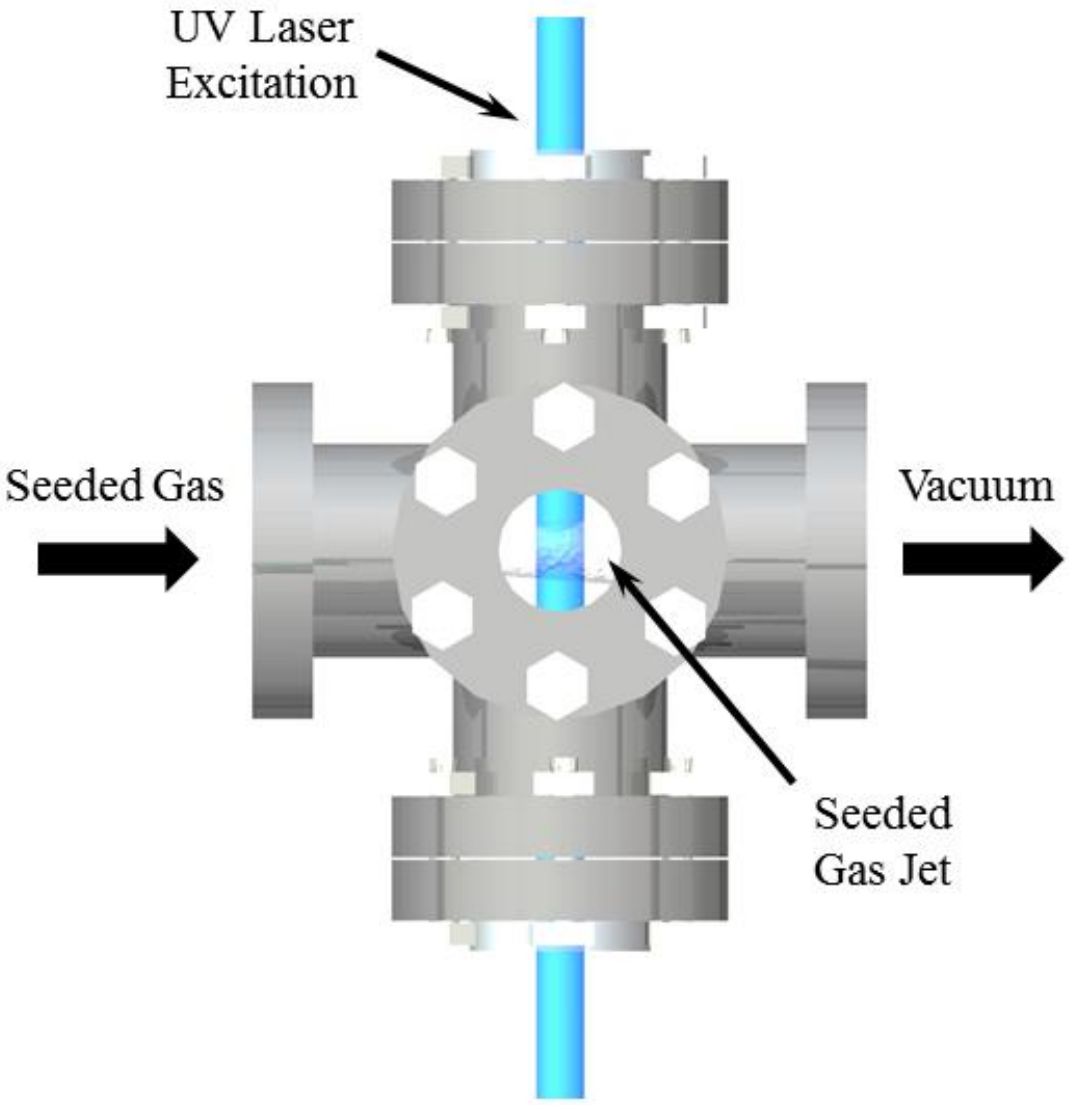

Figure 2.1: Schematic diagram of the temperature- and pressure-controlled fluorescence test cell.

Figure 2.2: Photograph of the temperature- and pressure-controlled fluorescence test cell with the PMT installed.

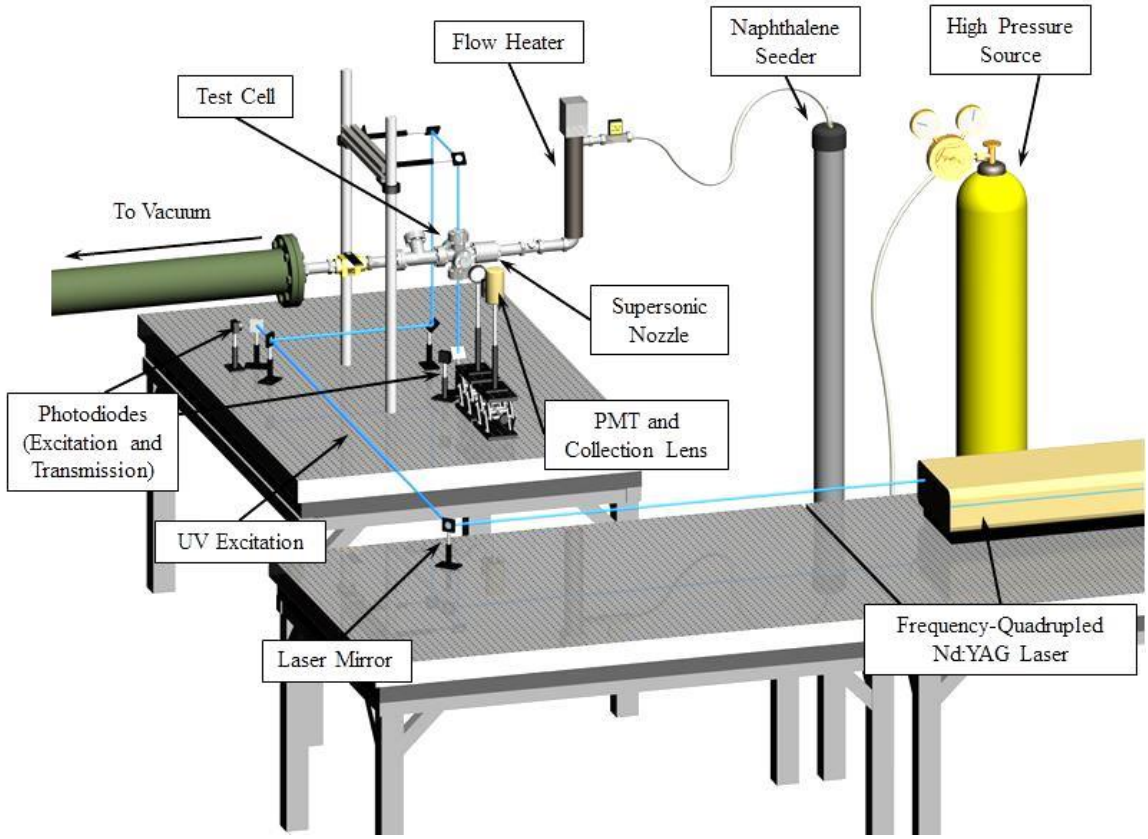

Figure 2.3: Experimental setup for the fluorescence calibration experiments using 266 nm excitation.

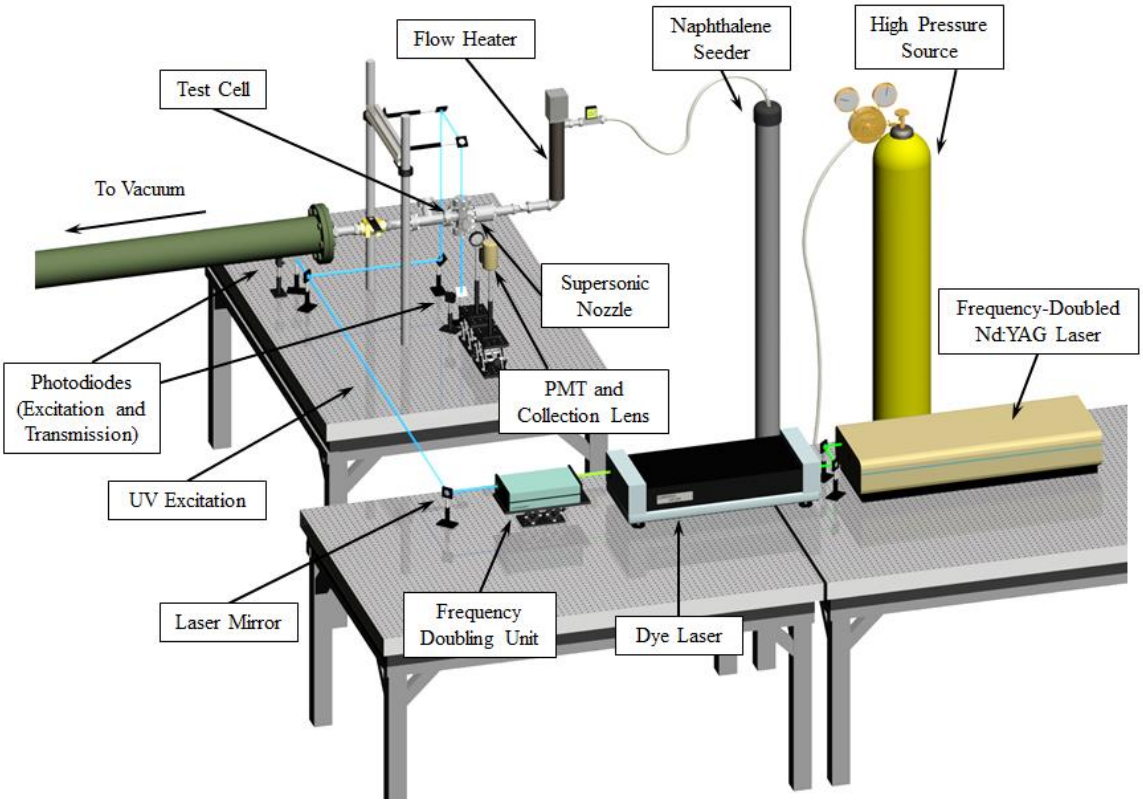

Figure 2.4: Experimental setup for the fluorescence calibration experiments using dye laser excitation.

The naphthalene vapor was introduced into the flow by a flow-through sublimating seeder, which is essentially a 75 mm diameter steel tube containing solid crystalline naphthalene (Acros Organics 99% purity). A carrier gas of air, O_2, and/or N_2 was used, which was supplied by pressurized gas cylinders. The flow exhausted to vacuum, which was created by a two-stage rotary positive vacuum pump (Roots Connersville). Inside the seeder, the solid naphthalene reached its saturation pressure and the resultant vapor-phase naphthalene was carried through the test cell by the carrier gas. For experiments employing 266 nm excitation, a frequency-quadrupled Nd:YAG laser (Quanta-Ray GCR-150) emitting light at 266 nm was used to excite the vapor particles.

The laser has a quoted linewidth of 1 cm^{-1}. For other experiments, discussed in Section 2.3.4, UV excitation ranging from 283 – 291 nm was obtained by frequency-doubling the output of a Bethune cell dye laser (Lumonics HyperDYE-300) that had a quoted linewidth of 0.5 cm^{-1}. The dye laser was pumped by a frequency-doubled Nd:YAG laser (Quanta-Ray GCR-150) emitting light at 532 nm and the dye used was Rhodamine 590 mixed in methanol with a concentration of approximately 1×10^{-4} mol/L. In both cases, the UV beam was transmitted to the test cell using laser mirrors and passed through the top and out the bottom of the test cell through fused silica windows. The resulting fluorescence was collected through a third fused silica window using a photomultiplier tube (Hamamatsu R363-10) and then displayed and recorded on an oscilloscope (Tektronix TDS-3054).

The temperature-controlled jet seeded with naphthalene was passed through the optically-accessible pressure-controlled cell. Measurements were made at pressures from 1 to 100 kPa by varying the gas flow rate or by adjusting the valve downstream of the cell. To achieve temperatures above 300 K, the gases were heated by an in-line electrical-resistance flow heater (Omega AHPF-121). In order to obtain flow temperatures below 300 K, the flow was expanded through a supersonic nozzle and the measurements were made near the nozzle exit. The combination of the supersonic nozzles and the in-line flow heater made it possible to attain static flow temperatures ranging from 100 K to 180 K with a Mach 3 nozzle, and from 175 K to 330 K with a Mach 1.8 nozzle. The stagnation temperature in the cell was monitored by a type-K thermocouple. The static cell pressure was monitored by a static pressure port (MKS Baratron 626A) while the stagnation pressure was monitored by a Pitot probe combined with a pressure transducer (Omega

PX-180B). Additionally, the mass flow rate of air was monitored and controlled by a mass flow controller (Alicat MCR-1000SLPM-D).

2.2.2 - Test Cell Fluorescence Data Processing

Measured fluorescence waveforms consisted of 128 consecutive waveforms that were averaged on the oscilloscope and saved to a computer using a custom-designed LabVIEW virtual instrument along with simultaneously-measured conditions from the test cell such as temperature, pressure, and flow rate. These averaged waveforms were then processed using a MATLAB script. The main objective of the script was to calculate the fluorescence lifetime of each waveform recorded by the PMT (example waveform shown in Figure 2.5) by deconvolving the fluorescence signal from the laser pulse (recorded using a photodiode, example shown in Figure 2.6). However, instead of deconvolving two measured signals and further enhancing noise, the code generated a simulated exponentially-decaying fluorescence pulse (example shown in Figure 2.7), which was then convolved with the measured laser pulse. This convolved signal was then iteratively fit to the measured signal using MATLAB's *lsqcurvefit* function until a suitable fluorescence waveform was found. The *lsqcurvefit* function was given an equation with a set of parameters that could be adjusted within a set of user-defined bounds in order to arrive at a solution. For the experiments in air where the bi-exponential component of the fluorescence was negligible, the following equation was employed:

$$S_f = H(t - t_1) * \left(1 - e^{-\frac{t-t_1}{t_2}}\right) * \left\{[1 - H(t - t_3)] + H(t - t_3) * e^{-\frac{t-t_3}{t_4}}\right\} \quad 2.1$$

where $H(t)$ represents a Heaviside function, t is time, t_1 and t_3 are temporal offsets, t_2 is the fluorescence rise time, and t_4 is the fluorescence lifetime (τ_f). Meanwhile, for the experiments in N_2 where the bi-exponential nature of the naphthalene fluorescence could not be neglected, a second fit function was employed:

$$S = H(t - t_1) * \left(1 - e^{-\frac{t-t_1}{t_2}}\right) * \left\{[1 - H(t - t_3)] + H(t - t_3) * \left[t_4 * e^{-\frac{t-t_3}{t_5}} + (1 - t_4) * e^{-\frac{t-t_3}{t_5+t_6}}\right]\right\} \quad 2.2$$

where t_1 and t_3 are again temporal offsets, t_2 is the fluorescence rise time, t_4 is a scaling factor used to normalize the two exponential decay functions, and t_5 and t_6 are the two components of the fluorescence lifetime (τ_1 and τ_2). A typical output from this fitting procedure is shown in Figure 2.5 along with the corresponding original waveform measured by a PMT.

The fluorescence lifetime was then extracted from the simulated fluorescence pulse functions. Only fits having an R^2-value greater than 0.99 were used to calculate fluorescence lifetimes. Each data point presented in the following figures represents the average of approximately 25 of these fits. This solution algorithm was developed in tandem with Burns (2014) who performed an uncertainty analysis and estimated an uncertainty due to the solver in fluorescence lifetime measurements of approximately 1% for waveforms with a signal to noise ratio greater than 10.

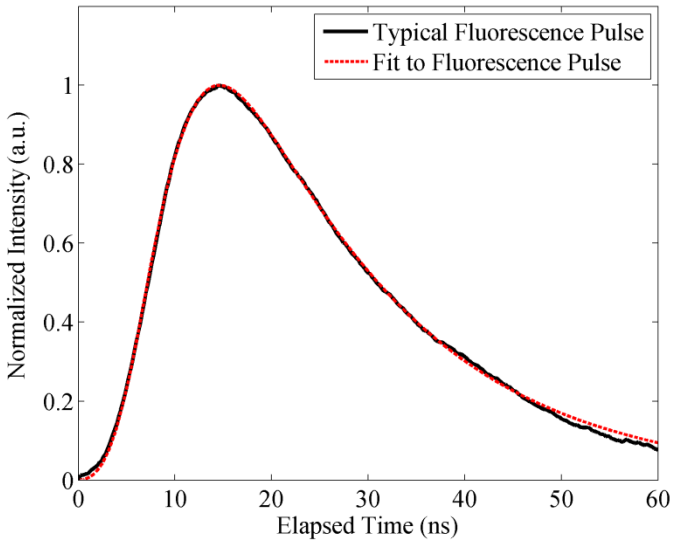

Figure 2.5: Typical plot of naphthalene fluorescence intensity with respect to time, as measured by a photomultiplier tube, along with the corresponding fit to the waveform.

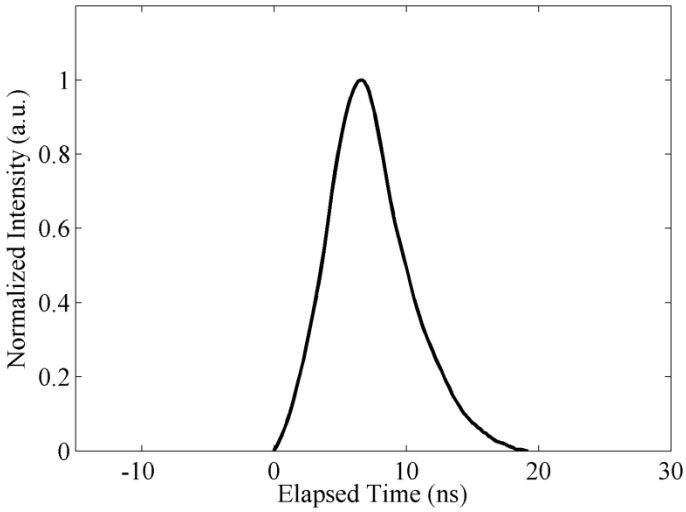

Figure 2.6: Typical plot of 266 nm laser pulse intensity, with respect to time, as measured by a photodiode.

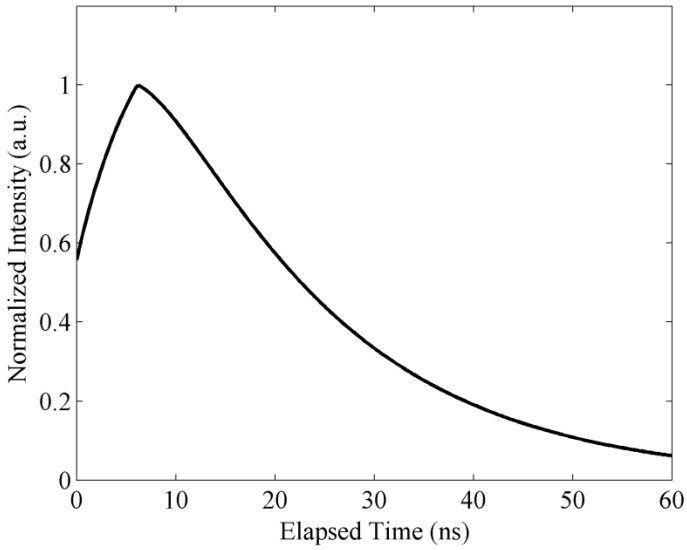

Figure 2.7: Typical simulated fluorescence pulse used in the deconvolution fitting procedure employed to calculate fluorescence lifetime.

2.3 - RESULTS AND DISCUSSION

2.3.1 - LIF Linearity with Laser Power Density

The linearity of the integrated fluorescence signal with respect to laser power density was investigated for 266 nm excitation. Here, the fluorescence signal from the naphthalene jet was collected using a PMT while the laser energy was varied. The frequency quadrupled Nd:YAG laser had a pulse duration measured at full width at half maximum (FWHM) of 7.0 ns. The laser beam was passed through the potential core of the air-naphthalene jet and the resulting fluorescence was collected. To obtain the area of the laser beam, a beam profile was measured using a scanning knife edge and photodiode. For the test cell experiments, the beam was measured to have a FWHM diameter of approximately 2.1 mm at the measurement location. The laser power density was then computed as the power per pulse divided by the area of the laser beam. The laser energy

was varied by placing a combination of a beam splitter (25% transmitting) and multiple fused silica flats into the beam. This method was used to maintain a constant beam profile as the energy was varied. The results are shown in Figure 2.8, which shows the fluorescence signal plotted as a function of varying laser power density. Each data point represents an average of 25 saved waveforms, each of which was composed of 128 waveforms averaged on the oscilloscope. Figure 2.8 shows that the signal is approximately linear over a wide range of laser power densities at 1 atm of air pressure, up to approximately 1.2 MW/mm^2—the maximum power density that could be achieved with the current laser setup. However, Lochman et al. (2010) showed that naphthalene fluorescence saturated at approximately 20 kW/mm^2 at atmospheric conditions. Additionally, Kaiser and Long (2005) restricted laser power density to below 5 kW/mm^2 due to a concern for saturation, although no linearity plot is provided. Faust et al. (2013), though, claim that naphthalene vapor should not saturate for power densities below 1.3 MW/mm^2, in excellent agreement with the findings of the current work. Also, Ossler et al. (2001) state that saturation was observed at 8 MW/mm^2, which was significantly higher than the values reported by other authors. The reason for this disagreement in the available literature is not known, however, the agreement of the current results with those of Faust et al. (2013) and Ossler et al. (2001) is encouraging. The study was continued under the assumption that experiments were being performed well below the saturation limit of naphthalene vapor.

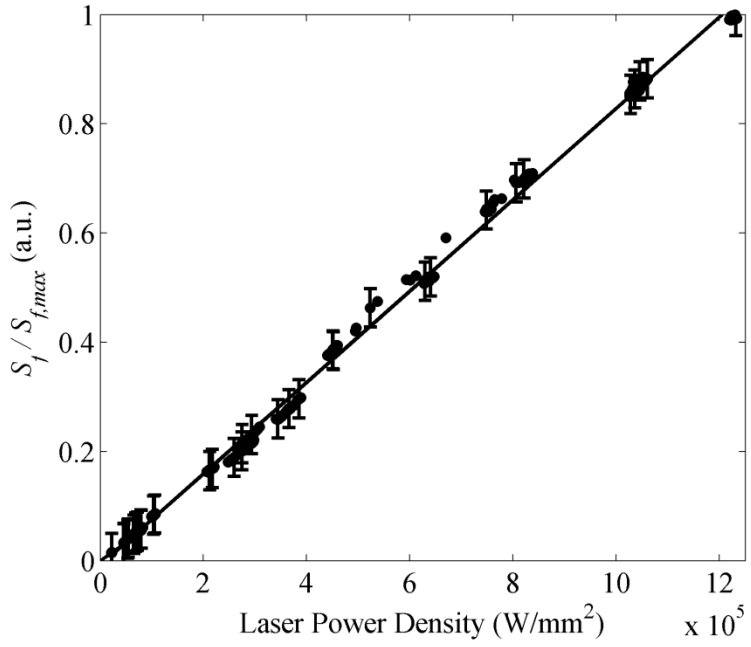

Figure 2.8: Normalized fluorescence signal at 290 K and 1 atm of air plotted versus 266 nm laser power density to verify that the signal varied linearly with laser energy. The symbols represent experimental data while the solid line is a linear fit to the data.

In PLIF imaging, it is generally desirable to operate in the linear regime of the fluorescence curve because this improves the quality of sheet corrections. However, this can limit the maximum energy that could be used to excite the naphthalene fluorescence and hence the fluorescence signals. In the current work this was not a concern as the measured fluorescence signal exhibited linear behavior up to the highest laser power density that could be achieved with the available equipment.

2.3.2 - LIF Pressure Dependence

The fluorescence lifetime of naphthalene vapor was measured at different pressures in a nitrogen environment and in a pure-air environment (ultra-zero air) with

266 nm excitation. The mole fraction of naphthalene during this study was maintained at approximately 1%. Nitrogen is not an efficient quencher of naphthalene fluorescence meaning the fluorescence decay in a nitrogen environment is due mainly to self-quenching (naphthalene-naphthalene collisions) and natural decay (spontaneous emission and non-radiative internal transfer). In contrast, the fluorescence decay in an air environment is dominated by oxygen quenching, which is very efficient (Beddard et al. 1973; Martinez et al. 2004; Kaiser and Long 2005). As discussed in Section 2.2.2, the fluorescence lifetimes were determined by fitting an exponential decay curve to the mean PMT-signal time-traces. It should be emphasized that the measured fluorescence decay is the average of the radiative decay from different vibrational levels; hence, fitting an exponential function to the observed signal provides the measure of the average lifetime of the different vibrational levels contributing to the emitted radiation. In general, fluorescence lifetimes were measured with an uncertainty of approximately ± 5%.

A preliminary study of the effect of nitrogen dilution on the fluorescence lifetime was conducted by measuring the fluorescence lifetime of naphthalene vapor in various bath gas compositions. Since nitrogen is a relatively weak quencher, the internal transfer mechanisms on the fluorescence lifetime are revealed. Figure 2.9 shows the variation of the inverse of the effective fluorescence lifetime (as seen in Eq. 1.5) with pressure in a nitrogen environment, and for reference, the inverse fluorescence lifetime variation in an air environment is also shown in Figure 2.10. In Figure 2.10, the points represent experimental data while the solid line represents a fit to the data. For reasons discussed in Section 1.1.4, the trend observed in a nitrogen environment is strikingly different from that in air. In contrast to the air case, the fluorescence lifetime of naphthalene in a nitrogen environment increases with increasing pressure and, beginning at about 50 kPa,

the inverse of the effective lifetime appears to asymptotically reach the value of 0.006 ns^{-1}, similar to trends observed by Faust et al. (2013) for naphthalene vapor in nitrogen at 373 K and 474 K. The results compare favorably to those of Lochman et al. (2010), as well. Furthermore, a qualitatively similar increase in lifetime with increasing pressure was reported by Beddard et al. (1973) and Soep et al. (1973) who excited naphthalene vapor in an argon environment using 268 nm and 265 nm light, respectively. However, the lifetimes measured by Beddard et al. (1973) approach a constant value at about 8 kPa. An estimate of the lifetime at high pressure (assuming an equilibrium distribution of population) using previously measured quenching cross sections was also made in Beddard et al. (1973). They estimated an inverse lifetime of 0.0056 ns^{-1} at a pressure of about 10 kPa (80 torr), which is very similar to the value obtained here at higher pressures (50 kPa). The differences observed in Figure 2.9 may be due to the weak quenching effects of nitrogen as compared to argon.

As seen in Figure 2.10, once oxygen is introduced the fluorescence lifetime decreases with increasing pressure due to oxygen quenching. This is expected since oxygen has been found to be an effective quencher of naphthalene fluorescence (Martinez et al. 2004). Additionally, the measured lifetimes agree well with the data from Lochman et al. (2010) and follow the same trend. The data also show a linear trend for pressures lower than 10 kPa, displaying the expected quenching-dominated Stern-Volmer behavior. However, for pressures greater than 10 kPa there is a clear deviation from linearity. This is most likely the result of limitations in the response time of the measurement system as the fluorescence lifetimes appear to be too short to accurately measure for air pressures greater than 10 kPa. With this in mind, the general agreement between the data shown in Figures 2.9 and 2.10 and the results of Lochman et al. (2010),

along with the demonstrated Stern-Volmer behavior, were considered to validate the test cell setup for air pressures below 10 kPa.

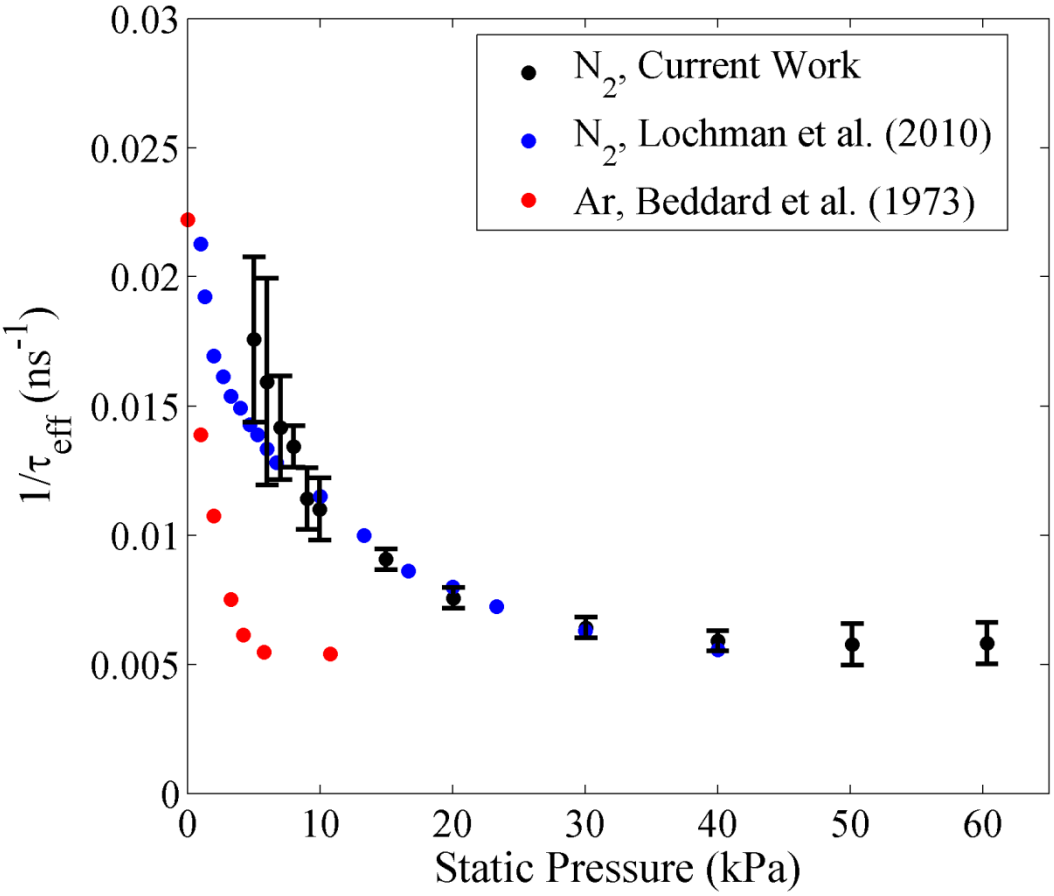

Figure 2.9: Inverse fluorescence lifetime measurements for naphthalene diluted in nitrogen at 292 K (current work and Lochman et al., 2010) and argon at 298 K (Beddard et al, 1973).

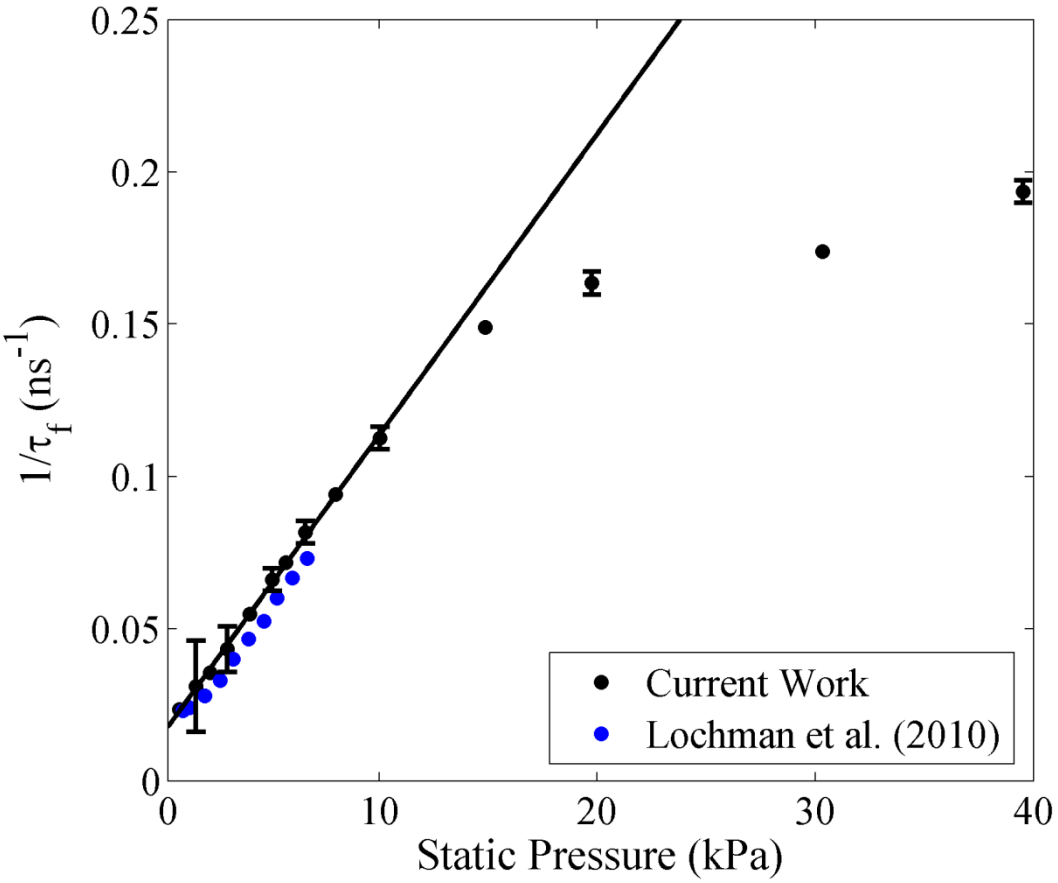

Figure 2.10: Inverse of the naphthalene fluorescence lifetime plotted versus static test cell pressure in an air environment at 292 K. The plot compares results from the current study to those collected previously by Lochman et al. (2010). The symbols represent experimental data while the solid line is a fit to the data.

Fluorescence lifetime measurements of naphthalene vapor were then made in various gas concentrations at room temperature, as shown in Figure 2.11 below. Again, the points represent experimental data, whereas the solid lines represent linear fits to the data. First, Figure 2.11 demonstrates that the lifetimes measured in the various gas environments are very similar as the ambient pressure approaches zero. This is expected

and provides some validation of the experimental technique employed. Furthermore, as shown before and discussed in Section 1.1.4, in a pure nitrogen environment the lifetime increases with increasing pressure and eventually levels off at pressures above approximately 50 kPa. Once oxygen is introduced, the fluorescence lifetime decreases with increasing pressure due to oxygen quenching. The effect is noticeable even for the lowest concentration of oxygen tested, 5%. Faster lifetimes were measured for increasing concentrations of oxygen, which was expected. The data also show agreement with the linear trend lines for pressures below 10 kPa for almost every case tested, suggesting Stern-Volmer behavior for the cases with oxygen. However, deviation from linearity is again observed for pressures greater than 10 kPa for several of the test conditions. The agreement with the linear trend lines is best for the cases with the lowest oxygen concentration, again suggesting that the measurement system could not accurately measure fluorescence lifetimes below a certain threshold.

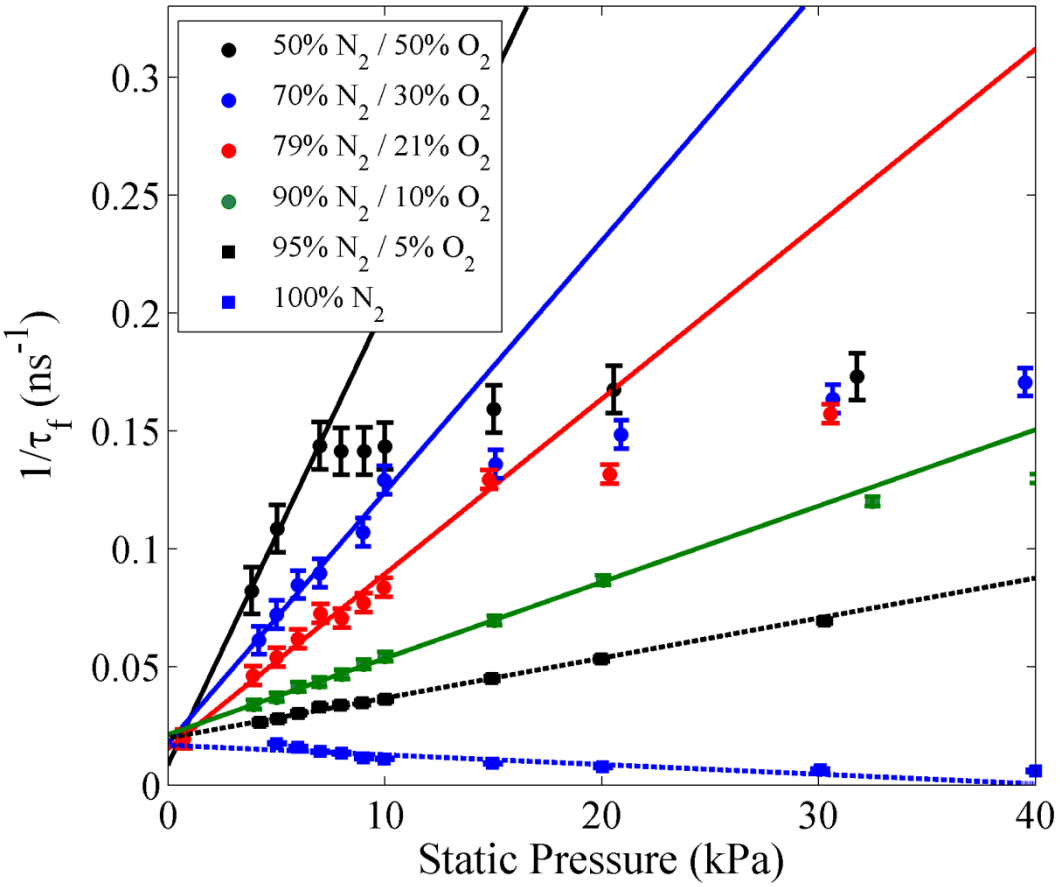

Figure 2.11: Inverse of the naphthalene fluorescence lifetime plotted versus static test cell pressure for various bath gas compositions at 290 K. The symbols represent experimental data while the solid lines are fits to the data.

2.3.3- LIF Temperature Dependence

The effect of temperature on naphthalene fluorescence was also investigated for 266 nm excitation. For these experiments, for a given run, the test cell pressure and mass flow rate of air and naphthalene vapor were held constant while temperature was controlled by varying the voltage supplied to an in-line flow heater. In Figure 2.12, fluorescence lifetime is plotted versus temperature for several different values of

pressure. A series of curve fits are also plotted as solid lines. The curve fits are of the form shown in Eq. 2.3 with fit parameters a_{ij},

$$\tau_f = \frac{1}{C_1 P + C_2} \qquad 2.3$$

$$where\ C_i = a_{i1} T^2 + a_{i2} T + a_{i3}$$

The form of the fit was chosen so that the inverse of the fluorescence lifetime would be linearly dependent on pressure, which is characteristic of the expected quenching-dominated Stern-Volmer behavior of naphthalene fluorescence.

The lifetimes plotted in Figure 2.12 appear to increase with increasing temperature for all pressure cases. However, at lower pressures the value of fluorescence lifetime begins to level off for temperatures above 400 K. Also, as expected, the measured lifetimes are shorter at higher pressures for a given temperature. These results compare favorably with those presented by Lochman et al. (2010) at 4.5 kPa and by Faust et al. (2013) at pressures above 1 atm. The normalized fluorescence signal is plotted versus temperature in Figure 2.13. The uncertainty in the integrated fluorescence signal measurements is approximately ± 9%. Similar to the fluorescence lifetime, the fluorescence signal appears to initially increase with temperature and then begins to decrease around 450 K. Measurements by Lochman et al. (2010) and Orain et al. (2011) agree with this result.

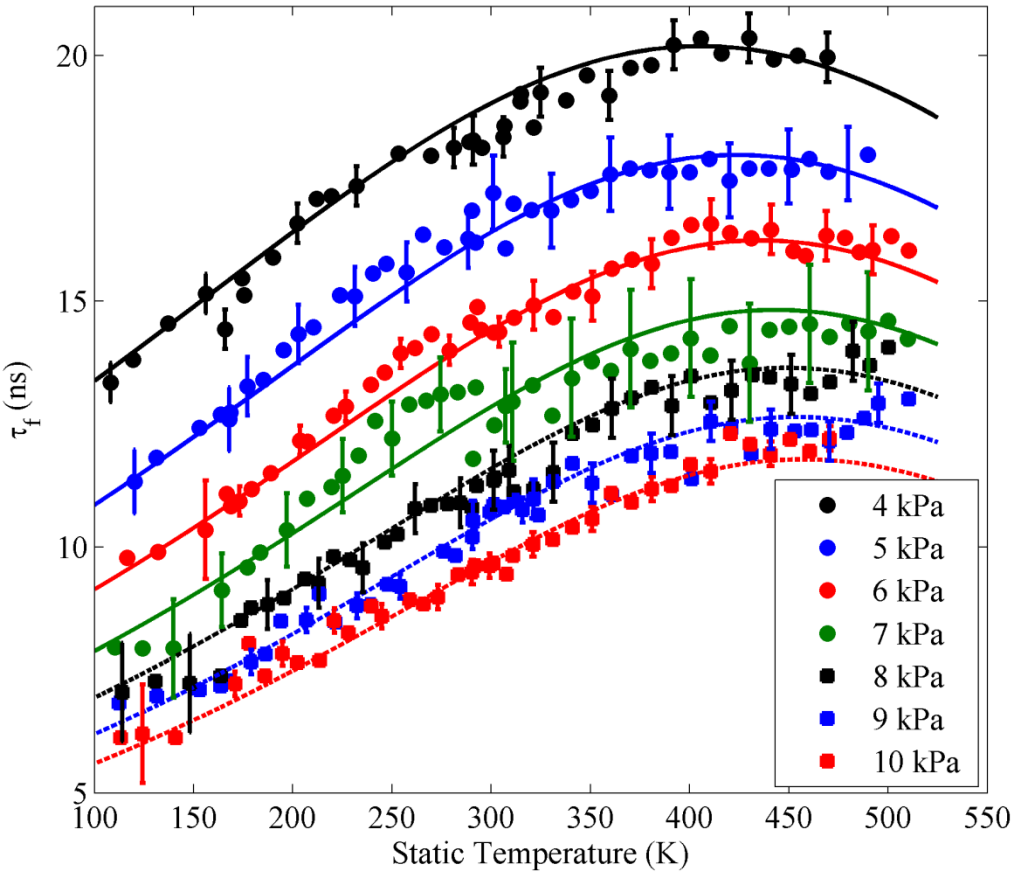

Figure 2.12: Naphthalene fluorescence lifetime plotted versus static test cell temperature at different pressures of air. The symbols represent experimental data while the solid lines are fits to the data.

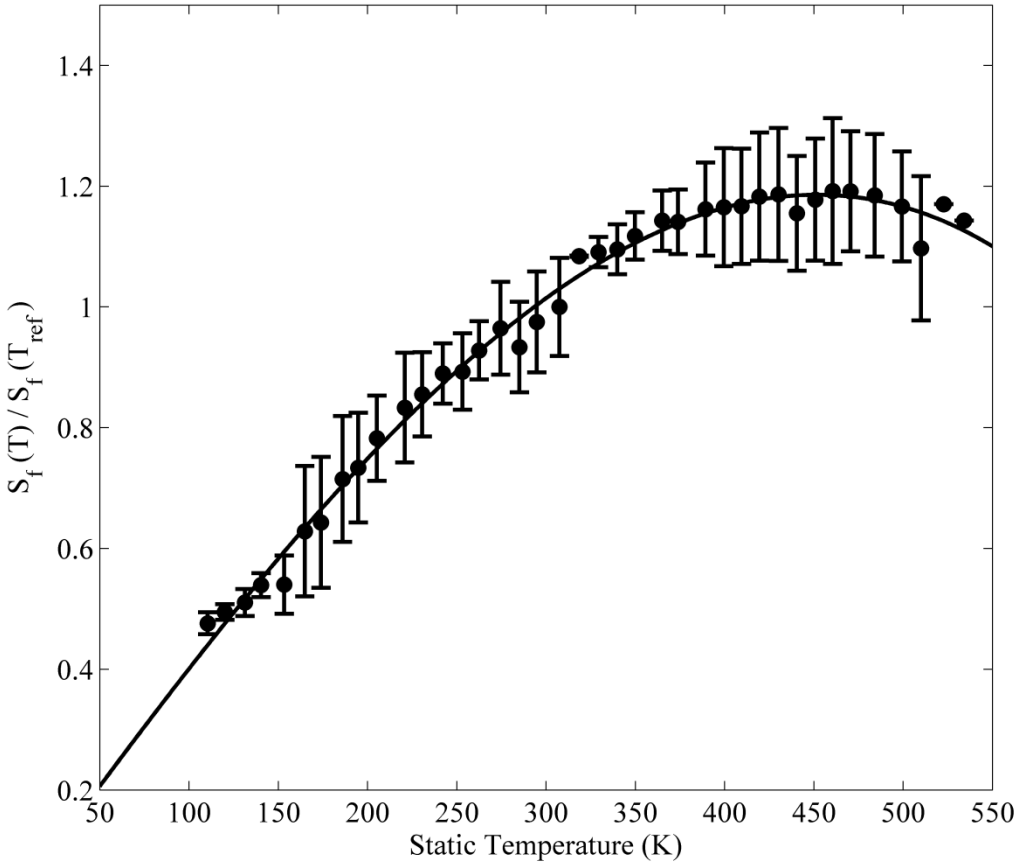

Figure 2.13: Integrated naphthalene fluorescence signal, normalized to the 300 K value, plotted versus static test cell temperature. The symbols represent experimental data while the solid line is a fit to the data.

The data shown in Figure 2.12 are plotted as a function of pressure in Stern-Volmer form in Figure 2.14 for four lines of constant temperature: 185 K, 240 K, 325 K, and 470 K. The same curve fit model plotted in Figure 2.12 is also presented in Figure 2.14 for lines of constant temperature. For oxygen-dominated quenching this plot should be linear, thus exhibiting Stern-Volmer behavior. Plotted in this form, the linear trend lines indeed fit the data, as expected based on previous research (Ossler et al. 2001;

Kaiser and Long 2005; Lochman et al. 2010; Orain 2011; Faust 2013). The quenching rate obtained from the slope of the fitted lines at 292 K is $k_Q = 0.86 \pm 0.07$ (bar ns)$^{-1}$. Since air is composed of 21% O_2, this gives a quenching rate of $k_Q = 4.1 \pm 0.3$ (bar ns)$^{-1}$ for O_2. This value is reasonably close to the value of $k_Q = 5.9 \pm 0.2$ (bar ns)$^{-1}$ measured by Martinez et al. (2004) using 308 nm excitation at 297 K and atmospheric pressure. In Figure 2.14, the y-intercept of the linear fit, which is related to the sum of the natural decay and non-radiative de-excitation, gives a lifetime of about 85.1 ns.

As illustrated by Koban et al. (2005), the slope of these linear fits is equal to the Stern-Volmer coefficient, k_{SV}. For the data in Figure 2.14 where O_2 is the dominant quencher we have:

$$\frac{\tau_0}{\tau_f} - 1 = k_{SV}^{O_2}[m^3]\, n_{O_2} = k_{SV}^{O_2}[bar^{-1}]\, P_{O_2}$$
$$where\ k_{SV}^{O_2} = \frac{k_Q^{O_2}}{A + k_{int}}. \qquad 2.4$$

Figure 2.15 shows that the slopes of the fits, and hence the Stern-Volmer coefficients, decrease with increasing temperature. This trend is again consistent with the available literature (Ossler et al. 2001; Kaiser and Long 2005; Orain 2011; Faust 2013). Figure 2.15 compares Stern-Volmer coefficients (with units bar^{-1} of O_2) calculated in the current work for naphthalene vapor quenched by oxygen to those presented in previous research by Lochman et al. (2010), Kaiser and Long (2005), Orain et al. (2011), and Faust et al. (2013). As can be seen in the figure, the Stern-Volmer coefficients from the current work show the same general trend found by previous researchers, although the particular values are noticeably different. Orain et al. (2011) and Faust et al. (2013) found the Stern-Volmer coefficient to decrease exponentially with increasing temperature,

which is roughly the trend found in the present study. These calculated Stern-Volmer coefficients agree with those found by Lochman et al. (2010) and Kaiser and Long (2005) within the experimental uncertainty. The Stern-Volmer coefficients were then used in Eq. 2.4 to calculate the collisional quenching cross section of naphthalene fluorescence due to oxygen with varying temperature. The resulting plot is shown in Figure 2.16. As can be seen in the figure, the quenching cross section decreases steadily with increasing temperature, decreasing by almost a factor of two over the temperature range investigated.

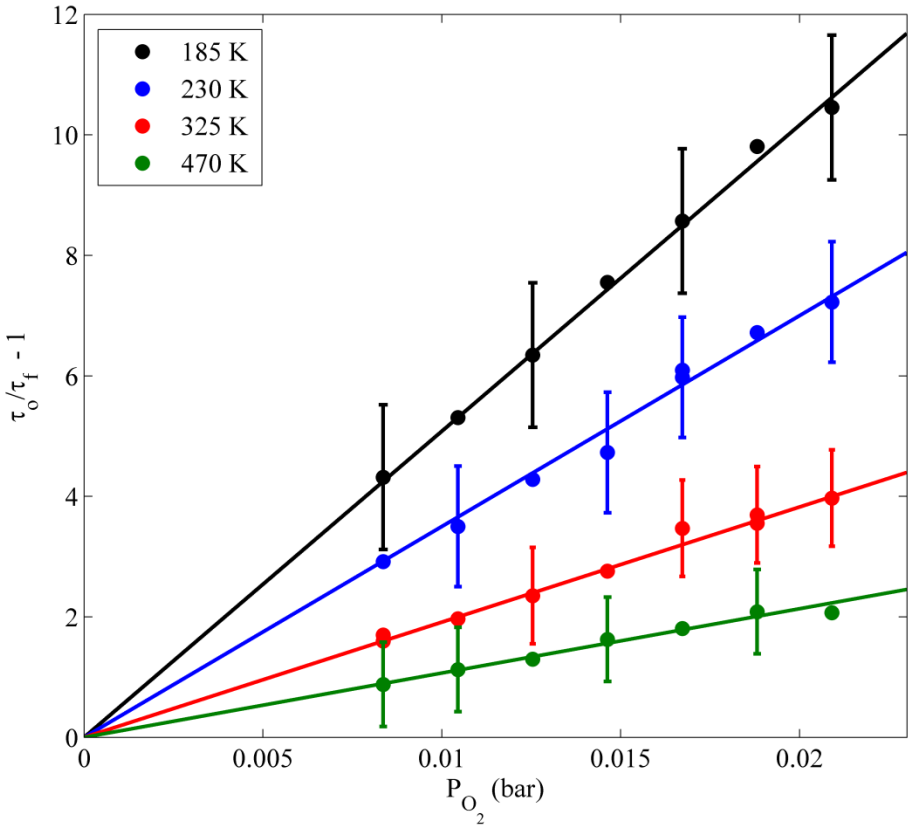

Figure 2.14: Stern-Volmer plot of naphthalene fluorescence in air at 185 K, 230 K, 325 K, and 470 K.

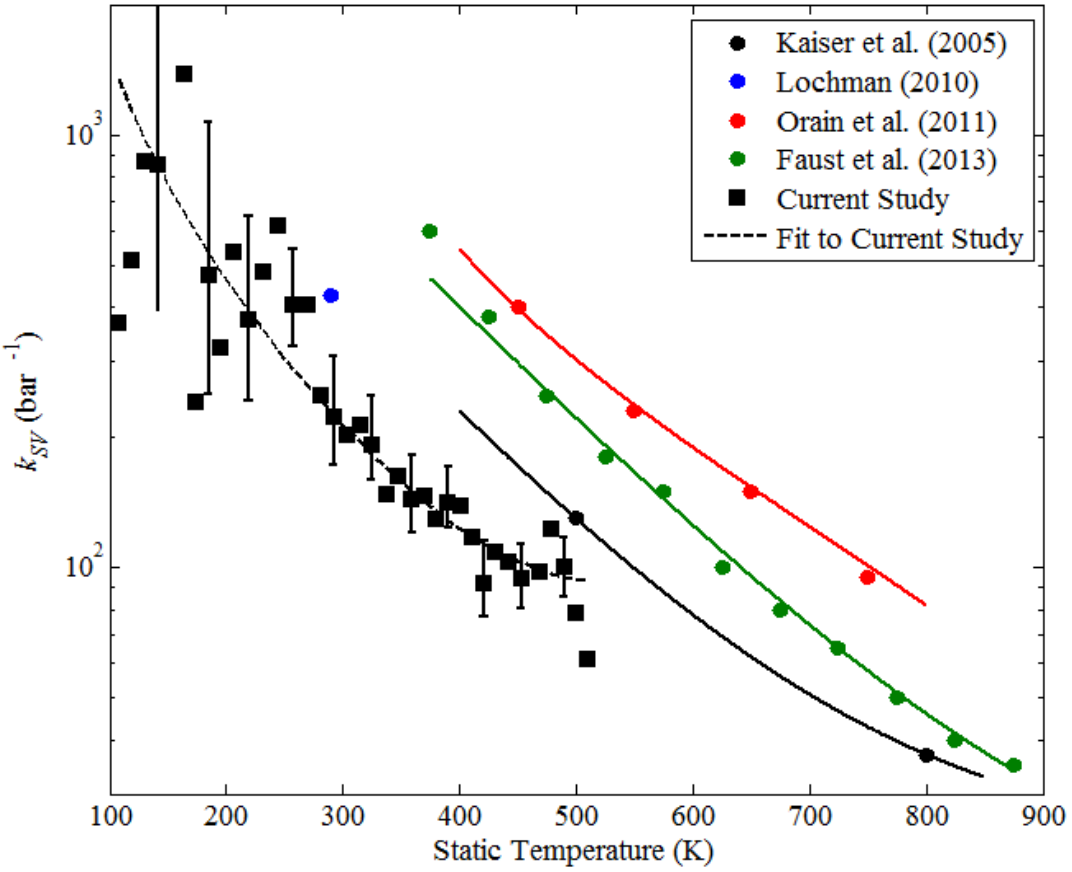

Figure 2.15: Naphthalene Stern-Volmer coefficients derived from oxygen quenching plotted versus temperature. The plot compares results from the current study to those from the available literature. The symbols represent experimental data while the solid lines are fits.

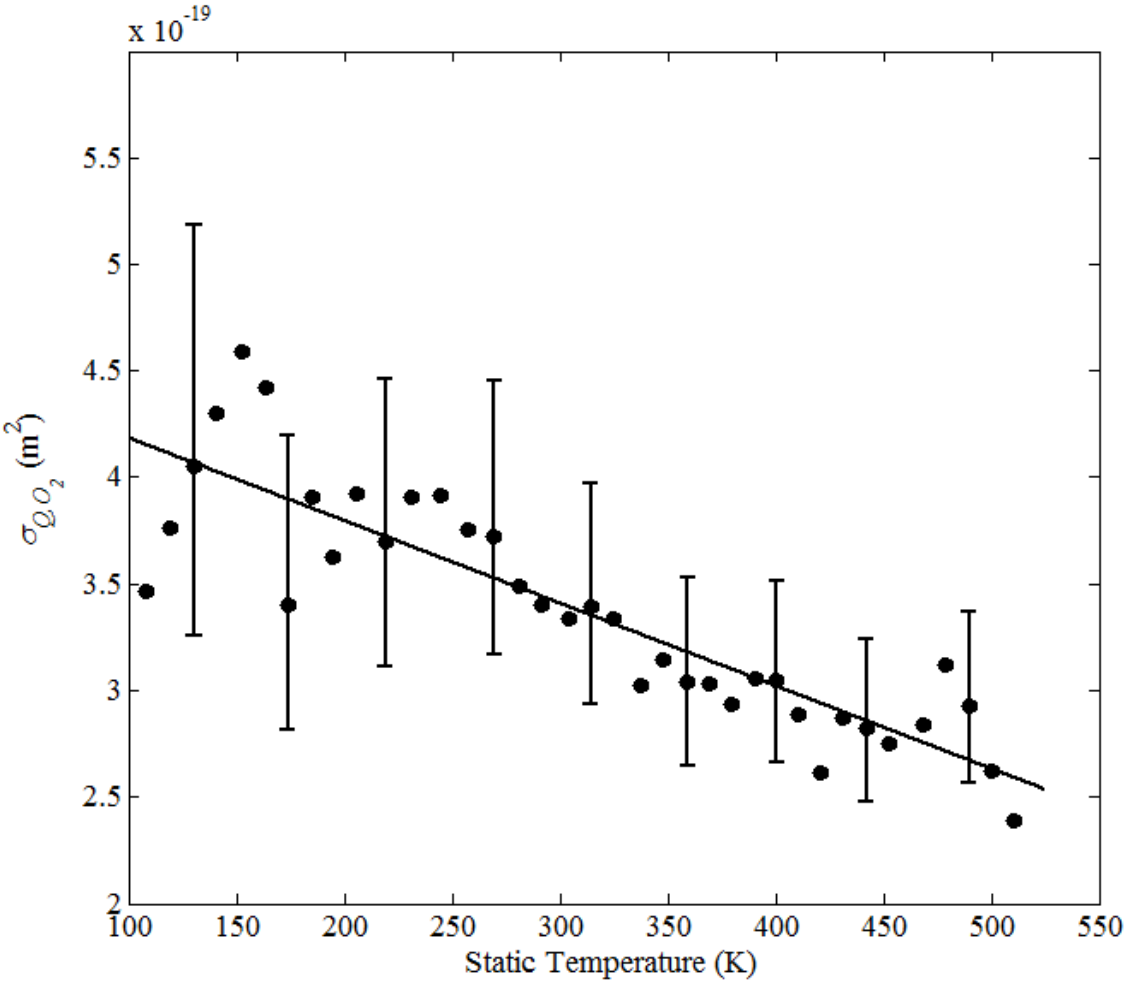

Figure 2.16: Computed cross section for quenching of naphthalene fluorescence by oxygen plotted versus static test cell temperature in air. The symbols represent experimental data while the solid line is a linear fit.

Equation 1.10 shows that relationships for the fluorescence yield and absorption cross section are necessary to convert naphthalene fluorescence signal into mole fraction. Toward this end, measured fluorescence decay times were converted to fluorescence yield and absorption cross section using Eqs. 1.7 and 1.8, respectively. Given that the

fluorescence lifetime measurements exhibited Stern-Volmer behavior, the fluorescence yield should obey some function of the form:

$$\frac{\varphi(T,P)}{\varphi(T_{ref},P_{ref})} = \frac{1}{C_1P + C_2} \Big/ \frac{1}{D_1P_{ref} + D_2}$$

$$where\ C_i = a_{i1}T^2 + a_{i2}T + a_{i3} \qquad 2.5$$

$$and\ D_i = a_{i1}{T_{ref}}^2 + a_{i2}T_{ref} + a_{i3}.$$

In light of this, curve fits were developed using Eq. 2.5 to fit to the calculated fluorescence yield data. The curve fit coefficients determined from the fitting procedure are shown in Table 2.1.

Table 2.1: Experimentally-determined coefficients in Eq. 2.5. The reference conditions used to correct the PLIF images were 4.92 ± 10 Pa and 295 K ± 2 K. While the values of the coefficients are independent of the chosen reference conditions, these fits are only valid over the tested temperature and pressure space of 100-525 K and 4-10 kPa in air.

a_{11}	7.77×10^{-8} 1/kPa/K^2	a_{21}	-4.12×10^{-8} 1/K^2
a_{12}	-7.57×10^{-5} 1/kPa/K	a_{22}	8.40×10^{-5} 1/K
a_{13}	2.41×10^{-2} 1/kPa	a_{23}	-2.61×10^{-3}

Equation 1.8 shows that the absorption cross section is dependent on the experimentally measured integrated fluorescence signal and the oxygen quenching cross section. In Figure 2.13 the integrated fluorescence signal appears to exhibit a polynomial dependence on temperature while the quenching cross section of naphthalene fluorescence due to oxygen appears to vary linearly with temperature in Figure 2.16. Combining this information with Eq. 1.8 led to the development of the following curve fit for absorption cross section:

$$\frac{\sigma_a(T)}{\sigma_a(T_{ref})} = \frac{S_f(T)}{S_{f,ref}(T_{ref})}\sqrt{\frac{T}{T_{ref}}}\frac{\sigma_{q,O_2}(T)}{\sigma_{q,O_2}(T_{ref})},$$

$$where\ S_f(T) = b_1T^3 + b_2T^2 + b_3T + b_4 \qquad 2.6$$

$$and\ \sigma_{q,O_2}(T) = c_1T + c_2.$$

The coefficients in Eq. 2.6 that result from the fitting procedure are given in Table 2.2.

Table 2.2: Experimentally-determined coefficients for curve fits to be used for calculating naphthalene absorption cross section. The reference conditions used to correct the PLIF images were 4.92 ± 10 Pa and 295 K ± 2 K. While the values of the coefficients are independent of the chosen reference conditions, these fits are only valid over the tested temperature and pressure space of 100-525 K and 4-10 kPa in air.

b_1	-8.72×10^{-9} 1/K^3	c_1	-3.88×10^{-22} 1/K
b_2	1.88×10^{-6} 1/K^2	c_2	4.57×10^{-19}
b_3	3.56×10^{-3} 1/K		
b_4	2.36×10^{-2}		

The resulting curve fits for normalized fluorescence yield and absorption cross section are shown in Figs. 2.17 and 2.18. Unsurprisingly, these two plots have very similar characteristics to Figs. 2.12 and 2.13 with fluorescence yield and absorption cross section increasing monotonically up to 400 K. This implies that in the boundary layer under investigation the fluorescence signal will have a linear dependence on both fluorescence yield and absorption cross section, given that the stagnation temperature of the wind tunnel facility is approximately 350 K. By using the curve fits from Eqs. 2.5 and 2.6 in Eq. 1.10 it is possible to convert naphthalene PLIF signal into naphthalene mole

fraction at locations in a flow where temperature and pressure are known, provided a reference image collected at known conditions is employed.

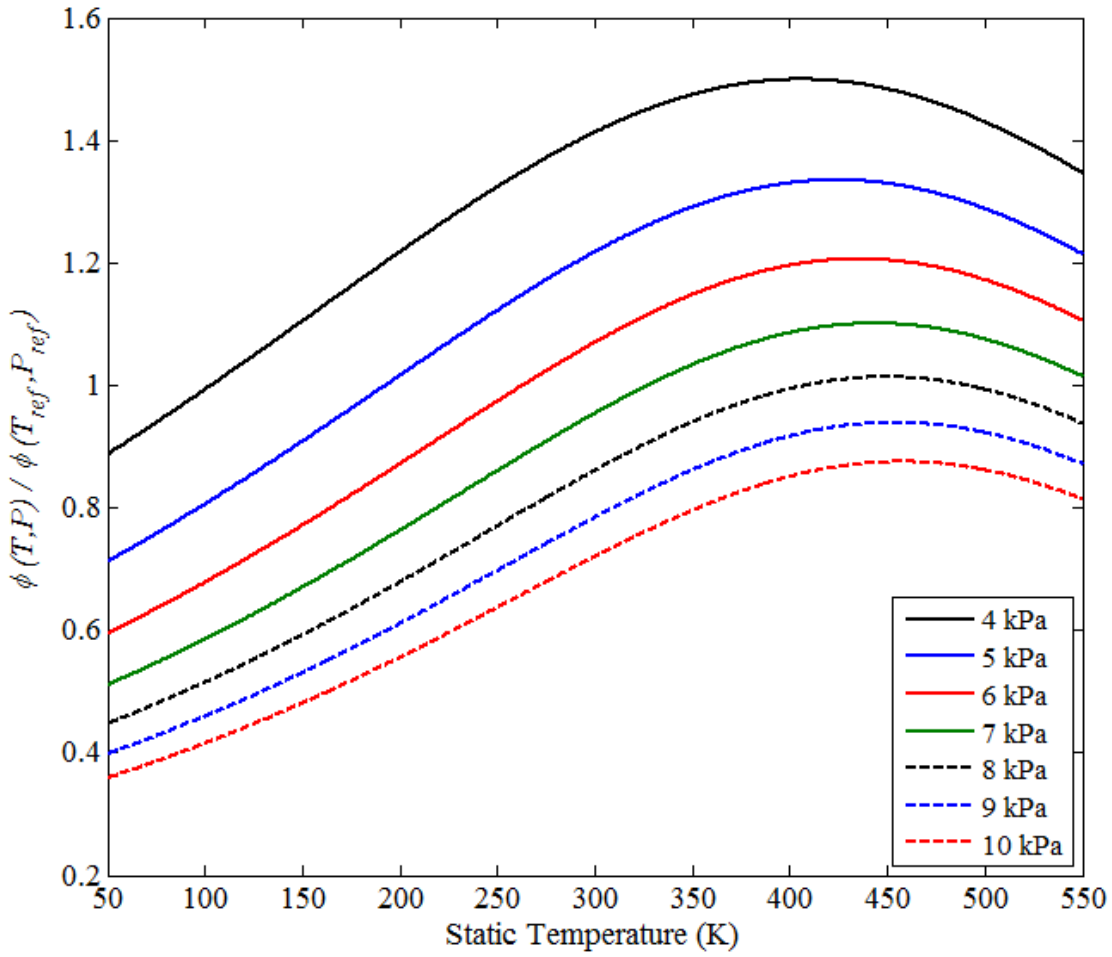

Figure 2.17: Computed normalized naphthalene fluorescence yield plotted versus static test cell temperature at different pressures of air. Reference conditions for the normalization were 6.13 kPa and 295 K.

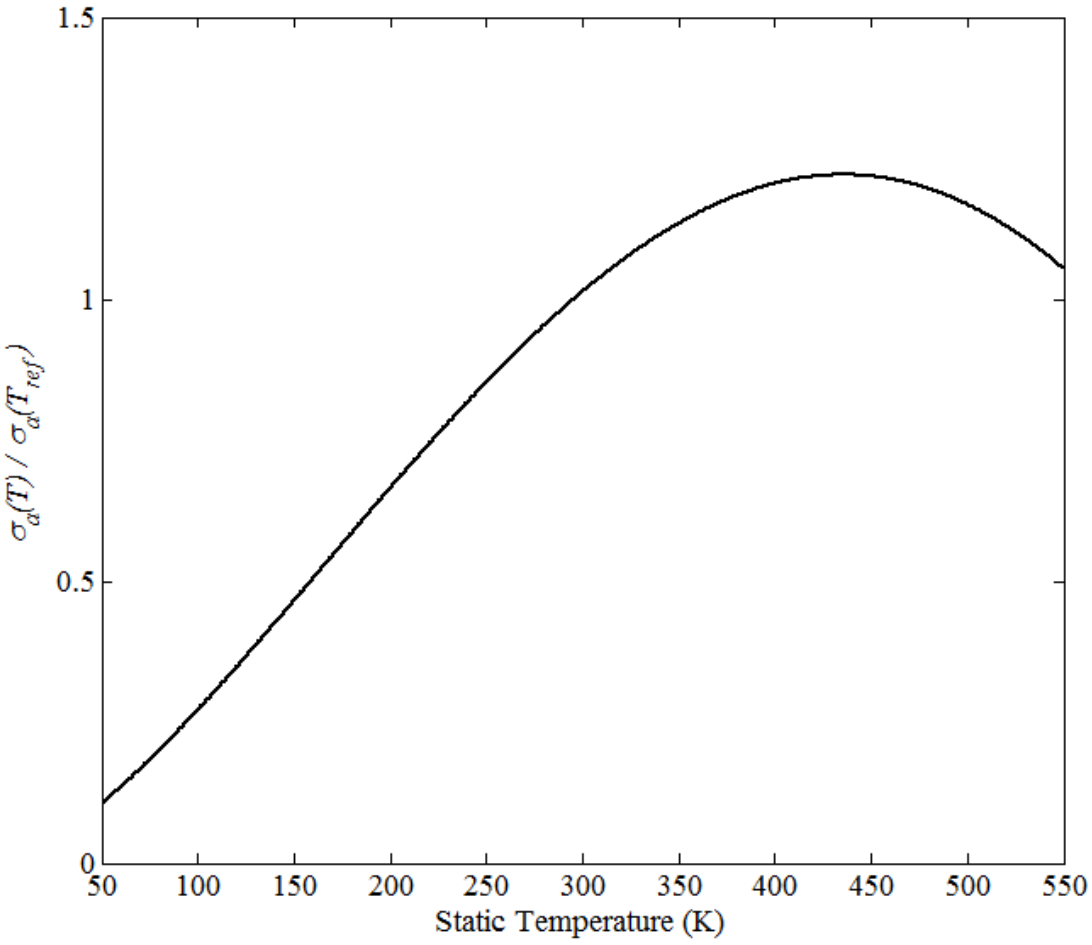

Figure 2.18: Computed normalized naphthalene absorption cross section plotted versus static test cell temperature in air. The reference temperature for the normalization was 295 K.

2.3.4 - LIF Excitation Wavelength Dependence

In addition to the spectroscopic LIF measurements collected using 266 nm excitation, the frequency-doubled output of a dye laser was employed to study the effect of varying excitation wavelength on naphthalene fluorescence. While the absorption and emission spectra of naphthalene have been well characterized in previous work (Beck et al., 1980; Beck et al., 1981; Du et al., 1988) the goal of the current study was to

make measurements that would enable a two-line ratiometric thermometry technique to be employed. As discussed in Section 1.1.4, knowledge of the temperature field is essential to the conversion of fluorescence signal to mole fraction. While approximations can be made to the temperature field using the Crocco-Busemann relation, this introduces a substantial uncertainty into the mole fraction calculation that can be mitigated with a simultaneous temperature measurement.

In contrast to the work by Kaiser and Long (2005) where fluorescence from a single excitation source was measured over different emission bands using optical filters, the current objective was to develop a technique with temperature sensitivity employing two separate excitation wavelengths, as done by Thurber et al. (1998). Kaiser and Long (2005) observed a sensitivity of approximately 2:1 over a 500 K temperature range using their technique, while Thurber et al. (1998) observed sensitivities with acetone as high as 14:1 over a 700 K temperature range for acetone fluorescence using the two-line excitation method. Furthermore, Kaiser and Long (2005) only achieved an SNR of approximately 5 for instantaneous temperature fields.

Figure 2.19 shows the normalized integrated fluorescence signal of naphthalene vapor versus static temperature when excited with four different excitation wavelengths: 266 nm, 283 nm, 287.5 nm, and 291 nm. It should be noted that the three additional wavelengths tested result in excitation to S_1 while 266 nm light results in excitation to S_2 (Watts and Strickler, 1966; Laor and Ludwig, 1971; Beddard et al., 1973). These plots were collected at constant pressure conditions between 4 and 6 kPa and at least four test cell runs were averaged to generate each plot. The symbols represent the experimental data while the solid lines represent curve fits to the data. The curve for 266 nm excitation has already been shown (Figure 2.13) and discussed in Section 2.3.3, and has minimal

temperature dependence above 300 K relative to the other excitation wavelengths. Excitation with 287.5 nm exhibited the strongest sensitivity to changing temperature over the range tested, increasing by a factor of four nearly linearly. The normalized fluorescence signal resulting from 291 nm excitation also showed a monotonic trend with a 3:1 increase in intensity from 100 to 500 K. Lastly, excitation with 283 nm light resulted in the opposite relationship, with fluorescence signal decreasing with increasing temperature by a factor of two. This trend was not observed with excitation by any other laser line but was consistent and repeatable, with error bars shown in Figure 2.19. It may be possible that this unique trend was observed with 283 nm excitation owing to its proximity to the boundary of the entangled S_1 and S_2 singlet states (279.21 nm) of the naphthalene molecule. A more thorough investigation to determine the relationship between the slopes of the curves in Figure 2.19 and excitation wavelength would be helpful in understanding this result.

The ratios of the integrated fluorescence signal curves presented in Figure 2.19 are shown in Figure 2.20. Since the highest excitation energy—and thus the largest resultant fluorescence signal—could be achieved with 266 nm excitation, this line was chosen as one of the two to be used for the two-line PLIF measurement. Therefore, in Figure 2.20, four of the five pairs presented are relative to the fluorescence signal resulting from 266 nm excitation. The lone exception is the ratio of fluorescence resulting from 287.5 nm excitation to fluorescence from 283 nm excitation, as this excitation pair resulted in the highest temperature sensitivity in the current work: 7:1 over the 400 K temperature range investigated. Also illustrated in the figure, even though excitation with 287.5 nm light resulted in the highest temperature sensitivity in Figure 2.19, this only results in a sensitivity of approximately 2:1 when compared to 266 nm excitation. The

curve for the fluorescence ratio from the 291 nm / 266 nm pair shows a similar trend; however, since fluorescence signal actually decreased with increasing temperature for 283 nm excitation, as illustrated in Figure 2.19, the ratio of fluorescence from 283 nm excitation to 266 nm excitation resulted in the highest temperature sensitivity over the temperature range investigated. Lines for both 266 nm / 283 nm and 283 nm / 266 nm are presented in Figure 2.20 so that the relative temperature sensitivity can be compared to the other excitation wavelengths. As seen in the figure, selecting 266 nm and 283 nm as the two excitation wavelengths results in a ratiometric sensitivity of over 4:1 for the 400 K temperature range investigated. Compared to the 2:1 sensitivity of the two-color imaging technique developed by Kaiser and Long (2005) it is clear that significantly more temperature sensitivity can be achieved with the current two-line excitation method. However, it should be noted that this technique introduces the added complexity of a second excitation source. Additionally, it may be possible to increase the sensitivity of either technique by choosing a different color filter or by selecting a different pair of laser excitation wavelengths. For example, it is clear from Figure 2.20 that the ratio of fluorescence from 287.5 nm excitation compared to 283 nm excitation would provide the highest sensitivity of the options presented. Nevertheless, the temperature sensitivity using the 266 nm / 283 nm excitation pair is approximately 3:1 over the temperature range that will be experienced in the Mach 5 boundary layer, which should be sufficient for making instantaneous temperature measurements.

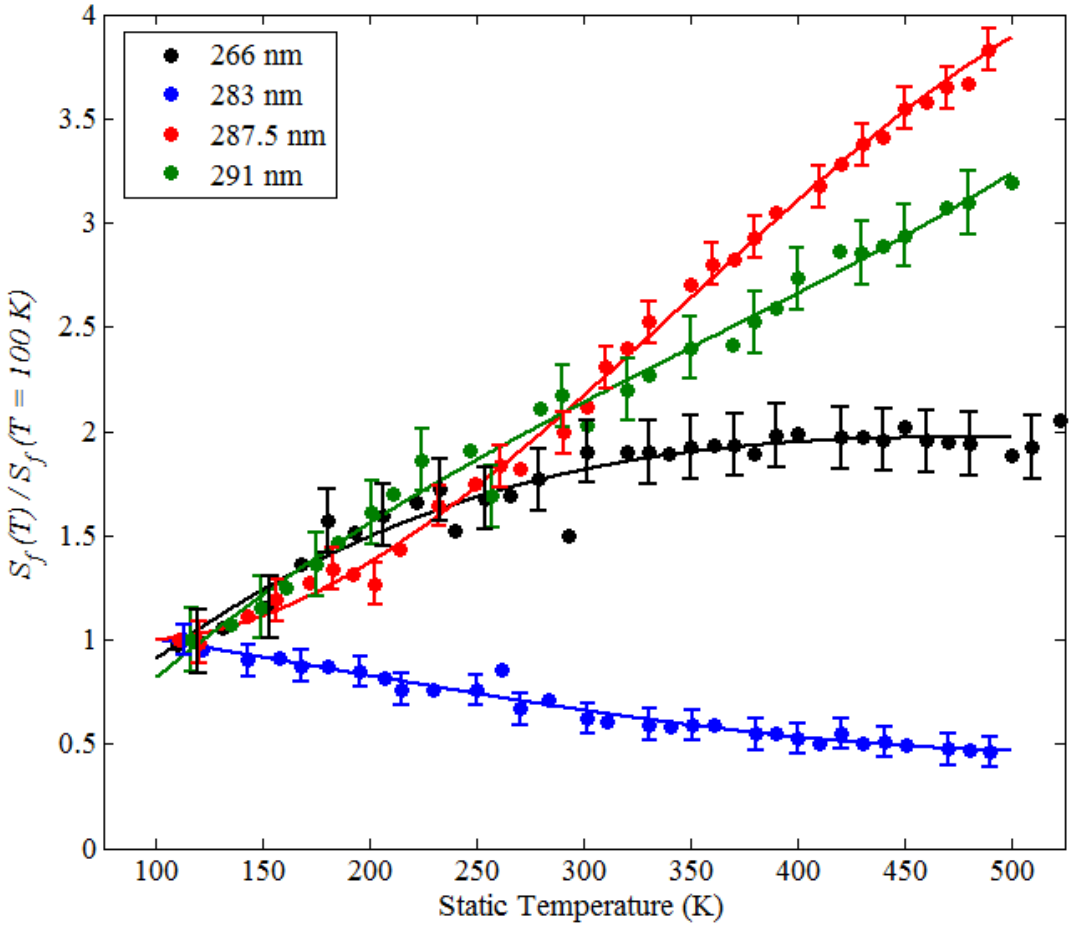

Figure 2.19: Integrated naphthalene fluorescence signal for four different excitation wavelengths (266 nm, 283 nm, 287.5 nm, and 291 nm), normalized to the 100 K value and plotted versus static test cell temperature. The symbols represent experimental data while the solid lines are fits to the data.

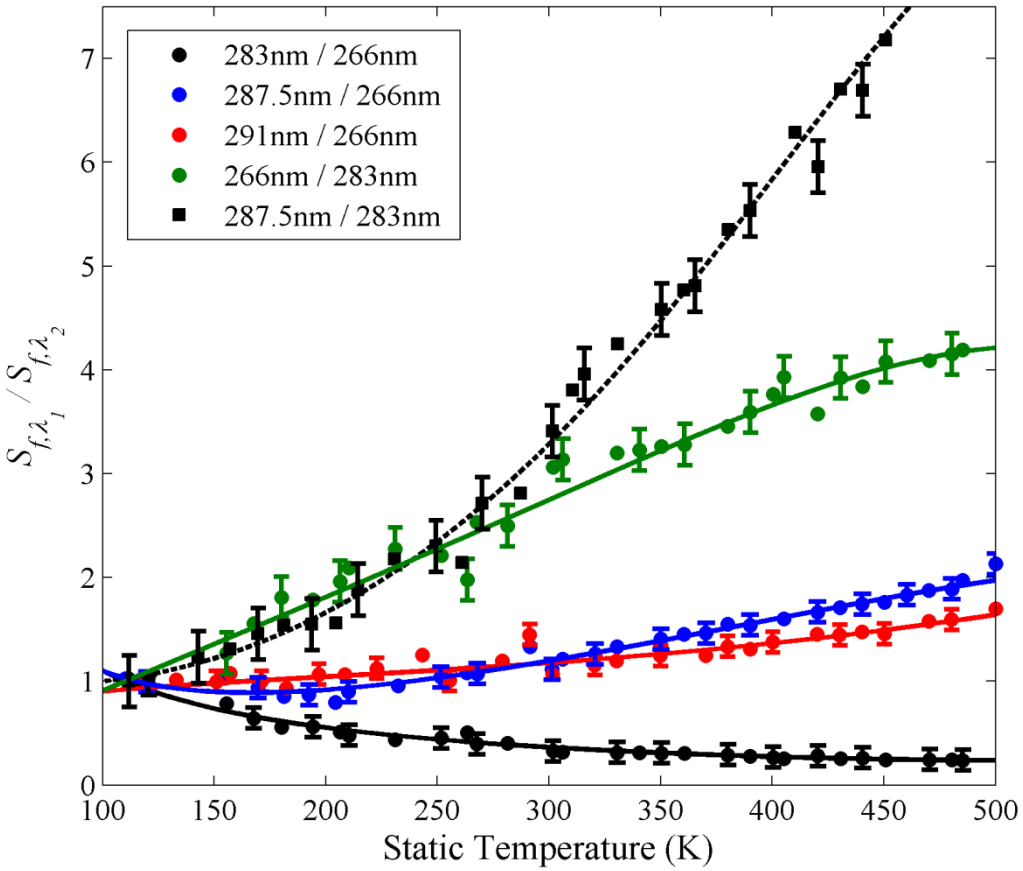

Figure 2.20: Ratios of integrated naphthalene fluorescence signal for three different excitation wavelengths (283 nm, 287.5 nm, and 291 nm) relative to 266 nm excitation, normalized to the 100 K value and plotted versus static test cell temperature. The ratio of fluorescence from the 287.5 nm / 283 nm excitation pair is also plotted. The symbols represent experimental data while the solid lines are fits to the data.

2.4 - CONCLUSION

To enable the quantification of naphthalene PLIF images, quantitative fluorescence and quenching measurements were made in a temperature- and pressure-regulated test cell. The test cell measurements were of the naphthalene fluorescence lifetime and integrated fluorescence signal over the temperature range of 100 K to 525 K

and pressure range of 1 kPa to 40 kPa in air. The fluorescence lifetime and signal were both observed to increase monotonically up to approximately 400 K. Calculated Stern-Volmer coefficients compared within the margin of experimental uncertainty with previous results and exhibited the same general trend with temperature (Kaiser and Long 2005; Lochman et al. 2010; Orain et al. 2011; Faust et al. 2013). The naphthalene fluorescence yield and absorption cross section data were then fit to simple functional forms for use in the calibration of the PLIF images. Lastly, the effect of varying excitation wavelength on the integrated fluorescence signal was investigated. While fluorescence signal increased with increasing temperature for 266 nm, 287.5 nm, and 291 nm excitation, the signal decreased with increasing temperature for 283 nm excitation. This result made excitation with 283 nm light the logical choice as the second line (paired with 266 nm excitation) to be used for two-line temperature imaging. The signal ratio resulting from the 266 nm / 283 nm excitation pair varied by a factor of approximately four over the 400 K temperature range tested, which should be sufficient for thermometry.

2.5 - SUGGESTED FUTURE WORK

There is a significant amount of work that could still be conducted to better understand naphthalene fluorescence. First and foremost, it is recommended that the fluorescence lifetime measurements be repeated with a PMT and oscilloscope with faster response times. The fall time of the PMT used in the current work was 6.6 ns while the response time of the oscilloscope was 500 MHz, both of which are significant compared to the time-scale of the lifetime measurements presented.

Considering that the freestream temperature of the Mach 5 wind tunnel facility is 60 K, it would also be desirable to make measurements down to this temperature, perhaps

with a Mach 5 nozzle. Even the measurements at Mach 3 in the current work were challenging due to the fast lifetime and relatively low signal of the naphthalene fluorescence. This could be mitigated by designing a Mach 5 nozzle with a relatively large exit diameter, however, a significant mass flow rate of test gas would be required.

A more comprehensive study of the temperature sensitivity of various excitation wavelengths would be beneficial as well. While 283 nm excitation exhibited sufficient sensitivity for the purposes of the current work, a more thorough study involving a larger number of test excitation wavelengths, selected at smaller intervals, may help identify an optimal second excitation wavelength for a two-line thermometry technique.

Chapter 3: Investigation of ablation products transport in a Mach 5 boundary layer using naphthalene PLIF

3.1 - INTRODUCTION

Once the fluorescence of naphthalene was characterized with respect to pressure, temperature, and gas composition, it was possible to explore the use of naphthalene PLIF for quantitative measurements in a high-speed flow. The focus of the quantitative PLIF program is to make measurements of the transport of ablation products in the turbulent boundary layer of the Mach 5 wind tunnel facility at The University of Texas at Austin, as discussed in Section 1.2. Here, the naphthalene vapor is introduced into the flow by sublimation of a solid naphthalene insert that was mounted to the floor of the wind tunnel. This chapter includes a description of the experimental methodology employed in the quantitative PLIF imaging campaign as well as a discussion of the results.

3.2 - EXPERIMENTAL PROGRAM

3.2.1 - Wind Tunnel Facility

The facility used for these experiments was a low-enthalpy blow-down Mach 5 wind tunnel. The wind tunnel was supplied by a 4 m^3 storage tank held at approximately 15.5 MPa and the plenum pressure was maintained at approximately 2.5 MPa ± 15 kPa. The flow was electrically heated to achieve a stagnation temperature of about 360 K ± 4 K. The test section of the facility had a constant cross section and was 152 mm wide by 178 mm tall. The freestream and boundary layer conditions were fully characterized in previous work by McClure (1992), with a freestream unit Reynolds number, Re, of 57.2×10^6 m^{-1} and freestream velocity of 770 m/s. Boundary layer transition occurred naturally upstream of the test section so that the incoming boundary layer was fully developed and fully turbulent with a boundary layer thickness, δ_{99}, of

19.3 mm, a momentum thickness, θ, of 0.76 mm and $Re_\theta = 4.4\times10^4$. Optical access for laser transmission and imaging was provided by fused silica windows on the wind tunnel floor, ceiling, and sidewall.

In these experiments, the naphthalene vapor was introduced into the flow by allowing a solid block of naphthalene to sublimate. The insert, which was mounted flush with the floor of the test section (as seen in Figure 3.1), had dimensions of 105 mm in the streamwise direction and 57 mm in the spanwise direction. The solid block of naphthalene was formed by pouring liquid naphthalene into the insert and then covering it during the cooling process to ensure a smooth, flat surface. After the naphthalene solidified, the cover was removed and the insert was installed into the test section floor. More details on the naphthalene insert geometry and molding procedure are provided in Appendix C. The sublimation rate of naphthalene at standard conditions is slow and no noticeable mass was lost if the insert was left in the test section for hours without flow. Only a small amount of ablation (a fraction of a millimeter) was observed over the course of a one minute wind tunnel run. Additionally, the placement of the naphthalene insert permitted optical access to the test section just downstream of the trailing edge of the insert.

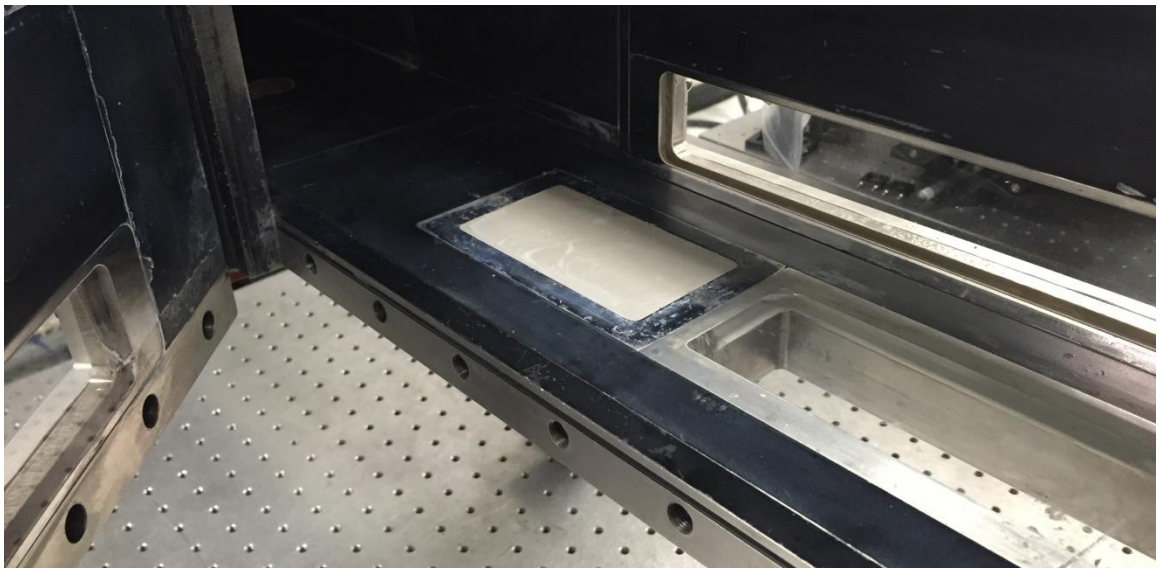

Figure 3.1: Photograph of the naphthalene floor insert installed in the Mach 5 test section.

3.2.2 - PLIF Experimental Setup

The naphthalene vapor was excited by a sheet of 266 nm light from a frequency-quadrupled Nd:YAG laser—shown schematically in Figure 3.2—operating at a repetition rate of 10 Hz. The laser energy was maintained at approximately 42 mJ/pulse, corresponding to an irradiance of 150 kW/mm^2. The UV laser beam was formed into a sheet using a 250 mm spherical lens and a 25 mm cylindrical lens then passed through the ceiling of the wind tunnel, as shown in Figure 3.2. The laser sheet was about 0.5 mm thick (FWHM) in the measurement region and approximately 50 mm wide. PLIF images were recorded using a back-illuminated CCD camera (Apogee Alta F-47) fitted with a 100 mm focal length, f/2.8 UV lens (Circo) operated at full aperture. The primary field of view employed is depicted in Figure 3.3. In order to reject scattered laser light and image only naphthalene fluorescence, one Schott WG-295 filter and one Schott UG-11 filter were placed in front of the camera. The imaging field of view was approximately 40 mm

wide by 20 mm tall. The images were obtained at a rate of approximately 1/3 Hz with a 40 ms exposure time and up to 30 images could be acquired per wind tunnel run. 1/3 Hz was the maximum acquisition rate of the Apogee camera and the maximum shutter speed of the camera was approximately 40 ms. However, the flow was effectively frozen considering that the lifetime of the naphthalene fluorescence and the laser pulse FWHM are both on the order of 10 ns. The coordinate system applied to the PLIF field of view is as follows: the x-direction is aligned with the freestream while the y-direction is normal to the wind tunnel floor, with the origin located at the trailing edge of the naphthalene insert and on the same plane as the laser sheet, as illustrated in Figure 3.3. The experiment was synchronized using multiple digital delay generators (Stanford Research Systems DG535) to ensure that images were acquired while the laser was firing.

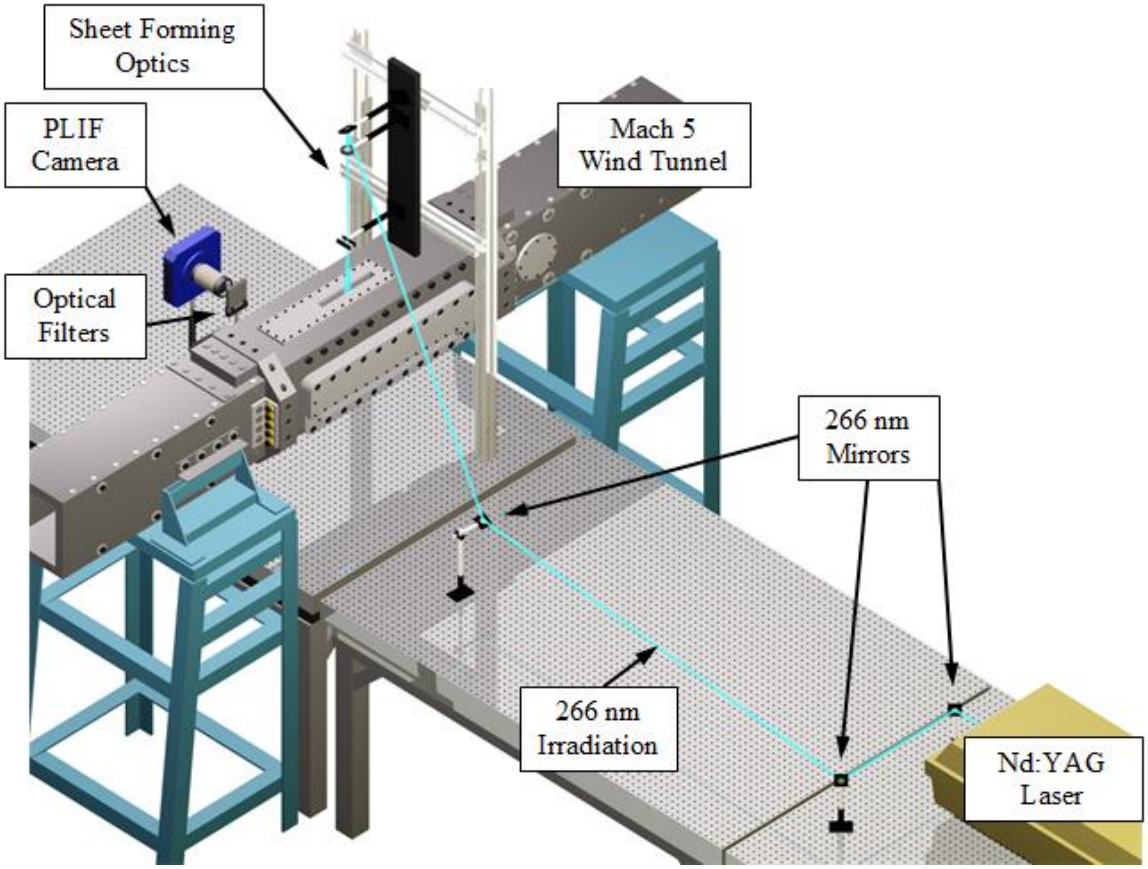

Figure 3.2: Schematic of the setup used for naphthalene PLIF experiments in the Mach 5 wind tunnel facility.

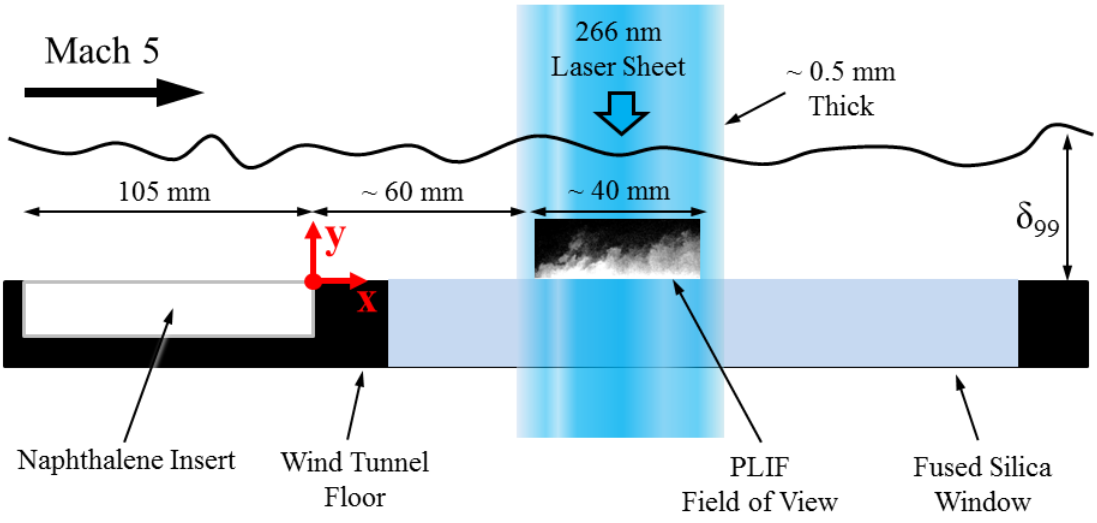

Figure 3.3: Schematic of the naphthalene floor insert with the primary PLIF field of view. The *x*-direction is aligned with the freestream while the *y*-direction is normal to the wind tunnel floor, with the origin located at the trailing edge of the naphthalene insert and on the same plane as the laser sheet.

3.2.3- PLIF Image Processing

Single-shot PLIF images were processed in MATLAB by first removing the background and then correcting for variations in the mean intensity profile of the laser sheet. Single-shot sheet corrections were not made. The mean laser sheet spatial intensity variation was measured using two different techniques. In one method, approximately 5 mL of acetone was placed on the floor of the wind tunnel. The acetone would quickly begin to evaporate and the resulting acetone vapor could be imaged with the CCD camera. However, the acetone evaporated fairly quickly, leaving a window of approximately one minute to acquire laser sheet images between applications of acetone. Additionally, the acetone vapor was not uniformly distributed in the imaging field of view, which required that the portion of the image close to the wall where the acetone

concentration was high be averaged in the wall-normal direction to create a laser sheet profile.

It was also observed that the naphthalene vapor introduced into the test section by the naphthalene insert at standard conditions (no wind tunnel flow) could be imaged using the Apogee CCD. This became the preferred technique for imaging the spatial intensity variation of the laser sheet for several reasons: (1) the naphthalene vapor was more uniformly distributed in the imaging field of view relative to the acetone vapor technique, (2) the sheet correction was based on fluorescence from the PLIF species, (3) the laser sheet images had signal levels comparable to the PLIF images, (4) these images could be easily collected without opening the test section. Unfortunately, there were certain days where naphthalene vapor was not observed in the test section and the acetone method had to be employed. This was the case for approximately 25% of the runs in this chapter. No correlation was found between the observation of naphthalene vapor in the quiescent test section and factors such as laser beam pulse energy, room temperature, naphthalene insert quality, and camera functionality. Furthermore, the presence of naphthalene vapor in the test section at standard conditions was not related to the signal level of the subsequent PLIF images.

With both techniques, approximately thirty images of the laser sheet spatial intensity distribution were averaged in order to determine a mean laser-sheet intensity profile. The single-shot PLIF images obtained during the runs were then divided by this laser-sheet intensity profile to correct for spatial variations in laser energy.

Additionally, a room temperature reference cell saturated with naphthalene vapor was evacuated to a pressure of 4.92 kPa ± 10 Pa, placed in the Mach 5 test section in the path of the 266 nm laser sheet, and imaged to generate reference images for quantifying

the fluorescence signal, as seen in Figure 3.4. These images were also corrected for variations in laser sheet intensity by using the techniques described above. The naphthalene reference cell was not used for making sheet corrections of the wind tunnel images because the cell could not be placed at a location that permitted imaging of the same field of view. Addtionally, the laser sheet was attenuated approximately 8% by the additional uncoated fused silica window on the top of the cell (~4% per surface). This was accounted for in the processing procedure by multiplying the measured reference cell laser energy by a factor of 0.92 in the mole fraction calculation.

Figure 3.4: Photograph of the room temperature, pressure-controlled reference cell inside the Mach 5 test section.

After correcting the images for non-uniformity of the laser sheet, the measured fluorescence signal and reference fluorescence signal were used in Eq. 1.10 along with evaluated curve fits for absorption cross section and fluorescence yield to solve for

naphthalene mole fraction. Using this procedure, the PLIF images were converted into two-dimensional plots of naphthalene mole fraction. To reduce noise, a 3×3 median filter was applied to all images.

No correction was made for potential laser absorption by naphthalene vapor. Absorption was neglected based on experiments using the naphthalene reference cell. In the direction of laser propagation, the intensity of naphthalene fluorescence in the cell was observed to remain effectively constant over the imaged path length of approximately 25 mm with no discernable trend detected. Since the boundary layer thickness in the Mach 5 facility is 19.3 mm it can therefore be assumed that absorption of the laser sheet by naphthalene vapor in the boundary layer is negligibly small. Absolute absorption cross-section measurements were not collected in the test cell experiments discussed in Chapter 2—only relative absorption cross section was determined—meaning that these measurements could not be used to calculate the estimated laser absorption. However, Orain et al. (2011) calculated absolute absorption cross section for high temperatures and presented a value of approximately 1.3×10^{-17} cm^2 at the wind tunnel recovery temperature. Using the Beer-Lambert law,

$$\frac{E}{E_o} = e^{-\sigma_a(\lambda,T) l n_{Naph}} \tag{3.1}$$

and employing a path length, l, of 20 mm, this results in a highly conservative estimate of laser energy attenuation through the boundary layer of approximately 3% for a naphthalene mole fraction of 1×10^{-3} that can serve as an upper bound for the maximum possible laser attenuation due to absorption by naphthalene vapor. Furthermore, considering that naphthalene vapor was generally present at concentrations of around 2×10^{-4} within 0.6δ (about 12 mm), a revised and perhaps more reasonable estimate of

the laser attenuation through the boundary layer is 0.4%. It is therefore concluded that neglecting the absorption of the laser beam through the boundary layer will have a minimal effect on the final PLIF images.

3.3 - Results and Discussion

3.3.1 - Instantaneous Quantitative PLIF Imaging

In all images the flow is depicted as moving from left to right. The field of view used for this imaging campaign is illustrated in Figure 3.3. Figure 3.5 is an instantaneous naphthalene PLIF image that has been normalized by the maximum signal in the image. The image has not been corrected for temperature and pressure effects using Equation 1.10 and the image is only qualitative although the fluorescence signal scales roughly with naphthalene concentration. Large-scale naphthalene vapor structures are evident in the boundary layer as the transport of scalar is clearly visualized. In general, the signal appears to decrease with increasing distance from the wall in the y-direction and very little fluorescence signal is visible outside $y/\delta = 0.6$. Using Rayleigh scattering, Smith et al. (1989) visualized similar large scale structures in a Mach 2.5 boundary layer out to distances of approximately $y/\delta = 0.8$ while Baumgartner et al. (1997) observed these features beyond $y/\delta = 1$ in a Mach 8 boundary layer. The structures in the current study do not extend as far out into the boundary layer since the scalar is introduced only a short distance upstream of the imaging location, and so the scalar does not have enough time to diffuse out to the edge of the boundary layer.

To convert the PLIF signal to naphthalene mole fraction, information on the temperature field is required, as discussed in Section 1.1.4. However, instantaneous temperature measurements are not available. Therefore, the mean temperature field is

obtained by using the Crocco-Busemann relation (White, 1991) and the mean velocity profile measured previously in the same facility (McClure, 1992), *viz*.,

$$T = T_{aw} - r\frac{U^2}{2c_p}, \tag{3.2}$$

where T_{aw} is the adiabatic wall temperature of the air, $r = \sqrt[3]{Pr}$ is the recovery factor, Pr is the Prandtl number, U is the streamwise component of velocity, and c_p is the heat capacity of air at constant pressure. Equation 3.2 assumes steady, adiabatic flow, zero pressure gradient, and that the transverse and cross-stream components of the velocity are negligible compared to the streamwise component. It was also assumed that c_p was a constant at 1.005 kJ/kg-K.

To gain an idea of the error involved in using mean temperature profiles to correct instantaneous PLIF images, we first estimate the magnitude of the temperature fluctuations. Gross and McKenzie (1985) made temperature measurements in a Mach 2 turbulent adiabatic boundary layer and reported $\sqrt{\overline{T'^2}}/\bar{T}$ no higher than 6%. Furthermore, Smith and Smits (1993) show that the instantaneous temperature fluctuation scales as

$$\frac{T'}{\overline{T}} = -(\gamma - 1)M^2\frac{u'}{\overline{U}} \tag{3.3}$$

Evaluating this equation—based on the measured u_{rms} in the boundary layer (presented in Chapter 4), the estimated temperature profile derived from the Crocco-Busemann relationship, and the measured velocity profile—yields an estimated $\sqrt{\overline{T'^2}}/\bar{T}$ of 20% for the current work, which in turn leads to an error of 15% in the inferred naphthalene mole fraction.

While this uncertainty could be adequate for some applications it might not be sufficient for others. In Appendix A the efficacy of determining an instantaneous

temperature field with a two-line naphthalene PLIF thermometry technique (Eckbreth, 1996) is discussed.

Applying this mean temperature correction and Eq. 1.10, the image in Figure 3.5 was then converted into a two-dimensional field of naphthalene mole fraction using Equation 1.10, with the result shown in Figure 3.6. The magnitude of the calculated naphthalene mole fraction in the turbulent structures between $0 < y/\delta < 0.2$ is on the order of 2×10^{-4}. The peak value of mole fraction measured is approximately 6% of the saturation mole fraction at the wind tunnel recovery temperature and static pressure ($\chi_{sat}(T) = P_{sat}(T)/P$). In the current work, the expected vapor pressure of naphthalene was calculated using data from De Kruif et al. (1981). An error analysis was performed and it was determined that naphthalene mole fraction was measured with an experimental uncertainty of ± 20%. This analysis considered quantifiable uncertainties in fluorescence lifetime measurements, integrated fluorescence signal measurements, PLIF signal intensity, wind tunnel test conditions, reference image conditions, laser energy, and the calculated error in the application of an estimated mean temperature profile to the instantaneous images. This analysis is discussed in greater detail in Appendix B, Section B.1. Comparing Figure 3.5 and Figure 3.6, the mole fraction field has many similarities with the uncorrected PLIF image. Relatively large-scale structures are still evident and the signal essentially vanishes by $y/\delta = 0.6$. However, the subtle effect of the temperature and pressure correction is present, as well. For example, it seems possible that certain naphthalene vapor structures become more uniform in composition after the images have been converted to mole fraction. Two instances of this occurrence are indicated by white circles labelled “Naphthalene Vapor Structures” in Figure 3.6. When comparing the regions inside the white circles in Figure 3.6 to the same locations in

Figure 3.5, one can see that scalar structures appear to be a continuation of the structures ejected from the wall; i.e., they are closer to having the wall mole fraction. It must be stressed, however, that without an instantaneous temperature correction, it is difficult to definitively say that structures of uniform naphthalene mole fraction are present in the boundary layer.

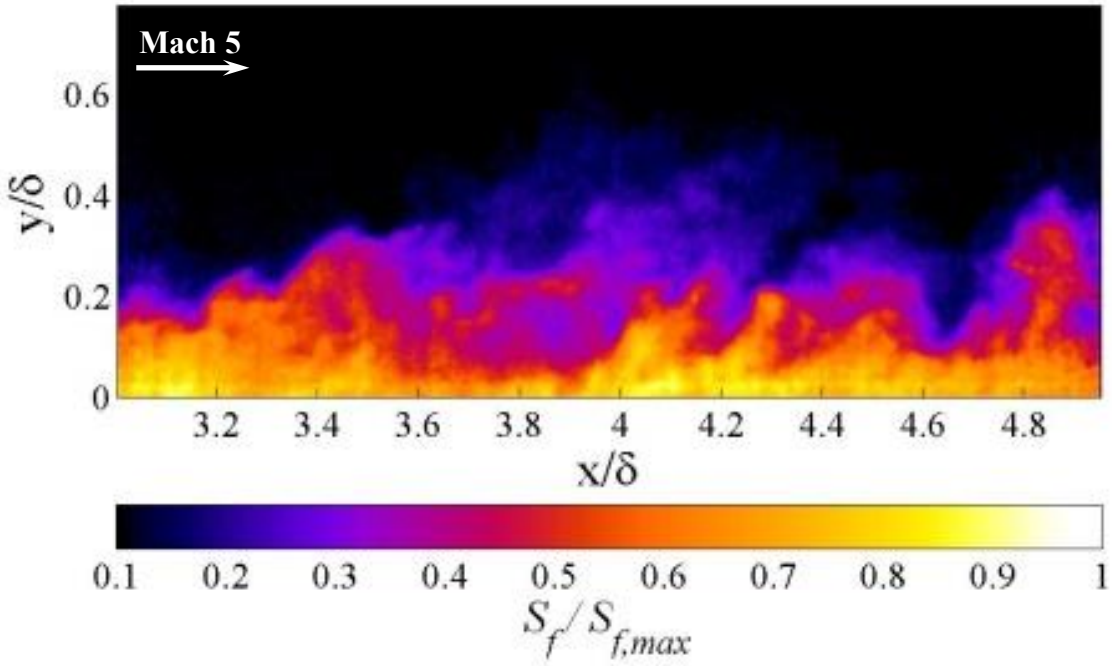

Figure 3.5: Normalized instantaneous naphthalene PLIF image in a Mach 5 turbulent boundary layer. Flow is from left to right.

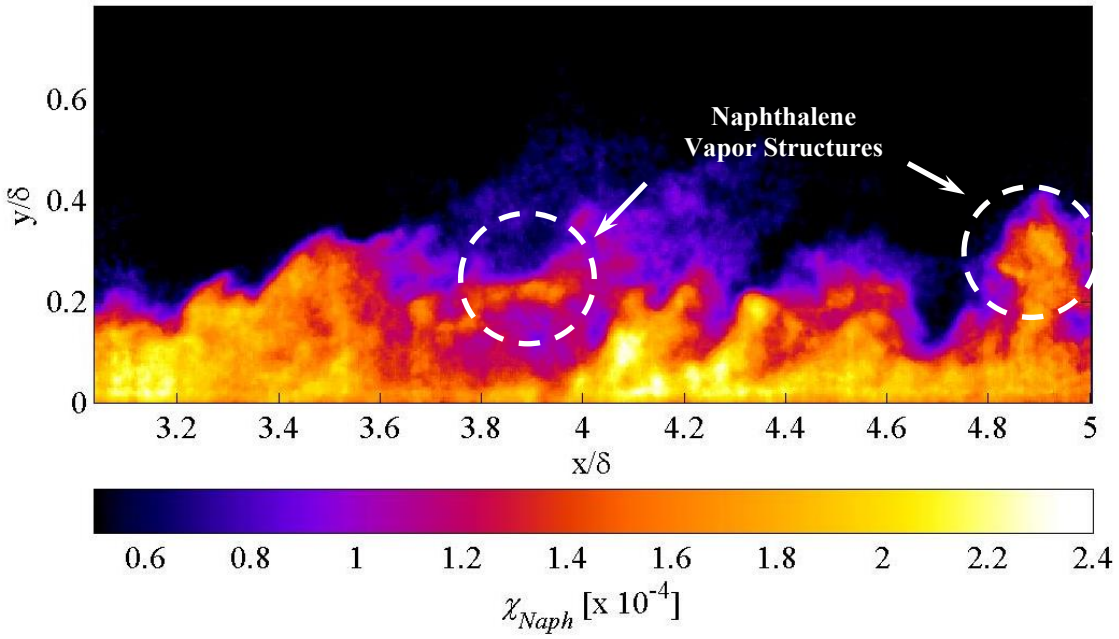

Figure 3.6: Instantaneous naphthalene mole fraction in a Mach 5 turbulent boundary layer. Flow is from left to right.

Uncorrelated image sequences collected during single wind tunnel runs at three separate imaging locations are shown in Figures 3.7 - 3.11. In each figure, images (a)-(j) are sequential in time and are separated by approximately three seconds each. All of the PLIF images have been corrected for mean temperature and pressure effects to provide two dimensional fields of naphthalene mole fraction.

Figure 3.7 depicts the scalar transport in the Mach 5 boundary layer from x/δ of 3-5. Notice that Figure 3.6 is image (f). As previously discussed, scalar structures are clearly evident in many of the images. However, looking at the image time series shows that these high mole fraction bursts are extremely sporadic compared to the time series shown in Figure 3.11 as the images vary between relatively high and low naphthalene mole fraction structures. Likewise, there does not appear to be a strong correlation

between run duration and naphthalene mole fraction, as may be expected based on the fact that the increasing temperature of the naphthalene insert with run time should result in a higher naphthalene sublimation rate. For example, Figure 3.7(a)—acquired just four seconds after wind tunnel start-up—exhibits naphthalene vapor concentration as high as any image in the sequence while Figure 3.7(j) has a relatively low amount of naphthalene vapor. It is possible that the seemingly random fluctuations in naphthalene mole fraction at this imaging station are the result of its proximity to the trailing edge of the naphthalene insert. While the momentum boundary layer is fully developed upon entering the test section, the naphthalene vapor has only had three δ to diffuse into the boundary layer; therefore, the presence of naphthalene vapor away from the wall is most likely extremely dependent on turbulent fluctuations away from the wall, thus resulting in images such as Figure 3.7(e) where almost no naphthalene vapor is present for $y/\delta > 0.05$. While this effect was observed in Figure 3.11, it is much more clear in Figure 3.7 as the images were collected further upstream. Also notice that the turbulent structures appear to be primarily restricted to wall distances of $y/\delta < 0.4$, whereas these features were often seen at $y/\delta > 0.6$ in Figure 3.11. This is surely a result of the shorter development length of the scalar boundary layer in the field of view for Figure 3.7.

Each image collected over the course of a 90 second wind tunnel run is presented sequentially in Figures 3.8-3.10. The imaging field of view in these images spans from x/δ of 3.75-5.75. Perhaps a result of the field of view being approximately 1δ farther downstream, the naphthalene mole fraction in the images is slightly more regular than in Figure 3.7. However, there are still instances, for example in Figure 3.9(a), where naphthalene vapor structures are sparse despite a relatively long run time. Owing to the length of the run and the number of images acquired, it is possible to observe the

expected correlation between run time and signal level when comparing the images in Figures 3.8-3.10. It is clear that, on the whole, the images in Figure 3.8 generally show the lowest value of naphthalene mole fraction while those in Figure 3.10 generally display the highest values of naphthalene mole fraction. It is most likely difficult to observe this trend in the other time series figures due to the sporadic nature of the scale and intensity of the naphthalene vapor structures. It is also observed that the magnitude of naphthalene mole fraction in the boundary layer structures at approximately $y/\delta = 0.2$ is on the order of 1×10^{-4}—comparable to the measurements made at x/δ = 7-9 but less than what was measured at x/δ = 3-5. Moreover, the naphthalene vapor structures in Figures 3.8-3.10 are generally located at wall distances of $y/\delta < 0.4$ but periodically approach $y/\delta = 0.6$, particularly at the downstream edge of the imaging field of view.

Figure 3.11 depicts the scalar transport in the Mach 5 boundary layer from x/δ of 6.5-10. Naphthalene vapor is again seen to be regularly ejected from the near wall region out to distances of approximately $y/\delta = 0.6$. As seen in Figure 3.11(c) and (g), these structures occasionally approach $y/\delta = 1$. While the images in Figure 3.11 show general similarities in scalar struture, the turbulent nature of the boundary layer and the significant instantaneous variations in naphthalene mole fraction are evident when comparing the ensemble. It appears to be slightly more probable that there will be a higher naphthalene mole fraction in the boundary layer later in a wind tunnel run, which is expected since the wind tunnel heats up over the course of the run and thus warms the naphthalene insert and increases the naphthalene sublimation rate. Still, this effect does not appear to be particularly strong, evidenced by the relatively low naphthalene mole fraction observed in Figure 3.11(f) and (h).

To test this hypothesis, Figure 3.12 was constructed. This is a plot of the mean naphthalene mole fraction for each image for the entire run presented in Figures 3.8-3.10. If the sublimation rate is increasing over time owing to heating of the tunnel then a systematic increase in signal over time is to be expected. The figure shows that the integrated signal fluctuates significantly during the run, but there does seem to be a systematic trend of increasing signal in time, as indicated by the trend line, which has a mild positive slope. However, the relationship is extremely noisy and the R^2-value of the fit is only 0.21.

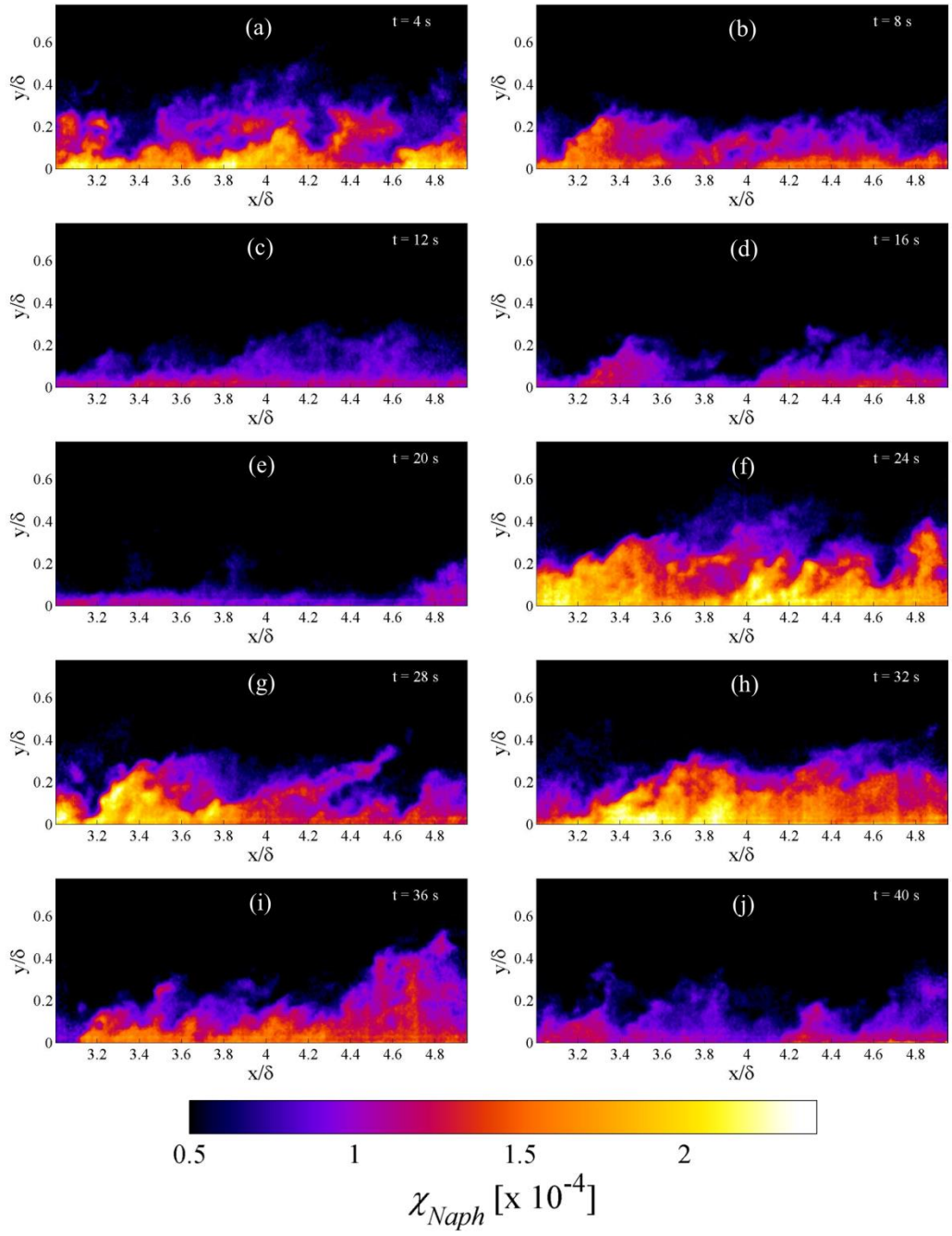

Figure 3.7: Two-dimensional fields of naphthalene mole fraction in a Mach 5 turbulent boundary layer collected using PLIF. Flow is from left to right. The images were collected during one run and (a)-(j) are sequential in time, separated by approximately three seconds each.

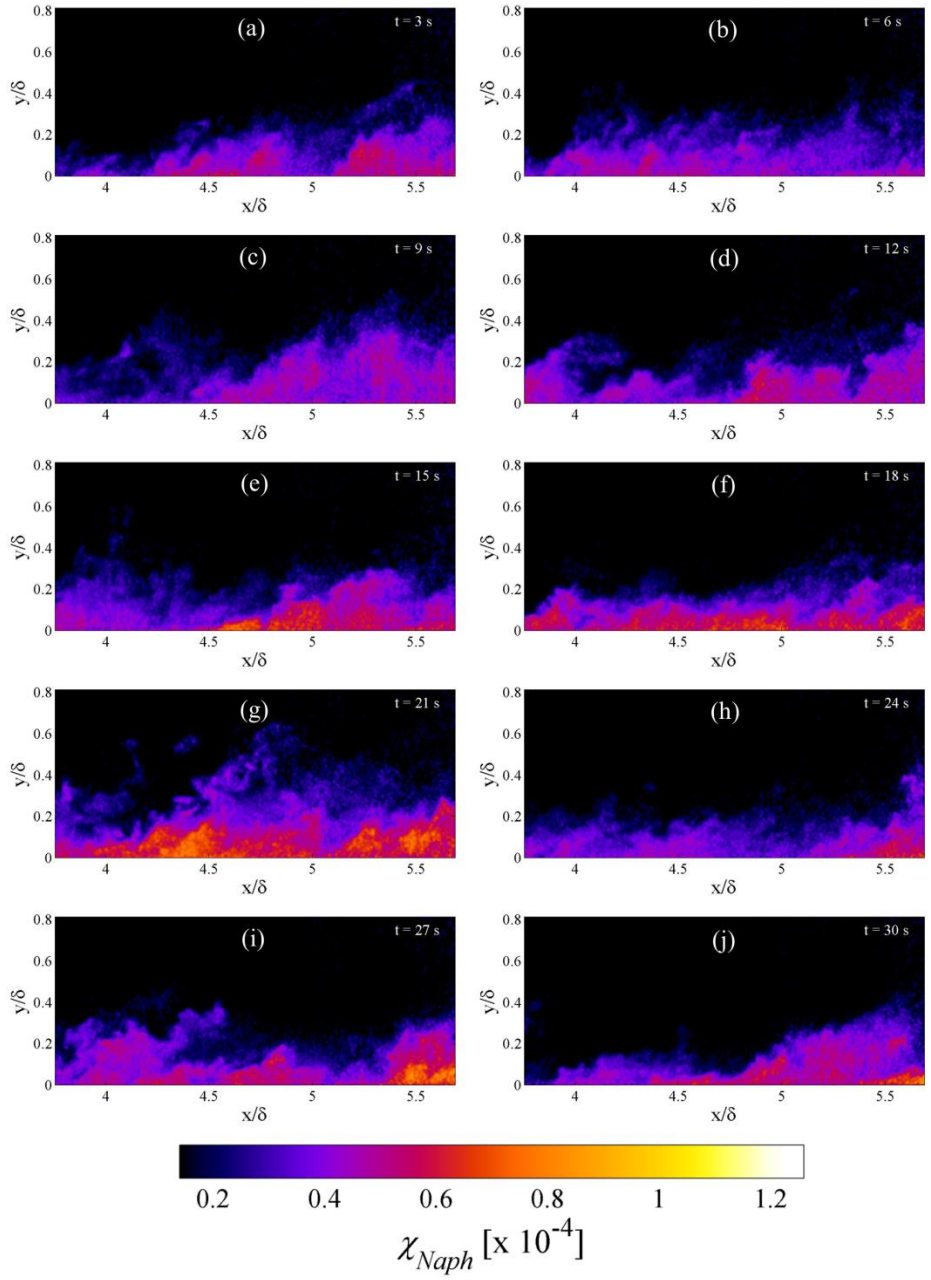

Figure 3.8: Two-dimensional fields of naphthalene mole fraction in a Mach 5 turbulent boundary layer collected using PLIF. Flow is from left to right. The images were collected during one run and (a)-(j) are sequential in time, separated by approximately three seconds each. The entire run is shown, in order, in Figures 3.8-3.10.

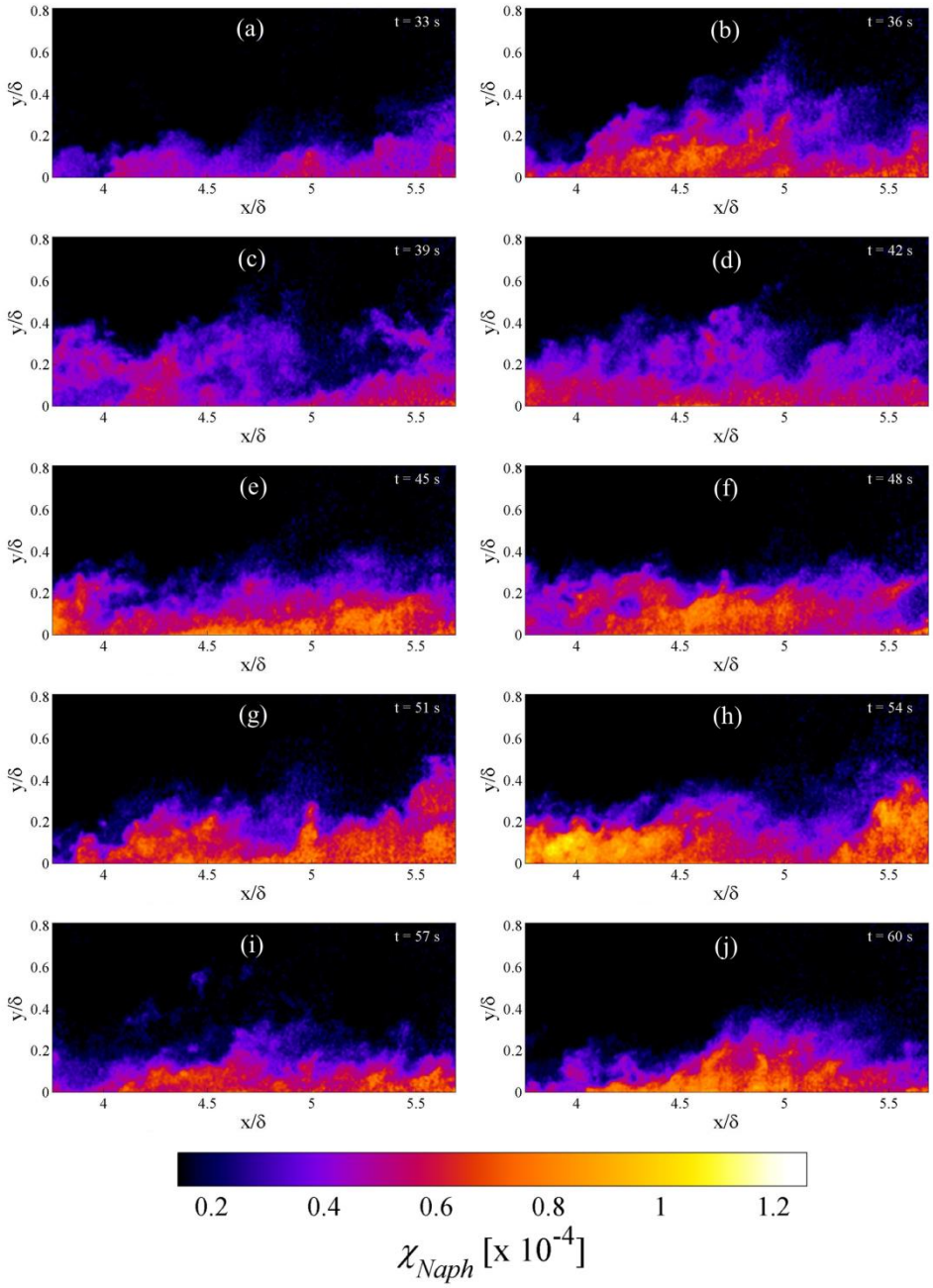

Figure 3.9: Two-dimensional fields of naphthalene mole fraction in a Mach 5 turbulent boundary layer collected using PLIF. Flow is from left to right. The images were collected during one run and (a)-(j) are sequential in time, separated by approximately three seconds each. The entire run is shown, in order, in Figures 3.8-3.10.

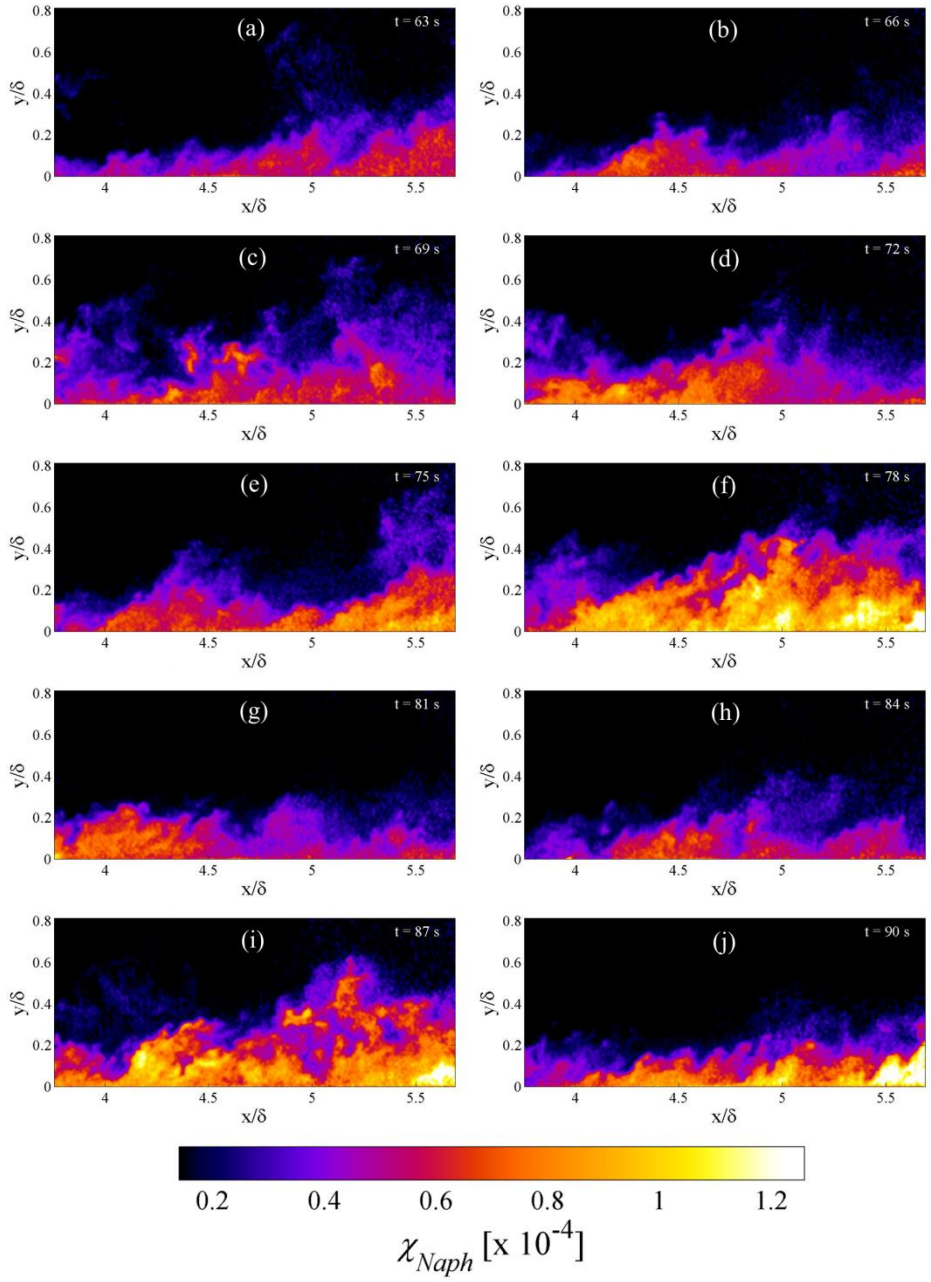

Figure 3.10: Two-dimensional fields of naphthalene mole fraction in a Mach 5 turbulent boundary layer collected using PLIF. Flow is from left to right. The images were collected during one run and (a)-(j) are sequential in time, separated by approximately three seconds each. The entire run is shown, in order, in Figures 3.8-3.10.

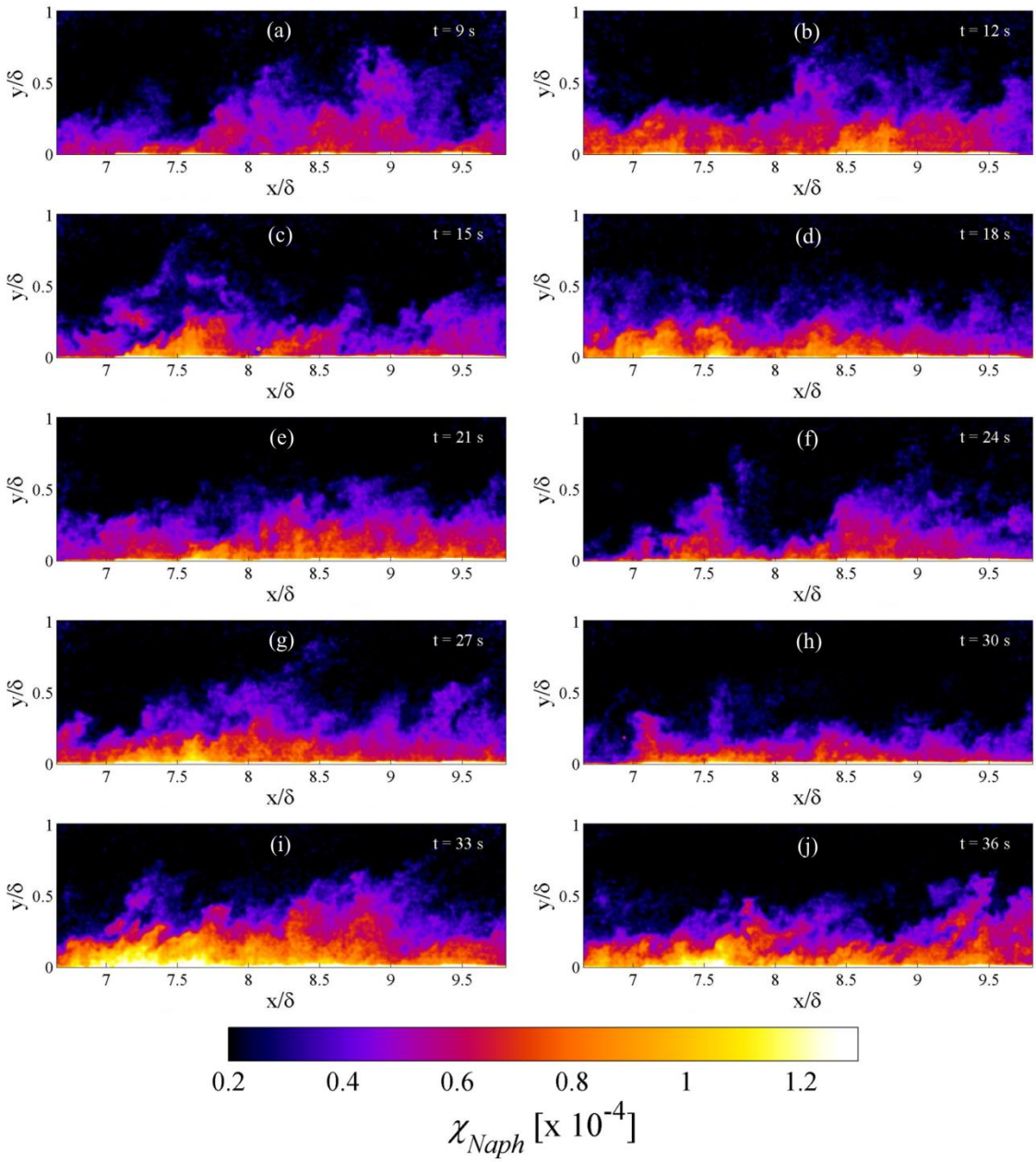

Figure 3.11: Two-dimensional fields of naphthalene mole fraction in a Mach 5 turbulent boundary layer collected using PLIF. Flow is from left to right. The images were collected during one run and (a)-(j) are sequential in time, separated by approximately three seconds each.

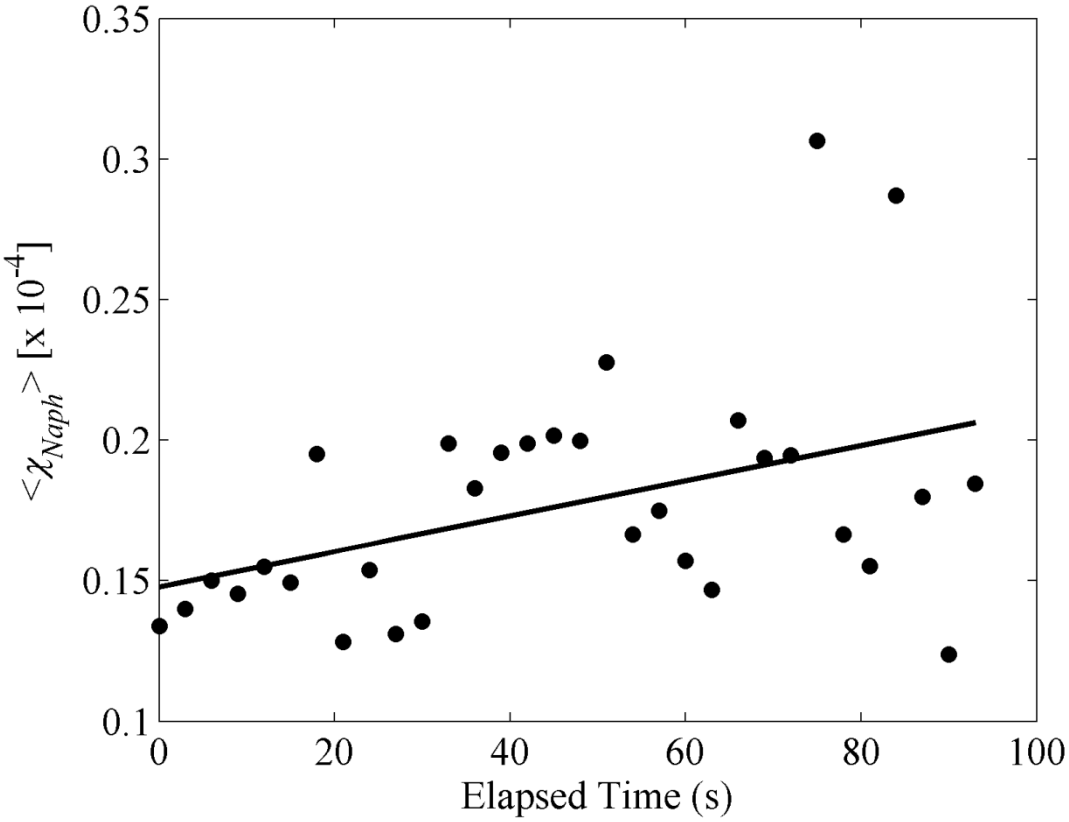

Figure 3.12: Plot of the mean naphthalene mole fraction in the imaging field of view for the run shown in Figures 3.8-3.10. The points represent experimental data while the solid line is a linear curve fit.

To further analyze large-scale features of scalar dispersion, Figures 3.13-3.15 were constructed. Each figure consists of four separate images collected during different runs at four distinct imaging locations in order to create a large field of view representation of the flowfield spanning $x/\delta = 2.5$ to 10. The mole fraction fields are presented in normalized form and several observations can be made about the flow from these figures. Firstly, the scalar field gradually thicknens with downstream distance, since the scalar is limited to $y/\delta < 0.2$ at $x/\delta = 2.5$, whereas it is limited to $y/\delta < 0.8$ at $x/\delta = 10$. Secondly, the naphthalene exhibits its highest mole fraction farther upstream and has

clearly been dispersed and diluted at the downstream imaging locations. These large scale compositions confirm the observations made when comparing the time series image sequences in Figures 3.7, 3.11, and 3.8-3.10.

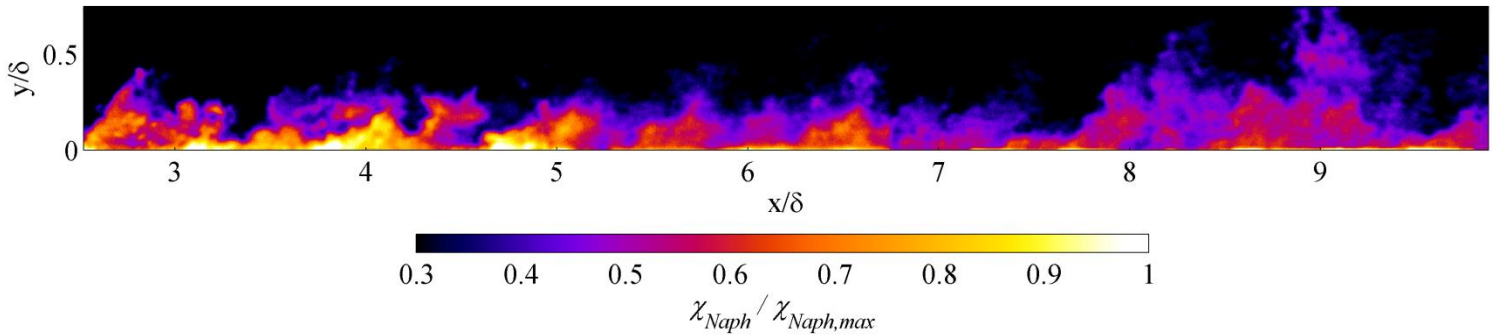

Figure 3.13: Instantaneous normalized naphthalene mole fraction in a Mach 5 turbulent boundary layer. Flow is from left to right. The image is composed of four images acquired during different runs to produce a large field of view.

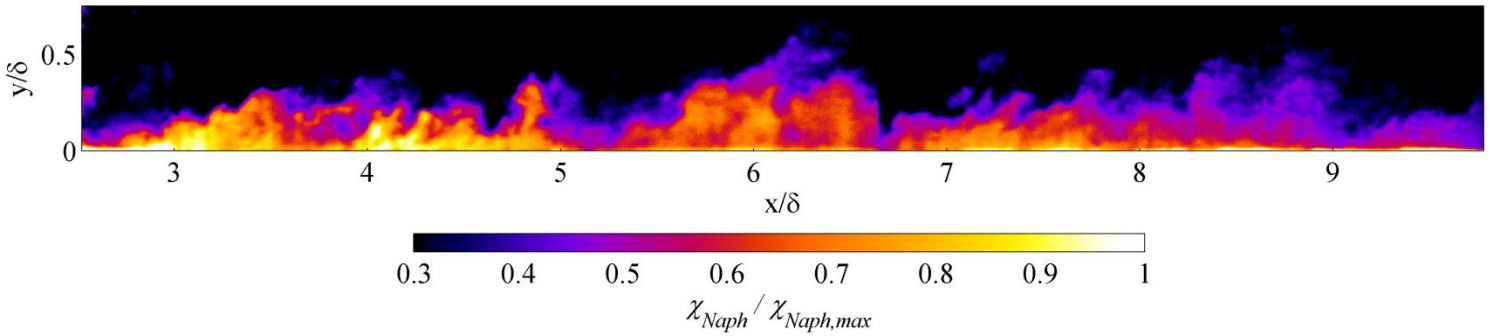

Figure 3.14: Instantaneous normalized naphthalene mole fraction in a Mach 5 turbulent boundary layer. Flow is from left to right. The image is composed of four images acquired during different runs to produce a large field of view.

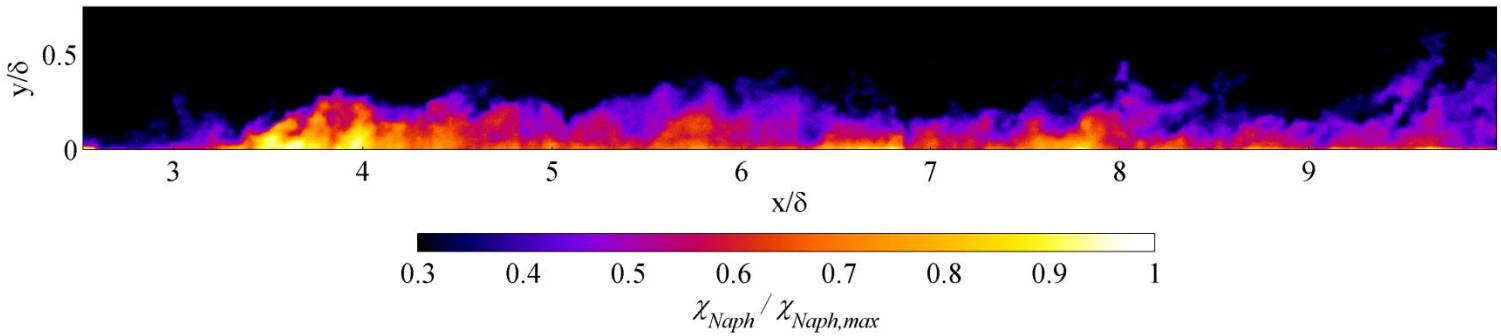

Figure 3.15: Instantaneous normalized naphthalene mole fraction in a Mach 5 turbulent boundary layer. Flow is from left to right. The image is composed of four images acquired during different runs to produce a large field of view.

3.3.2 - Mean Scalar and Velocity Profiles

To further analyze the effect of the temperature and pressure corrections applied to the PLIF signal, 85 PLIF images acquired during 7 wind tunnel runs at the same streamwise location were averaged, as seen in Figure 3.16. The mean two-dimensional fields of PLIF signal (Figure 3.16) and mole fraction (Figure 3.17) look extremely similar qualitatively, with high values near the wall decaying towards a zero value further out in the boundary layer. This decay appears to be smooth and appears to occur at a similar rate when comparing the two-dimensional fields by eye. However, it is more instructive to compare plots of the transverse profiles of fluorescence signal and naphthalene mole fraction through the boundary layer. Therefore, fields from eight runs, totaling 134 images, were ensemble averaged, resulting in mean boundary layer profiles which are presented in normalized form in Figure 3.18. The mean boundary layer velocity profile from the current work that was used for determining the mean temperature field is plotted in Figure 3.18 as well. Looking at the one-dimensional profiles it is clear that the mean naphthalene mole fraction decreases steadily with increasing distance from the wall, as expected. This trend is quite similar in both the uncorrected and corrected profiles. By a wall distance of approximately $y/\delta = 0.5$ the naphthalene mole fraction is effectively zero, corresponding to the signal level observed in the images. When comparing the mean mole fraction profile to the mean velocity profile it is also clear that regions with large negative values of $\partial\chi_{Naph}/\partial y$ correspond to areas with relatively high $\partial u/\partial y$. The scalar profile shows good agreement with those measured by Poreh and Cermak (1964), who passively bled ammonia into a low-speed turbulent boundary layer. Additionally, Gross and McKenzie (1985) measured profiles of temperature in a two-dimensional Mach 2 turbulent boundary layer using NO PLIF and found a scalar profile with a similar shape

as the one in Figure 3.18. Carvin et al. (1988) similarly made measurements of temperature profiles in a Mach 2.3 turbulent boundary layer using a constant current anemometer and observed a similar scalar profile for the case where $T_w = 2T_r$. Temperature profiles measured by Fletcher and McKenzie (1992) in a Mach 2 turbulent boundary layer using a combination technique involving O_2 LIF and Raman scattering also showed a very similar scalar profile for a hot wall case, with the highest temperature at the wall and a steady decay to the freestream value. However, with the exception of the work by Poreh and Cermak (1964), it is difficult to compare the majority of the scalar profiles from the literature to the current case given that the scalar is seeded into a turbulent boundary layer that is already fully developed. Furthermore, the scalar under investigation in the current work is independent of velocity while temperature is not.

While the profiles of normalized fluorescence signal and naphthalene mole fraction appear extremely similar in Figure 3.18, it is also instructive to demonstrate the effect of the signal correction on the relative magnitude of the scalar layer profile (e.g., the magnitude at the wall relative to the magnitude at y = 0.7δ). Here, a variable Σ is introduced that accounts for the various terms in Eq. 1.10 involving the thermodynamic state of the flow and is defined by:

$$\chi_i = \Sigma \frac{\chi_{i,ref}}{S_{f,ref}} S_f$$

$$where\ \Sigma = \frac{P_{ref} T}{P T_{ref}} \frac{\sigma_a(T_{ref})}{\sigma_a(T)} \frac{\varphi(T_{ref}, P_{ref}, \chi_{ref})}{\varphi(T, P, \chi)} \qquad 3.4$$

The variation of Σ is plotted versus wall distance in Figure 3.19. The plot shows that Σ is lowest near the wall and highest at the edge of the boundary layer. Considering

that pressure is assumed constant in the boundary layer, the trend observed in Figure 3.19 is primarily due to the fact that the mean temperature is highest in this near-wall region, resulting in a higher fluorescence signal (see Figure 2.13).

The influence of the image correction factor Σ is demonstrated in Figure 3.20. It can be seen that while the general shape of the profile remains the same, the magnitude at the wall decreases by approximately 50%. This is relevant considering that in previous work, Lochman et al. (2010) and Buxton et al. (2012) suggested that the high signal region adjacent to the wind tunnel floor was due to the reflection of the laser sheet off of the wind tunnel floor or perhaps fluorescence from solid-phase naphthalene that had been deposited on the wind tunnel floor. Considering the relative magnitude of the uncorrected fluorescence signal near the wall to that further out in the boundary layer, this was a reasonable assumption to make. However, given that the near-wall magnitude of the corrected signal is 50% of the uncorrected signal and the calculated mole fraction nearest to the wall was approximately 5% of χ_{sat}, it seems likely that fluorescence from vapor-phase naphthalene is being imaged in this near-wall region. Additionally, no naphthalene residue could be found on the wind tunnel floor after runs and the high signal region near the wall vanished in the PLIF images immediately after wind tunnel shut down.

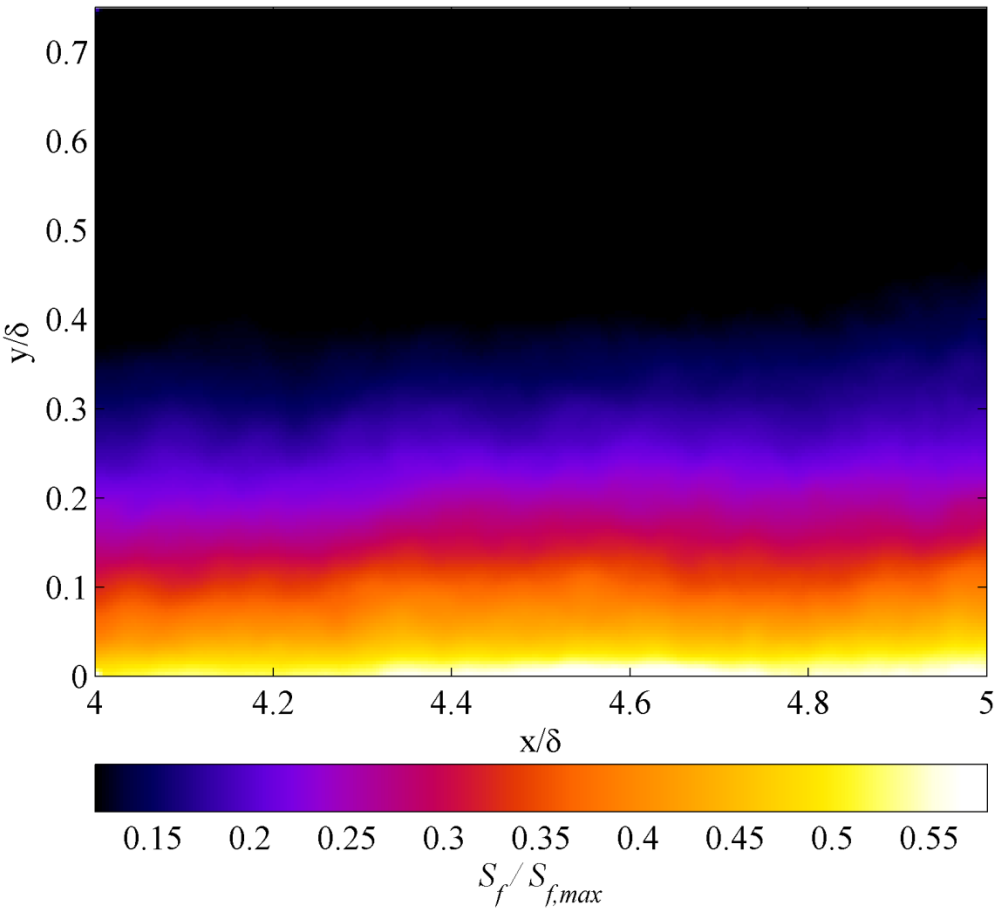

Figure 3.16: Mean normalized naphthalene PLIF signal in a Mach 5 turbulent boundary layer. Flow is from left to right.

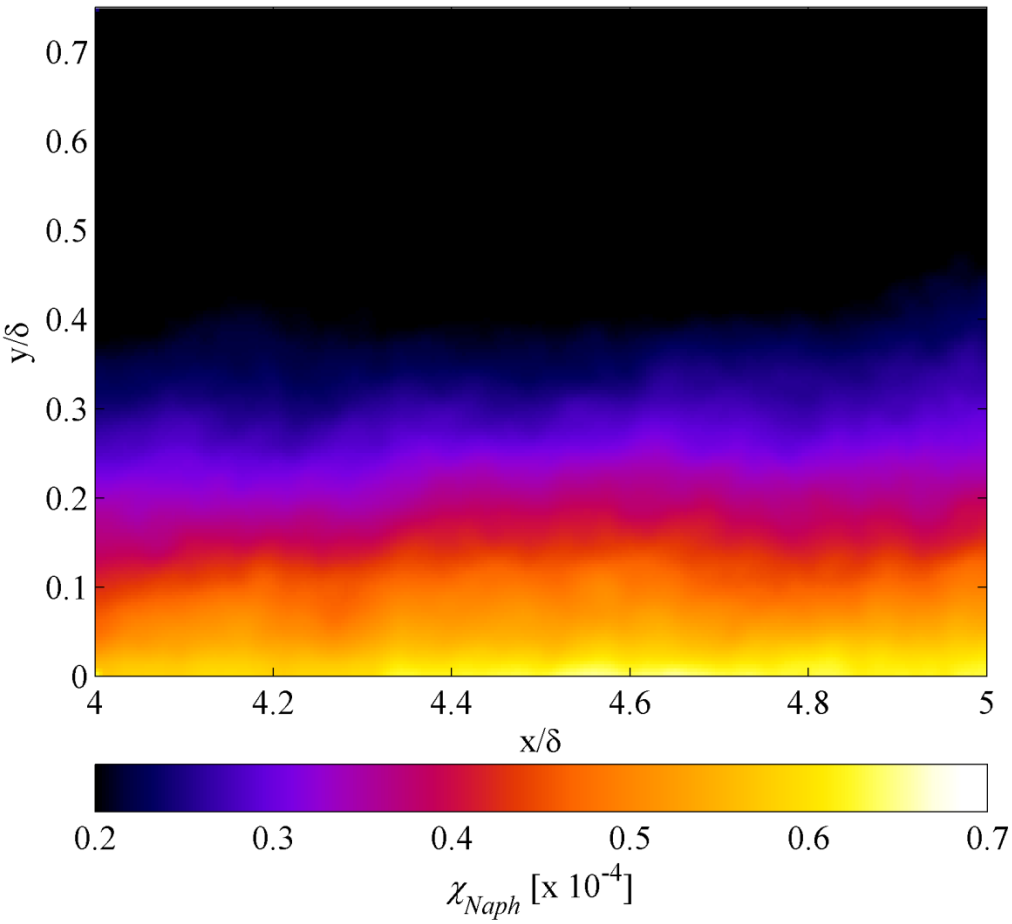

Figure 3.17: Mean naphthalene mole fraction in a Mach 5 turbulent boundary layer. Flow is from left to right.

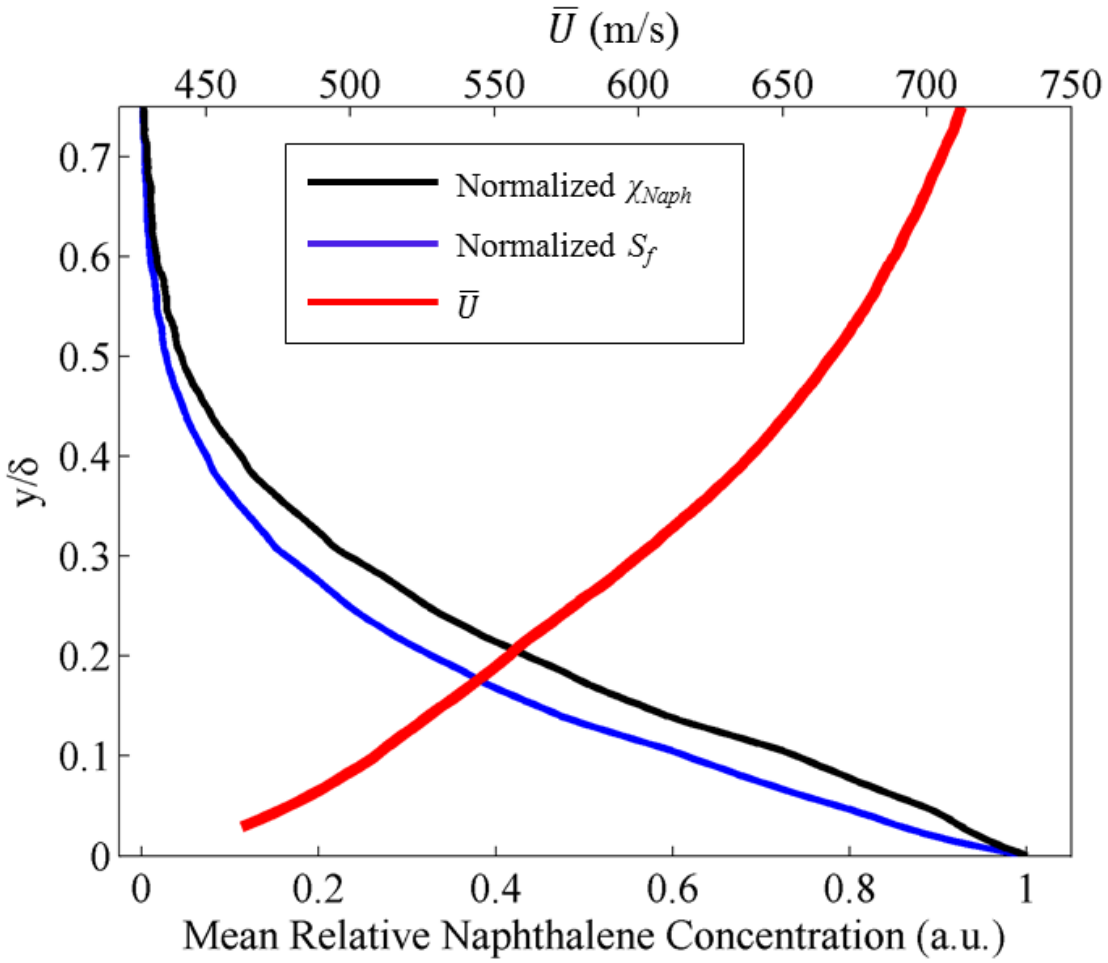

Figure 3.18: Comparison of normalized boundary layer profiles of fluorescence signal and naphthalene mole fraction. The mean velocity profile from the current work is also plotted.

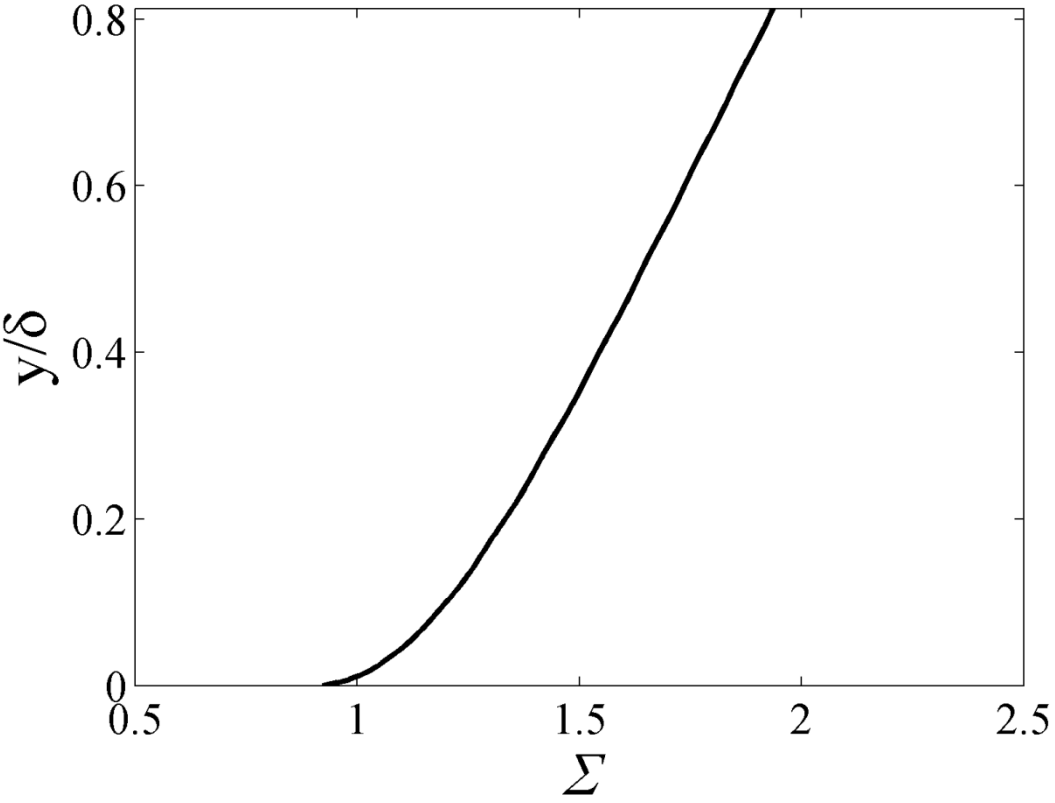

Figure 3.19: Naphthalene PLIF image correction factor, Σ (defined in Eq. 3.4), plotted versus normalized wall distance in the Mach 5 boundary layer.

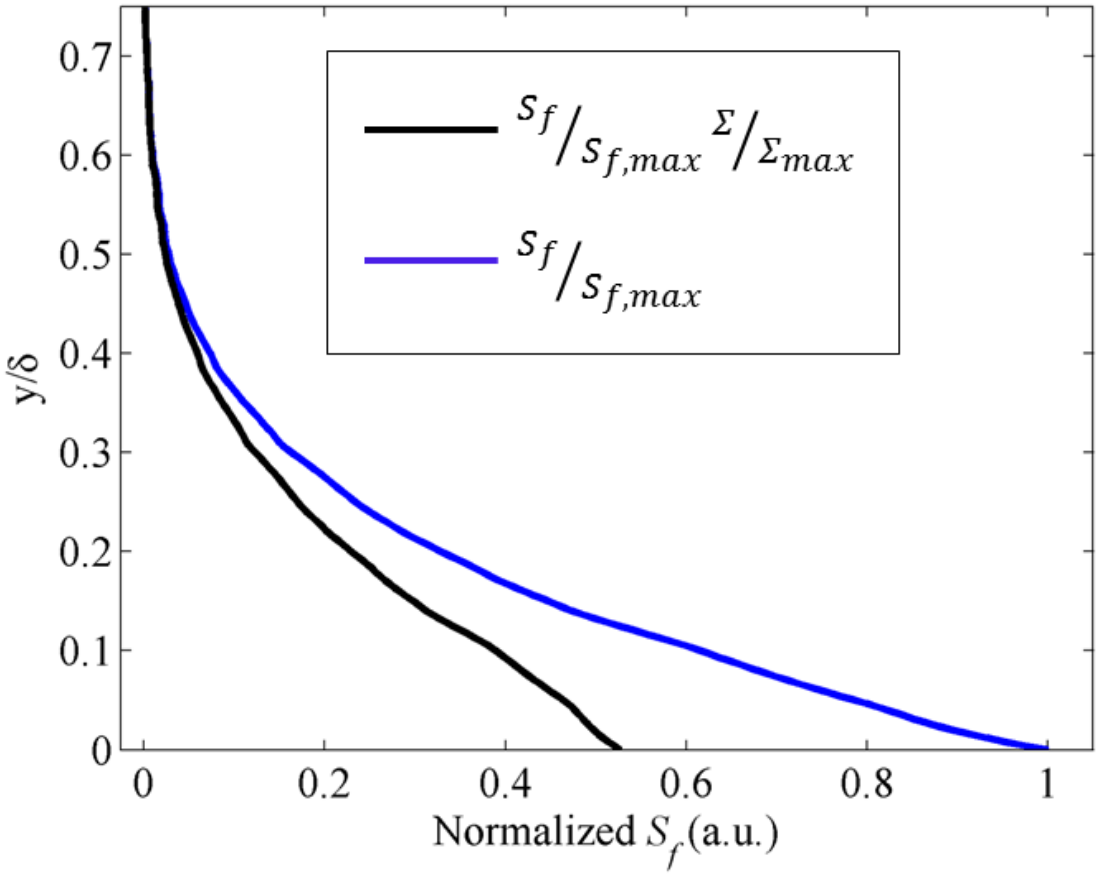

Figure 3.20: Normalized naphthalene PLIF signal compared to the normalized signal multiplied by the normalized image correction factor, Σ (defined in Eq. 3.4), plotted versus normalized wall distance in the Mach 5 boundary layer.

While there are few experimental studies in the literature that are true comparisons to the current flowfield, Braman et al. (2011) performed DNS of an "ablating patch" at Mach 5, where the ablation boundary condition was simulated by the introduction of a passive scalar into the flow from a square surface. This computational study was designed to simulate scalar transport of naphthalene in the Mach 5 wind tunnel at The University of Texas at Austin and the mass transfer rate across the boundary was partially based on an estimated sublimation rate of naphthalene. The patch employed in

the DNS was $0.4\delta \times 0.4\delta$, which is approximately 1% of the surface area of the insert used in the current work. Additionally, the DNS profiles shown here were collected 2δ downstream of the patch.

Figure 3.21 compares scalar profiles from the current naphthalene PLIF work and the DNS by Braman et al. (2011). The profiles are seen to have a similar shape but the magnitude of scalar near the wall is significantly higher than what was measured with PLIF by a factor of 10. This discrepancy is well beyond the bounds of the estimated ± 20% error in the naphthalene mole fraction calculation. Braman et al. (2011) determined the mass flow from the ablating patch based on the sublimation rate of naphthalene at the wall recovery temperature of the Mach 5 flow. However, the mass transfer from the surface may be difficult to predict given the sensitivity of naphthalene vapor pressure (and hence sublimation rate) to temperature. For example, near the recovery temperature of the Mach 5 flow, a 10 K deviation from the true temperature of the naphthalene block results in a change in the vapor pressure of naphthalene by a factor of two. Variations in wind tunnel stagnation temperature of this magnitude are common at the facility used for this work, even between runs performed during the same day. Furthermore, Lochman (2010) showed using thermocouple measurements that the temperature of the naphthalene insert 1 mm below the surface increased by only 6 K during a 100 second run—approximately 40 K lower than the recovery temperature of the flow. This could partially explain the discrepancy between the magnitudes of the two profiles. Moreover, it is likely that employing a mass transfer model that assumes saturated naphthalene vapor at the surface of the naphthalene insert is inaccurate.

With these factors in mind, it is perhaps more appropriate to compare normalized scalar concentration profiles from the current PLIF work and the DNS by

Braman et al. (2011). This comparison is shown in Figure 3.22. It is still apparent that the profiles have the same general shape, with the highest value near the wall and a steady decay towards zero further out in the boundary layer. Additionally, both profiles show that there is very little scalar concentration beyond $y/\delta = 0.5$. Upon close inspection, both profiles also exhibit a second, more subtle inflection point near the wall suggesting that $\partial\chi_{Naph}/\partial y$ is approaching zero. A zero derivative at the wall seems to make sense for measurements beyond the naphthalene insert, given that no more mass can be transferred across the wall boundary. This shape was also seen by Poreh and Cermak (1962) for a passive scalar. The main difference between the two profiles is that the experimental scalar layer thickness is more full than the one calculated by Braman et al. (2011), showing higher concentrations of naphthalene at larger wall distances. This is most likely a consequence of the large naphthalene insert used in the current work relative to the size of the ablating patch in the DNS. The larger ablating surface provides a larger distance over which the scalar could diffuse into the flow before it passes the back edge of the surface.

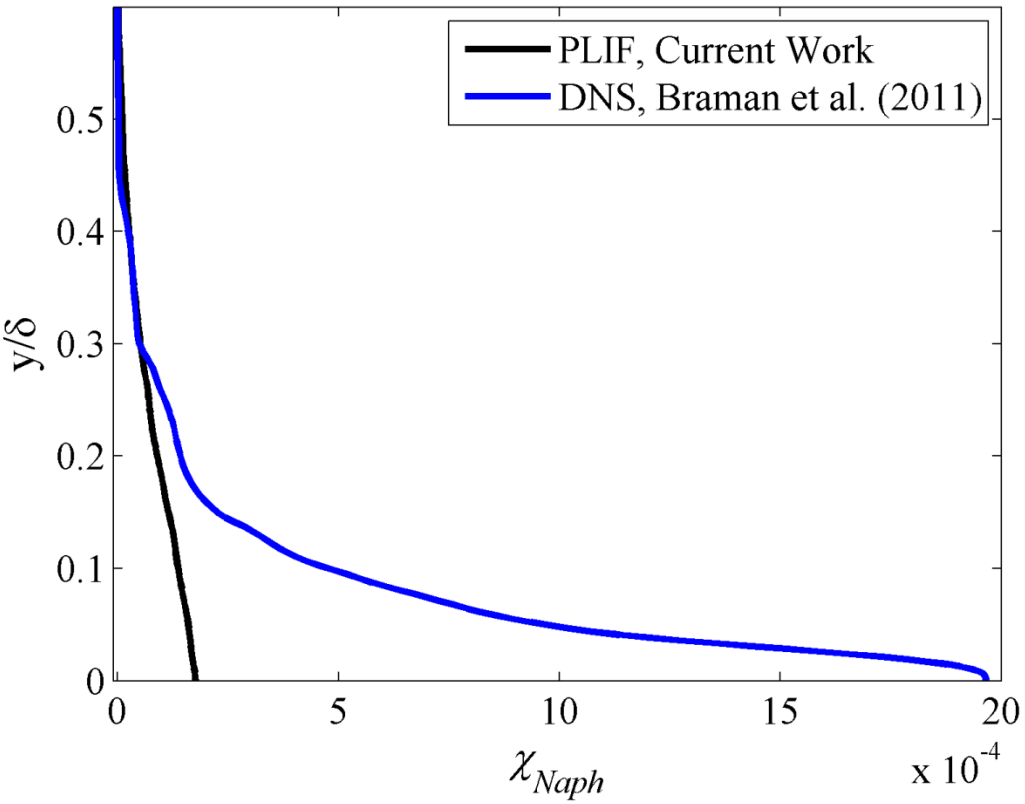

Figure 3.21: Comparison of mole fraction profiles in the Mach 5 boundary layer from naphthalene PLIF in the current work and from DNS of an ablating patch (Braman et al., 2011).

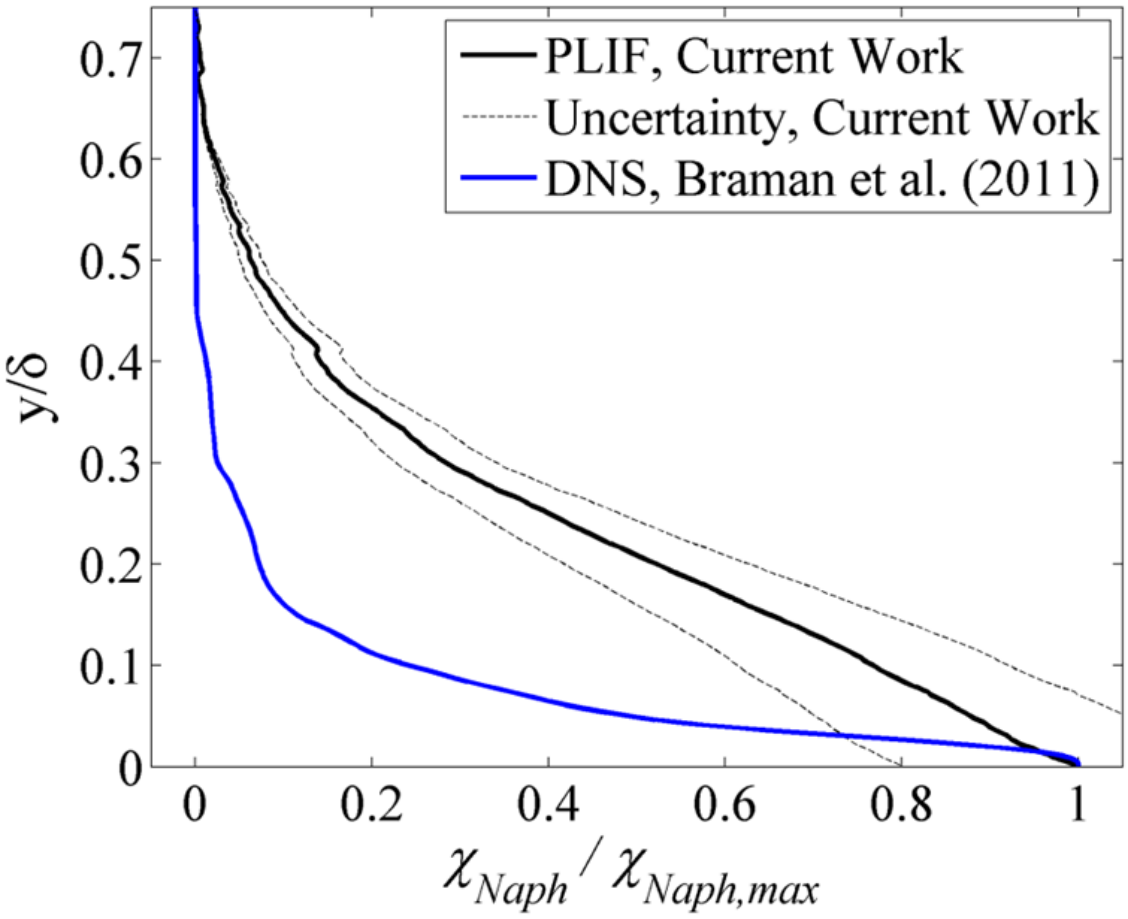

Figure 3.22: Comparison of normalized mole fraction profiles in the Mach 5 boundary layer from naphthalene PLIF in the current work and from DNS of an ablating patch (Braman et al., 2011).

Mean profiles were also recorded at different x/δ stations to compare the evolution of the scalar boundary layer with respect to streamwise location. In Figure 3.23 naphthalene vapor mole fraction profiles recorded at three different locations in the Mach 5 test section—x/δ = 3, 5, and 8—are presented. The profiles have a relatively similar shape, as expected, with the peak mole fraction value always occurring at the wall and a steady decay to zero by approximately y/δ = 0.5 in all three cases. Additionally, the concentration is highest for the stations closest to the naphthalene insert, as one would

expect, since there is no source of scalar at the wall and thus the finite amount of scalar is increasingly dispersed with increasing distance downstream. Furthermore, the area under the profiles is not equal given that the scalar is dispersed in three dimensions—out of the two-dimensional PLIF field of view. The shapes and behavior of these profiles echo the observations made in Section 3.3.1 regarding the time series images in Figures 3.7-3.10 and the large field of view images in Figures 3.13-3.15. Additionally, this result corresponds to the findings of the DNS performed by Braman et al. (2011), who similarly showed that the naphthalene concentration in the boundary layer should steadily decrease with increasing streamwise distance from the naphthalene insert while the shape of the profile remains approximately the same.

The profiles can also be normalized using the method employed by Poreh and Cermak (1962) while studying diffusion of ammonia gas from a line source into a fully developed turbulent boundary layer. In the work, profiles of concentration (in this case mole fraction) were normalized by the maximum concentration measured at a given x/δ station. Additionally, the wall distance units were normalized by a characteristic scalar boundary layer height, λ, which is defined as $\chi(\lambda)/\chi_{max}$ = 0.5 (Poreh and Cermak, 1962). In the same way that velocity profiles can be normalized by a freestream value to collapse the momentum boundary layer height into a "universal" velocity boundary layer profile, this normalization allows the mole fraction profiles to collapse into a sort of "universal" scalar layer profile. As can be seen in Figure 3.24, this normalization indeed shows that the three profiles presented in Figure 3.23 are approximately similar. Furthermore, when compared to the normalized results presented by Poreh and Cermak (1962) for measurement stations in a still-developing scalar boundary layer (termed the "Intermediate Zone") the plots are extremely similar.

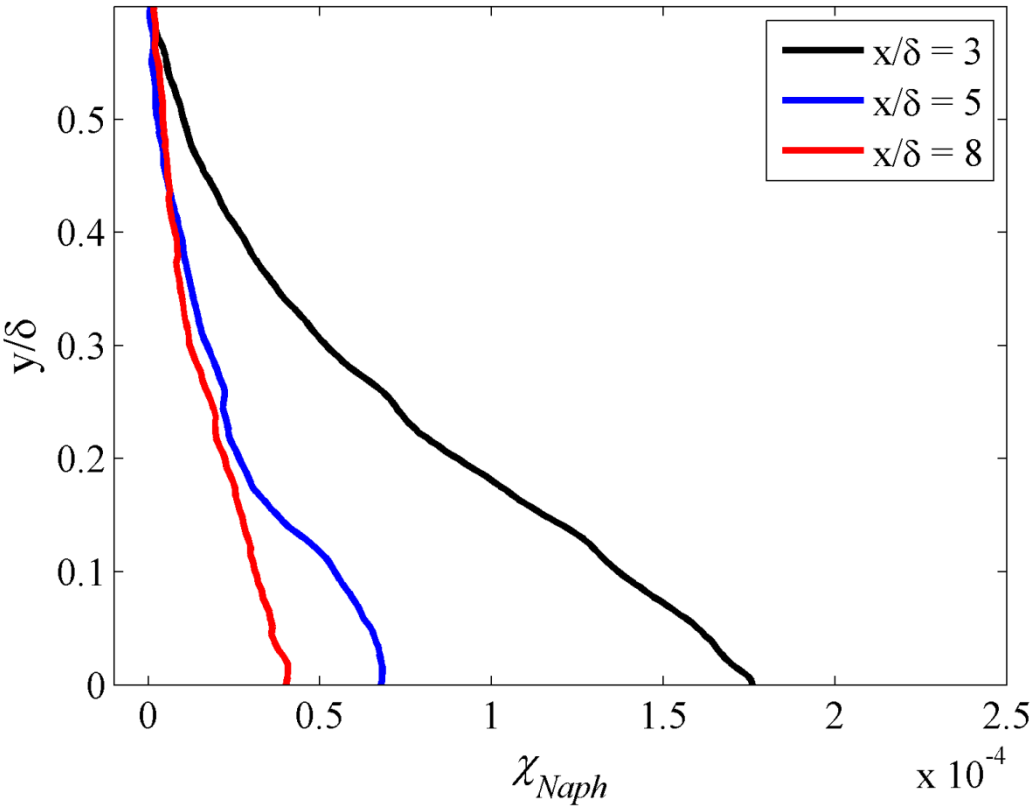

Figure 3.23: Comparison of mole fraction profiles in the Mach 5 boundary layer from naphthalene PLIF at three different stations: $x/\delta = 3$, $x/\delta = 5$, and $x/\delta = 8$.

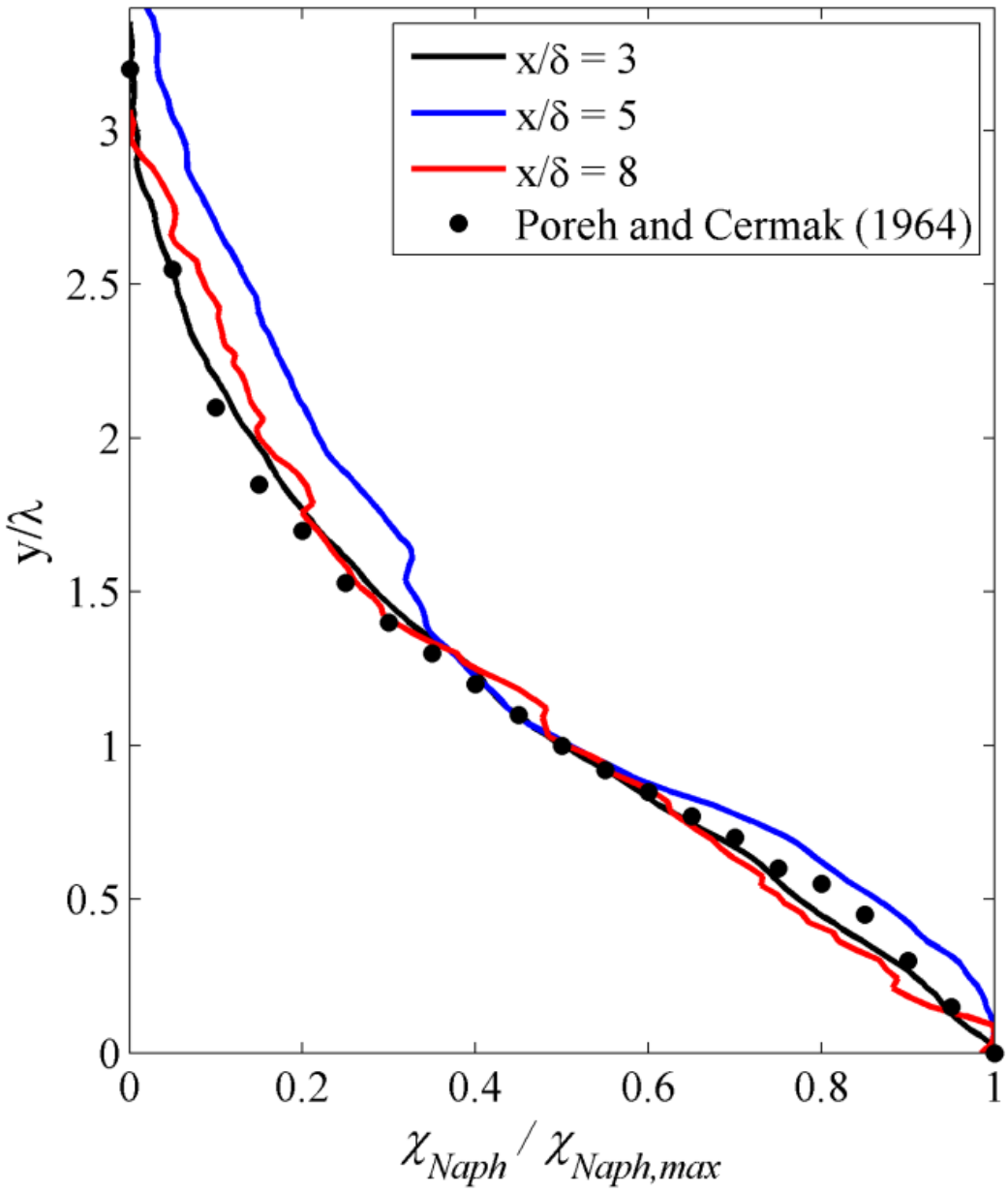

Figure 3.24: Comparison of mole fraction profiles in the Mach 5 boundary layer from naphthalene PLIF at three different stations: x/δ = 3, x/δ = 4, and x/δ = 8, plotted with data from Poreh and Cermak (1964). Profiles were normalized by the mole fraction value at the wall and a characteristic height (λ) of the scalar boundary layer.

The root-mean-square (r.m.s.) values of the naphthalene mole fraction were also calculated. A profile of the r.m.s with respect to wall distance from an ensemble average of 8 runs is shown in Figure 3.25. In addition to the r.m.s. calculated in the current work using naphthalene PLIF, Figure 3.25 also presents the scalar concentration r.m.s. from the DNS performed by Braman et al. (2011). Since the magnitudes of mole fraction measured in the current work were not in agreement with the DNS from Braman et al. (2011)—see Figure 3.21—the magnitudes of the r.m.s. plots were normalized by the peak mole fraction measured in the boundary layer in each case. Inspection of Figure 3.25 shows that the peak r.m.s. value occurs at the wall, most likely resulting from insufficient resolution near the wall. Buxton et al. (2012) measured a naphthalene PLIF signal r.m.s. that peaked at the wall and cited limited near-wall resolution due to laser scatter as the cause for this likely unphysical result. DNS from Kasagi et al. (1992) of a channel flow with heated walls showed the peak of the temperature r.m.s. profile at approximately $y^+ = 20$, well within the resolution of the current work. The temperature r.m.s. steadily decayed from $y^+ = 20$ to the limit of the presented data at $y^+ = 200$, which is the same general trend shown by the data in Figure 3.25. Thermocouple data collected by Li et al. (2004) in the turbulent boundary layer of a water channel flow also show the peak of the r.m.s. profile at $y^+ = 20$ but show the r.m.s. reaching its steady, freestream value at $y^+ = 60$. Meanwhile, the DNS results of Braman et al. (2011) show a peak at approximately $y/\delta = 0.05$, similar to the trend observed with a turbulent streamwise velocity r.m.s. profile. Furthermore, the peak r.m.s values are in good agreement in Figure 3.25 with the PLIF results indicating a peak r.m.s. of approximately 25% while the DNS predicts a peak mole fraction r.m.s. of approximately 45% near the wall. These two results are also in relative agreement with the findings of Buxton et al. (2012) who

measured a maximum naphthalene PLIF r.m.s. of 30% at the wall. Data presented by Smits and Dussauge (2006) show a peak T_{rms} at $y/\delta < 0.05$ of 11% in a Mach 2.3 turbulent boundary layer, which is significantly lower than the findings in the current work and the DNS by Braman et al. (2011). While the slopes of the mole fraction r.m.s. profiles from the naphthalene PLIF results and DNS (Braman et al., 2011) are in general agreement from $0.2 < y/\delta < 0.4$, the DNS r.m.s. plot decays to zero by $y/\delta = 0.6$ while the PLIF r.m.s. profile appears to level off at approximately 4%. This is most likely an artifact of background noise that is on the same order as the PLIF signal measured in this region, and will be difficult to completely eliminate in an experiment. Collecting images with higher signal-to-noise ratios would reduce this effect.

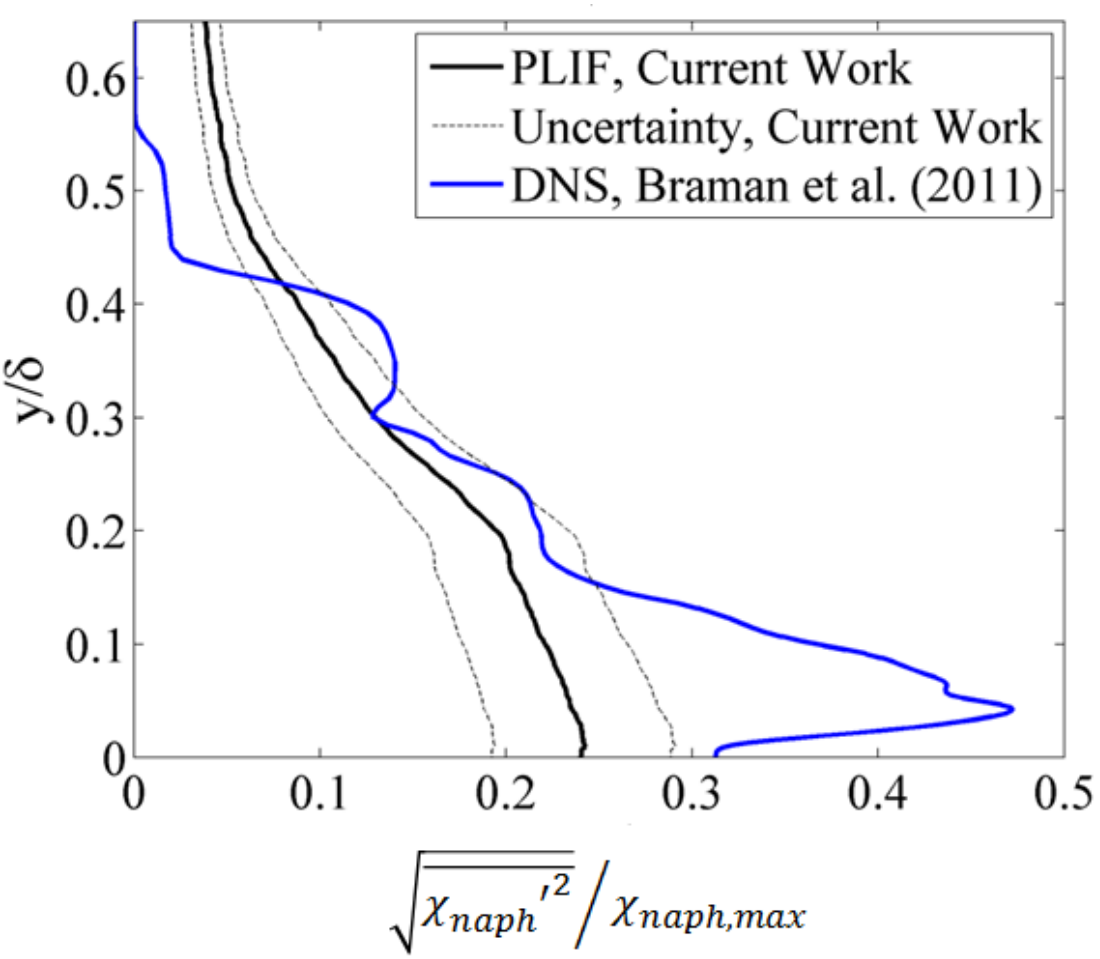

Figure 3.25: Comparison of $\chi_{Naph,rms}$ profiles in the Mach 5 boundary layer from naphthalene PLIF in the current work and from DNS of an ablating patch (Braman et al., 2011).

Lastly, Figure 3.26 is a comparison of the mean boundary layer profiles of naphthalene mole fraction and velocity plotted in wall units. Naphthalene mole fraction is presented as $1-<\chi_{Naph}>/\chi_{Naph,max}$ and the Van Driest transformation has been applied to the velocity profile. As seen in the figure, the profiles of velocity and normalized mole fraction both agree with the log law from approximately $100 < y^+ < 300$ (Van Driest, 1951). Additionally, the velocity and scalar profiles both appear to have a

similar shape for the entire range of y^+ for which data was acquired. Deviation from the log law is observed for $y^+ > 300$. Unalmis (1995) observed logarithmic behavior of the velocity profile in the same Mach 5 boundary layer from $100 < y^+ < 300$, in agreement with the current results. However, the velocity profile measured by Unalmis (1995) did not agree with the log law and was offset by a u^+ of approximately 1-2. Unalmis (1995) also showed a similar deviation from the log law for $y^+ > 300$, as seen in the current work.

The logarithmic behavior observed in the scalar profile, similar to what is seen in the velocity profile, has been discussed in many other studies in the literature. Kader (1981) observed a logarithmic dependence of the temperature profile on wall distance in various turbulent channel and pipe flows over a wide range of Prandtl numbers. For the case of turbulent air flow in a channel, the profile was logarithmic from approximately $40 < y^+ < 200$, which is in good agreement with the current work. Kim and Moin (1989) performed DNS in a turbulent channel flow with a constant-temperature wall, and calculated temperature profiles that also exhibited a logarithmic dependence on y^+ from $30 < y^+ < 150$. Furthermore, DNS by Kasagi et al. (1992) in a turbulent channel flow of air with a constant wall heat flux boundary condition produced temperature profiles with logarithmic behavior from $40 < y^+ < 100$. Kasagi et al. (1992) also showed that when the temperature profiles were converted into normalized wall units and plotted versus y^+, excellent agreement can be observed between their work and that of Kader (1981) and Kim and Moin (1989). However, the temperature profiles plotted in wall units did not match the velocity profiles plotted in u^+ and required different log law constants.

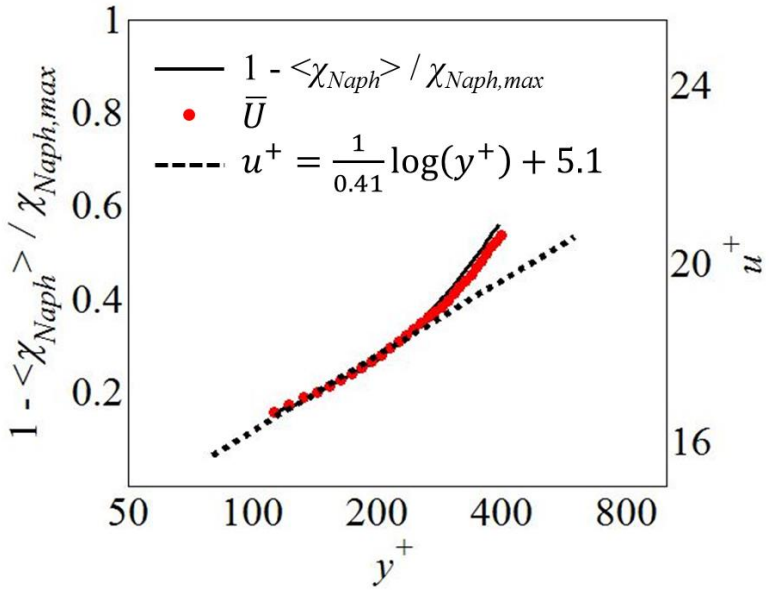

Figure 3.26: Profiles of $1-<\chi_{Naph}>/\chi_{Naph,max}$ and the Van Driest transformed mean streamwise velocity profile compared to the log law and plotted in normalized wall units.

3.4 - CONCLUSION

Quantitative naphthalene PLIF has been employed to measure the transport of ablation products in a Mach 5 turbulent boundary layer. Naphthalene vapor was introduced into the flow by ablation of a solid naphthalene insert located upstream of the imaging field of view and mounted flush with the wind tunnel floor. An uncertainty analysis shows the PLIF images were converted into two-dimensional fields of naphthalene mole fraction—using the relationships developed in Chapter 2—with an uncertainty of ± 20%, with the largest contributor to the uncertainty being the mean temperature correction.

The images revealed large-scale naphthalene vapor structures that were regularly ejected into the turbulent boundary layer out to wall distances of approximately y/δ = 0.6. A high signal region was found in the near wall region (y/δ < 0.05). It was also observed

that certain naphthalene vapor structures became more identifiable after the images had been converted to mole fraction. The magnitude of the calculated naphthalene mole fraction in these structures at $y/\delta = 0.2$ ranged from approximately 1-6% of the saturation mole fraction at the wind tunnel recovery temperature and static pressure. Large field of view images were also constructed by combining images from multiple fields of view to visualize the large scale structure of the scalar transport.

In analyzing the mean profile of naphthalene mole fraction it was clear that scalar concentration steadily decreased with increasing distance from the wall, as expected. Additionally, converting the PLIF images to fields of naphthalene mole fraction significantly changed the relative magnitude of the high signal in the near-wall region ($y/\delta < 0.05$). This thin layer of high signal was previously discounted by Lochman et al. (2010) and Buxton et al. (2012) as either laser scatter or fluorescence from deposition of solid-phase naphthalene on the wall. However, upon conversion of the PLIF signal to naphthalene mole fraction it was found that the peak calculated mole fraction near the wall was between 5-10% of the saturation mole fraction, suggesting the possibility that this high PLIF signal is actually the result of fluorescence from vapor-phase naphthalene.

Mean and r.m.s. profiles of the naphthalene mole fraction in the boundary layer were also acquired and were compared to DNS from Braman et al. (2011). While the DNS results predicted a maximum mole fraction at the wall approximately 10 times higher than what was measured using PLIF, this was most likely due to a discrepancy in the sublimation model employed in the DNS as well as a difference in the size of the naphthalene insert.

Furthermore, mole fraction was observed to decrease with increasing streamwise distance away from the naphthalene insert. Mean mole fraction profiles collected at

different streamwise locations were normalized by the mole fraction measured at the wall and a characteristic height of the scalar boundary layer. Using this normalization, the profiles were shown to collapse into one "universal" mole fraction profile, as shown by Poreh and Cermak (1962).

Lastly, profiles of velocity and naphthalene mole fraction were both shown to exhibit logarithmic behavior from $100 < y^+ < 300$ when plotted in wall units and compared to the law of the wall.

3.5 - SUGGESTED FUTURE WORK

The quantitative naphthalene PLIF technique underwent significant development and growth during the course of this research but there is much work that can still be done. The collection of mole fraction fields in various planes at different transverse distances off of the wind tunnel centerline would be extremely interesting and would provide information on the three-dimensional characteristics of the scalar dispersion. This would permit a sort of three-dimensional reconstruction of the scalar transport. In the same vein, images could be collected in different transverse planes (i.e., with the laser sheet passing horizontally through the wind tunnel and the camera imaging either from the top or bottom of the test section). Acquiring larger instantaneous fields of view would also prove instructive. This may require multiple cameras whose fields of view would be mapped together. A more powerful laser source or the ability to pass the laser sheet through the test section a second (or third) time may also be necessary.

Furthermore, it would be useful to make more measurements of the temperature of the naphthalene insert near the wind tunnel floor to help provide improved boundary conditions for those performing simulations of the experiment.

Lastly, it would be interesting to study the effect of different sized naphthalene inserts and investigate the scalar dispersion immediately at the trailing edge of these inserts to image the scalar when it first diffuses into the flow.

Chapter 4: Investigation of ablation products transport in a Mach 5 boundary layer using simultaneous PIV and quantitative naphthalene PLIF

4.1 - INTRODUCTION

This chapter discusses progress toward combining the quantitiative naphthalene PLIF technique with PIV measurements to enable the calculation of scalar-velocity correlations. In this work, naphthalene vapor is again dispersed in the form of a passive scalar in a Mach 5 turbulent boundary layer via a solid naphthalene insert mounted in the floor of the wind tunnel. Two-dimensional fields of naphthalene mole fraction and velocity are obtained by using simultaneous PIV and PLIF to obtain quantitative scalar-velocity data on the turbulent transport of ablation products in the boundary layer. Empirical relationships for naphthalene fluorescence signal and yield discussed in Chapter 2 are employed in this section. Constant static pressure across the boundary layer is assumed. Temperature is estimated by applying a mean temperature correction derived from the Crocco-Busemann relation based on a mean velocity profile measured with PIV. Combining the naphthalene mole fraction fields with simultaneously-acquired PIV data permits analysis of scalar-velocity correlations in the Mach 5 turbulent boundary layer.

4.2 - EXPERIMENTAL PROGRAM

4.2.1 - Wind Tunnel Facility

The facility used for these experiments was the same low-enthalpy blow-down Mach 5 wind tunnel described in Section 3.2.1. The wind tunnel was supplied by a 4 m^3 storage tank held at approximately 15.5 MPa and the plenum pressure was maintained at approximately 2.5 MPa ± 15 kPa. The flow was electrically heated to achieve a stagnation temperature of up to 368 K ± 4 K. The test section and flow properties were

the same as those discussed in Section 3.2.1. Optical access for laser transmission and imaging was provided by fused silica windows on the wind tunnel floor, ceiling, and sidewall.

As in Chapter 3, the naphthalene vapor was introduced into the flow by sublimation of a solid naphthalene insert (105 mm long x 57 mm wide) that was mounted to the floor of the wind tunnel. The solid block of naphthalene, depicted in Figures 4.1 and 4.2, was formed by pouring liquid naphthalene into a mold and then covering it during the cooling process to ensure a smooth, flush surface. After the naphthalene solidified, the cover was removed and the insert was installed into the test section floor. The sublimation rate of naphthalene at standard conditions is slow and no noticeable mass was lost if the insert was left in the test section for hours without flow. Only a small amount of ablation (less than a fraction of a millimeter) was observed over the course of a one minute wind tunnel run.

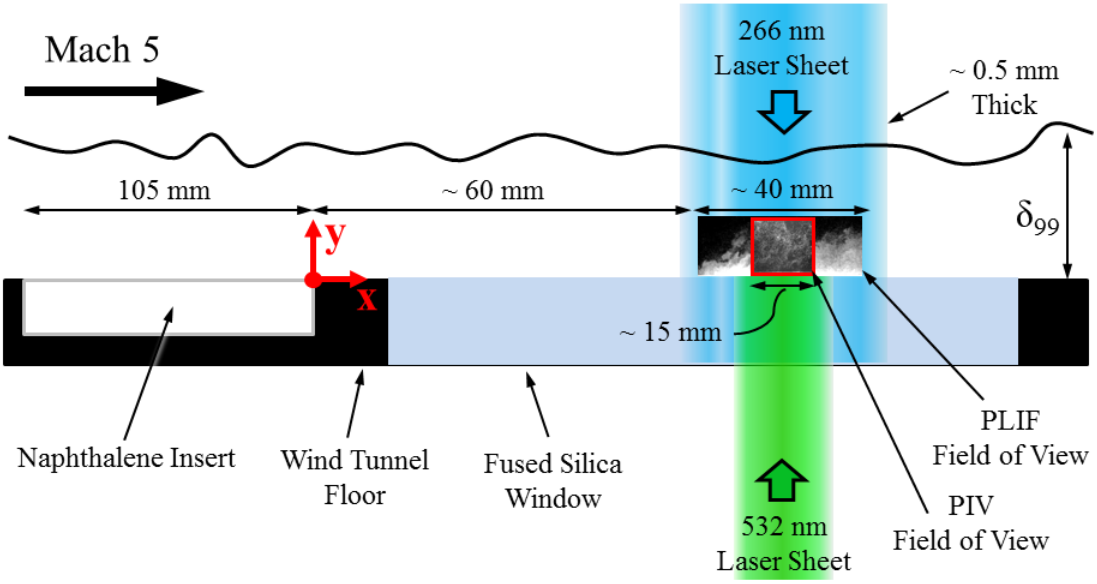

Figure 4.1: Schematic of the naphthalene insert and imaging field of view during the first imaging campaign. The coordinate system employed is indicated by the red axes.

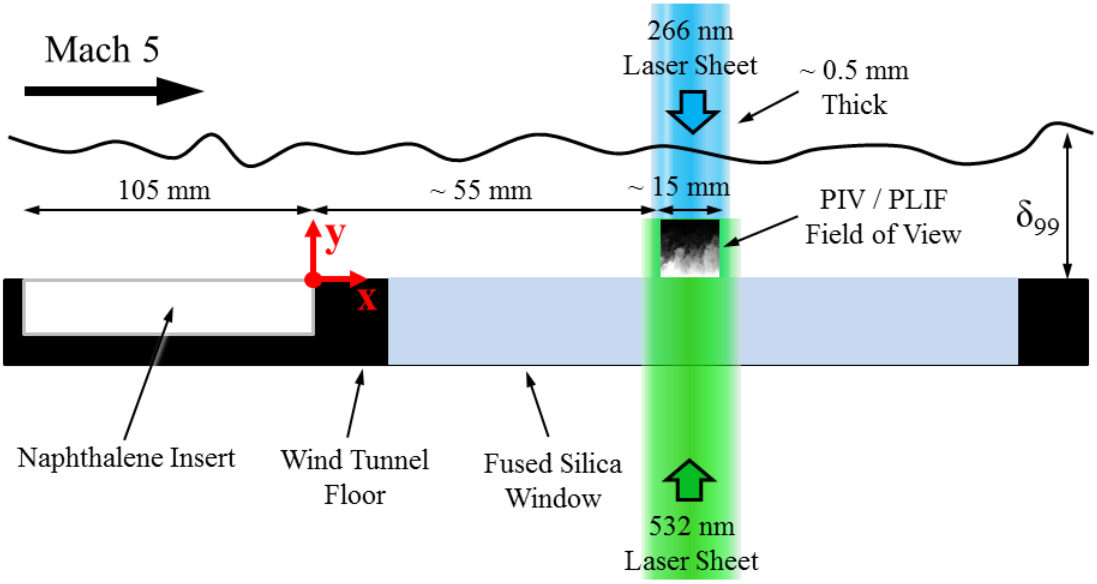

Figure 4.2: Schematic of the naphthalene insert and imaging field of view during the second imaging campaign. The coordinate system employed is indicated by the red axes.

4.2.2 - PLIF Experimental Setup

The naphthalene vapor was excited by a sheet of 266 nm light from a frequency-quadrupled Nd:YAG laser (Spectra-Physics Quanta-Ray GCR-150)—depicted in Figure 4.3—operating at a rate of 10 Hz with its energy maintained at approximately 42 mJ/pulse. The UV laser beam was oriented by a series of laser mirrors so that it passed up to the top of the wind tunnel facility where it was formed into a laser sheet using a 250 mm spherical lens and a 25 mm cylindrical lens and transmitted through the test section, as seen in Figure 4.3. The resulting laser sheet was about 0.5 mm thick (FWHM) in the measurement region and approximately 40 mm wide during the first campaign and 15 mm wide during the second campaign. PLIF images were recorded using a back-illuminated high-UV quantum efficiency CCD camera (Apogee Alta F47, 1024×1024) fitted with a 100 mm focal length, f/2.8 UV lens (Circo) operated at full aperture. In order

to reject scattered laser light and image only naphthalene fluorescence, one Schott WG-295 filter and one Schott UG-11 filter were placed in front of the camera. The imaging field of view was approximately 40 mm wide by 16 mm tall in the first imaging campaign and approximately 15 mm wide by 16 mm tall in the second imaging campaign. The images were obtained at a rate of approximately 1/3 Hz with a 40 ms exposure time and as many as 30 images could be acquired per wind tunnel run. 1/3 Hz was the maximum acquisition rate of the Apogee camera and the maximum shutter speed of the camera was approximately 40 ms. However, the flow was effectively frozen considering that the lifetime of the naphthalene fluorescence and the laser pulse FWHM are both on the order of 10 ns. The coordinate system applied to the PLIF and PIV fields of view is as follows: the x-direction is aligned with the freestream while the y-direction is normal to the wind tunnel floor, with the origin located at the trailing edge of the naphthalene insert and on the same plane as the laser sheet, as illustrated in Figures 4.1 and 4.2. The experiment was synchronized using three Stanford Research Systems digital delay generators to ensure that images were acquired while the laser was firing.

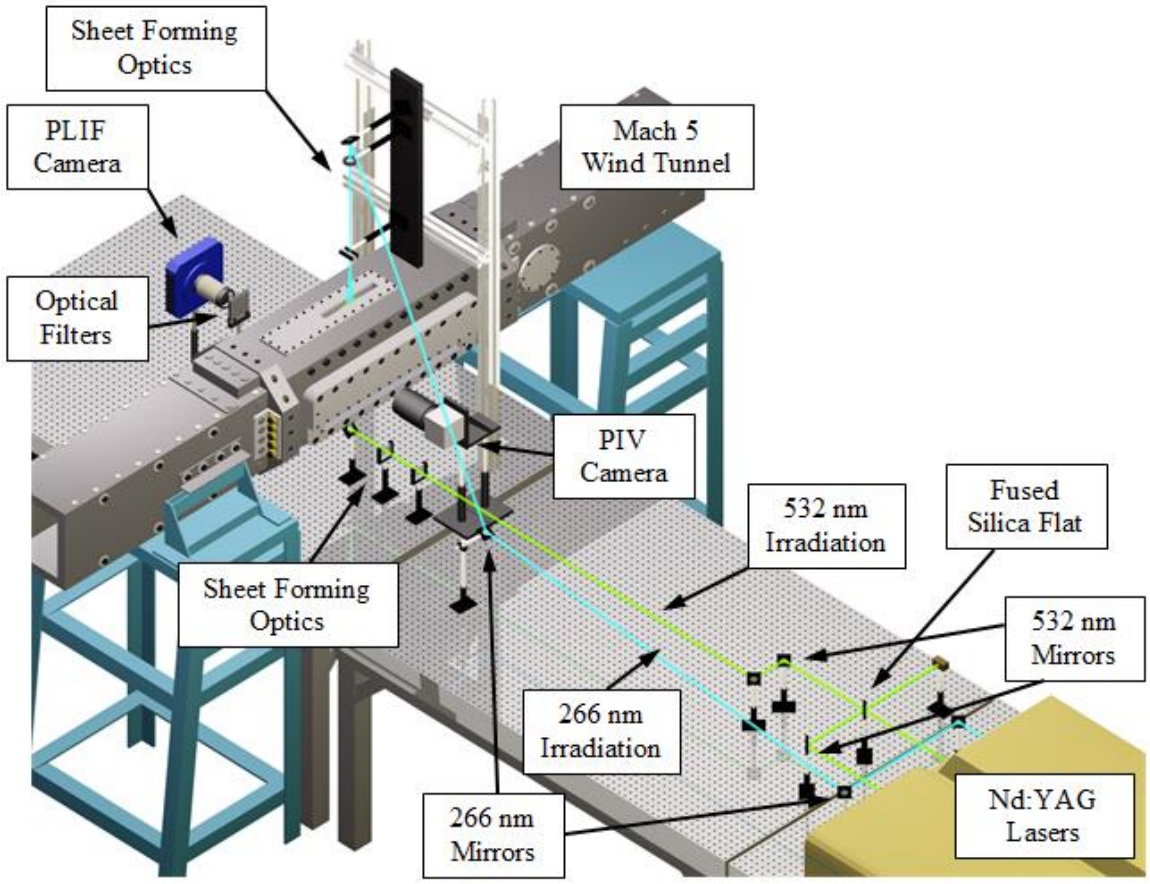

Figure 4.3: Simultaneous PIV/PLIF Setup.

4.2.3 - PIV Experimental Setup

Titanium Dioxide (TiO_2) was used as the seed particle for PIV. The particles were seeded via a two-stage fluidized bed driven by compressed air into a cyclone separator system and injected directly into the boundary layer of the lower wall, just upstream of the convergent section of the wind tunnel nozzle. Hou (2003) studied particle seeding in the wind tunnel used for the present work and measured the nominal particle diameter to be approximately 0.26 μm and calculated the particle response time to be 2.9 μs. This results in a particle Stokes number of 0.11 for the Mach 5 boundary layer conditions, satisfying the guideline established by Samimy and Lele (1991) of a particle Stokes

number < 0.5 for reliable flow tracking. Other potential sources of error in the PIV system are discussed in more detail in Appendix B, Section B.2.

The seed particles were illuminated by two sheets of 532 nm irradiation from frequency-doubled Nd:YAG lasers and imaged using a high-speed CCD camera (Princeton Instruments MegaPlus ES4020, 2048×2048), as seen in Figure 4.3. The camera was equipped with a Nikkor 105 mm macro lens operated at an aperture of f/5.6, which resulted in a field of view of approximately 16×16 mm.

The first laser sheet was generated by the residual 532 nm light from the GCR-150 laser used for PLIF excitation and was thus synchronized with the PLIF image. A single cavity from a Spectra-Physics Quanta-Ray PIV-400 laser was used to generate the second laser sheet and was delayed by 300 ns relative to the GCR-150. As shown in Figure 4.3, the laser pulses were combined using an uncoated fused silica flat. The GCR-150 beam passed through the fused silica flat and combined with the approximately 10% reflection from the PIV-400 beam that was incident to the flat 90° relative to the GCR-150 beam. This resulted in two coincident beams with pulse energies of approximately 15 mJ/pulse each.

The light sheets formed for PIV and PLIF were then aligned so that they were coincident and the two fields of view overlap, as illustrated in Figures 4.1 and 4.2.

4.2.4 - PLIF Image Processing

Single-shot PLIF images were processed in the same manner as described in Section 3.2.3 in MATLAB by first removing the background and then were corrected for variations in the mean intensity profile of the laser sheet. Single-shot sheet corrections were not made. As in the second PLIF imaging campaign discussed in Chapter 3, the mean laser sheet spatial intensity variation was measured by one of two methods: (1)

imaging the mean fluorescence of naphthalene vapor present in the test section (preferred) or (2) imaging the mean fluorescence of acetone vapor in the test section. These images would be collected prior to a run with the same CCD camera used for the PLIF experiments. Upon averaging approximately 30 of these images, a two-dimensional laser sheet profile was observed. The single-shot images obtained during the runs were then divided by this laser-sheet intensity profile to correct for spatial variations in laser energy.

Additionally, a room temperature reference cell saturated with naphthalene vapor was pulled to a vacuum (4.92 kPa ± 10 Pa), placed in the Mach 5 test section in the path of the 266 nm laser sheet, and imaged to generate reference images for quantifying the fluorescence signal. These images were also corrected for variations in laser sheet intensity by using the same technique described above. The naphthalene reference cell was not used for making sheet corrections of the wind tunnel images because the cell could not be oriented in a way that permitted imaging the same field of view.

After correcting the images for non-uniformities in the laser sheet the measured fluorescence signal and reference fluorescence signal were input into Eq. 1.10, using the fits for absorption cross section and fluorescence yield described in Section 2.3.3 to solve for naphthalene mole fraction.

Using the described procedure and curve fits, the PLIF images were converted into two-dimensional plots of naphthalene mole fraction. To reduce noise, a 3×3 median filter was applied to all images.

No correction was made for potential laser absorption by naphthalene vapor since negligible absorption was observed in the test cell over a distance larger than the boundary layer thickness and calculations based on measurements of absorption cross

section by Orain et al. (2011) indicate potential laser beam attenuation through the boundary layer between 0.4% and 3%, as discussed in Section 3.2.3.

4.2.5 - PIV Image Processing

The raw PIV particle image pairs were processed in LaVision's DaVis software. The software recursively refined the interrogation window from 256×256 pixels to a final interrogation window of 32×32 pixels with a 50% overlap between interrogation windows. Given the magnification of approximately 8 μm/pixel, the final interrogation window had a physical size of approximately 512 μm and the resulting vector field had a size of 64×64 vectors. The number of spurious vectors removed by the DaVis software was less than 10% in all cases, and these missing vectors were interpolated using a nearest neighbor linear interpolation technique. PIV resolution was determined by imaging a ruler placed in the Mach 5 test section. Additionally, to map the PIV and PLIF fields of view onto one another, the same ruler (which had uniform markings on each side) was imaged by both the PIV and PLIF cameras. Common points on the ruler in the portion of the field of view in which naphthalene vapor was generally present were manually identified in each image and were used as markers for a mapping procedure. The magnification of each image was then determined using the ruler image. Based on the measured magnification and the pixel locations of the markers, the images were resized, rotated (if necessary), and cropped so that the images from both cameras were aligned. This procedure was completed in MATLAB and was verified by matching the original ruler images recorded with both cameras. The PIV velocity data are estimated to have an uncertainty of approximately ± 8%, as discussed in Appendix B, Section B.2.

4.3 - RESULTS AND DISCUSSION

4.3.1 - Simultaneous PIV and Naphthalene PLIF Images: First Campaign

Figure 4.4 presents some typical instantaneous fields of normalized naphthalene mole fraction paired with the simultaneously-acquired instantaneous streamwise and wall-normal velocity fields collected during the first imaging campaign. The measured fluorescence signal intensity was significantly lower when making simultaneous PIV measurements compared to runs where only PLIF images were collected. Similar problems were encountered by Buxton et al. (2012) and led to concern that the naphthalene PLIF signal was simply not strong enough to produce high SNR images simultaneously with PIV. This issue was subsequently investigated and let to significant improvements in the PLIF images acquired during a second imaging campaign, discussed in Section 4.3.2.

Examining the images reveals that, in general, the regions with high naphthalene mole fraction tend to correspond with structures having a relatively low streamwise velocity component, u. Additionally, the naphthalene vapor structures again appear to be confined within $y/\delta < 0.6$ along with the regions of low streamwise velocity, similar to what was observed by Buxton et al. (2012). Meanwhile, a correlation with the wall-normal velocity component, v, is not as obvious with the fluctuations about zero appearing to be relatively disconnected from the scalar field.

Unfortunately, only a small number of PLIF images were collected with sufficient signal to make mole fraction measurements over the course of a week-long wind tunnel testing campaign. Additionally, it was found that the PLIF signal was actually degrading with each successive wind tunnel run.

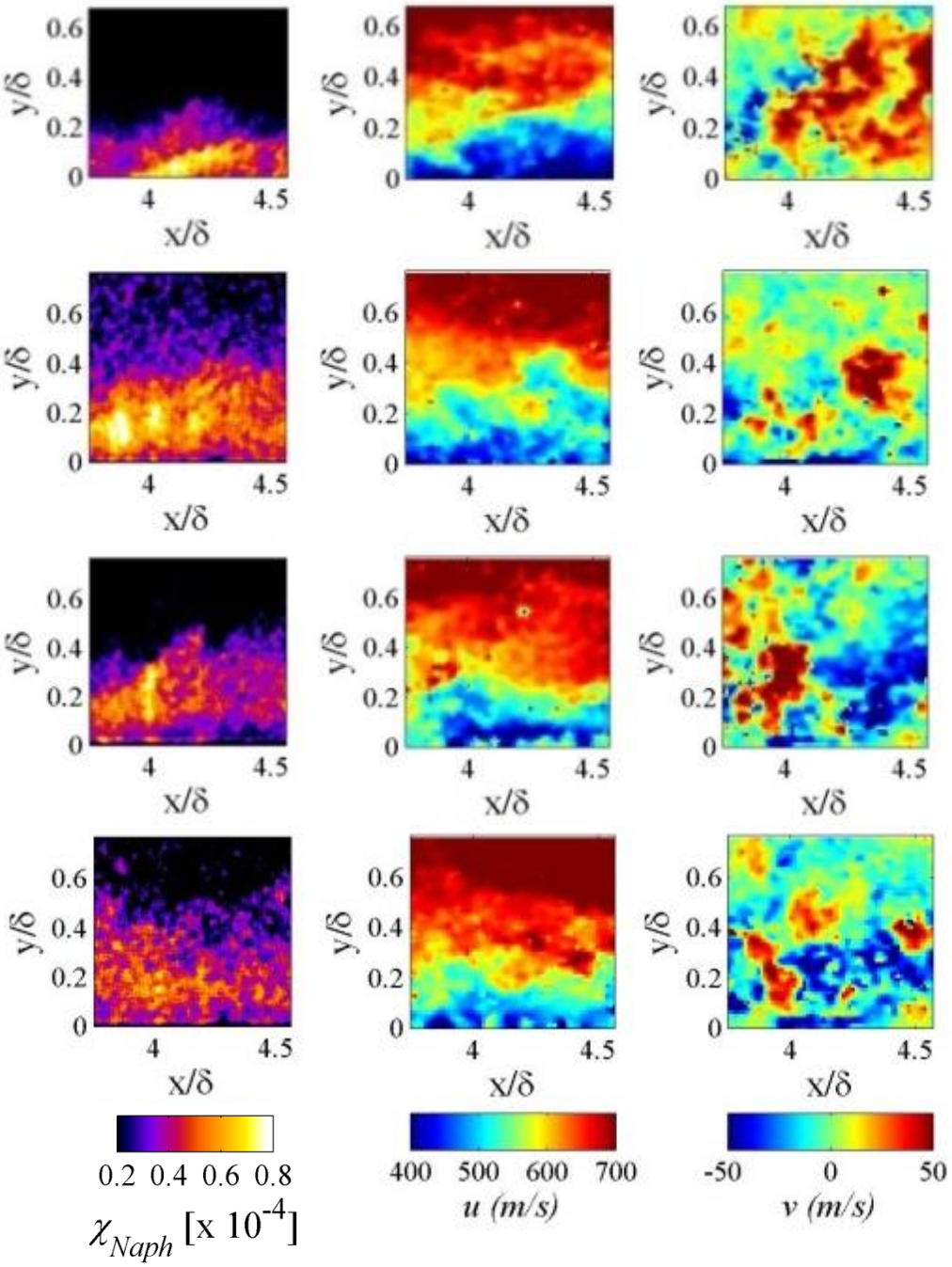

Figure 4.4: Typical instantaneous fields (rows) of normalized naphthalene mole fraction (left column) paired with simultaneously acquired streamwise (center column) and wall-normal (right column) velocity fields when the test section was not cleaned prior to a run and a mean Crocco-Busemann temperature correction was used for the PLIF images.

4.3.2 - Simultaneous PIV and Naphthalene PLIF Images: Second Campaign

After an initial series of wind tunnel runs that only proved moderately successful at acquiring simultaneous PIV and quantitative naphthalene PLIF, it became a priority to determine the cause of the decrease in PLIF signal that occurs when conducting simultaneous PIV. One key observation following the first campaign was that by the end of the testing schedule, PLIF images acquired without PIV were of unacceptable quality. This led to the hypothesis that perhaps the PIV particles accumulate on the surfaces of the wind tunnel test section (including the naphthalene insert) and inhibit sublimation. This idea was also supported by the fact that the quality of the PLIF images was seen to deteriorate over the course of the first PIV/PLIF imaging campaign. Figure 4.5 illustrates the difference between a recently cleaned test section and the appearance of the test section after several runs with particle seeding. It can be seen that all surfaces in the test section are coated with TiO_2 particles after several PIV runs including the fused silica windows for laser transmission and PLIF imaging as well as the naphthalene insert itself. In light of this realization, it was determined that part of the testing procedure for the second PIV/PLIF imaging campaign would be to thoroughly clean the interior of the Mach 5 facility from the nozzle throat to the downstream edge of the test section to ensure that the TiO_2 residue on the interior surfaces would be at a minimum at the start of each wind tunnel run.

The laser fluence was also increased almost by a factor of three by decreasing the width of the laser sheet to match the size of the PIV field of view. This was achieved by moving the cylindrical lens that formed the laser beam into a sheet closer to the test section. Since the laser power density was well within the linear regime, this change was motivated by the fact that any increase in laser power density should result in an equal

increase in PLIF signal. Additionally, given that the PIV field of view was small compared to the PLIF field of view in the first imaging campaign, this change could be enacted without decreasing the size of the domain on which PIV and PLIF were simultaneously acquired.

Furthermore, the imaging field of view was moved further upstream where the naphthalene concentration should be higher (see the discussion in Section 3.3.2).

The final change made in the second imaging campaign was an attempt to increase the temperature of the Mach 5 flow and thus increase the temperature of the naphthalene insert. This would then lead to an increase in the sublimation rate of naphthalene vapor from the block and a subsequent rise in PLIF signal. In order to increase the stagnation temperature of the flow, a "warm-up" run was conducted prior to each wind tunnel test. The "warm-up" runs would consist of a relatively short wind tunnel start up and shut down, lasting approximately 20 seconds in total, to preheat the Mach 5 facility. This resulted in an increase in the peak stagnation temperature during runs of approximately 5 to 10 K, with the peak stagnation temperature observed during a run of 368 K (compared to typical runs in previous campaigns where stagnation temperature was generally between 350 and 360 K). This increase in stagnation temperature corresponds to a 5 to 10 K increase in recovery temperature, which could cause an increase in vapor pressure of naphthalene by a factor of two.

Additionally, during wind tunnel runs where images were to be collected, PIV particles were not seeded into the flow until approximately 20 seconds after the wind tunnel had started to allow time for the stagnation temperature of the flow and the naphthalene insert to increase.

Figure 4.5: Photograph of the naphthalene insert in the Mach 5 test section before (top) and after (bottom) several wind tunnel runs with PIV particle seeding.

Figures 4.6 and 4.7 present some typical fields of naphthalene mole fraction captured with PLIF paired with simultaneously acquired fields of streamwise and wall-

normal velocity acquired during the second PIV/PLIF campaign. As seen in the figures, the changes to the test procedure led to a significant increase in the PLIF signal observed in the second campaign compared to the first campaign. Notice that when comparing the PLIF images in Figure 4.6 to those in Figure 4.4, the magnitude of naphthalene mole fraction in the large scale structures in Figure 4.6 is approximately double that of those in Figure 4.4, while the mole fraction observed in Figure 4.7 has increased by approximately 30% compared to the images in Figure 4.4. It should be noted that the images presented in Figure 4.6 were collected later in the day than the images in Figure 4.7, most likely leading to a warmer naphthalene insert. This behavior was predicted in the discussion on the changes to the test procedure; however, it should be noted that despite these changes the PLIF signal could be seen to noticeably decrease as soon as TiO_2 particles were introduced into the flow. Upon reviewing the raw PIV particle images and the corresponding simultaneously acquired PLIF images, there was a clear correlation between particle seeding density and naphthalene PLIF signal, which indicates that the TiO_2 particles in the flow are inhibiting the naphthalene fluorescence from reaching the CCD in some manner. Due to the nature of the injection seeding method, TiO_2 density steadily decreased over the course of a run, with the highest seeding density occurring the moment the injection valve was opened. For this reason, the best PIV images (containing the most valid vectors) occurred early in the run and the best PLIF images (those with the highest signal counts) occurred towards the end of the run. This relationship was further enhanced by the fact that the naphthalene insert is continually heating up during a run, thus the sublimation rate of naphthalene vapor from the plug increases with run time. Therefore, the majority of the useful image sets came from the middle portion of the wind tunnel runs as the PLIF images early in the run were

extremely noisy and the PIV images at the end of the run often did not possess sufficient particle seeding density for processing.

With this in mind, one can begin to examine the physical features of Figures 4.6 and 4.7. As was observed in Figure 4.4 the regions with high naphthalene mole fraction tend to correspond with structures having a relatively low streamwise velocity component, u. Here, the naphthalene vapor structures appear to be primarily confined within $y/\delta < 0.4$ compared to $y/\delta < 0.6$ in Figure 4.4. This difference is most likely a result of the change in the imaging field of view, as the location further downstream should exhibit a thicker scalar layer. Once again, a correlation with the wall-normal velocity component, v, is not as obvious but there do appear to be regions of large positive v' that correspond with regions of high naphthalene mole fraction in the final image of Figure 4.6 and the second image in Figure 4.7.

To highlight these apparent correlations, Figures 4.8 and 4.9 are shown, which present the same image sets from Figures 4.6 and 4.7, respectively, but with the fluctuating streamwise and wall-normal velocity fields displayed instead of the velocity magnitudes. While the wall-normal fields appear almost identical given that the mean wall-normal velocity is approximately zero, these figures make it easier to see the relationship between the naphthalene mole fraction concentration and the fluctuating streamwise velocity, u'. In most instances, as in the final image of Figure 4.8, there is a clear relationship between a large scale naphthalene vapor structure and a negative fluctuation in u. This image additionally shows a large scale region with positive v' and corresponding high naphthalene mole fraction. Examples of the converse of this relationship are also on display, as the first image in Figure 4.9 shows a region with positive u' around $0.1 < y/\delta < 0.3$ with a subsequently low measurement of naphthalene

mole fraction. In the same region, there simultaneously exists a structure with negative v'. While these types of examples are common, there do appear to be exceptions to this rule. Consider the final image in Figure 4.9, where there is a region with high naphthalene PLIF signal but a corresponding zone with positive u' and negative v'. However, in this case the high mole fraction region in question is primarily near the wind tunnel floor where the mole fraction has been shown to almost always be high. Therefore, it may be most appropriate to investigate the relationship between χ_{Naph}' with u' and v'.

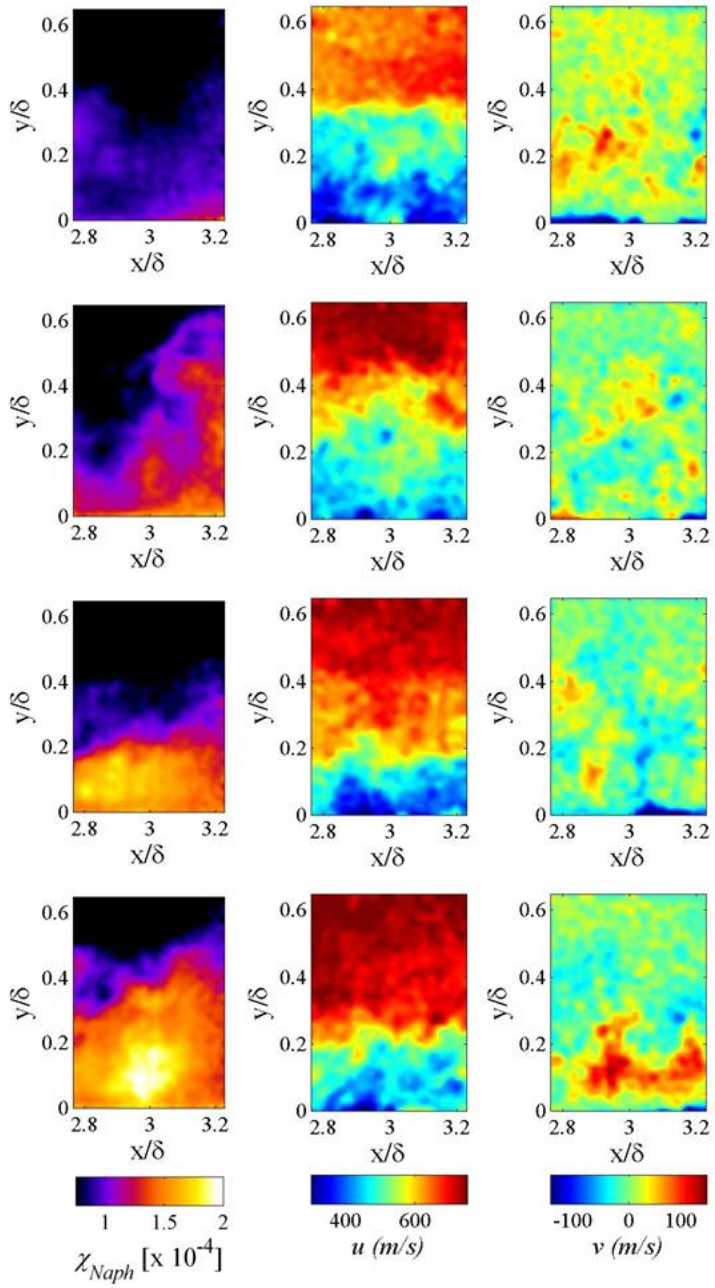

Figure 4.6: Typical instantaneous fields (rows) of naphthalene mole fraction (left column) paired with simultaneously acquired streamwise (center column) and wall-normal (right column) velocity fields during the second PIV/PLIF campaign when the mean Crocco-Busemann temperature correction was used for the PLIF images.

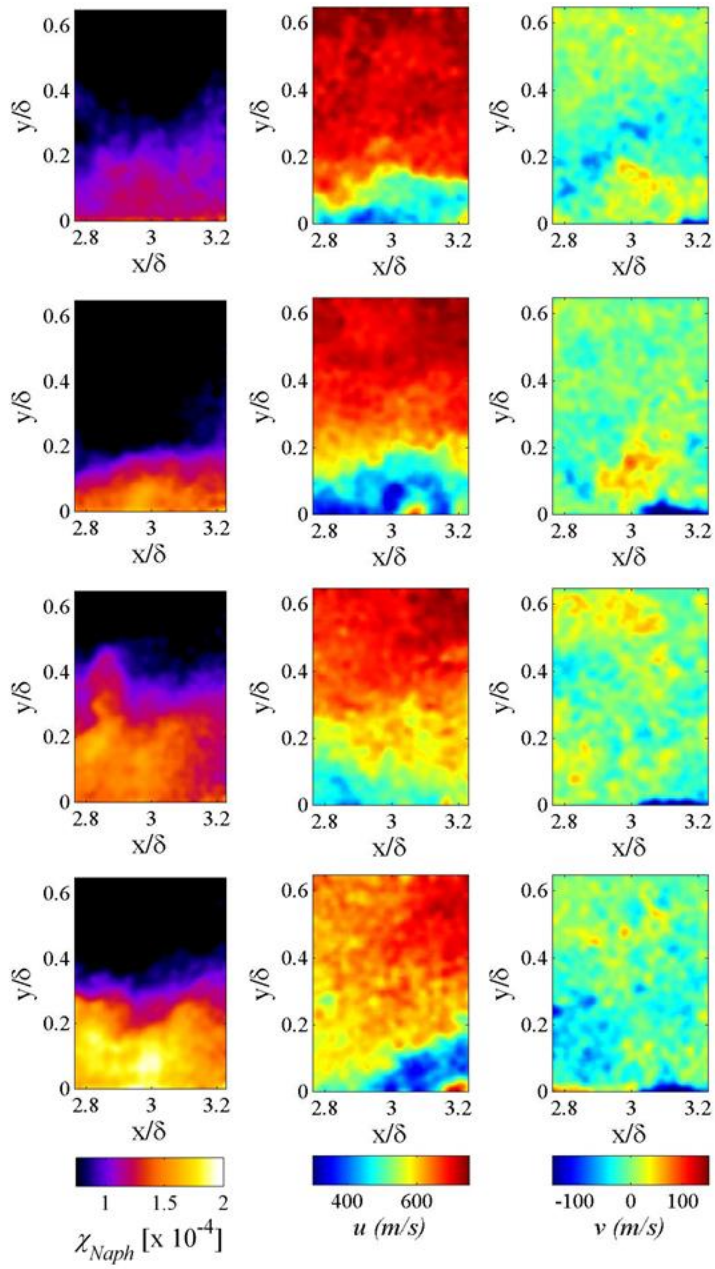

Figure 4.7: Typical instantaneous fields (rows) of naphthalene mole fraction (left column) paired with simultaneously acquired streamwise (center column) and wall-normal (right column) velocity fields during the second PIV/PLIF campaign when the mean Crocco-Busemann temperature correction was used for the PLIF images.

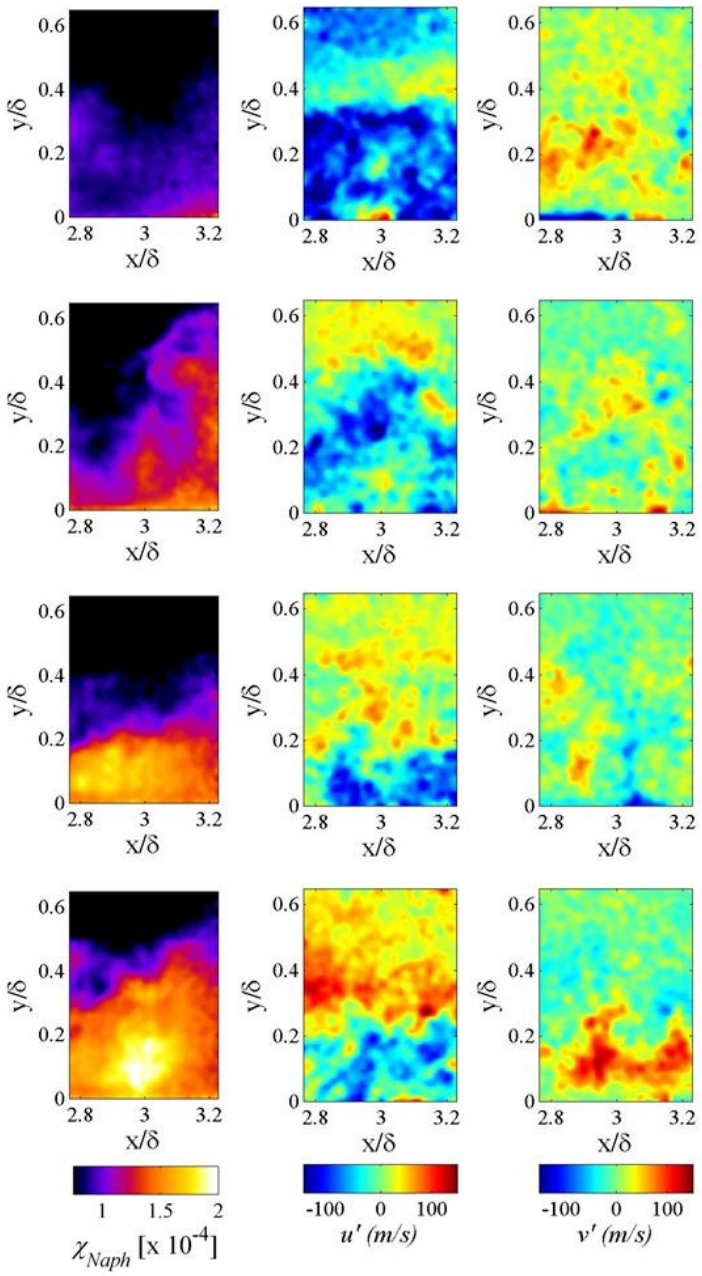

Figure 4.8: Typical instantaneous fields (rows) of naphthalene mole fraction (left column) paired with simultaneously acquired streamwise (center column) and wall-normal (right column) velocity fluctuation fields during the second PIV/PLIF campaign when the mean Crocco-Busemann temperature correction was used for the PLIF images. The images are the same as those seen in Figure 4.6.

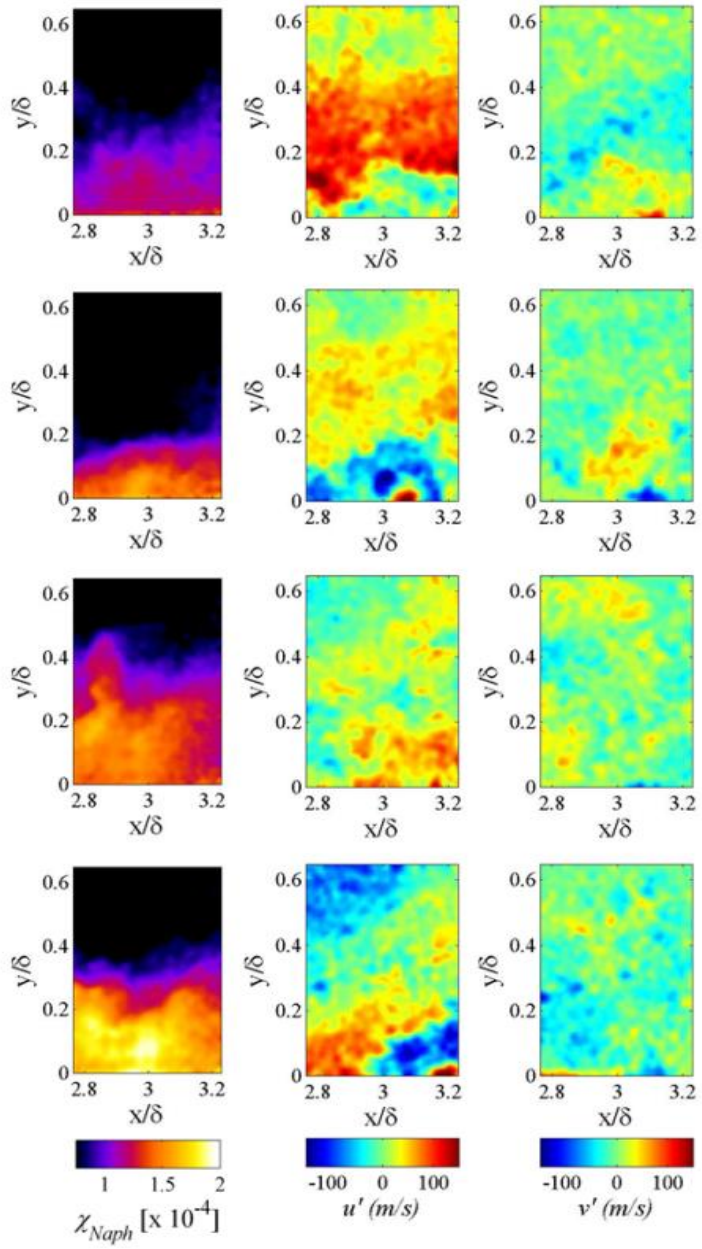

Figure 4.9: Typical instantaneous fields (rows) of naphthalene mole fraction (left column) paired with simultaneously acquired streamwise (center column) and wall-normal (right column) velocity fluctuation fields during the second PIV/PLIF campaign when the mean Crocco-Busemann temperature correction was used for the PLIF images. The images are the same as those seen in Figure 4.7.

4.3.3 - Mean Velocity Statistics

Before examining correlation statistics between χ_{Naph} and velocity, the mean characteristics of the velocity fields collected from the PIV were examined and compared to related work in the literature to provide confidence in the validity of the PIV data. Figure 4.10 is a two dimensional mean streamwise velocity field collected from 270 vector fields collected during a single dedicated PIV run in the current work. Meanwhile, Figure 4.11 compares the mean velocity profile from the current work—computed using data from 11 separate runs and a total of 512 vector fields, which is sufficient for convergence based on the analysis in Appendix B, Section B.2—to velocity profiles collected in the same Mach 5 boundary layer by McClure (1992) using a pitot probe survey and Beresh (1999) using PIV, as well as the velocity profile from the DNS of Braman et al. (2011). As seen in the figure, the current PIV profile appears to be approaching a similar freestream velocity as the work by McClure (1992) and Braman et al. (2011) with a discrepancy of approximately 3%, which is within the estimated 8% uncertainty in the current PIV measurements. For wall distances greater than $y/\delta = 0.05$ the PIV data appears to show velocities lower than what is expected from the pitot survey (McClure, 1992) and DNS (Braman et al., 2011) with the greatest discrepancy between the profiles occurring at approximately $y/\delta = 0.1$ of around 12%. This deviation is slightly larger than the estimated uncertainty of the current measurements. It is unclear if the difference in the profiles is a result of unforeseen bias errors in the PIV processing procedure or is a manifestation of some change in the flowfield caused by the injection of PIV particles into the plenum. As discussed by Beresh (1999), the injection of particles into the flow can cause changes to the measured velocity profile in the form of wake effects. Furthermore, since the particle stream was

effectively at room temperature an immediate decrease in flow stagnation temperature could be observed upon injecting PIV seed particles into the flow. Regardless, the mean profile appears to make physical sense and shows agreement with previous PIV studies collected at Mach 5 in the same facility.

A mean profile of u_{rms} is provided in Figure 4.12 along with u_{rms} from the Braman et al. (2011) DNS. Good agreement can be seen between the two profiles, with the peak $u_{rms}/\bar{u}$ measured at approximately 13% (105 m/s) at the wall and the peak u_{rms} from the DNS occurring just away from the wall with a value of approximately 14% (110 m/s). The DNS shows the r.m.s. dropping close to zero at the wall while the plot from the current work does not, which is most likely the result of limited spatial resolution near the wall for the PIV data. Similar u_{rms} plots were also given by Beresh (1999) and Buxton et al. (2012) who showed peak u_{rms} values at the wall of approximately 110 m/s and 55 m/s, respectively. It is likely that the relatively low number of images available for averaging in the work by Buxton et al. (2012) led to the discrepancy from the current work, Beresh (1999), and Braman et al. (2011) in the peak u_{rms} measurements. Additionally, Smith and Smits (1993) found u_{rms} to equal 6.3% at $y/\delta = 0.1$ for a Mach 2.89 flow, which is slightly lower than the current study which found u_{rms} to be 9.7% at $y/\delta = 0.1$. All three experimental studies in the Mach 5 boundary layer show good agreement in the measurement of u_{rms} at the extent of the current work's field of view ($y/\delta = 0.6$), with each study measuring a value between 25-40 m/s at this location, or about 3-5% of the freestream velocity. Smith and Smits (1993) also measured u_{rms} as 4.3% of the freestream velocity in a Mach 2.89 flow. Meanwhile, the DNS results of Braman et al. (2011) calculated a comparable value of 30 m/s (3.9%) at $y/\delta = 0.6$.

The profiles of u_{rms} are compared to several other studies in the literature in Figure 4.13 with a reproduced figure from Elena and Lacharme (1988). This figure can be found in Figure 4.13(a) while data from the current work is presented in Figure 4.13(b). The comparison is performed by presenting the data in normalized form, using the normalization of u_{rms} proposed by Morkovin (1962) for compressible flows, which accounts for the variation of density through the boundary layer. Figure 4.13(a) includes Morkovin-normalized u_{rms} profiles from hot wire and LDA data from 8 different sources over a Mach number range of 1.7 - 4.7. Comparing to the current work, these profiles are slightly lower than the u_{rms} profile in Figure 4.13(b), which is approximately 7% higher than the upper bound of the data in Figure 4.13(a). However, the trends are approximately the same as the slopes are extremely similar. The plot also indicates that the near-wall u_{rms} peak is most likely not correct. Hou (2013) performed a similar comparison using Mach 2 PIV data and also found a u_{rms} profile that had a slightly positive offset from the upper bound of the LDA data in Elena and Lacharme (1988).

Overall, the comparison of the mean and r.m.s. velocity profiles from the current work to previous research is sufficient to provide confidence in the PIV measurements.

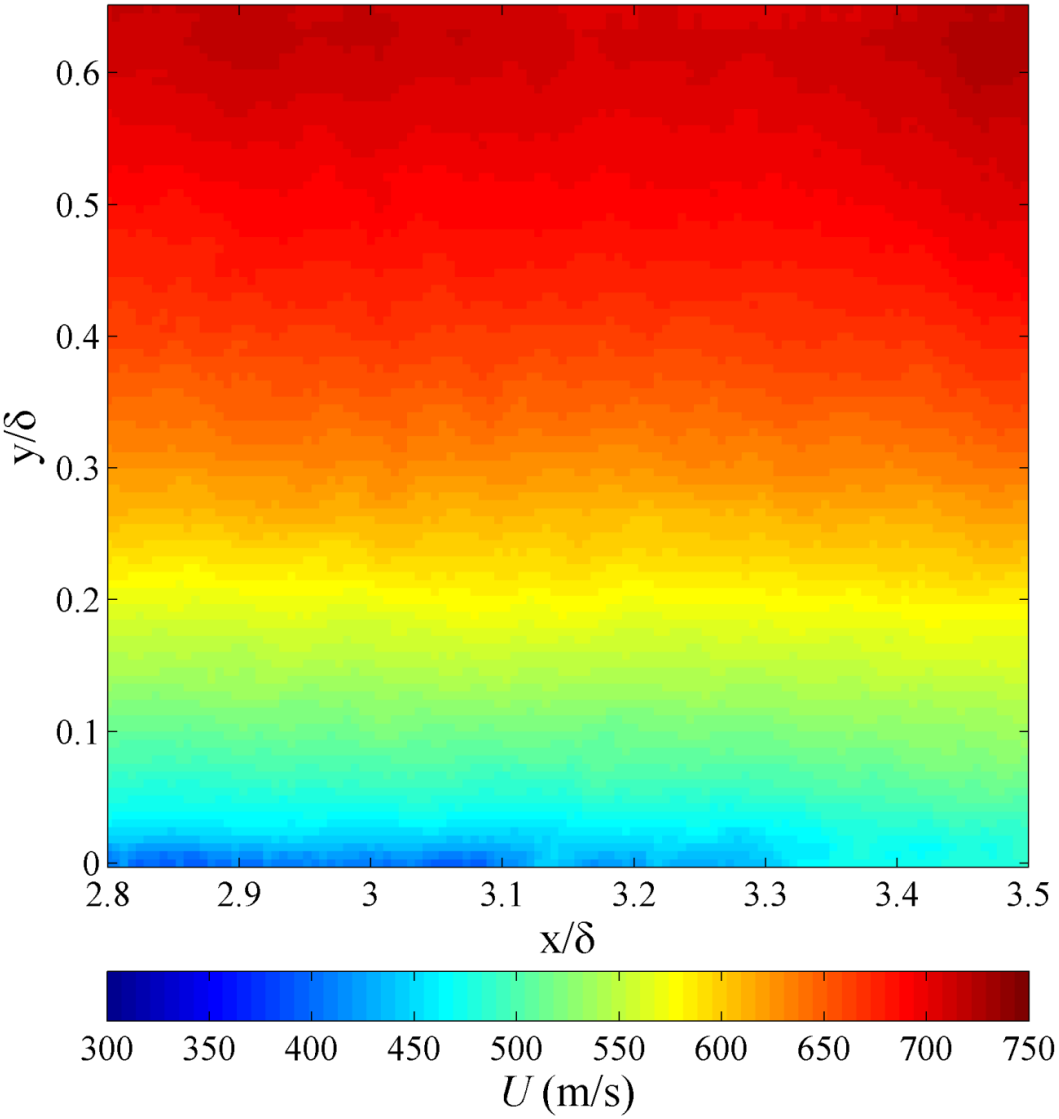

Figure 4.10: Mean streamwise velocity field in the Mach 5 boundary layer.

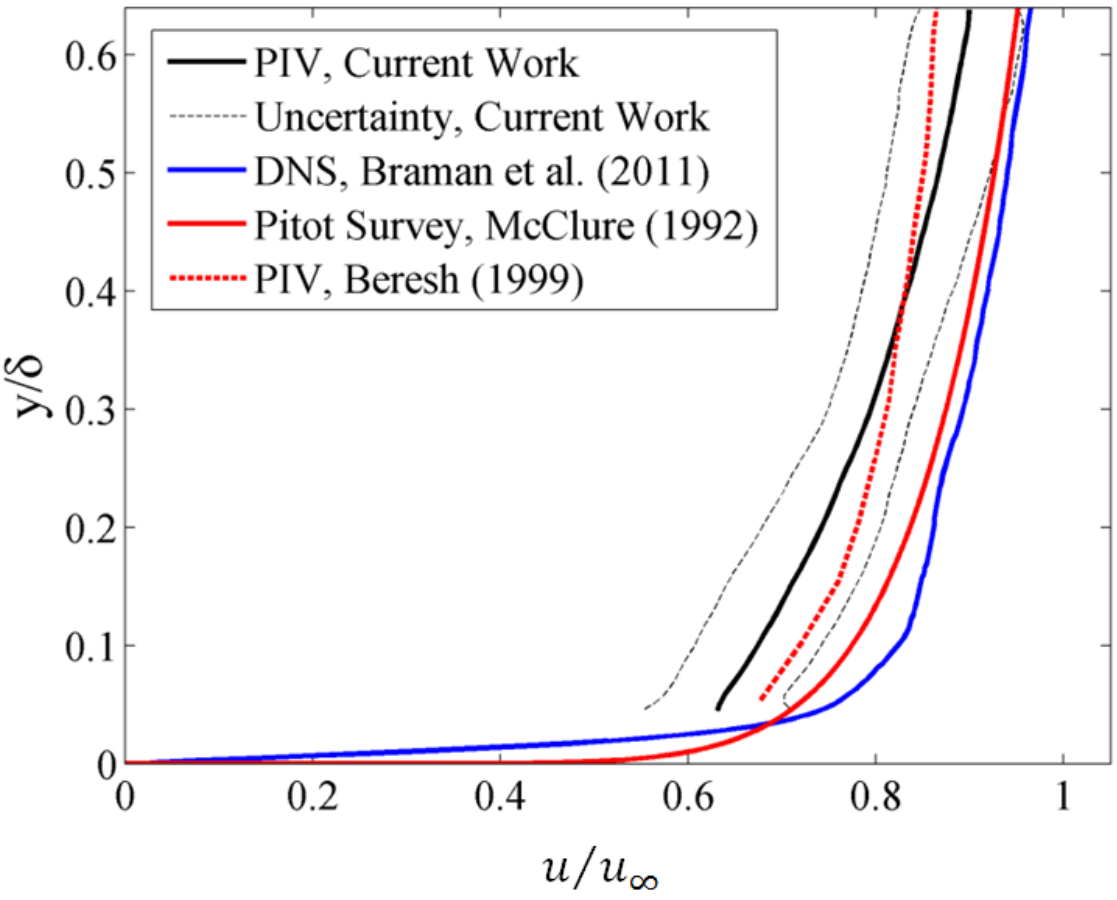

Figure 4.11: Comparison of mean streamwise velocity profiles in the Mach 5 boundary layer with respect to wall distance from the current study using PIV, a pitot probe survey conducted by McClure (1992), a PIV study from Beresh (1999), and DNS by Braman et al. (2011).

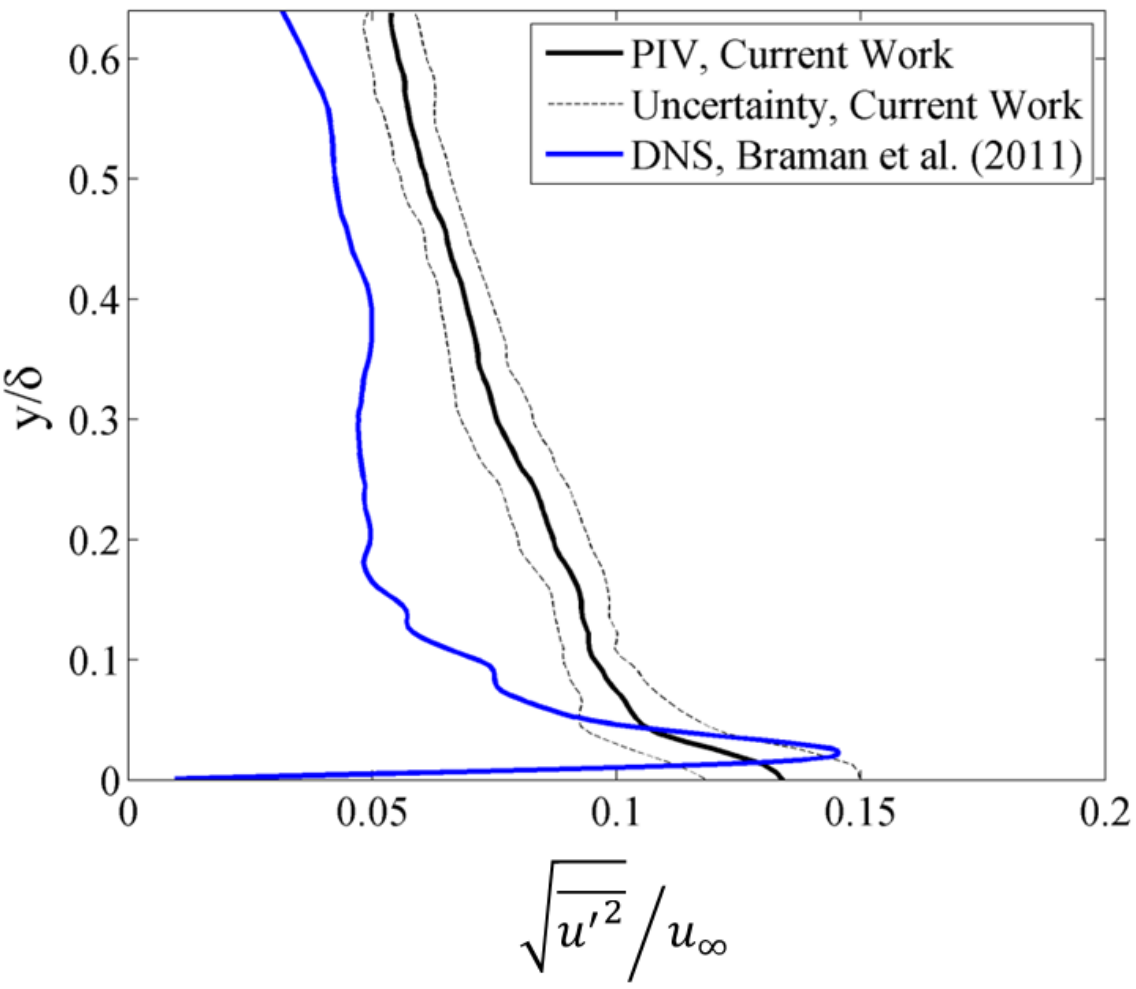

Figure 4.12: Comparison of u_{rms} streamwise velocity profiles in the Mach 5 boundary layer with respect to wall distance from PIV in the current work and from DNS by Braman et al. (2011).

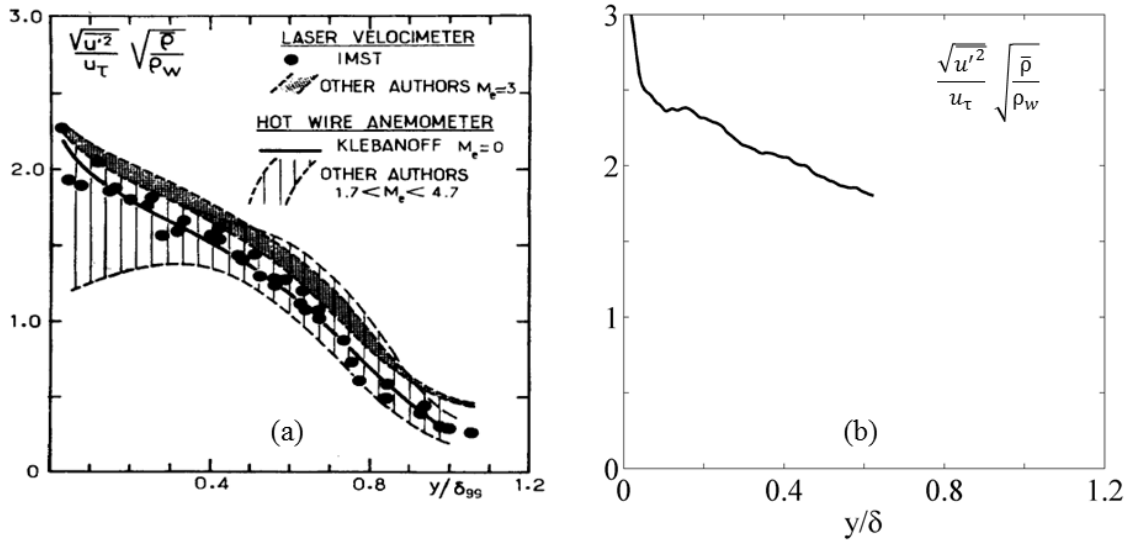

Figure 4.13: Comparison of Morkovin (1962) normalized u_{rms} streamwise velocity profiles from (a) Elena and Lacharme (1988) Figure 6—which includes hot wire and LDA data from 8 different sources over a Mach number range of 1.7 ~ 4.7—and the (b) current work.

4.3.4 - Scalar-Velocity Correlations

To further examine the relationship between scalar concentration and velocity, Figure 4.14 is presented, which shows the covariance, ρ, of the naphthalene mole fraction with both components of velocity, where

$$\rho_{x,y} = \frac{< (x - < x >) * (y - < y >) >}{\sigma(x)\sigma(y)} \qquad 4.1$$

and $\sigma(x)$ is the standard deviation of x. Image sets from 7 separate runs, totaling 130 simultaneous fields of mole fraction and velocity, were used to generate the following figures. Additionally, Figure 4.15 is a reproduction of Figure 4.14 where the covariance is plotted versus normalized wall units. The plots first confirm the relationship between u and χ that is illustrated by the image sets in Figures 4.8 and 4.9, as negative fluctuations in u are shown to correspond with higher naphthalene mole fraction. This correlation

reaches a trough near the wall and shows a peak between $0.1 < y/\delta < 0.2$ ($y^+ \sim 200$), which corresponds to the location of the outer edge of most of the naphthalene vapor structures. Buxton et al. (2012) noticed a similar peak at $y/\delta = 0.3$. DNS of turbulent channel flows by Kim and Moin (1989) and Kasagi et al. (1992) and DNS of turbulent flow over a flat plate by Li et al. (2009) shows the same positive correlation between streamwise velocity and temperature in the boundary layer, however the peak is found to occur between $10 < y^+ < 20$.

Figure 4.14 also illuminates a correlation between v and χ, with increased naphthalene mole fraction appearing to generally coincide with positive fluctuations in v. Considering that u' and v' should remain negatively correlated in a turbulent boundary layer (White, 1991) it makes sense that the two correlations should be of opposite sign. For confirmation, the covariance of u' and v'—a corrolary to the Reynolds stress term—is presented in Figure 4.16. As seen in the figure, the correlation is negative throughout the boundary layer, as expected. Similar to the correlation between u and χ, the covariance of v and χ reaches a positive peak between $0.2 < y/\delta < 0.3$ ($y^+ \sim 400$). This result is also observed in the DNS of Kim and Moin (1989), Kasagi et al. (1992), and Li et al. (2009), with slightly more ambiguous correlation peaks (relative to the correlation with streamwise velocity) observed around $y^+ = 30$. Furthermore, in the turbulent boundary layer of a water channel flow, Li et al. (2004) calculated the correlation between v and χ and found a very similar trend to what is seen in Figure 4.15 with the correlation peaking at $y^+ = 100$.

The DNS results (Kim and Moin, 1989; Kasagi et al., 1992; Li et al., 2009) also indicate that both correlations should go to zero at the wall, which is not observed in the current work, most likely due to poor near wall resolution. Finally, both profiles appear to

be approaching zero at the extent of the measurement region, which makes sense considering there is little naphthalene vapor present at wall distances greater than 0.5δ. The correlations measured by Li et al. (2004) also appear to be trending towards zero at the extent of the presented data ($y^+ = 400$).

Considering the correlations observed, it becomes evident that the naphthalene vapor structures present in the boundary layer beyond $y/\delta = 0.1$ are the result of an ejection mechanism, whereby fluid near the wall—traveling at relatively low streamwise velocity and containing a relatively high concentration of naphthalene vapor—is ejected out into the boundary layer by a turbulent burst with a relatively high wall-normal velocity component, as previously discussed by Spina et al. (1994).

In addition to providing value in analyzing the correlation between scalar and velocity, the covariance values plotted are essentially a normalized version of the turbulent scalar fluxes that are essential to the computation of scalar transport. These profiles are presented in Figure 4.17 and are similar to those presented in a computational study by Braman and Raman (2011) for an ablating graphite surface in a Mach 1.2 flow. The plots shown in Figure 4.17 were generated from the data in Figure 4.14. Additionally, Figure 4.18 is a reproduction of Figure 4.17 where the turbulent fluxes are plotted versus normalized wall units. Since these plots are effectively scaled versions of the profiles in Figures 4.14 and 4.15, the trends are of course the same. Furthermore, the DNS results of Kim and Moin (1989), Kasagi et al. (1992), and Li et al. (2009) show the same trends as Figures 4.17 and 4.18.

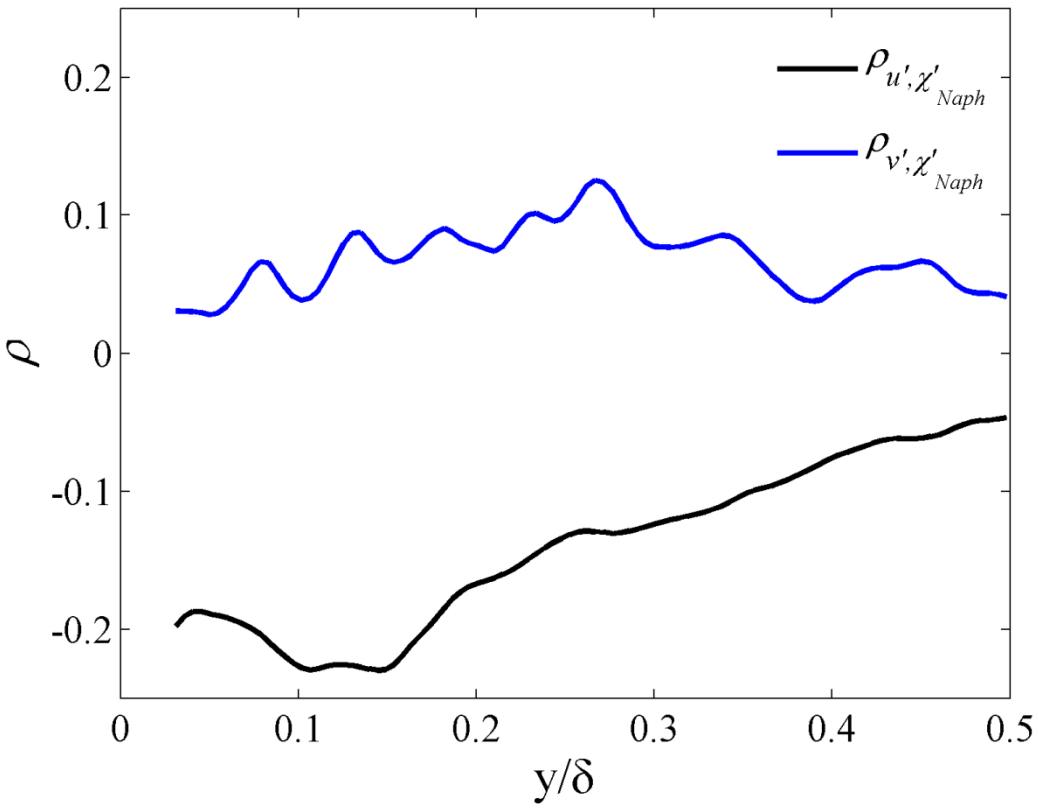

Figure 4.14: Plots of covariance between u' and χ'_{Naph} (black) and v' and χ'_{Naph} (blue) in the wall-normal direction when the temperature field employed for quantifying the PLIF images was obtained using a mean Crocco-Busemann approximation.

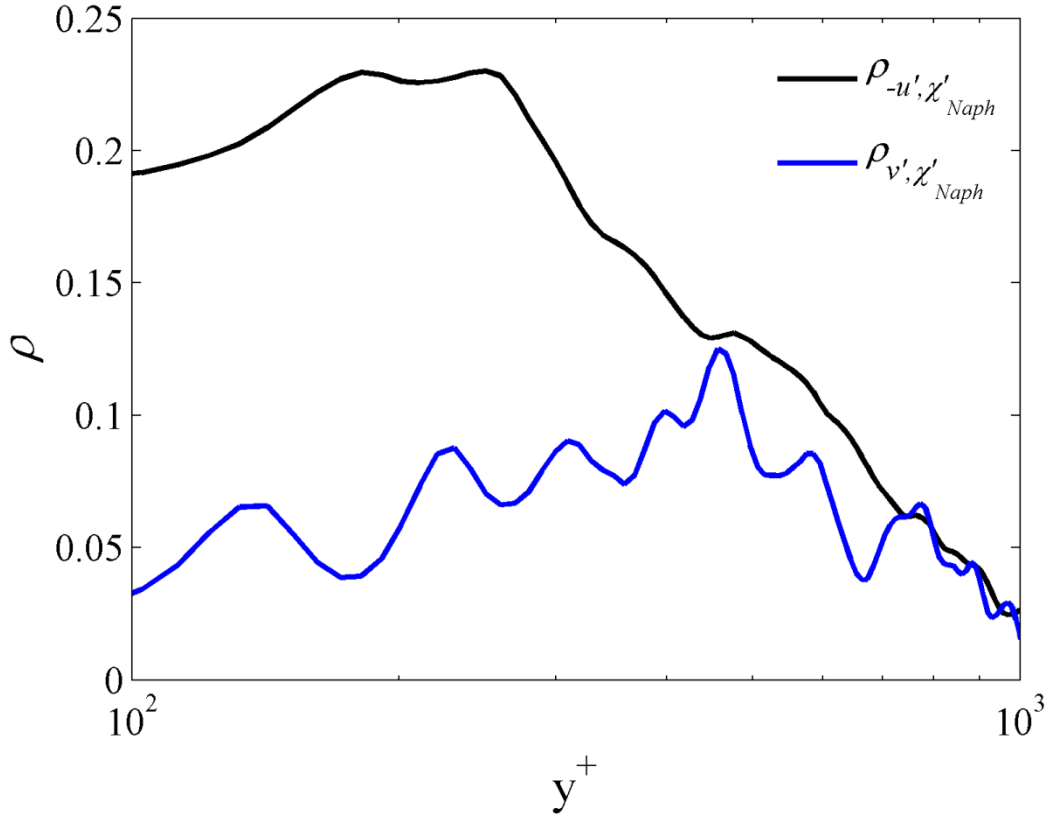

Figure 4.15: Plots of covariance between $-u'$ and χ'_{Naph} (black) and v' and χ'_{Naph} (blue) in the wall-normal direction when the temperature field employed for quantifying the PLIF images was obtained using a mean Crocco-Busemann approximation plotted versus normalized wall units.

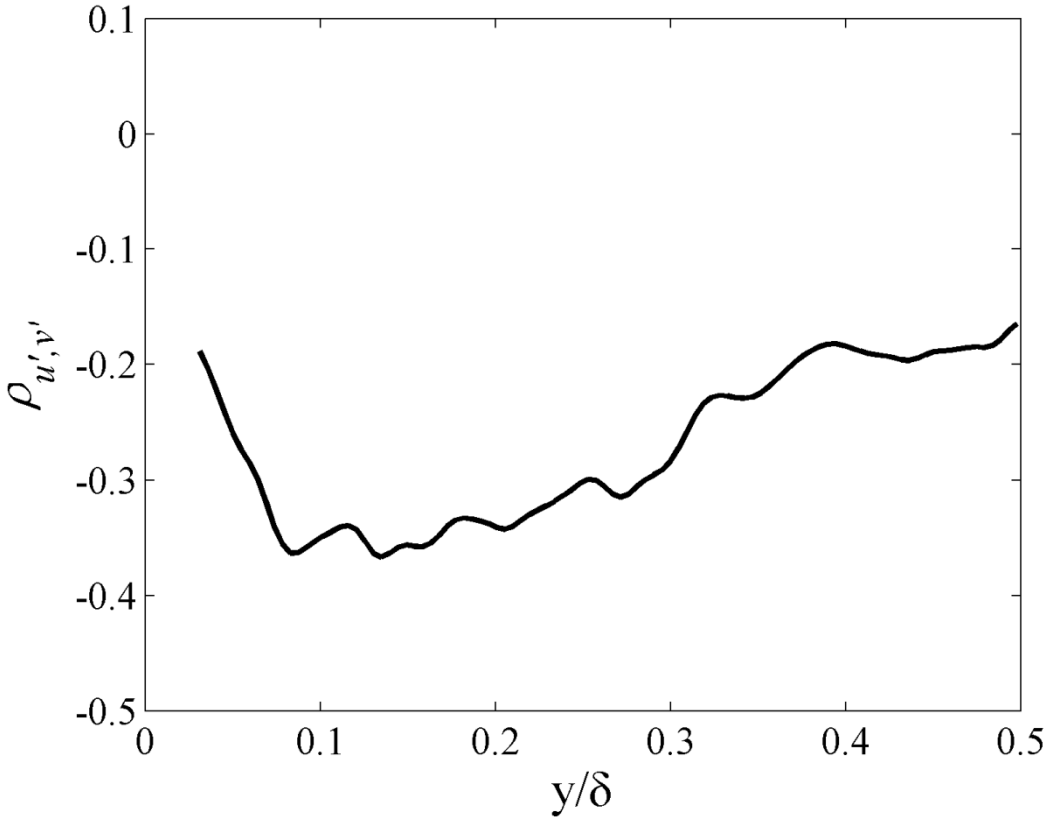

Figure 4.16: Plot of covariance between u' and v' in the wall-normal direction.

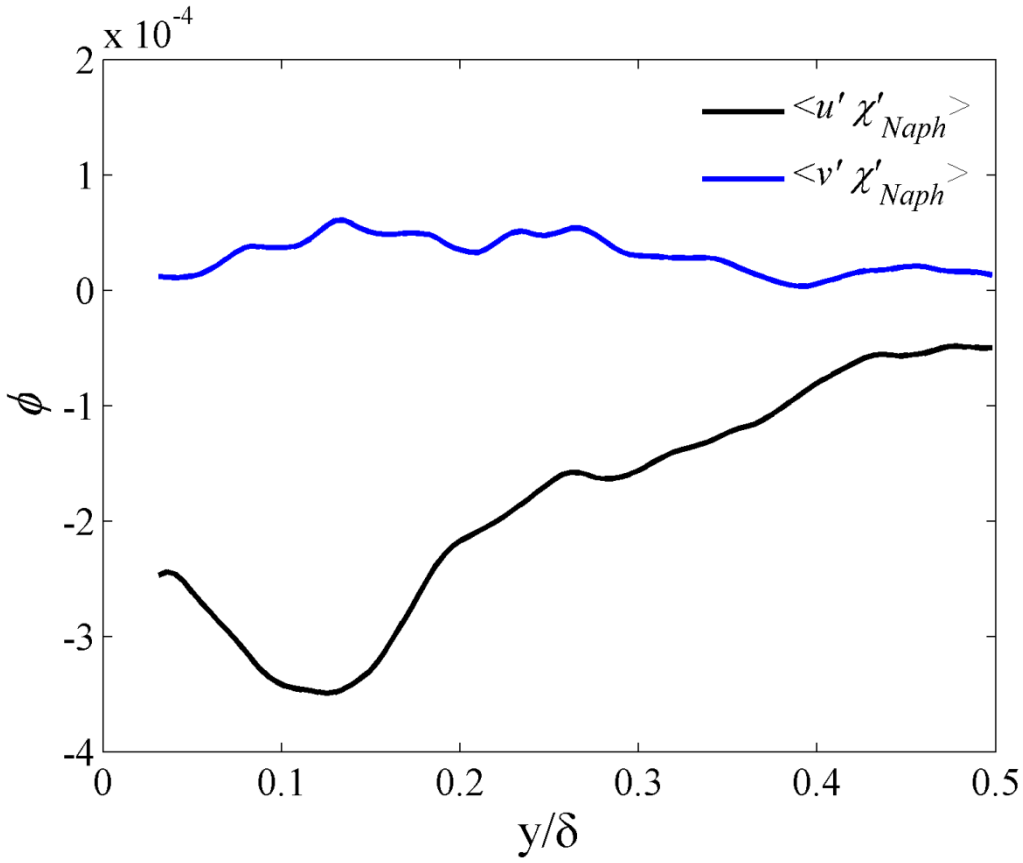

Figure 4.17: Plots of the turbulent fluxes for u' and χ'_{Naph} (black) and v' and χ'_{Naph} (blue) in the wall-normal direction when the temperature field employed for quantifying the PLIF images was obtained using a mean Crocco-Busemann approximation.

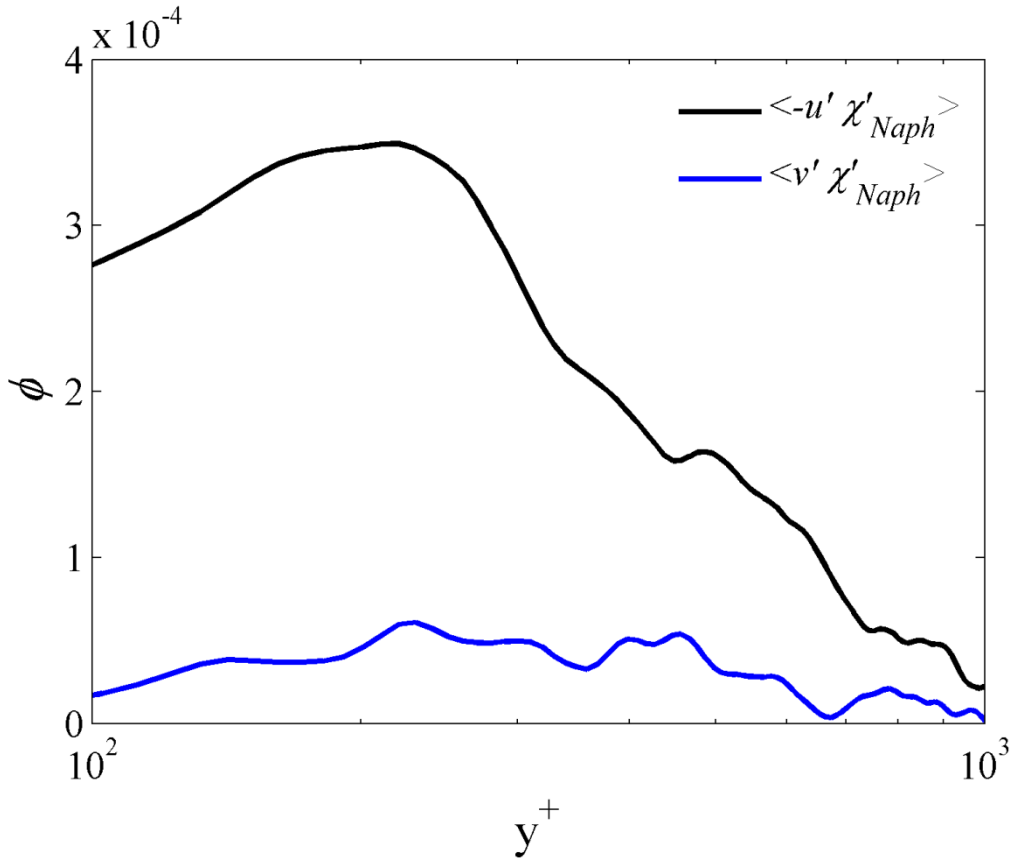

Figure 4.18: Plots of the turbulent fluxes for $-u'$ and χ'_{Naph} (black) and v' and χ'_{Naph} (blue) in the wall-normal direction when the temperature field employed for quantifying the PLIF images was obtained using a mean Crocco-Busemann approximation plotted versus normalized wall units.

4.4 - CONCLUSION

Quantitative naphthalene PLIF was employed simultaneously with PIV to acquire simultaneous two-dimensional fields of naphthalene mole fraction and velocity. Large-scale naphthalene vapor structures out to wall distances of approximately $y/\delta = 0.6$ were revealed that coincide with regions of relatively low streamwise velocity. These turbulent structures between $0 < y/\delta < 0.2$ have a naphthalene mole fraction on the order of 1×10^{-4}, which is approximately 1% of the saturation mole fraction in the boundary layer, with a

measurement uncertainty of ± 20%. The measured fluorescence signal intensity was significantly lower when making simultaneous PIV measurements compared to runs where only PLIF images were collected (as in Chapter 3). A series of improvements were made to the test procedure—including cleaning the test section of TiO_2 particles between runs and successful efforts to increase the flow stagnation temperature—between the first and second PIV/PLIF imaging campaigns, which led to a noticeable increase in the quality of the PLIF images.

It was demonstrated that regions of high scalar coincided with negative fluctuations in streamwise velocity and positive fluctuations in wall-normal velocity away from the wall, similar to observations made by Buxton et al. (2012) and indicating that an ejection mechanism is transporting low-momentum, high-scalar-concentration fluid away from the wall (Spina et al., 1994). The covariance profiles and turbulent fluxes are also qualitatively similar to many others presented in the literature (Kasagi et al, 1992; Li et al., 2004; Li et al., 2009; Braman and Raman, 2011).

4.5 - Suggested Future Work

Images were only collected at one imaging location and with a limited field of view during the second imaging campaign. It would be beneficial to collect images over a similar streamwise domain as the images collected in Chapter 3. Considering the success of the changes to the test procedure implemented between the first and second PIV/PLIF campaigns, the PIV and PLIF fields of view could likely be expanded. If fluorescence signal is not adequate with an expanded laser sheet and a laser source of higher power is not available, it may be possible to reflect the 266 nm laser sheet back through the test section to boost the excitation energy. Moreover, if the second heater stage is repaired for

the Mach 5 wind tunnel facility, a vast improvement in naphthalene PLIF signal should be observed.

Much like the recommendations made in Section 3.5, the collection of simultaneous PIV/PLIF images in various planes at different transverse distances off of the wind tunnel centerline would permit a three-dimensional reconstruction of the scalar transport and velocity fields. In the same vein, images could be collected in different transverse planes (i.e., with the laser sheet passing horizontally through the wind tunnel and the camera imaging either from the top or bottom of the test section).

It would also be interesting to attempt to make velocity measurements using naphthalene PLIF flow tagging velocimetry. This could be performed simultaneously with PIV to compare the two techniques. The main concern is that the lifetime of naphthalene in air may be too short at these conditions (between 10-20 ns) for velocity profiles to evolve. This experiment may be more suited for a facility where N_2 or Argon can be used as a test gas, for which the fluorescence lifetimes are much longer (order 100 ns).

Chapter 5: Naphthalene PLIF imaging applied to an Orion reentry capsule geometry

5.1 - INTRODUCTION

The previous chapters focused on the development of the naphthalene PLIF technique and its application in a Mach 5 turbulent boundary layer. In this section, a demonstration of the naphthalene PLIF technique is presented where both qualitative and quantitative visualizations of the transport of ablation products from the heat shield of a reentry capsule model are collected. This application underscores the potential of naphthalene PLIF for exploring ablation physics in a more applied setting and makes clear the versatility of the technique to be implemented on virtually any geometry. Below, a description of the experimental methods employed in the capsule flow visualization campaign and a discussion of the images obtained are provided.

5.2 - EXPERIMENTAL PROGRAM

5.2.1 - Experimental Facility

The facility used for these experiments was the same low-enthalpy blowdown Mach 5 wind tunnel used in Chapters 3 and 4. The test section of the facility was 152 mm wide by 178 mm tall. Optical access for laser transmission and imaging was provided by fused silica windows on the wind tunnel floor, ceiling, and sidewall. The wind tunnel was supplied by a 4 m^3 storage tank held at approximately 15.5 MPa and the plenum pressure was maintained at approximately 2.48 MPa. The flow was electrically heated to achieve a stagnation temperature of about 360 K in order to increase the sublimation rate of the naphthalene heat shield. These conditions resulted in a Reynolds number based on model diameter (Re_D) of 1×10^6.

5.2.2 - Model Geometry

The model geometry for the current work consisted of a scaled Orion Multi-Purpose Crew Vehicle (MPCV) shaped model with smooth outer mold lines. The model consisted of an aluminum capsule backshell, a separate heat shield piece, and a wire "mesh" to give the solid naphthalene heat shield structural integrity. The aluminum model was scaled to have a 50 mm maximum heat shield diameter and was attached to a 12.7 mm diameter stainless steel sting. The sting was mounted to a strut that was fixed to the wind tunnel floor. Four different strut configurations were used in this experimental campaign, allowing four different angles of attack (0°, 12°, 24°, and 52°) to be tested. A new heat shield was molded before each wind tunnel run and a completed model is shown in Figure 5.1 below. During wind tunnel shutdown, the remaining naphthalene on the model was destroyed, preventing images of the model from being captured post-run. Further details of the capsule geometry and molding procedure are provided in Appendix C.

Schlieren imaging was conducted in a different experimental campaign than the PLIF and used a solid aluminum heat shield rather than a naphthalene one.

Figure 5.1: Orion MPCV model at 52° angle of attack configuration with naphthalene heat shield installed in the Mach 5 wind tunnel facility at The University of Texas at Austin.

5.2.3 - PLIF Experimental Setup

PLIF of naphthalene vapor was used to obtain both a qualitative and quantitative measure of the concentration of ablation products in the flow. The laser system consisted of a frequency-quadrupled Nd:YAG laser with a 266 nm output operating at a rate of 10 Hz. The laser energy was maintained at approximately 30 mJ/pulse, corresponding to an irradiance of 18 kW/mm^2, in order to remain below the saturation threshold of the naphthalene vapor based on previous research (Lochman, 2010). However, it was later found (see Section 2.3.1) that the saturation limit of naphthalene vapor is significantly higher than predicted by Lochman (2010). Regardless, PLIF signal levels were sufficiently high despite the reduced laser energy. It was also confirmed that the ablation process was not significantly altered by the laser impinging on the surface of the model. The UV laser beam was oriented by a series of laser mirrors so that it passed up to the top of the wind tunnel facility where it was formed into a laser sheet using a 250 mm

spherical lens and a 25 mm cylindrical lens and then transmitted through the test section, as seen in Figure 5.2. The resulting laser sheet was about 0.5 mm thick (FWHM) in the measurement region and approximately 75 mm wide. The naphthalene fluorescence was imaged onto a back-illuminated CCD camera (Apogee Alta U47), which had a quantum efficiency of about 57% in the near UV and read noise of 9 e^- RMS. The camera was oriented normal to the laser sheet. The camera was fitted with a 100 mm focal length f/2.8 UV lens (Cerco) operated at full aperture and included a 20 mm extension ring for close focusing. A series of Schott colored glass filters (two WG-295 filters and one UG-11 filter) were placed in front of the lens to block scattered laser light and reduce the amount of solid state naphthalene fluorescence imaged by the CCD. The imaging field of view was about 50 mm × 50 mm. The images were obtained at a rate of approximately 1/3 Hz with a 30 ms exposure time and about 20 images were acquired per wind tunnel run. The fluorescence lifetime of the naphthalene vapor was on the order of 10 ns meaning the imaged flow was effectively frozen. The experiment was synchronized using several Stanford Research Systems digital delay generators to ensure that images were acquired while the laser was firing.

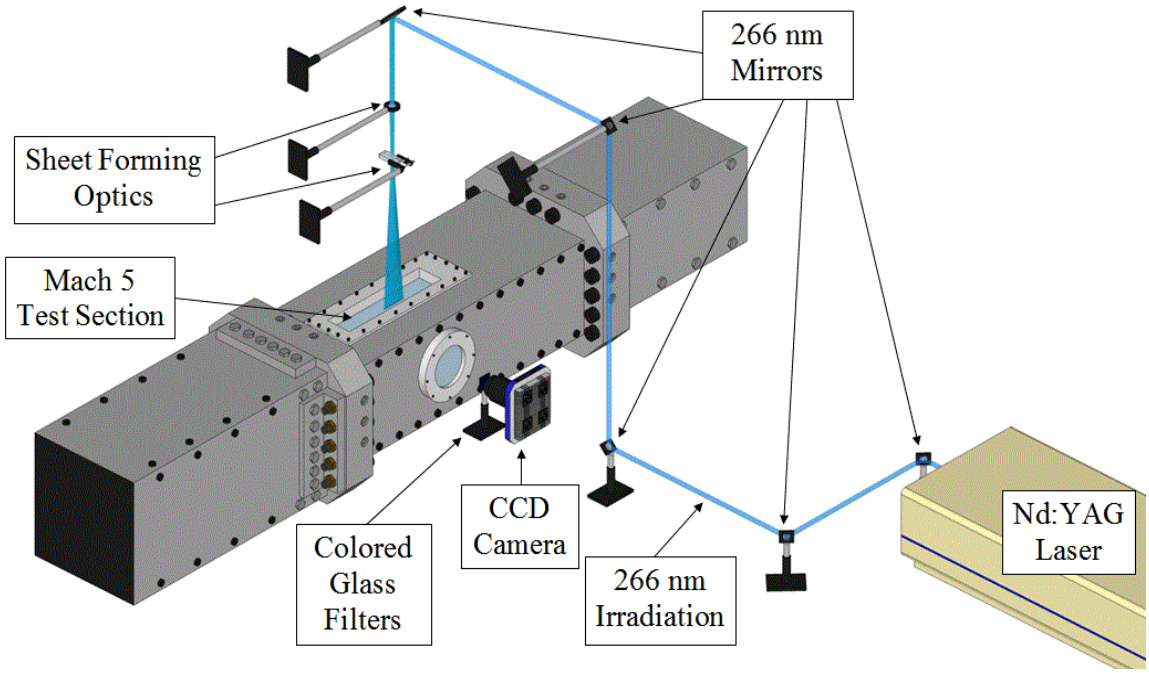

Figure 5.2: Schematic of the setup used for naphthalene PLIF experiments in the Mach 5 wind tunnel facility.

5.2.4 - PLIF Image Processing

Single-shot PLIF images were processed by first removing the background and were then corrected for variations in the mean intensity profile of the laser sheet. Single-shot sheet corrections were not made. The mean laser sheet spatial intensity variation was measured by imaging the fluorescence from a cell filled with acetone vapor, as discussed in Section 3.2.3. In order to determine a mean laser-sheet intensity profile, 50 acetone fluorescence cell images were averaged. The single-shot images obtained during the runs were then divided by this laser-sheet intensity profile to correct for spatial variations in laser energy. No correction was made for potential laser absorption by naphthalene vapor as previously discussed. Additionally, in many of the subsequent figures, the PLIF

intensity is presented in a logarithmic scale to improve the visibility of the entire flowfield without saturating other parts of the image.

For the quantitative images presented in Section 5.3.2, the mean temperature and pressure fields were taken from unpublished simulations of the capsule flowfield by Dr. Scott Murman at NASA Ames Research Center. Computations were completed using the OVERFLOW solver developed by NASA (Murman et al., 2015). The simulations used the Reynolds-averaged Navier-Stokes method and were three-dimensional and steady. The pressure and temperature fields extracted from the simulation were time-averaged two-dimensional slices of the flow solution along the model centerline. The Mach number and Reynolds number of the capsule flow in the current experiment were matched in the simulations and the non-dimensional nature of the OVERFLOW solver permits scaling of the thermodynamic outputs to match the freestream conditions of the flow. Furthermore, the outer mold lines of the Orion capsule geometry employed in the simulations matched the capsule geometry in the current work with the exception of the sting and the cutout on the windward side of the model used for filling the heat shield mold.

To solve for naphthalene mole fraction, the measured fluorescence signal and test cell reference images were input into Eq. 1.10 along with curve fits for absorption cross section and fluorescence yield evaluated at the temperatures and pressures from the simulated flowfields. Reference images from the second imaging campaign in Chapter 3 were employed given that the camera, camera lens, laser, and transmission optics were all identical between these two experimental campaigns. Using this procedure, the PLIF images were converted into two-dimensional plots of naphthalene mole fraction.

One caveat of this procedure is that the range of pressures in the capsule flow environment—based on the OVERFLOW simulations—is much larger than the range investigated with the test cell measurements in Chapter 2. With that said, the temperatures are essentially within the valid range of the developed fits for absorption cross section and fluorescence yield. Given that absorption cross section is not pressure-dependent, this fit should be valid. Furthermore, the fluorescence yield fits are based on the Stern-Volmer behavior of the quenching of naphthalene fluorescence by oxygen. While fits for fluorescence yield were not verified experimentally for pressures above 10 kPa due to limitations in available equipment, other works (Kaiser and Long, 2005; Faust et al., 2013) have demonstrated Stern-Volmer behavior at pressures above 1 atm. It is also worth noting that, given the nature of the dependence of the fluorescence yield on pressure, the potential for error in the relative fluorescence yield measurement decreases with increasing pressure until there is effectively no dependence at higher pressures. Considering these factors, it was determined that the application of the empirical fits developed in Chapter 2 to the capsule flowfield would be sufficiently accurate.

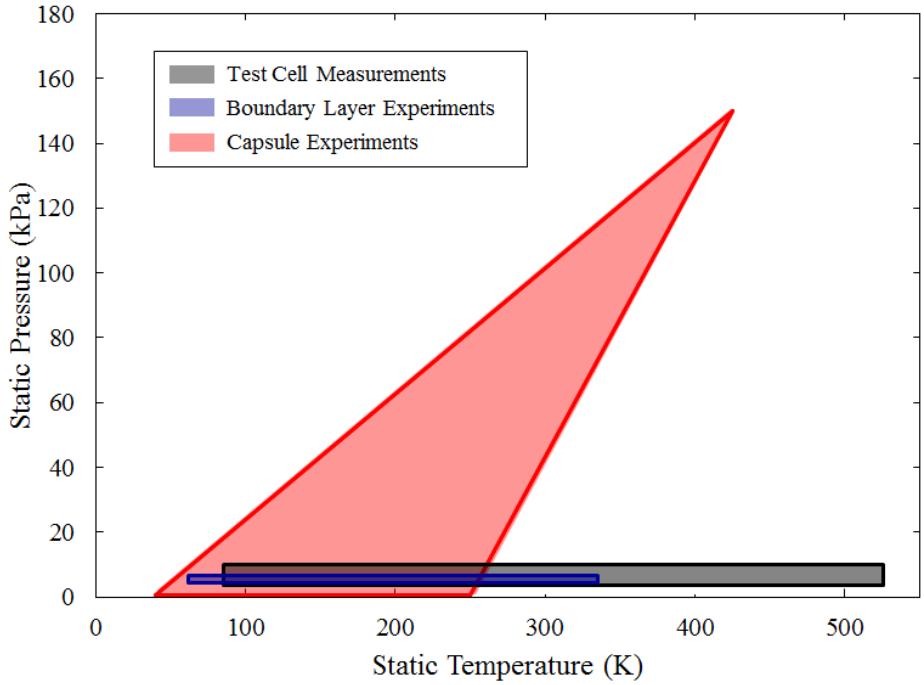

Figure 5.3: Comparison of the range of temperatures and pressures experienced in the Mach 5 boundary layer experiments and the capsule flow experiments, relative to the range of conditions studied in the test cell measurements discussed in Chapter 2.

5.2.5 - Virtual Diagnostics Interface (ViDI)

The Virtual Diagnostics Interface (ViDI; Schwartz, 2003) is a software tool developed at NASA Langley Research Center that provides unified data handling and interactive three-dimensional display of experimental data and computational predictions. It is a combination of custom-developed software applications and Autodesk® 3ds Max®, a commercially available, CAD-like software package for three-dimensional rendering and animation (Autodesk, Inc., 2006). ViDI technology can be applied to three main areas: 1) pre-test planning and optimization; 2) visualization and analysis of experimental data and/or computational predictions; and 3) establishment of a central hub

to visualize, store, and retrieve experimental results. For this experiment, ViDI was used primarily for post-test visualization of the PLIF data as in Alderfer et al. (2007).

5.3 - Results and Discussion

5.3.1 - Qualitative Images

Naphthalene PLIF images were collected in the Mach 5 wind tunnel facility at The University of Texas at Austin's Pickle Research Campus. The first image set is shown in Figure 5.4, a time-sequence of PLIF images at 0° angle of attack. The elapsed time between Figure 5.4(a) and Figure 5.4(f) is approximately one minute. The shear layer is clearly marked in Figure 5.4 by the naphthalene PLIF technique since naphthalene vapor accumulates in the afterbody recirculation region. In Figure 5.4 the shear layer appears to be laminar near the leeward shoulder of the capsule with potentially turbulent structures further downstream. In general, the shear layer appears to be most laminar near the leeward shoulder of the capsule for all images and shows signs of transition to turbulence further downstream, which is consistent with previous investigations of capsule shear layers (Danehy et al., 2009; Combs et al., 2015). These potentially turbulent structures occur further upstream with each successive image, causing the shear layer to appear more turbulent over the course of the run. In Figure 5.4(f) the shear layer looks to have undergone a complete transition to turbulence as laminar structures are not evident even at the leeward shoulder of the capsule. Another change that can be seen in the images with respect to elapsed time is that the naphthalene PLIF signal increases significantly over the course of a wind tunnel run. This increase in signal is a result of the naphthalene heat shield heating up during the run. Since the vapor pressure of naphthalene is a strong function of temperature, the sublimation rate of

naphthalene increases substantially as the model heats up, leading to elevated concentrations of naphthalene vapor introduced into the flow and thus a rise in PLIF signal. Lastly, there appears to be a region of relatively low naphthalene signal located near the sting on the capsule afterbody in the separated flow region in Figure 5.4. This low-signal region appears to stay in approximately the same location for all the images in the figure. Less noticeable, there is another low-signal region located farther upstream near the leeward shoulder of the capsule whose position also remains relatively fixed during the run. These structures—most likely the result of cross-flow-induced vortices—are indicated by arrows in Figure 5.4(e) but can be seen in the other images as well.

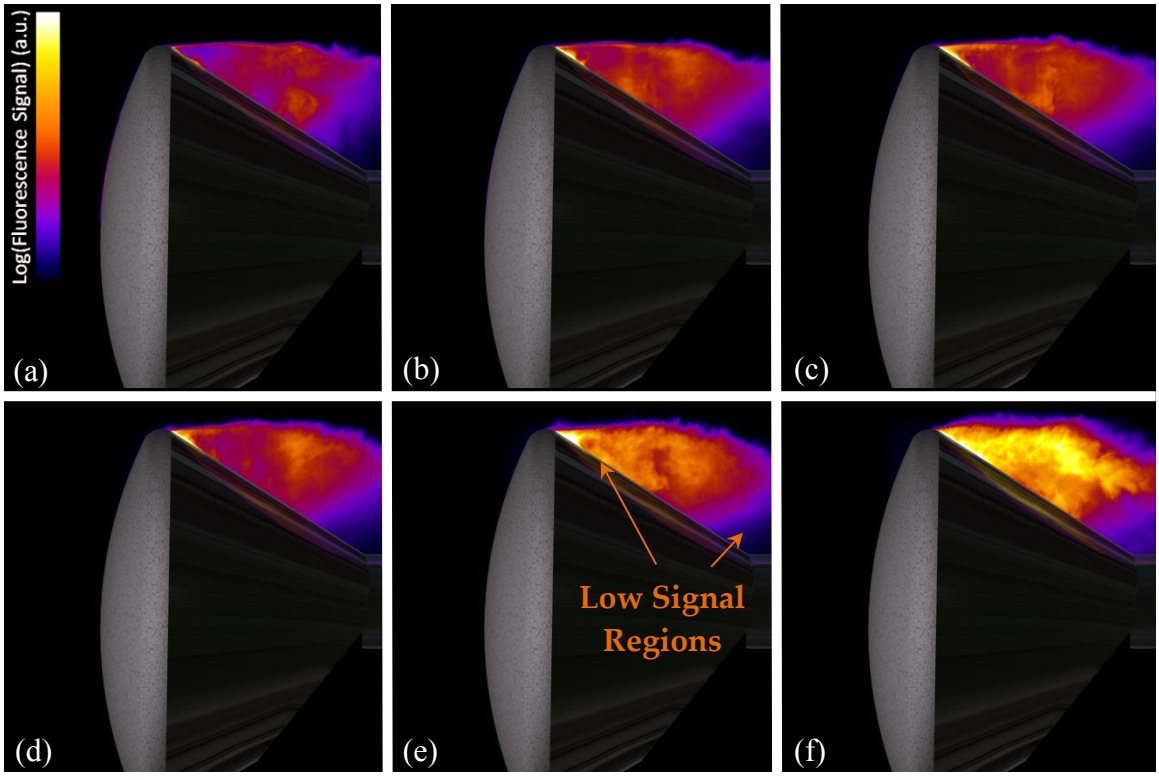

Figure 5.4: Naphthalene PLIF images of a capsule model at 0° angle of attack. Images were collected during one run and images a-f are sequential in time, separated by approximately ten seconds each.

Figure 5.5 is also a time-sequence of PLIF images recorded during a single run but for the case of a 12° angle of attack. Once again, the elapsed time between Figure 5.5(a) and Figure 5.5(f) is approximately one minute. Similar to what is seen in Figure 5.4, the shear layer is visualized in the images by the naphthalene vapor accumulated in the capsule afterbody recirculation region. Another similarity to Figure 5.4 is the development of the shear layer during the wind tunnel run. While the shear layer appears to be laminar near the leeward shoulder of the capsule in Figure 5.5(a), transition to turbulence appears to have occurred by the end of the run, depicted in Figure 5.5(f). The PLIF signal can also be seen to increase with time, reemphasizing that the model is heating up over the course of the run, leading to increased naphthalene sublimation and a subsequently elevated PLIF signal. Regions of relatively low PLIF signal are also shown in the images in Figure 5.5. The relatively laminar region near the sting appears to be smaller than the one seen in Figure 5.4, however, in Figure 5.5(f) a well-defined elliptical boundary between high and low signal can be seen, further suggesting the presence of a spanwise vortical structure on the capsule afterbody preventing naphthalene vapor from entering its core. The upstream low-signal region near the leeward shoulder of the capsule is present in Figure 5.5 as well. As in Figure 5.4, this feature is more subtle and has a poorly defined boundary compared to the low-signal region near the sting. There are, however, some flow structures that can be identified in the 12° case in Figure 5.5 that were not visualized for the 0° case in Figure 5.4. First, intermittent turbulent structures on the heat shield surface can be seen in all six images of Figure 5.5 but not Figure 5.4. These structures were most likely not visualized in the 0° angle of attack case due to the relatively short development length for the boundary layer on the heat shield surface,

leading to a physically thinner boundary layer (perhaps still laminar) that is difficult to visualize.

Another flow feature visualized exclusively for the 12° angle of attack case is a series of elongated naphthalene vapor structures that emanate from the upper edge of the shear layer, seen most clearly in Figure 5.5(d)-(f). Four zoomed-in images focusing on this feature can also be found in Figure 5.6. These wispy streaks are nearly vertical in the images but are at an angle of about 45° with respect to the flow direction, with the features propagating in the opposite direction of a Mach wave or shock in a left-to-right supersonic flow. The source of these structures is not known at this time, but it is possible they are turbulent structures that originate in the upstream boundary layer and then are strained and stretched by the rapid expansion around the leeward shoulder.

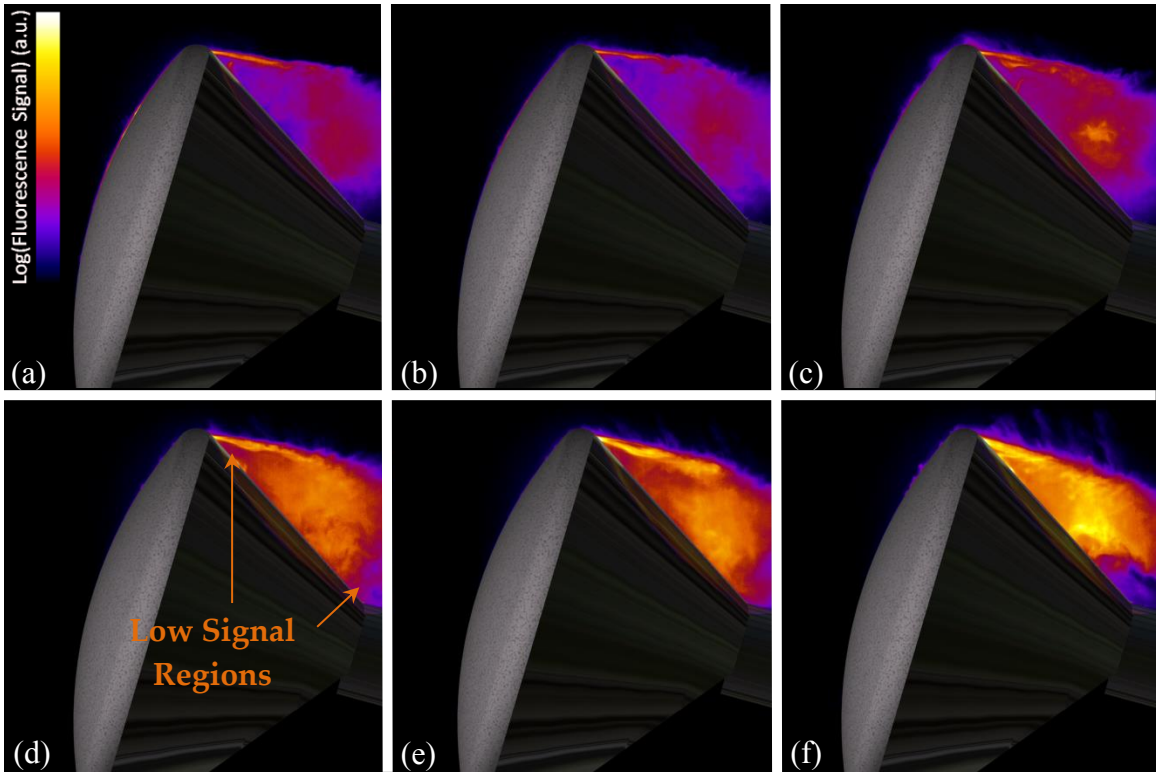

Figure 5.5: Naphthalene PLIF images of a capsule model at 12° angle of attack. Images were collected during one run and images a-f are sequential in time, separated by approximately ten seconds each.

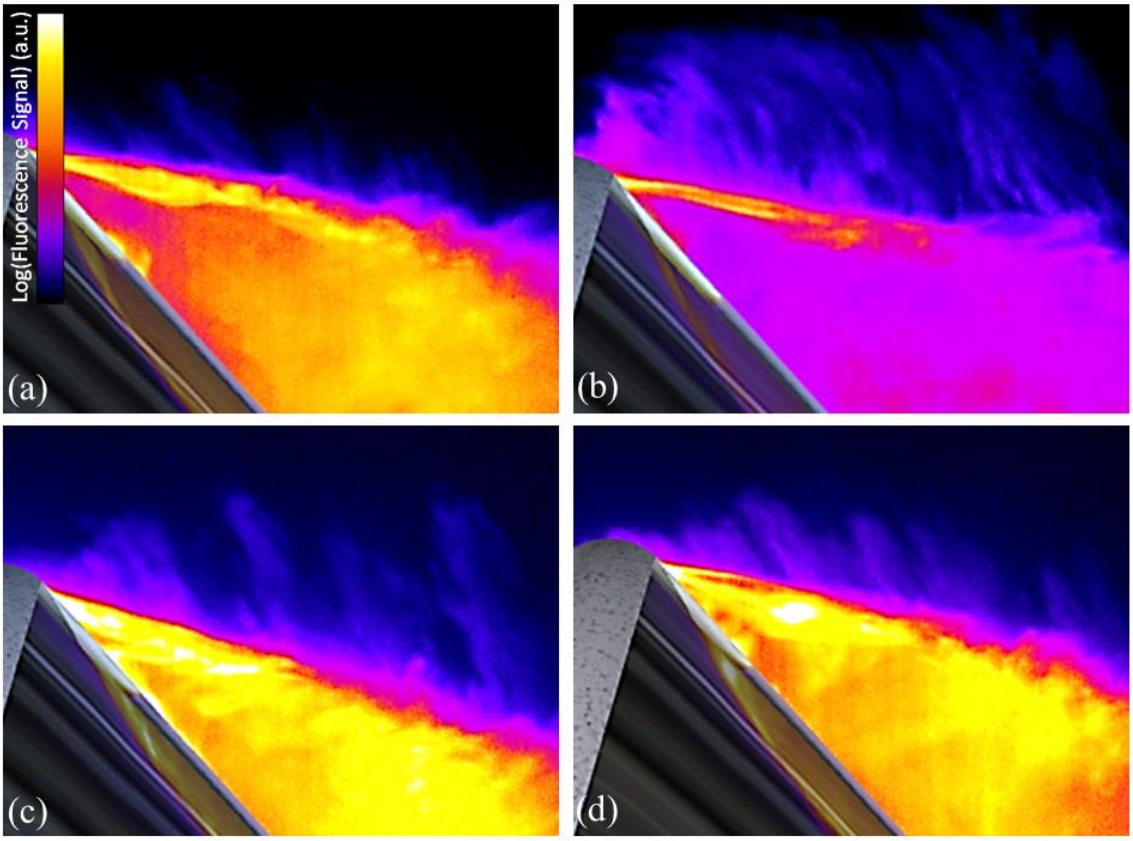

Figure 5.6: Naphthalene PLIF images highlighting elongated blue-colored (low signal intensity) naphthalene structures emanating from the upper edge of the shear layer at 12° angle of attack.

A time-sequence of PLIF images for the 24° angle of attack case is presented in Figure 5.7 where the elapsed time between Figure 5.7(a) and Figure 5.7(f) is approximately one minute. As expected based on the previous figures, the PLIF signal can be seen to increase with time due to the heating of the model. Also, as in the previous figures, the shear layer is the most clearly visualized flow structure in the image set due to the high concentration of naphthalene in the afterbody recirculation region. However, while the shear layer appeared to transition from a laminar to a turbulent condition over the course of the 0° and 12° runs, the shear layer appears to stay effectively laminar for

the majority of the images shown in Figure 5.7. While a small disturbance far downstream of the leeward shoulder can begin to be seen in Figure 5.7(c), this disturbance does not become amplified and propagate upstream in later images. The exact nature of the shear layer is difficult to determine in each image—particularly in Figure 5.7(f)—but there are fewer instabilities visualized than in Figure 5.4 or Figure 5.5. Considering that the freestream Reynolds number is effectively constant over the course of the run, the onset of transition is most likely due to the change in the nature of the heat shield surface as a result of the ablation process. As the heat shield ablates, its surface becomes rough, which could lead to transition to turbulence. Additionally, the mass transfer rate or blowing rate of naphthalene vapor on the heat shield surface increases over the course of the run, which could affect turbulent transition. Given that at lower angles of attack the model appears as a larger obstruction to the flow, one would imagine that, for example, the 0° angle of attack case would undergo a more rapid change in heat shield surface than the 24° angle of attack case. This would mean that the heat shield is altered more rapidly at lower angles of attack, leading to turbulent transition in the shear layer earlier in the run. Indeed, the shear layer transitions earliest for the 0° angle of attack case and might not transition at all in the 24° angle of attack case.

Not visualized in Figure 5.7 are intermittent turbulent structures on the heat shield surface. This feature was expected to be seen in this image set since turbulent structures existed on the heat shield surface for the 12° case and the 24° case has a longer development length for the heat shield boundary layer from the stagnation point. However, the image set in Figure 5.7 has a lower signal-to-noise ratio than the set in Figure 5.5, which could be the reason these structures are not observed. It can be seen in Figure 5.7 that there is a certain amount of naphthalene vapor visualized on the heat

shield surface but the signal-to-noise ratio is not high enough for individual flow structures to be resolved. Similarly, it is possible that the elongated streaks seen in Figure 5.5 and Figure 5.6 exist for the 24° case as well but were not visualized in the image set presented in Figure 5.7 due to low signal levels. Looking closely at the images in Figure 5.7, a noticeable amount of PLIF signal can be seen above the shear layer but the signal level is again not high enough for detailed structures like those seen in Figure 5.6 to be identified.

In addition to the flow structures already discussed, the regions of relatively low PLIF signal are again visualized in Figure 5.7. The region near the leeward shoulder is difficult to detect due to the low overall signal levels in the images but the boundary between low and high signal in the region near the sting is perhaps more crisp than in any other image set. Similar to what was seen in Figure 5.5 this boundary could be broadly termed as elliptical and is reminiscent of a vortex core. Examples of these low signal regions are presented in Figure 5.8 and Figure 5.9, where Figure 5.8 provides examples of the low-signal region near the capsule sting and select examples of low-signal regions near the leeward shoulder of the capsule can be found in Figure 5.9. Again, notice how sharp the separation between high and low signal can be near the capsule sting, as seen in Figure 5.8. As mentioned before, this evidence coupled with the often rounded shape of these regions indicates the structures are the result of relatively steady spanwise vortices forming in the recirculation region on the capsule backshell surface. The images in Figure 5.9 corroborate this claim as the low-signal region near the leeward shoulder of the capsule is highlighted in four different examples. Most interestingly, Figure 5.9(a) contains an almost perfectly circular low-signal region near the leeward shoulder of the

capsule, suggesting a spanwise vortex. A highly similar structure is visualized in Figure 5.9(d).

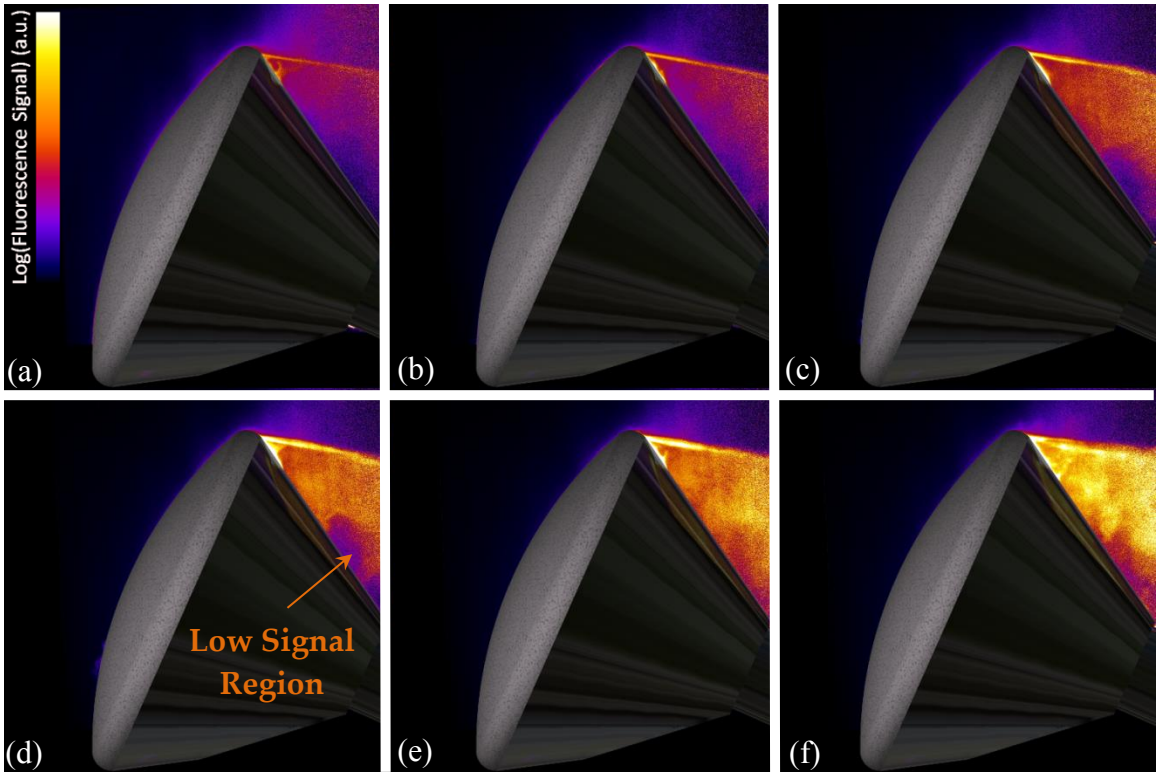

Figure 5.7: Naphthalene PLIF images of a capsule model at 24° angle of attack. Images were collected during one run and images a-f are sequential in time, separated by approximately ten seconds each.

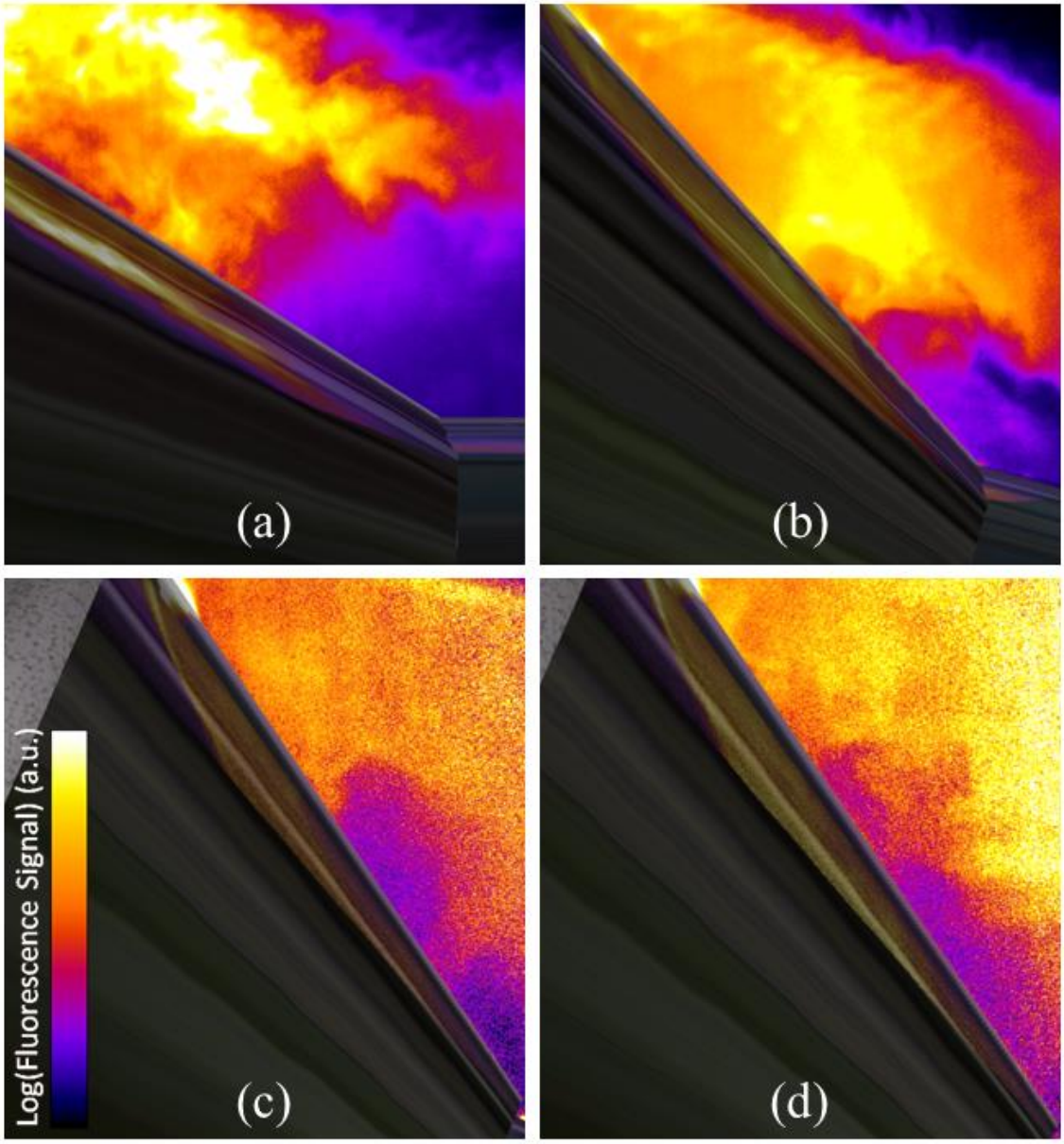

Figure 5.8: Higher magnification naphthalene PLIF images highlighting low signal regions observed in the capsule recirculation zone near the model sting at (a) 0°, (b) 12°, and (c and d) 24° angle of attack.

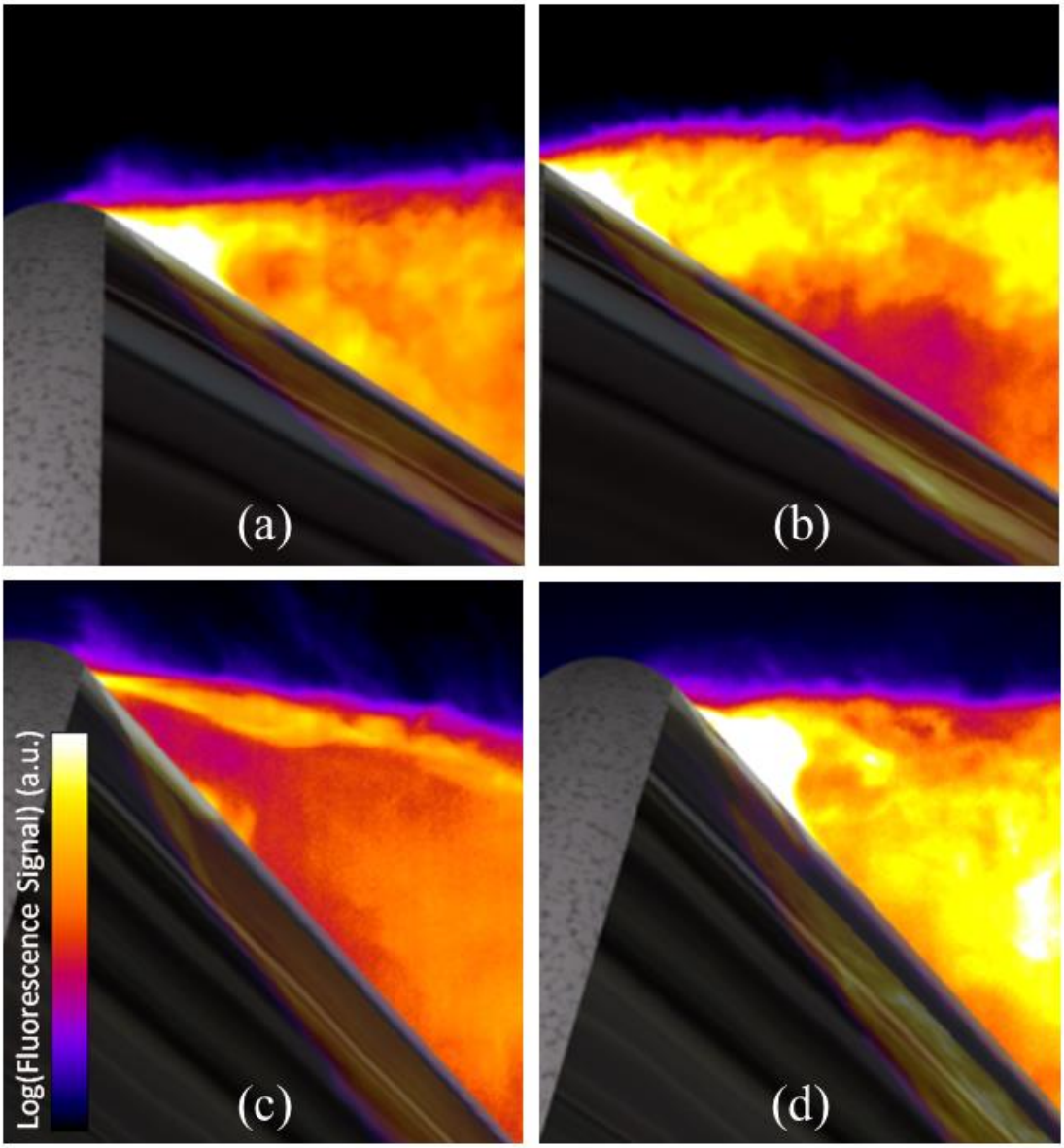

Figure 5.9: Higher Magnification naphthalene PLIF images highlighting low signal regions observed in the capsule recirculation zone near the leeward shoulder at 0° angle of attack (a and b) and 12° angle of attack (c and d).

A time-sequence of PLIF images at 52° angle of attack is shown in Figure 5.10. As in the previous image sequences, the elapsed time between Figure 5.10(a) and Figure

5.10(f) is approximately one minute. Owing to the large change in angle of attack, this image set is quite different than the ones shown for the 0° (Figure 5.4), 12° (Figure 5.5), and 24° (Figure 5.7) angle of attack cases. Although the PLIF signal is still relatively high in the shear layer, the field of view for this image set was focused on the heat shield surface. At such a high angle of attack the surface of the heat shield occupied almost the entire field of view, preventing any determinations as to the nature of the shear layer from being made. Turbulent structures on the heat-shield surface were consistently visualized for the 52° angle of attack case and can be seen most clearly in Figure 5.10(e) and Figure 5.10(f). These structures appeared more frequently for the 52° angle of attack case than any other case tested because this angle of attack has the longest development length for the boundary layer (from the stagnation point which moved further upstream as the angle of attack increased) and the boundary layer seems to be the most turbulent and the thickest at the leeward shoulder (and hence the easiest to visualize). Interestingly, the presence of turbulent structures on the heat shield surface does not seem to correlate with transition of the shear layer since the shear layer was more likely to be laminar at higher angles of attack but the presence of intermittent structures on the heat shield surface is also most likely at higher angles of attack.

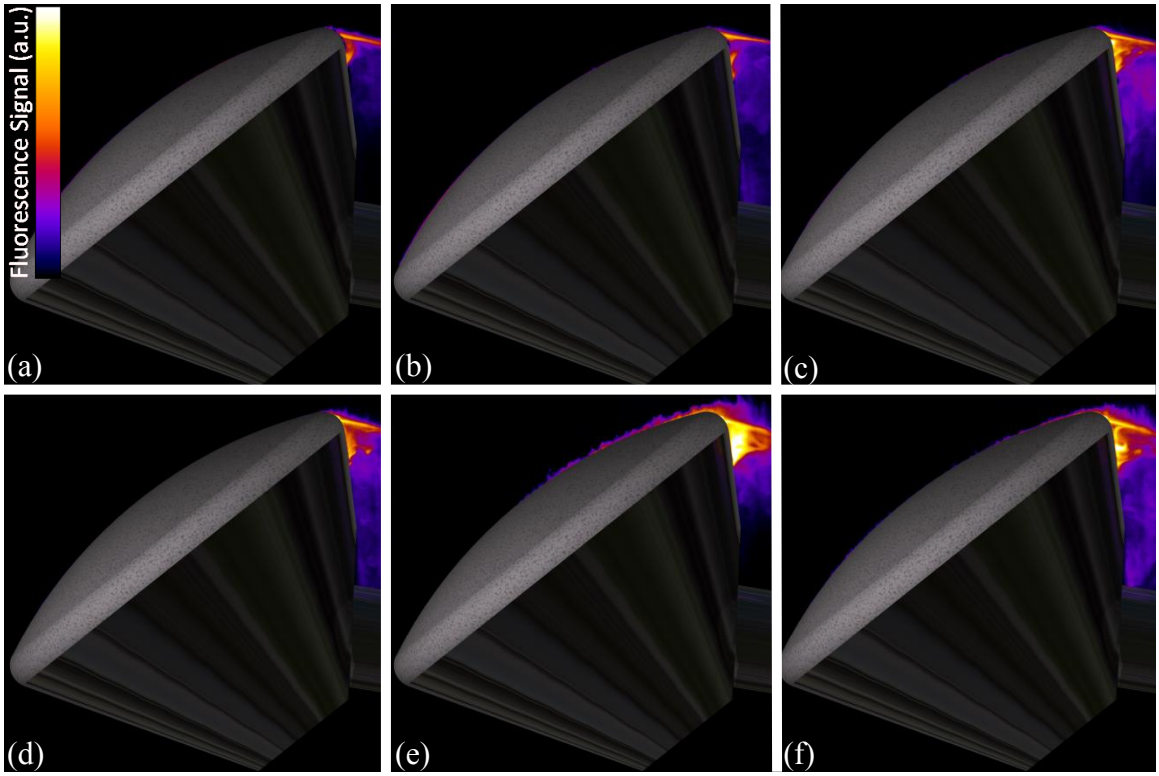

Figure 5.10: Naphthalene PLIF images of a capsule model at 52° angle of attack. Images were collected during one run and images a-f are sequential in time, separated by approximately ten seconds each.

To further investigate the nature of the structures observed on the surface of the heat shield at a 52° angle of attack, additional runs were conducted with the camera field of view focused on the approximate center of the heat shield surface (Figure 5.11) and on the leeward shoulder of the capsule (Figure 5.12). The images in Figure 5.11 were recorded sequentially in time and approximately six seconds elapsed between the acquisition of each image while approximately three seconds elapsed between the acquisition of each image in Figure 5.12. Some of the same trends observed in the capsule recirculation region for the lower angle of attack cases can be found in the image sets presented in Figure 5.11 and Figure 5.12 when looking at the turbulent structures on

the heat shield surface. First, it can be seen in both figures that the size of the structures increases with run time, with the largest structures observed in the later images. This suggests that the boundary layer on the heat shield surface is becoming more turbulent as run time increases. Again, this is most likely the result of roughening of the heat shield surface and an increased naphthalene blowing rate. The increased naphthalene sublimation rate with run time also results in an overall increase in PLIF signal intensity, as the later images (Figure 5.11(e) and , Figure 5.11(f), Figure 5.12(e) and , and Figure 5.12(f)) have higher signal levels than at the earlier times (Figure 5.11(a) and , Figure 5.11(b), Figure 5.12(a) and , and Figure 5.12(b)). Lastly, comparing Figure 5.11 and Figure 5.12 illustrates the growth of the turbulent boundary layer on the surface of the heat shield. As one would expect, for a similar amount of elapsed time, the structures in Figure 5.12 are always larger than the ones seen in Figure 5.11. For example, examining Figure 5.11(a), the turbulent structures are few and exist on a relatively small scale near the center of the heat shield surface. However, further downstream in Figure 5.12(a) (at approximately the same time after the beginning of the run), significantly larger structures can be seen passing over the leeward shoulder of the capsule as the turbulent boundary layer has developed along the heat shield surface.

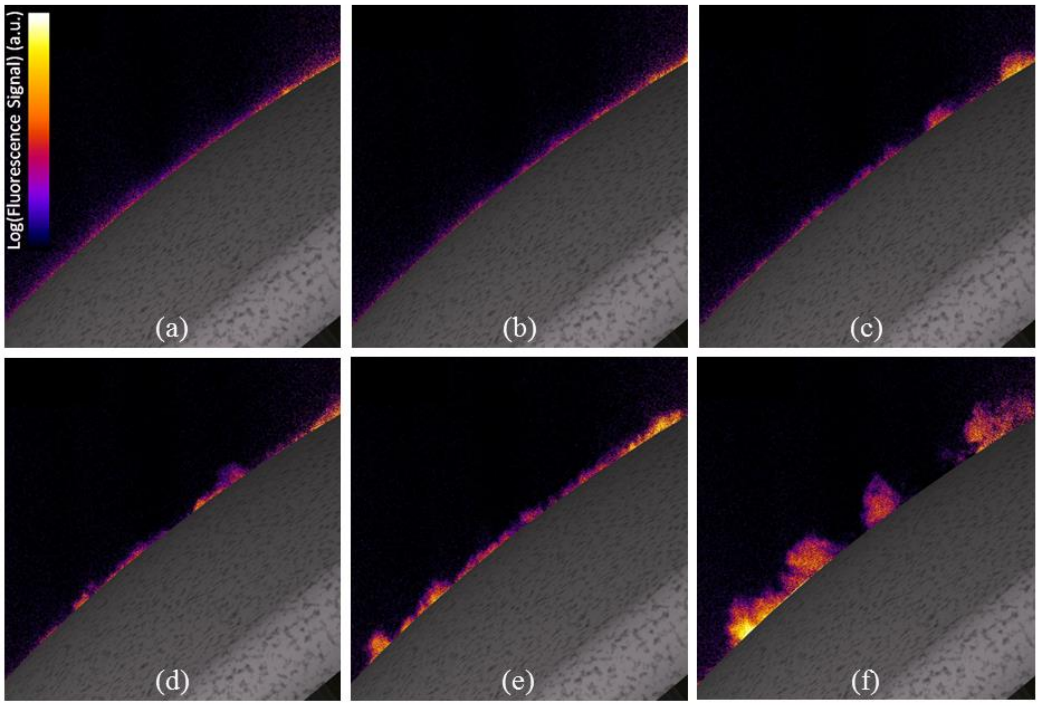

Figure 5.11: Naphthalene PLIF images of a capsule model at 52° angle of attack focused on the surface of the heat shield. Images were collected during one run and images a-f are sequential in time, separated by approximately six seconds each.

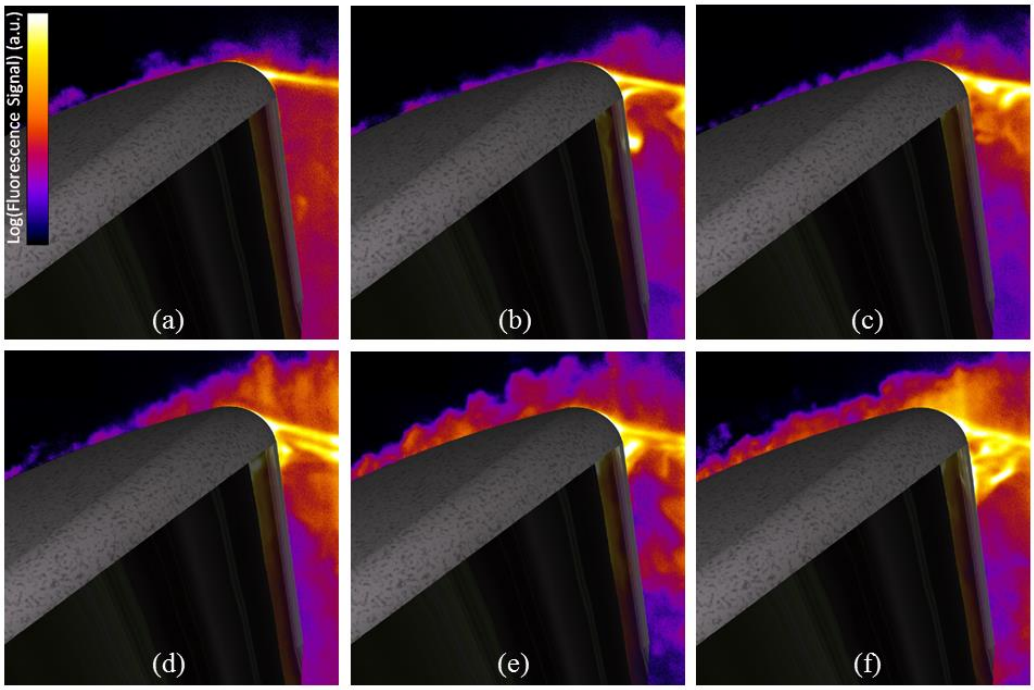

Figure 5.12: Naphthalene PLIF images of a capsule model at 52° angle of attack focused on the capsule leeward shoulder. Images were collected during one run and images a-f are sequential in time, separated by approximately three seconds each.

Figures 5.13 through 5.16 depict the capsule model at various angles of attack with instantaneous naphthalene PLIF images superimposed on instantaneous Schlieren images. The naphthalene PLIF and Schlieren images were not collected simultaneously. For the Schlieren imaging campaign, an aluminum heat shield was used. Therefore, the Schlieren images show no effects of ablation. In each figure a bow shock can be seen in front of the model and the standoff distance of the bow shock appears to decrease with increasing angle of attack. Expansion fans are also visible off both shoulders. Less obvious—and seen most clearly in Figure 5.13(a) — are the shear layer and lip shock just downstream of the capsule shoulders. Shocks occurring as a result of the presence of the sting are seen in Figures Figure 5.14 through Figure 5.16. Also, a third expansion fan is

visualized in Figure 5.16 emanating from the aft edge of the windward capsule afterbody. These visualizations provide a way to view the naphthalene PLIF images in the context of the main features of the flowfield. One comparison that can be made between the Schlieren images and the naphthalene PLIF images is the location of the shear layer, which compares favorably in the figures below. The PLIF images show detailed information about the state of the boundary layer and shear layer that is not seen clearly in the Schlieren images. Furthermore, since the PLIF technique makes measurements on a planar slice whereas Schlieren images are path averaged, local flow information can be identified. For example, the Schlieren images (particularly Figure 5.13(a) and Figure 5.14(a)) appear to show a structure emanating from the middle of the capsule backshell. Combining the Schlieren and PLIF images, it can be determined that this is almost certainly a three-dimensional effect due to the path-integrated nature of the Schlieren technique. The structure is most likely the reflection of the bow shock off of the windows of the wind tunnel because if this flow feature was on the center plane of the capsule model there would be evidence of its existence in the naphthalene PLIF images shown in Figure 5.13(b) and Figure 5.14(b). Also, the flow in the capsule recirculation region is most likely not supersonic, so it is unlikely that a shock structure could be supported there. It would be difficult to draw such a definitive conclusion with the Schlieren imaging alone. However, the PLIF images do not visualize the flow features away from the model (i.e. shocks and expansion fans), hence the complementary nature of the two techniques.

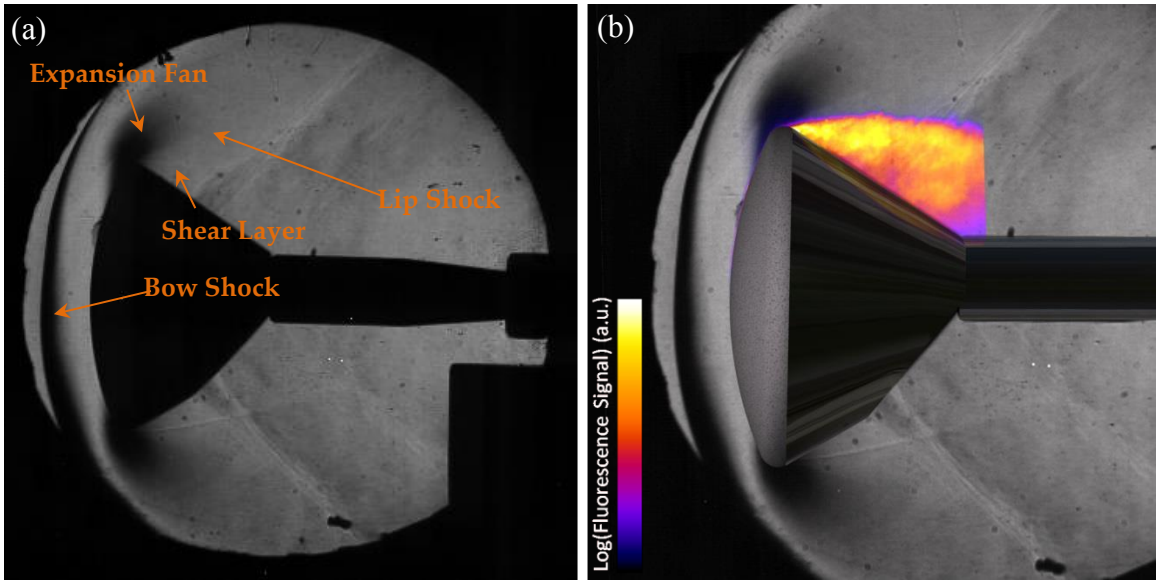

Figure 5.13: Orion capsule model in a Mach 5 flow at 0° angle of attack with (a) Schlieren visualization and (b) naphthalene PLIF image superimposed on a Schlieren visualization of the flowfield.

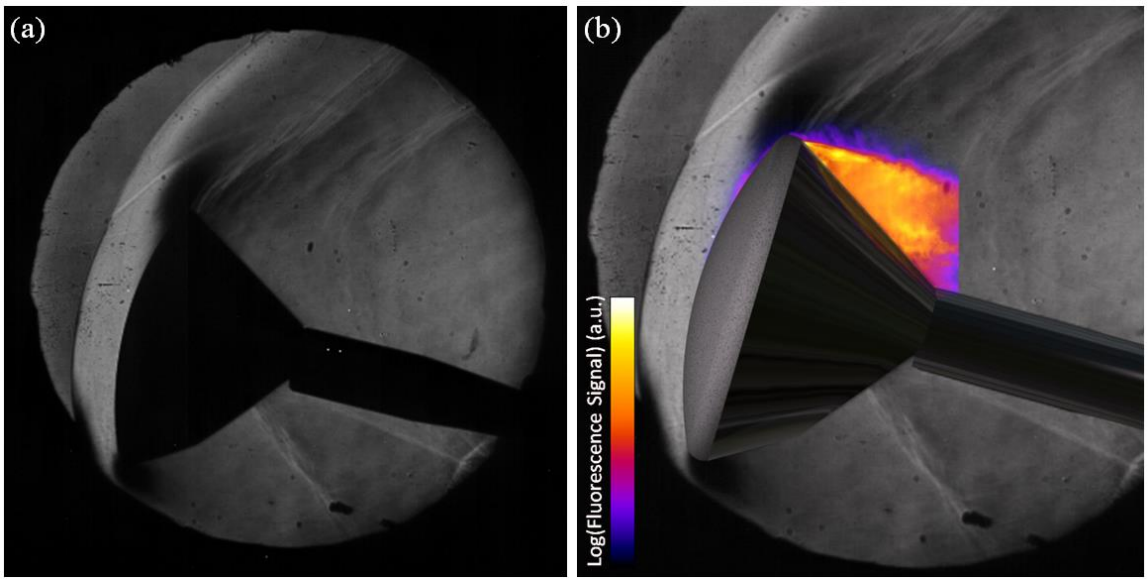

Figure 5.14: Orion capsule model in a Mach 5 flow at 12° angle of attack with (a) Schlieren visualization and (b) naphthalene PLIF image superimposed on a Schlieren visualization of the flowfield.

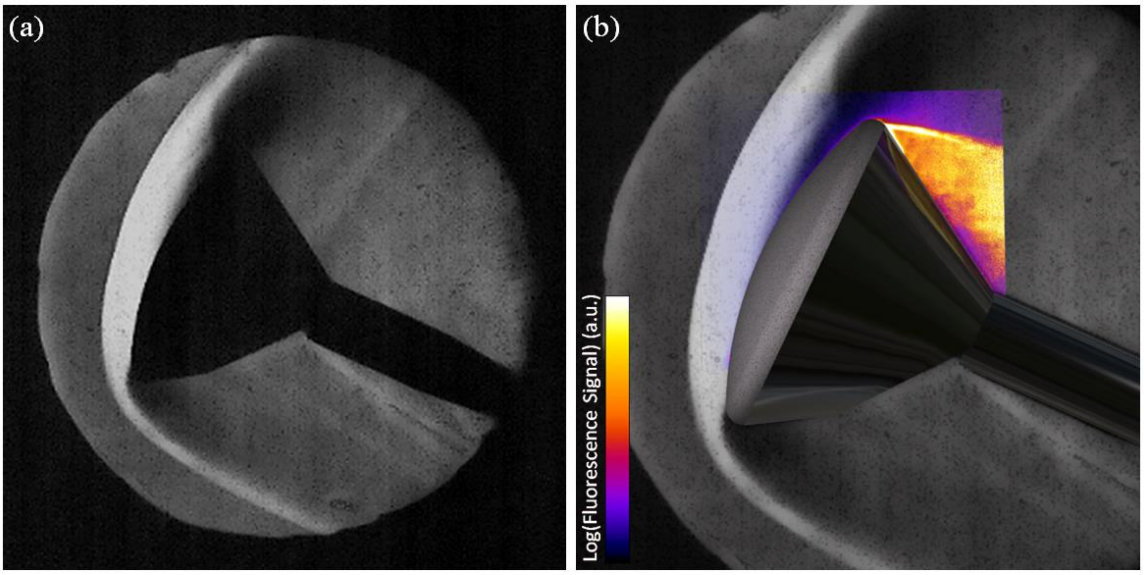

Figure 5.15: Orion capsule model in a Mach 5 flow at 24° angle of attack with (a) Schlieren visualization and (b) naphthalene PLIF image superimposed on a Schlieren visualization of the flowfield.

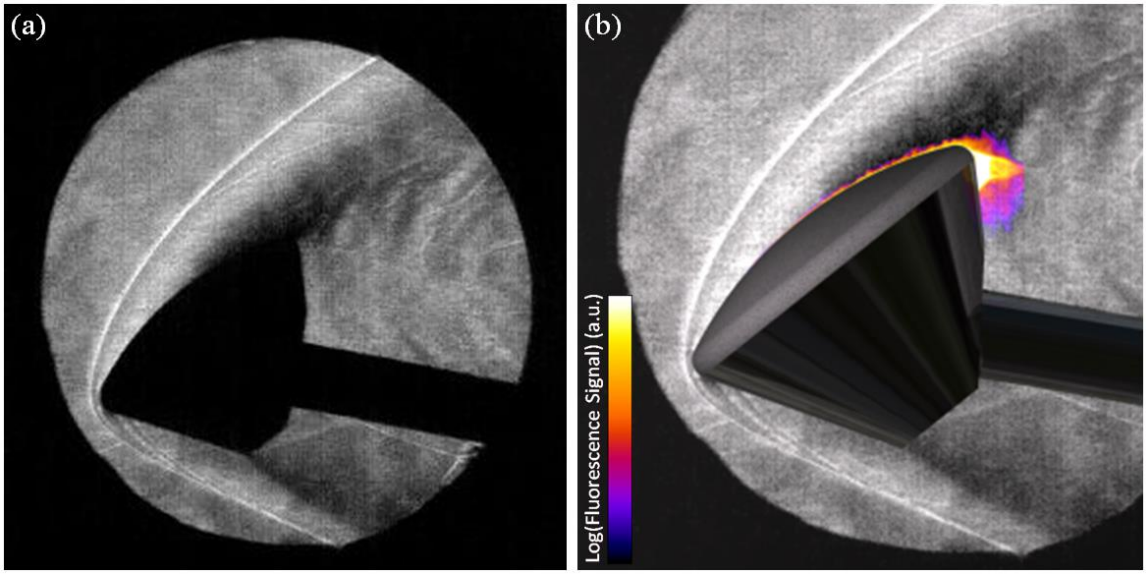

Figure 5.16: Orion capsule model in a Mach 5 flow at 52° angle of attack with (a) Schlieren visualization and (b) naphthalene PLIF image superimposed on a Schlieren visualization of the flowfield.

5.3.2 - Quantitative Images

The primary hindrance to converting the capsule PLIF images into quantitative fields of naphthalene mole fraction—as was done for the boundary layer cases in Chapters 3, 4, and Appendix A—is the difficulty in determining the temperature and pressure fields for the flow. While the boundary layer case permits a constant pressure assumption and an approximation of the temperature field using the Crocco-Busemann relationship, these types of engineering approximations are not possible with the complex capsule flowfield. A simultaneous measurement of pressure and temperature would be ideal, however, no pressure diagnostic is currently available using naphthalene PLIF and the two-line thermometry technique is not capable of being applied to such a large field of view. Therefore, as discussed in Section 5.2.4 a simulation of the temperature and pressure fields was sought using CFD to serve as a mean approximation to be used in the conversion of the PLIF images to naphthalene mole fraction. The temperatures and pressures output by the OVERFLOW solver (Murman et al., 2015) for the Mach 5 capsule flowfield at 0°, 12°, and 24°, AoA are presented in Figures 5.17-5.19 below. In the regions of interest—where naphthalene vapor was generally present—the temperature is primarily between 100-350 K. The pressure throughout the field of view is considerably higher than the pressure in the boundary layer, with values as high as 150 kPa on the capsule heat shield surface and lower pressure in the wake region around 5 kPa.

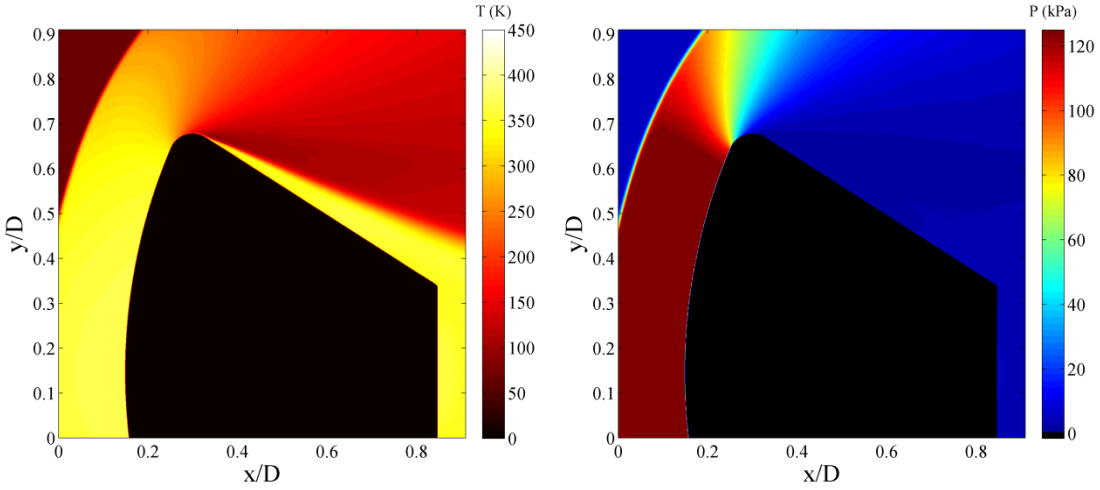

Figure 5.17: Temperature and pressure fields calculated by the OVERFLOW solver (Murman et al., 2015) for the 0° capsule flowfield.

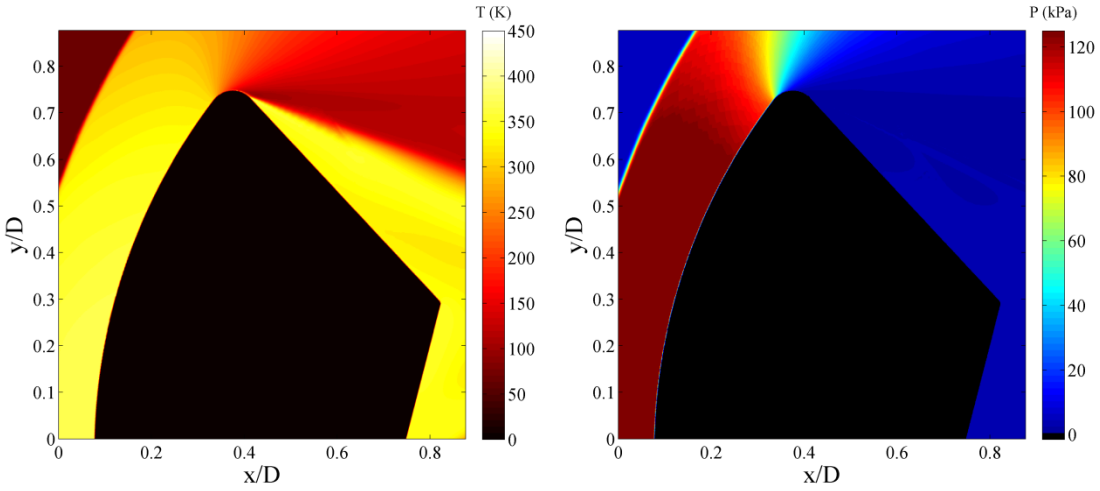

Figure 5.18: Temperature and pressure fields calculated by the OVERFLOW solver (Murman et al., 2015) for the 12° capsule flowfield.

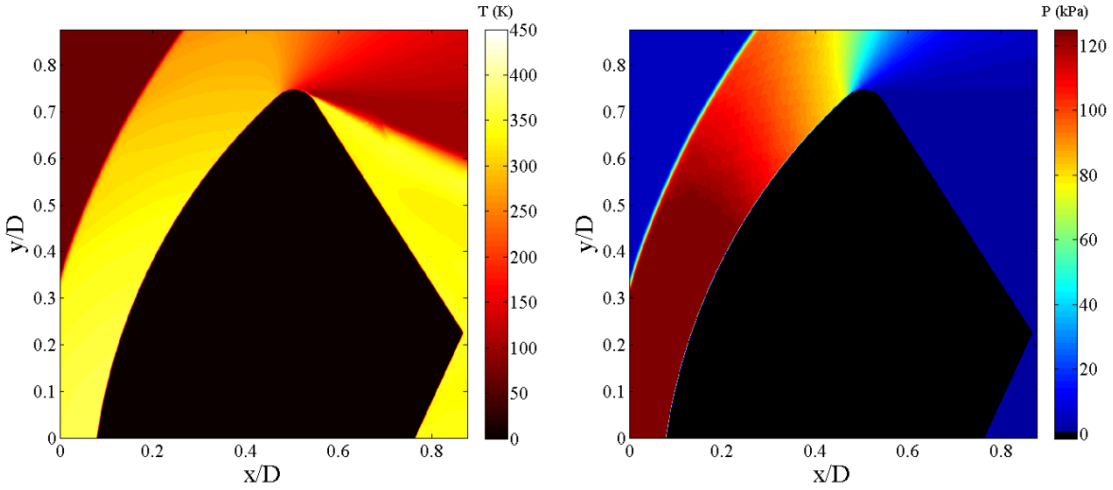

Figure 5.19: Temperature and pressure fields calculated by the OVERFLOW solver (Murman et al., 2015) for the 24° capsule flowfield.

The PLIF image correction factor Σ was introduced in Section 3.3.2 with Eq. 3.4. This variable represents the relative multiplicative factor applied to the PLIF images in the conversion to mole fraction and can illustrate the effect of temperature and pressure in a given flowfield on a given PLIF image. Figure 5.20 presents the two-dimensional fields of Σ for the capsule flowfield at 0°, 12°, and 24°, based on the temperature and pressure fields computed by the OVERFLOW calculations presented in Figures 5.17-5.19. First, note that all three plots of Σ appear qualitatively similar, which is to be expected. Furthermore, the range of Σ present in Figure 5.20 is approximately 0.5-2, which is close to the same as the range of 1-2 in the Mach 5 boundary layer. This result was not necessarily expected given the much wider range of pressures and temperatures present in the capsule flowfield, and implies that the sum effects of the higher pressures and temperatures may have cancelled each other out. It is also worth noting that Σ appears much lower—approximately 0.7—near the heat shield surface compared to the wake region (about 1.25). This means that the intermittent naphthalene vapor structures

observed on the heat shield surface should be even more difficult to see in the mole fraction images, as the relative magnitude of the signal in this region will be decreased by the mole fraction calculation process. Lastly, the angle of the shear layer in all the capsule flowfields calculated by the OVERFLOW solver do not appear to match the PLIF images. This is most likely caused by the fact that the CFD simulations of the flowfield did not contain the model sting, which should result in a pressure increase in the wake and a shallower shear layer angle. For the purposes of the current work, however, these simulations should be sufficient to provide a rough approximation of the temperature and pressure in the capsule flowfield to permit the calculation of naphthalene mole fraction from the PLIF images.

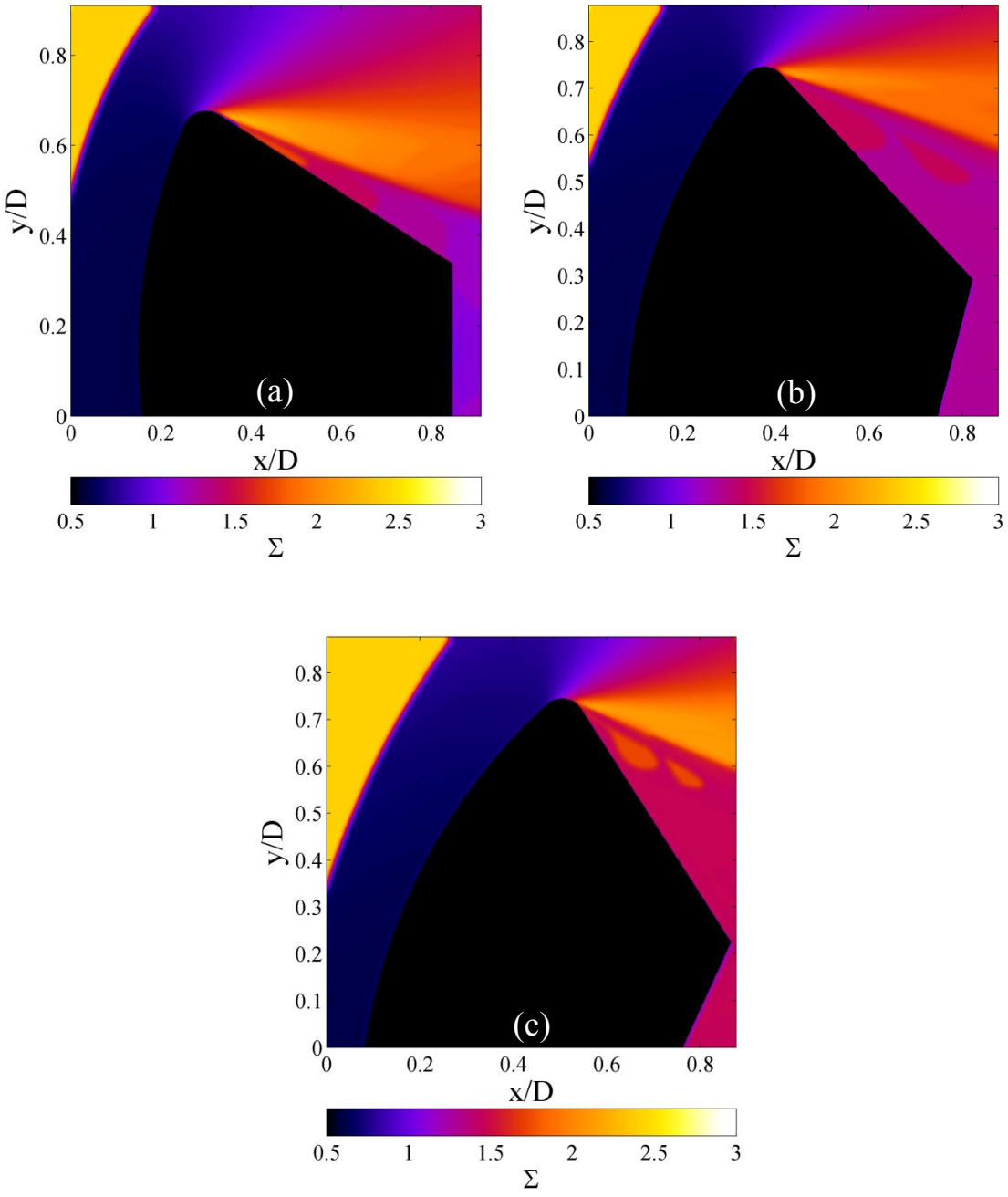

Figure 5.20: Naphthalene PLIF image correction factor, Σ (defined in Eq. 3.4), for the (a) 0°, (b) 12°, and (c) 24°, capsule flowfields.

The results of the mole fraction calculations are presented in Figures 5.21-5.23. The figures compare instantaneous naphthalene PLIF images for the Orion MPCV capsule flowfield with corresponding fields of calculated naphthalene mole fraction at 0°, 12°, and 24° AoA, respectively. First, in each case the mole fraction fields still look generally similar to the original PLIF images, with the highest concentration in the wake and few naphthalene vapor structures evident elsewhere. This somewhat validates the assumption used throughout this chapter that uncorrected PLIF images provide a general representation of the mole fraction of the PLIF species in the flow. The low signal regions in the wake as well as the streaks of naphthalene vapor observed in the 12° images are still present in the mole fraction fields as well. In the few instances where naphthalene vapor structures were observed on the surface of the capsule heat shield at these conditions (primarily at 12° AoA) the structures are still present after the mole fraction conversion. While the plots of Σ presented in Figure 5.20 indicted it may not be possible to see these structures once the PLIF images were converted to mole fraction, it appears that this effect was relatively small.

There are, however, some noticeable differences between the PLIF images and the calculated fields of naphthalene mole fraction. The primary discrepancy appears to be the result of the difference in the shear layer angle for the PLIF images compared to the CFD. As seen in Figures 5.21-5.23, the upper portion of the high PLIF signal region (termed the wake region in the current work) is elevated relative to the rest of the high signal region upon conversion of the PLIF signal to mole fraction. This effect is most striking for the 0° case, where the difference in shear layer angle between experiment and simulation was most pronounced. Meanwhile, the effect appears to be relatively small for the 12° case. When comparing the 12° PLIF images to the OVERFLOW computations of

the flowfield at 12° AoA, it seems that the difference in shear layer angle was relatively small compared to the other two AoA cases. It may be possible to mitigate this discrepancy with future computations of the flowfield that include the sting (and perhaps the strut) of the capsule model.

Finally, the magnitude of naphthalene mole fraction calculated for the three different capsule flowfields ranged from approximately 4×10^{-4} to 5×10^{-3} in the wake region. By comparison, this is approximately 10 times more naphthalene vapor than was observed in the Mach 5 boundary layer experiments. This observation makes sense considering the heat shield should experience a much higher heat transfer rate than the naphthalene insert on the floor of the tunnel. It was also observed that the mole fraction calculated for the 0° case was about three times higher in the wake region than for the 12° and 24° cases, which were quite similar. This can perhaps be partly explained by the significant discrepancy in the shear layer angle found by the experiment when compared to the CFD simulations. However, the region within the wake of the CFD simulations still resulted in a calculated naphthalene mole fraction primarily between 1×10^{-3} to 3×10^{-3}—still higher than the measurements for the 12° and 24° cases. The recorded wind tunnel stagnation temperature was the same for each of the three runs, so it is unlikely that run conditions played a part in the difference in calculated mole fraction. It is therefore probable that the 0° case results in a higher heat transfer rate due to the fact that the capsule is more of an obstruction to the flow at this AoA (Bertin, 1966).

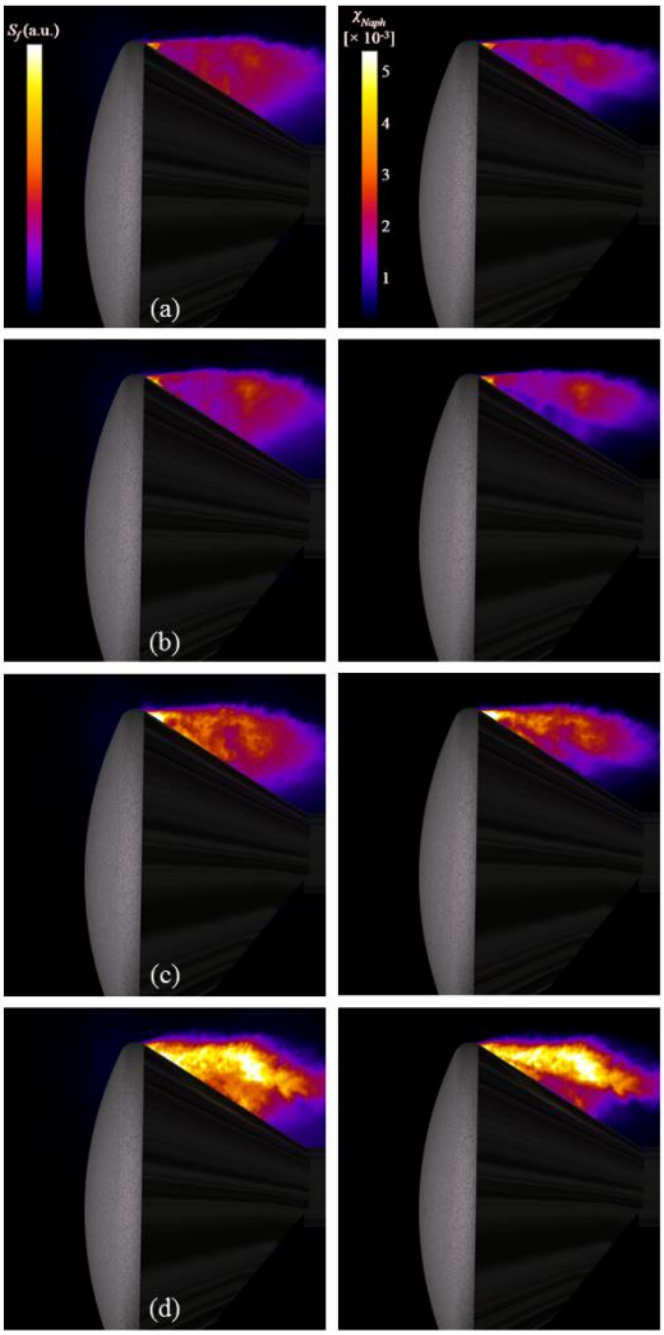

Figure 5.21: Naphthalene PLIF images of a capsule model at 0° angle of attack. Images of normalized PLIF signal are presented on the left while the corresponding fields of calculated naphthalene mole fraction are on the right.

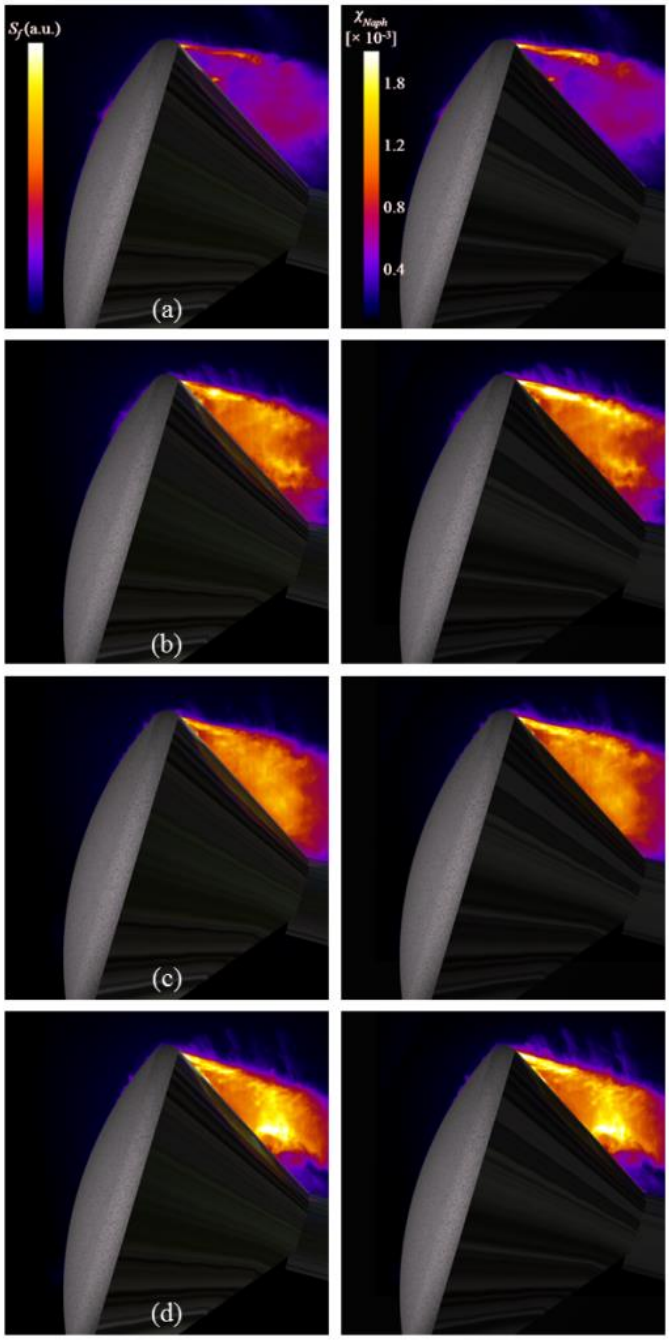

Figure 5.22: Naphthalene PLIF images of a capsule model at 12° angle of attack. Images of normalized PLIF signal are presented on the left while the corresponding fields of calculated naphthalene mole fraction are on the right.

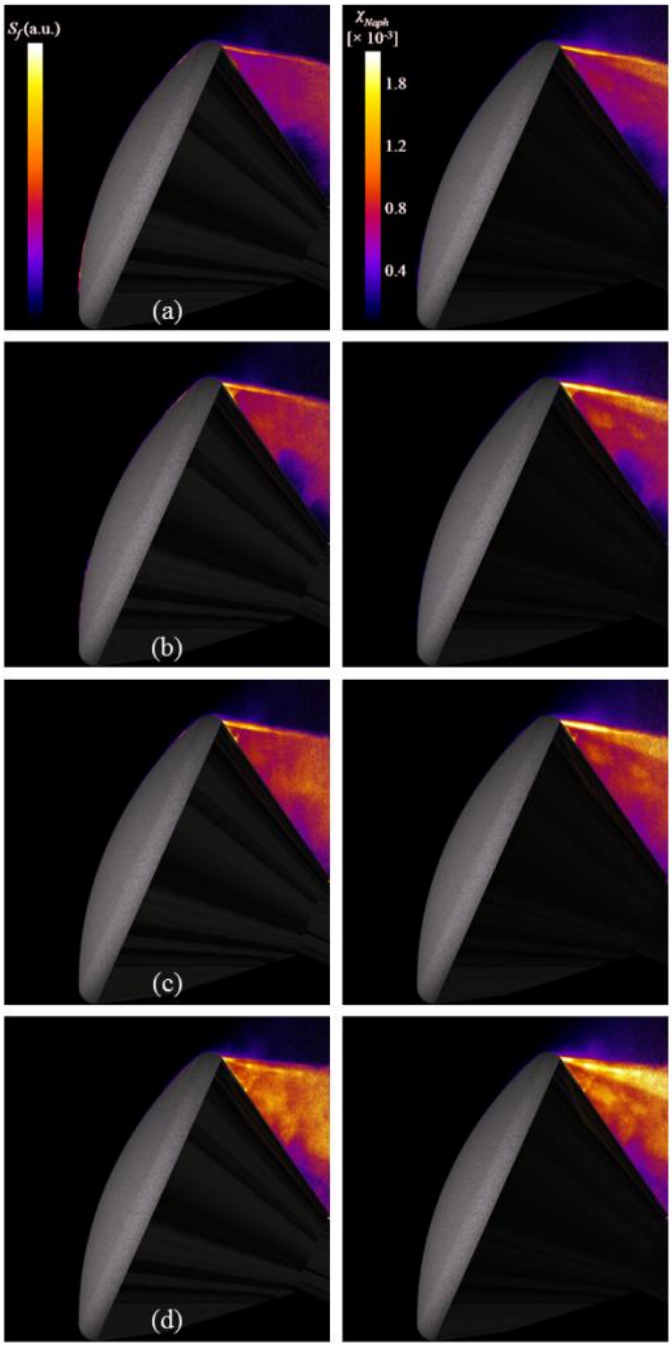

Figure 5.23: Naphthalene PLIF images of a capsule model at 24° angle of attack. Images of normalized PLIF signal are presented on the left while the corresponding fields of calculated naphthalene mole fraction are on the right.

5.4 - CONCLUSION

Naphthalene PLIF has been used to visualize the dispersion of gas-phase ablation products on a scaled NASA Orion MPCV model at four different angles of attack in the Mach 5 wind tunnel facility at The University of Texas at Austin. With this set of experiments, it was demonstrated that naphthalene PLIF is a viable technique for imaging ablation-products transport on a reentry capsule geometry. The naphthalene PLIF flow visualization was complemented by Schlieren imaging, and the structure of the capsule shear layer compared favorably when imaged with both techniques. In the naphthalene PLIF images, high concentrations of scalar were imaged in the capsule recirculation region. Additionally, intermittent turbulent structures were visualized on the heat shield surface, particularly for the 12° and 52° AoA cases. The most prominent structures seen on the heat shield occurred for the 52° case, which consistently led to the visualization of turbulent naphthalene structures on the heat shield surface. The shear layer appeared to be laminar in the 24° case, whereas in the 12° and 0° cases the shear layer appeared to transition from laminar to turbulent (or at least became more unsteady) over the course of the run. Owing to the positioning of the laser sheet, not enough naphthalene vapor was visualized in the shear layer for the 52° case to make a determination as to the nature of the shear layer. In general, the shear layer appeared to be more unsteady at lower angles of attack. Moreover, the shear layer became increasingly unsteady over the course of a wind tunnel run, most likely due to increased surface deformation and roughness, and possibly the increased blowing rate. The PLIF images also demonstrated that the model would heat up over the course of a wind tunnel run, leading to more ablation and significantly more naphthalene present in the afterbody separated flow region. Several other interesting flow features were identified in the PLIF images as well. First, the shear

layer appeared to be more steady at the leeward capsule shoulder compared to further downstream, which was consistent with previous research. Also, regions of relatively low naphthalene signal were identified in the capsule recirculation region. These low signal regions are most likely the result of spanwise structures, such as vortices, on the capsule afterbody. A series of elongated naphthalene structures emanating from the upper edge of the shear layer were identified in multiple images as well, but the cause of this flow feature is currently undetermined.

CFD simulations of the capsule flowfield temperature and pressure fields at 0°, 12°, and 24 ° AoA (provided by Dr. Scott Murman at NASA Ames) were then used to compute naphthalene mole fraction from the PLIF images. The resulting mole fraction fields were grossly similar to the PLIF images with discrepancies most likely resulting from the fact that the CFD simulations did not account for the model sting. The major flow structures observed in the qualitative PLIF images were all still apparent. The magnitude of naphthalene mole fraction in the wake region varied from 0.4-5 $\times$ 10^{-3}, roughly 10 times higher than the magnitude of naphthalene mole fraction measured in the Mach 5 boundary layer. The calculated mole fraction for the 0° case was slightly higher than what was calculated for the 12° and 24° cases, due in part to a discrepancy in the angle of the shear layer for the 0° CFD simulation but also the result of a higher ablation rate for the 0° case.

5.5 - Suggested Future Work

At present the application of naphthalene PLIF to a capsule geometry merely serves as a proof-of-concept experiment to show the capability of the technique. However, applications of naphthalene PLIF to complex heat shield geometries may be the next logical step in the development of the technique. Improvements to the two-line

naphthalene PLIF thermometry technique could enable simultaneous temperature measurements, which coupled with approximations to the pressure field from CFD simulations could be used to quantify the PLIF images. Additionally, other relevant geometries could be investigated (cones, hemispheres, other capsule designs) with little further development of the technique required.

There is also more work that could be accomplished with the current capsule investigation. First, an investigation of different imaging planes displaced from the capsule centerline could be used to reconstruct the three-dimensional flowfield. Additionally, imaging of the windward side of the capsule was not conducted in the current work and would help complete the imaging of the flowfield. This could be completed in dedicated runs but could also be achieved simultaneously with imaging of the leeward side of the capsule. Simultaneous acquisition of both halves of the flowfield could be accomplished by using a 50/50 beam splitter to divide the laser beam, forming two laser sheets, then passing one component through the top and one component through the bottom of the test section. Since fluorescence signal was significantly higher in the capsule flow experiments compared to the boundary layer experiments, halving the laser power should still provide adequate SNR images.

Another modification would be to develop a naphthalene-based composite or naphthalene-polymer solution that could better withstand wind tunnel start up and shut down. Many runs were lost during this imaging campaign due to damaged naphthalene heat shields. Another solution would be to construct a model injection system compatible with the Mach 5 test section that could insert the model into the flow after wind tunnel startup.

A final, tangential experiment of interest would be to perform three-dimensional laser dot projection photogrammetry of the naphthalene heat shield surface during a run. This would provide valuable information on the recession of the heat shield at various locations during the run and would permit three-dimensional reconstructions of the heat shield surface with respect to elapsed time.

Appendix A: Development of a two-line naphthalene PLIF ratiometric thermometry technique

A.1 - INTRODUCTION

The ability to successfully collect quantitative data with simultaneous naphthalene PLIF and PIV was demonstrated in the boundary layer of the Mach 5 facility at The University of Texas at Austin, and reported in Chapters 3 and 4. However, the largest source of error in the naphthalene PLIF measurements results from the uncertainty in the instantaneous temperature field (~15%). While mean Crocco-Busemann approximations can be made, it remains only a correction to the mean temperature distribution. Furthermore, the use of Crocco-Busemann is dependent on simultaneously acquiring PIV data, which may not be possible in many large-scale flow facilities.

In light of this, it is desired to develop a non-intrusive temperature diagnostic based on the temperature sensitivity of naphthalene fluorescence. This technique employs two laser sources that nearly simultaneously excite the naphthalene vapor in the flow. The fluorescence resulting from each excitation source is then imaged and the subsequent fluorescence ratio is used to calculate temperature, using the relationship illustrated in Figure 2.20. The procedure employed in the current work to execute these temperature measurements is discussed in this appendix, and mean and instantaneous temperature profiles are presented. Additionally, a comparison is made between the temperature measurements collected using two-line naphthalene PLIF thermometry and the Crocco-Busemann scheme. Mole fraction fields are then calculated using the two temperature calculation techniques and compared.

A.2 - EXPERIMENTAL PROGRAM

A.2.1 - Wind Tunnel Facility

The facility used for these experiments was the same low-enthalpy blow-down Mach 5 wind tunnel described in Section 3.2.1. The wind tunnel was supplied by a 4 m^3 storage tank held at approximately 15.5 MPa and the plenum pressure was maintained at approximately 2.5 MPa ± 15 kPa. The flow was electrically heated to achieve a stagnation temperature of up to 368 K ± 4 K. The test section and flow properties were the same as those discussed in Section 3.2.1. Optical access for laser transmission and imaging was provided by fused silica windows on the wind tunnel floor, ceiling, and sidewall.

As in Chapters 3 and 4, the naphthalene vapor was introduced into the flow by sublimation of a solid naphthalene insert (105 mm long x 57 mm wide) that was mounted to the floor of the wind tunnel. The solid block of naphthalene, depicted in Figure A.1, was formed by pouring liquid naphthalene into a mold and then covering it during the cooling process to ensure a smooth, flush surface. After the naphthalene solidified, the cover was removed and the insert was installed into the test section floor. The sublimation rate of naphthalene at standard conditions is slow and no noticeable mass was lost if the insert was left in the test section for hours without flow. Only a small amount of ablation (less than a fraction of a millimeter) was observed over the course of a one minute wind tunnel run.

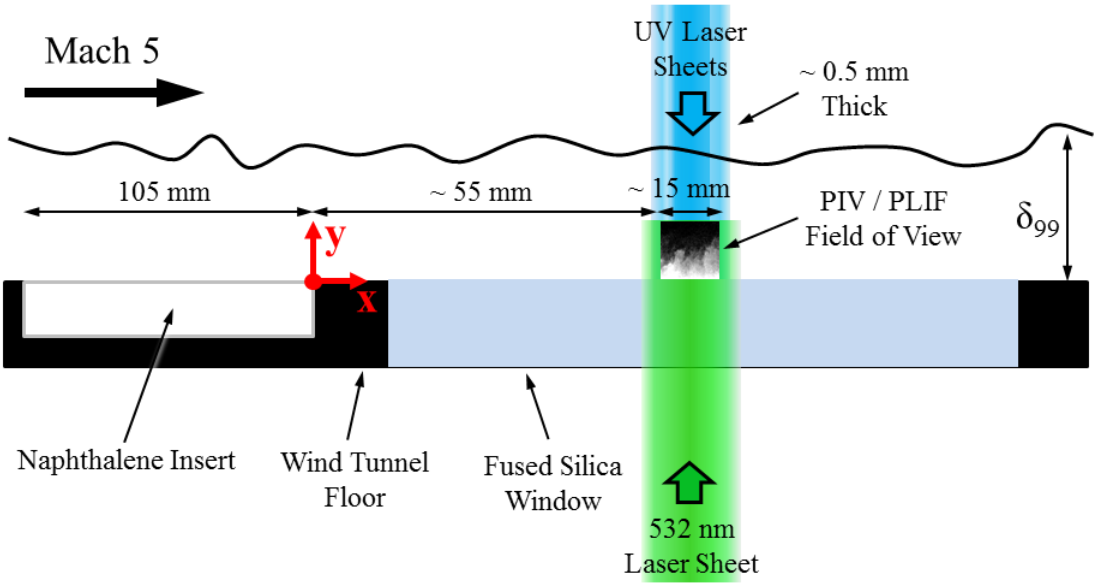

Figure A.1: Schematic of the naphthalene insert and imaging field of view for the two-line PLIF thermometry measurements. The coordinate system employed is indicated by the red axes.

A.2.2 - PLIF Experimental Setup

Photographs of the experimental setup for the two-line PLIF thermometry technique are shown in Figures A.2 and A.3 while a computer-generated three-dimensional schematic of the setup is presented in Figure A.4. As seen in the figures, the naphthalene vapor was first excited by a sheet of 266 nm light from a frequency-quadrupled Nd:YAG laser (Spectra-Physics Quanta-Ray GCR-150) operating at a rate of 10 Hz with its energy maintained at approximately 42 mJ/pulse. To make two-line PLIF measurements, the naphthalene vapor was also excited with 283 nm light from a frequency-doubled Lumonics HyperDYE-300 dye laser, with a Bethune cell amplifier. The dye laser was pumped by approximately 350 mJ of 532 nm light from a frequency-doubled Nd:YAG laser (Spectra-Physics Quanta-Ray PIV-400). The 532 nm light pumped Rhodamine 590 dye diluted in methanol which was circulated through the

oscillator and amplifier dye cells at concentrations of 1.6×10^{-4} mol/L and 8.5×10^{-5} mol/L, respectively. The resultant output of the dye laser was approximately 32 mJ/pulse of 566 nm light. The efficiency of the dye laser was limited in part because the target emission wavelength of 566 nm was off of the peak of the Rhodamine 590 dye, where output energies as high as 65 mJ/pulse were observed for 575 nm output. The 566 nm output from the dye laser was then frequency-doubled in an Inrad frequency conversion unit to achieve between 1-2 mJ/pulse of 283 nm light, which was then aligned with the 266 nm beam. As the dye laser was pumped by the same laser source used to produce the second PIV beam, the two beams were temporally offset by 300 ns. Given the magnification of the field of view was 75 μm/pixel, a flow structure moving at a velocity of 500 m/s would translate approximately 2 pixels over the 300 ns delay. This translation is not ideal but is considerably smaller than the size of the Gaussian filter (10×10 pixels) employed in the imaging processing and does not appear to have significantly impacted the uncertainty of the measurements.

The UV laser beams were then oriented by a series of laser mirrors so that they passed up to the top of the wind tunnel facility where they were formed into two coincident laser sheets using a 250 mm spherical lens and a 25 mm cylindrical lens and transmitted through the test section, as seen in Figure A.4. The resulting 266 nm laser sheet was about 0.5 mm thick (FWHM) in the measurement region and approximately 15 mm wide while the 283 nm laser sheet was about 0.5 mm thick (FWHM) in the measurement region and approximately 8 mm wide. The 283 nm laser sheet was made narrower than the 266 nm laser sheet in order to increase the power density of the sheet.

PLIF images from excitation with both laser sheets were recorded using a back-illuminated CCD camera (Apogee Alta F47, 1024×1024) with high quantum efficiency in

the UV (approximately 55% between 300 and 400 nm), fitted with a 100 mm focal length, f/2.8 UV lens (Circo) operated at full aperture. A gated intensified CCD camera (PI-Max 3 Unigen II, 1024×1024) was used to image the fluorescence from the 266 nm excitation only, and was also fitted with a 100 mm focal length, f/2.8 UV lens (Circo) operated at full aperture. The gain of the PI-Max camera was set to 95 for all runs. Unfortunately, the quantum efficiency of the PI-Max camera was only 10% between 300-400 nm. The Apogee and PixelVision cameras previously used for PLIF experiments in Chapters 3 and 4 could not shutter quickly enough to isolate fluorescence from one excitation source. In order to reject scattered laser light and image only naphthalene fluorescence, one Schott WG-295 filter and one Schott UG-11 filter were placed in front of each camera. The imaging field of view was approximately 8 mm wide by 16 mm tall as only the portion of the image with excitation from both laser sheets could be used for calculating temperature. To minimize image distortion the Apogee camera imaged the fluorescence at a 90° angle to the laser sheets while the PI-Max camera was offset slightly and imaged at an angle of approximately 85° relative to the laser sheets. The images were obtained at a rate of approximately 1/3 Hz with a 40 ms exposure time for the Apogee camera and a 100 ns exposure time for the PI-Max camera (sufficient to capture the entire fluorescence pulse which generally had a lifetime of approximately 15 ns and a duration of around 60 ns), with as many as 30 sets of images acquired per wind tunnel run. The coordinate system applied to the PLIF and PIV fields of view is the same as that used in Chapters 3 and 4 and is as follows: the x-direction is aligned with the freestream while the y-direction is normal to the wind tunnel floor, with the origin located at the trailing edge of the naphthalene insert and on the same plane as the laser sheet, as illustrated in Figures 4.1 and 4.2. The experiment was synchronized using three Stanford

Research Systems digital delay generators to ensure that images were acquired while the lasers were firing.

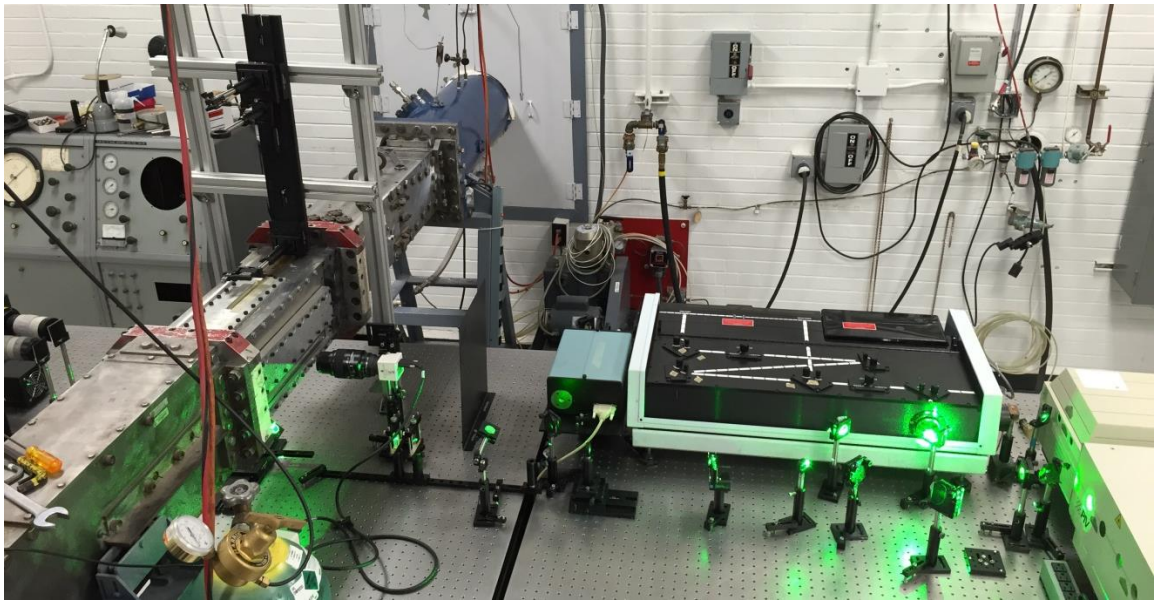

Figure A.2: Photograph of the experimental setup employed in Appendix A.

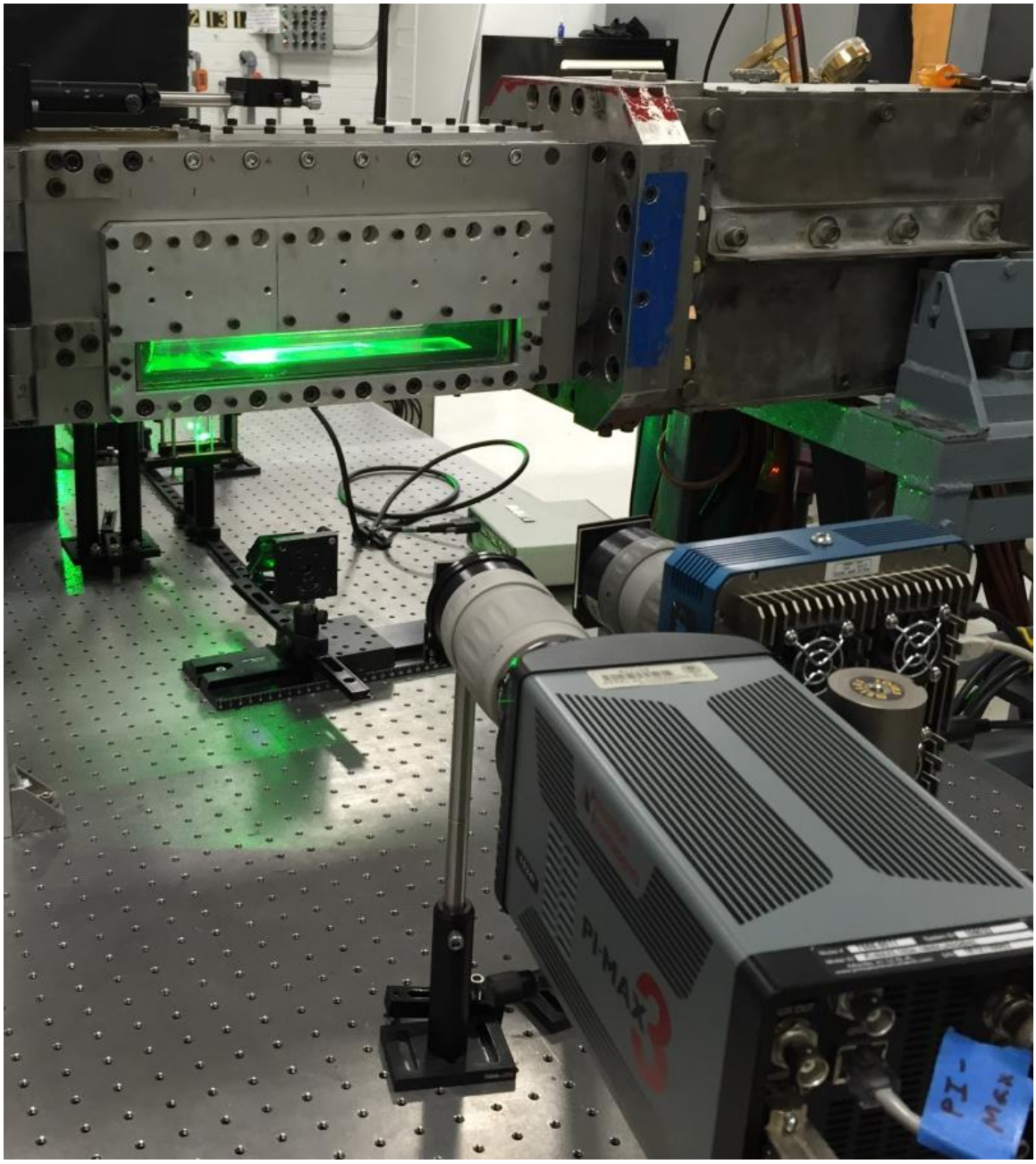

Figure A.3: Photograph of the two PLIF cameras and the Mach 5 test section.

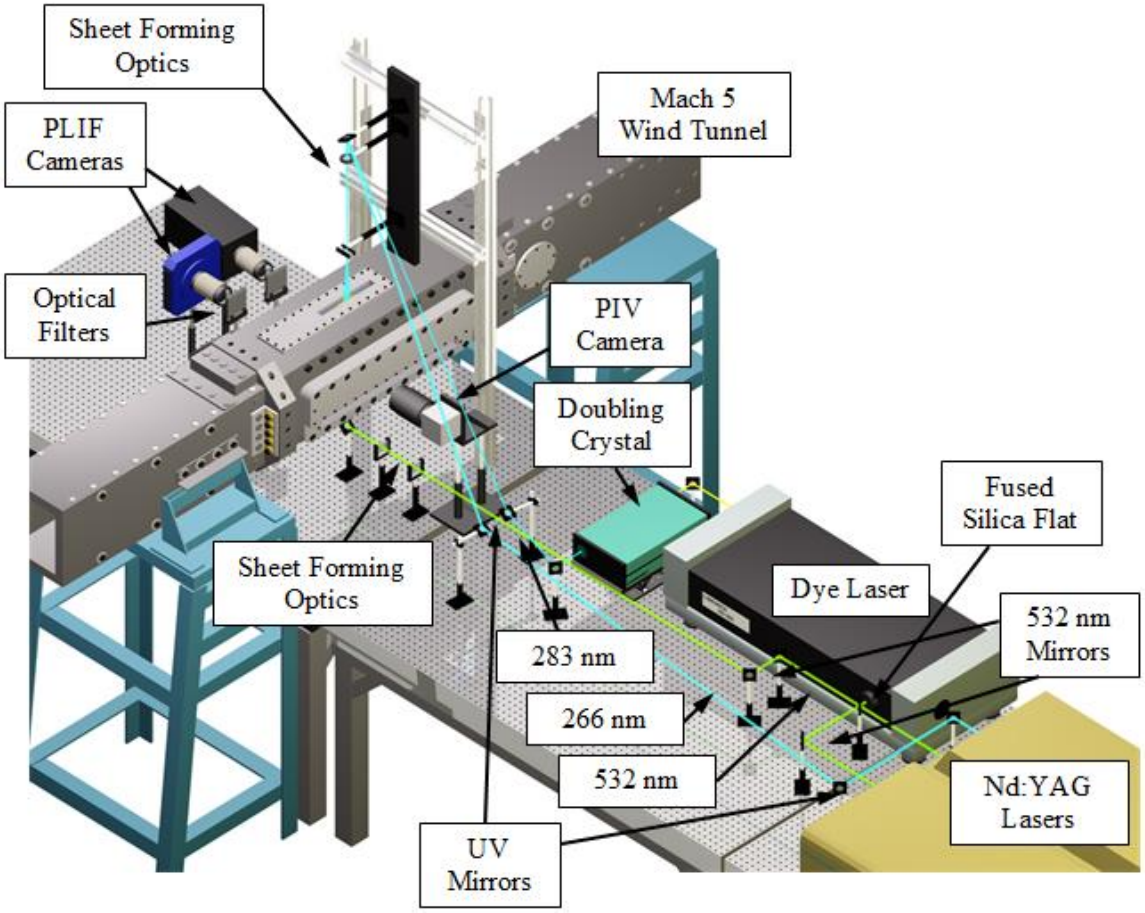

Figure A.4: Simultaneous PIV/Two-Line PLIF Setup.

A.2.3 - PIV Experimental Setup

The PIV experimental setup was essentially the same as the one described in Section 4.2.3, with Titanium Dioxide (TiO_2) used as the seed particle for PIV. PIV images were not acquired during every run in which two-line PLIF thermometry was performed, as the PLIF signal has been shown to be lower when seeding PIV particles (see discussion in Section 4.3.2).

As before, the first laser sheet was generated by the residual 532 nm light from the GCR-150 laser used for 266 nm excitation and was thus synchronized with the first

PLIF pulse. Both cavities from the PIV-400 laser used to pump the dye laser were used to generate the second laser sheet and were delayed by 300 ns relative to the GCR-150 (the time delay between the two pulses was minimized to < 1 ns). As shown in Figure A.4, the laser pulses were combined using an uncoated fused silica flat. The GCR-150 beam passed through the fused silica flat and combined with the approximately 10% reflection from the PIV-400 beam that was incident to the flat 90° relative to the GCR-150 beam. The other 90% of the PIV-400 beam was used to pump the dye laser. After the fused silica flat, a spatial filter was used to crop a small portion of the PIV-400 beam to match the power from the GCR-150 beam. This resulted in two coincident beams with pulse energies of approximately 15 mJ/pulse each.

The light sheets formed for PIV and PLIF were then aligned so that they were coincident and the two fields of view overlap, as illustrated in Figure A.1.

A.2.4 - PLIF Image Processing

Single-shot PLIF images were processed in MATLAB. The first step was to map the images from the PI-Max and Apogee cameras onto the same grid so that all points in each image were at the same physical location. This was achieved by imaging a ruler placed in the test section and mapping each image onto the same grid using a set of known “markers” on the ruler in each image. The mapping procedure was performed using a custom MATLAB script.

After the image mapping was complete, the images were processed in a manner similar to the procedure that was used for processing images in Chapters 3 and 4. First, the background was removed. Then, mean laser sheet intensity profiles were determined for three cases: (1) 266 nm sheet for the Apogee camera, (2) 266 nm sheet for the PI-Max camera, and (3) 283 nm sheet for the Apogee camera. Single-shot sheet corrections were

not made. As in the second PLIF imaging campaign discussed in Chapter 3 and the PLIF imaging in Chapter 4, the mean laser sheet spatial intensity variation was measured by one of two methods: (1) imaging the mean fluorescence of naphthalene vapor present in the test section (preferred) or (2) imaging the mean fluorescence of acetone vapor in the test section. The second method (acetone vapor) was employed most frequently in this set of experiments as the low signal levels from the PI-Max camera made it difficult to image a 266 nm laser sheet from naphthalene vapor present in the test section and the low power of the 283 nm laser made it difficult to image a laser sheet profile using the Apogee camera. These images were collected prior to a run with both the Apogee and PI-Max cameras. Upon averaging approximately 30 of these images, two-dimensional laser sheet profiles were obtained.

Additionally, a room temperature reference cell saturated with naphthalene vapor was pulled to a vacuum (4.92 kPa ± 10 Pa), placed in the Mach 5 test section in the path of each laser sheet (separately), and imaged to generate reference images for quantifying the fluorescence signal. These images were also corrected for variations in laser sheet intensity by using the same technique described above.

Correcting the images for non-uniformities in the laser sheet profile was not as straightforward as in Chapters 3 and 4 considering that the Apogee camera was recording images from two separate laser sheets. Consider the following formulation of the problem, beginning with a formulation of the fluorescence equation:

$$S_{f,266} = \frac{E_{266}}{\frac{hc}{\lambda}} \eta \Delta V \chi_i n(P,T) \sigma_a(266\ nm, T) \varphi(266\ nm, T, P, \chi) \qquad \text{A.1}$$

where the terms are still defined in the same way as in Chapter 1 and the subscript *266* denotes 266 nm excitation. Combining the constants into one term, C_{266}, the equation can be further reduced to the form:

$$S_{f,266} = C_{266}\,\chi_{naph} n\, E_{266}\,\sigma_{a,266}\,\varphi_{266} \tag{A.2}$$

This result can be replicated for 283 nm excitation as well:

$$S_{f,283} = C_{283}\,\chi_{naph} n\, E_{283}\,\sigma_{a,283}\,\varphi_{283} \tag{A.3}$$

Next, consider the fluorescence signal imaged by the Apogee camera,

$$\begin{aligned} S_{f,Apogee} = {} & C_{266,Apogee}\,\chi_{naph} n\, E_{266}\,\sigma_{a,266}\,\varphi_{266} \\ & + C_{283,Apogee}\,\chi_{naph} n\, E_{283}\,\sigma_{a,283}\,\varphi_{283} \end{aligned} \tag{A.4}$$

where $S_{f,Apogee}$ represents the background subtracted PLIF image from the Apogee camera. Additionally, the PI-Max image can be represented as:

$$\begin{aligned} S_{f,PI-Max} &= C_{266,PI-Max}\,\chi_{naph} n\, E_{266}\,\sigma_{a,266}\,\varphi_{266} \\ &= C_{266,Apogee}\,\chi_{naph} n\, E_{266}\,\sigma_{a,266}\,\varphi_{266}\,\frac{C_{266,PI-Max}}{C_{266,Apogee}} \end{aligned} \tag{A.5}$$

where $S_{f,PI-Max}$ represents the background subtracted PLIF image from the PI-Max camera. The ratio $C_{266,PI-Max}/C_{266,Apogee}$ can be calculated by taking the ratio of the fluorescence signal measured from the same test cell simultaneously by each camera and was calculated as 3.74 in the current experiments. Keep in mind that the desired result is to calculate a ratio of the fluorescence from 266 nm and 283 nm excitation as a function of known quantities.

From Eq. A.5, it can be deduced that:

$$C_{266,Apogee}\,\chi_{naph}n\,\sigma_{a,266}\,\varphi_{266} = \frac{S_{f,PI-Max}}{E_{266}}\,\frac{C_{266,Apogee}}{C_{266,PI-Max}} \quad \text{A.6}$$

Dividing the Apogee image by its 266 nm laser sheet correction and subtracting the adjusted PI-Max image (Eq. A.6) yields Eq. A.7 below:

$$\frac{S_{f,Apogee}}{E_{266}} - \frac{S_{f,PI-Max}}{E_{266}}\,\frac{C_{266,Apogee}}{C_{266,PI-Max}} = \frac{C_{283,Apogee}\,\chi_{naph}n\,E_{283}\,\sigma_{a,283}\,\varphi_{283}}{E_{266}} \quad \text{A.7}$$

To isolate the component of the Apogee image resulting from 283 nm excitation, Eq. A.7 must be divided by the 283 nm sheet correction and multiplied by the 266 nm sheet correction, as seen in Eq. A.8:

$$C_{283,Apogee}\,\chi_{naph}n\,\sigma_{a,283}\,\varphi_{283} = \left(\frac{S_{f,Apogee}}{E_{266}} - \frac{S_{f,PI-Max}}{E_{266}}\,\frac{C_{266,Apogee}}{C_{266,PI-Max}}\right)E_{266}/E_{283} \quad \text{A.8}$$

At this point, the components of the fluorescence signal resulting from 283 nm and 266 nm excitation on the Apogee CCD have been identified in terms of known quantities with Eqs. A.6 and A.8, respectively. All that is left is to divide Eq. A.6 by Eq. A.8 and apply a second calibration factor:

$$\frac{\dfrac{S_{f,PI-Max}}{E_{266}}\dfrac{C_{266,Apogee}}{C_{266,PI-Max}}}{\left(\dfrac{S_{f,Apogee}}{E_{266}}-\dfrac{S_{f,PI-Max}}{E_{266}}\dfrac{C_{266,Apogee}}{C_{266,PI-Max}}\right)E_{266}/E_{283}}\frac{C_{283,Apogee}}{C_{266,Apogee}}$$

$$=\frac{C_{266,Apogee}\,\chi_{naph}n\,\sigma_{a,266}\,\varphi_{266}}{C_{283,Apogee}\,\chi_{naph}n\,\sigma_{a,283}\,\varphi_{283}}\frac{C_{283,Apogee}}{C_{266,Apogee}} \qquad \text{A.9}$$

$$=\frac{\sigma_{a,266}\,\varphi_{266}}{\sigma_{a,283}\,\varphi_{283}}=\frac{S_{f,266}}{S_{f,283}}=f(T)$$

Using Eq. 1.11, Eq. A.9 reduces to $S_{f,266}/S_{f,283}$, which represents the true ratio of fluorescence from the two excitation sources and is equivalent to $f(T)$—representing a temperature-dependent function that can be solved to determine *T*. As with the other collection efficiency terms, the ratio $C_{283,Apogee}/C_{266,Apogee}$ was determined through test cell measurements and was measured as 0.32 for the current experiments. The fluorescence ratio function, $f(T)$, was derived from the data presented in Figure 2.20. The data were slightly modified to be normalized to 295 K— rather than the 100 K value depicted in Figure 2.20—as this was the temperature of the reference cell.

However, since temperature was the variable sought and the fluorescence signal ratio was known, the data from Figure 2.20 were fit to a second order polynomial of the form:

$$T=f\left(\frac{S_{f,266}}{S_{f,283}}\right)=g_1\left(\frac{S_{f,266}}{S_{f,283}}\right)^2+g_2\left(\frac{S_{f,266}}{S_{f,283}}\right)+g_3 \qquad \text{A.10}$$

The curve fit coefficients determined from the fitting procedure are shown in Table A.1.

Table A.1: Experimentally-determined coefficients for curve fits to be used for calculating temperature from the measured fluorescence signal ratio. The reference conditions used to correct the PLIF images were 4.92 ± 10 Pa and 295 K ± 2 K. While the values of the coefficients are independent of the chosen reference conditions, these fits are only valid over the tested temperature and pressure space of 100-525 K and 4-6 kPa in air.

g_1	40.1 K
g_2	227.1 K
g_3	26.1 K

Inputting the fluorescence signal ratio images into Eq. A.10 yielded two-dimensional fields of temperature. One final step in determining the temperature field was the removal of invalid points in the field. Locations where the temperature was found to be over 475 K or below 30 K were removed and replaced by the respective maximum or minimum allowable temperature value, respectively. After replacing the invalid pixels, the image was filtered once again with a 6×6 Gaussian blur filter. This allowable temperature range was determined based on temperatures that are 50% lower than the freestream value and 50% greater than the wall recovery temperature. Generally between 85-95% of the pixels in the calculated temperature fields were within the allowable temperature range.

After determining the temperature field, the raw PI-Max images were processed in the same manner described in Section 4.2.4 including a background subtraction, laser sheet correction, and mole fraction calculation using Eq. 1.10 coupled with the fits for absorption cross section and fluorescence yield described in Section 2.3.3. Here, pressure was still assumed to be constant in the boundary layer but the temperature field employed in the calculation was measured using two-line PLIF thermometry. Therefore, the field of view for the mole fraction calculation was limited to the area where there was sufficient

naphthalene PLIF signal. This meant that measurements could generally not be made for wall distances greater than $y/\delta = 0.25$. For comparison, full field of view images were calculated using a mean Crocco-Busemann correction based on the velocity profile measured using a pitot probe survey (McClure, 1992).

The Apogee images could not be used to calculate mole fraction as they contained fluorescence due to 283 nm excitation. Also, by definition, subtracting the calculated 283 nm component from the image using the equations above would simply yield the PI-Max image. Unfortunately, the PI-Max images were substantially noisier than the Apogee images owing to the low UV quantum efficiency of the CCD.

Using the described procedure and curve fits, the PLIF images were converted into two-dimensional plots of naphthalene mole fraction. To reduce noise, a 6×6 median filter was applied to all images.

No correction was made for potential laser absorption by naphthalene vapor since negligible absorption was observed in the test cell over a distance larger than the boundary layer thickness in the current experiments, as discussed in Section 3.2.3.

A.2.5 - PIV Image Processing

The PIV images were processed in LaVision's DaVis using the same procedure as described in Section 4.2.5. To map the PIV and PLIF fields of view onto one another, the same ruler used to determine image magnification (which had uniform markings on each side) was imaged by both the PIV and PLIF cameras simultaneously. Common points on the ruler in images from both cameras were input into a custom MATLAB code which was used to align the two fields of view, as discussed in Section 4.2.5.

A.3 - Results and Discussion

A.3.1 - Instantaneous Results of Two-Line Naphthalene PLIF Thermometry

To provide context for the relative quality of the images acquired using the two cameras, completely unprocessed raw images from the PI-Max and Apogee cameras are shown in Figure A.5. An example of the result of the two-line naphthalene PLIF thermometry processing procedure described in Section A.2.4 is shown in Figure A.6. Displayed in the figure are the components of the fluorescence signal resulting from 266 nm and 283 nm excitation. The field of view for the images, as previously discussed, is approximately 0.3δ wide by 0.25δ tall. The signal resulting from 266 nm excitation appears to generally be highest near the wall and lowest away from the wall. Meanwhile, the fluorescence resulting from 283 nm excitation exhibits a high signal region that extends beyond $y/\delta = 0.1$. Based on the relationship displayed in Figure 2.19 this behavior is expected as the 283 nm signal should be higher away from the wall relative to the fluorescence from 266 nm excitation. The figure also contains an image of the corrected ratios of the two signal components (Eq. A.9) and the computed temperature field (Eq. A.10). The ratio image contains a range of ratios primarily between 0.5 and 1.5, as expected, with the highest ratio values often occurring closest to the wall. The temperature image contains a range of temperatures primarily between 100-400 K, which is again expected, with the highest temperatures close to the wall. Unfortunately, these instantaneous images are too noisy to permit further analysis of the temperature field.

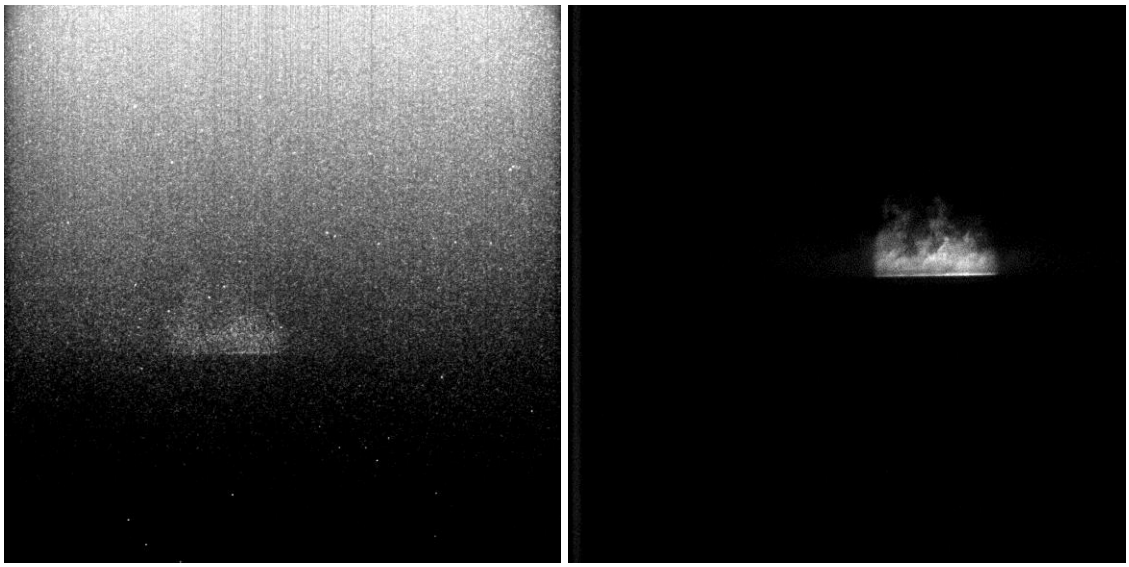

Figure A.5: Raw images of fluorescence signal from the PI-Max camera (left) and the Apogee camera (right) before any image processing was completed.

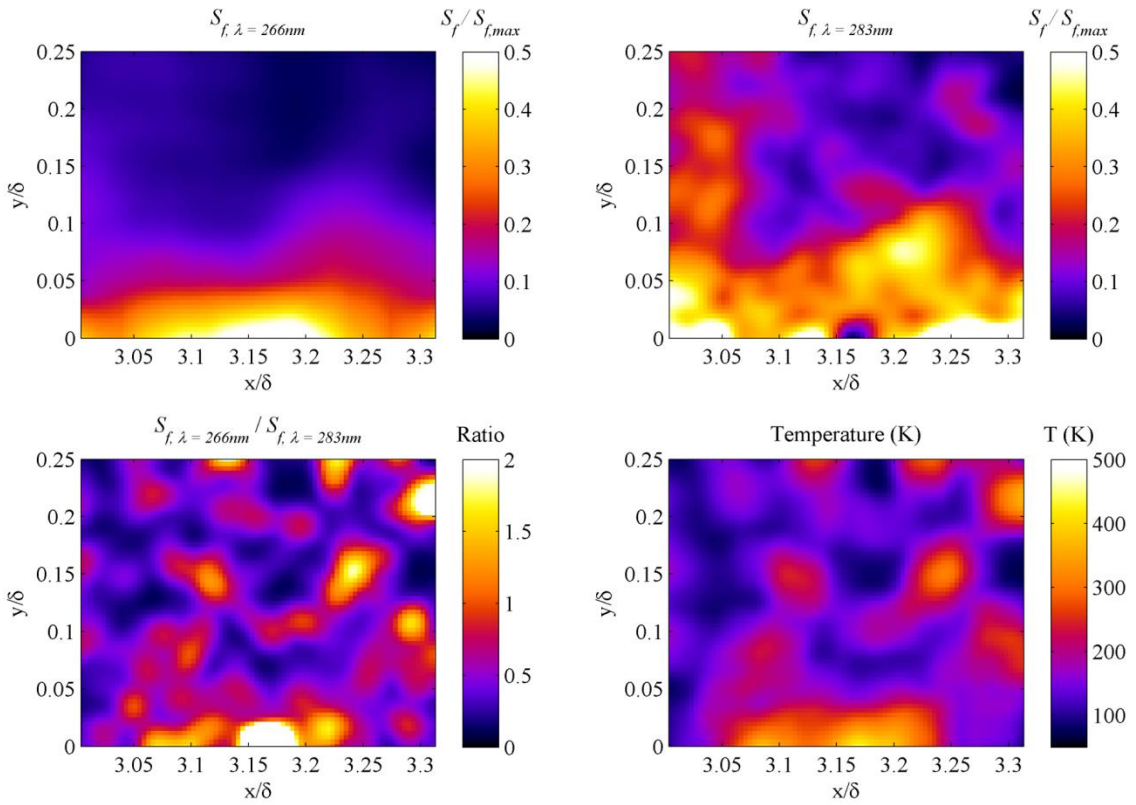

Figure A.6: Instantaneous images of fluorescence signal resulting from 266 nm and 283 nm excitation along with the ratio of the two corrected fields and the resulting instantaneous temperature field.

A.3.2 - Mean Results of Two-Line Naphthalene PLIF Thermometry

The mean temperature field collected using the two-line thermometry technique was averaged in the streamwise direction and the resulting boundary layer temperature profile is presented in Figure A.7. For comparison, other profiles are also plotted: a typical instantaneous profile from the two-line thermometry technique, a mean profile from the Crocco-Busemann method, and ± 20% error bars to capture the predicted uncertainty in the Crocco-Busemann temperature approximation. In the figure, the mean profile collected from the two-line naphthalene PLIF thermometry agrees with the mean

Crocco-Busemann temperature profile within the ± 20% error bars with a mean deviation of 12%. However, the profile has a slightly convex shape that does not appear realistic. It is possible that the profile is not reliable beyond $y/\delta = 0.15$. Furthermore, the convex shape may be a result of the accumulation of error due to the steadily decreasing PLIF signal in the boundary layer with increasing wall distance. The PI-Max camera had the noisier signal and would thus be more sensitive to a decrease in PLIF signal. It is possible that small concentrations of naphthalene were sufficiently illuminated with 266 nm light but did not produce sufficient signal when excited with 283 nm light due to this laser sheet's lower power density. This would result in the fluorescence signal from 266 nm excitation appearing artificially high, which would increase the signal ratio and result in an erroneously high temperature reading. This technique is clearly extremely sensitive to many potential sources of error, which include laser sheet corrections, calibration measurements, and sufficient local mole fraction of naphthalene, with an estimated uncertainty of ± 65% in the current work. For these reasons, it is currently recommended that the technique be limited to regions with a local naphthalene mole fraction of at least 4×10^{-5}.

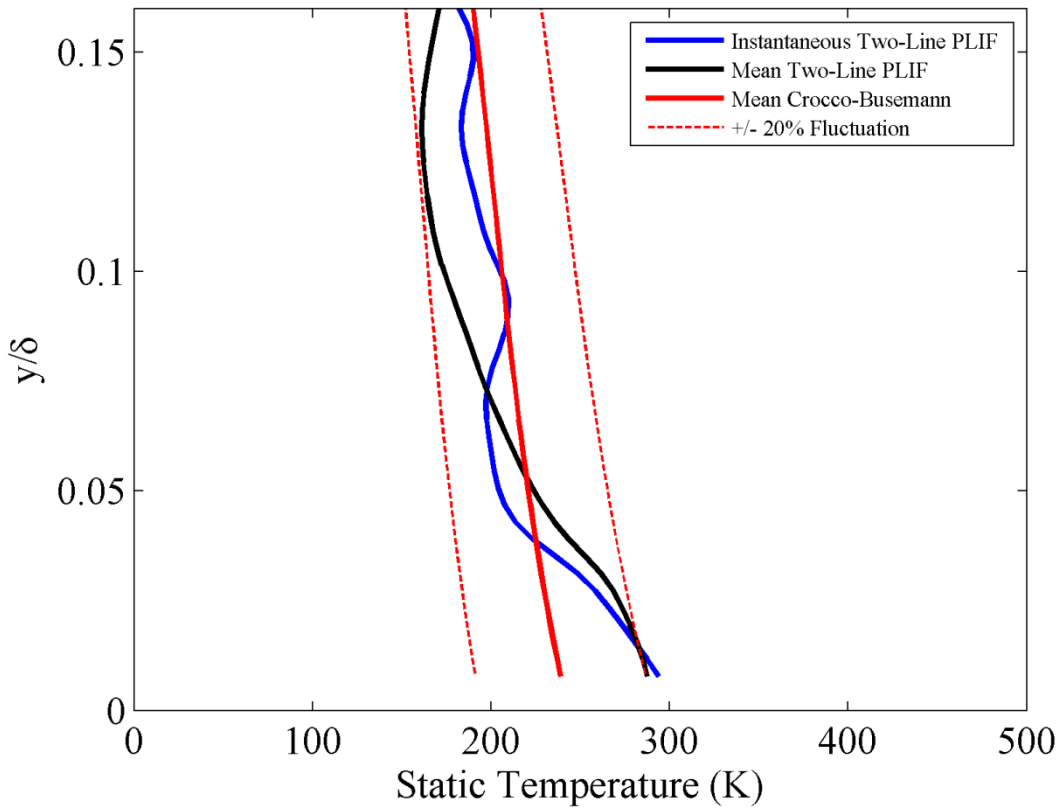

Figure A.7: Comparison of typical mean and instantaneous temperature profiles (averaged in the streamwise direction) with respect to wall distance, acquired using the two-line naphthalene PLIF thermometry technique and the mean Crocco-Busemann technique. Error bounds of ± 20% are included to indicate the expected magnitude of the temperature fluctuations, based on Eq. 3.3.

A.3.3 - Comparison of Calculated Mole Fraction to the Crocco-Busemann Method

After computing a mean temperature profile with the two-line naphthalene PLIF thermometry technique and comparing it to the Crocco-Busemann calculation, the next step was to apply the temperature profile to a naphthalene mole fraction calculation. Due to low SNR measurements, the mean temperature profile from the PLIF thermometry technique was applied uniformly in the *x*-direction, in the same manner the Crocco-Busemann-derived temperature profile has been applied to the PLIF images. Figures A.8 and A.9 present some typical instantaneous naphthalene mole fraction fields calculated using both of the temperature calculation schemes discussed in this appendix. The images in Figure A.9 are the same as those in Figure A.8 but are presented in the limited view permitted by the two-line PLIF thermometry correction. Also note that the PLIF images presented here were recorded using the PI-Max camera, as discussed in Section A.2.4. It is evident from the figures that the scale of naphthalene mole fraction calculated using each technique is effectively the same, with naphthalene vapor structures within $y/\delta < 0.2$ calculated to have a mole fraction between $4\text{-}8\times10^{-5}$. Considering that the calculated temperatures were primarily within the same range for each of the three techniques, this is to be expected.

It is difficult to make a comparison to the two-line PLIF thermometry technique with Figure A.8, thus necessitating the closer look provided by Figure A.9. In the figure it appears that the mole fraction fields calculated using the two-line PLIF technique show good agreement with the mean Crocco-Busemann scheme in both structure and mole fraction magnitude. This is to be expected considering that the temperature fields calculated using these two methods were in good agreement (within 12%).

To more quantitatively investigate the difference in calculated mole fraction through the use of the two temperature calculation schemes, Figure A.10 is presented. In this figure two different fields are presented: (1) the instantaneous difference between mole fraction fields calculated using two-line naphthalene PLIF thermometry and the Crocco-Busemann method and (2) the difference between the mean mole fraction fields calculated using two-line naphthalene PLIF thermometry and the Crocco-Busemann method. All differences are plotted in mole fraction on the same scale as the images in Figures A.8 and A.9. From the figure it is clear that the difference between the two techniques is small when plotted on the scale of the naphthalene mole fraction present in the boundary layer. Since temperature is only one contributing factor to the naphthalene mole fraction calculation, the percent difference between the calculation methods is actually lower for a naphthalene mole fraction calculation compared to the temperature difference. Comparing the Crocco-Busemann method and the two-line PLIF thermometry technique, the peak instantaneous difference in calculated naphthalene mole fraction is 10% while the mean difference between the mean fields is 5%. Furthermore, the difference between the temperature correction methods appears to be fairly uniform in space, with a slightly higher error closer to the wall. This is to be expected when considering the results plotted in Figure A.7 and considering that the two temperature corrections were applied uniformly in the x-direction.

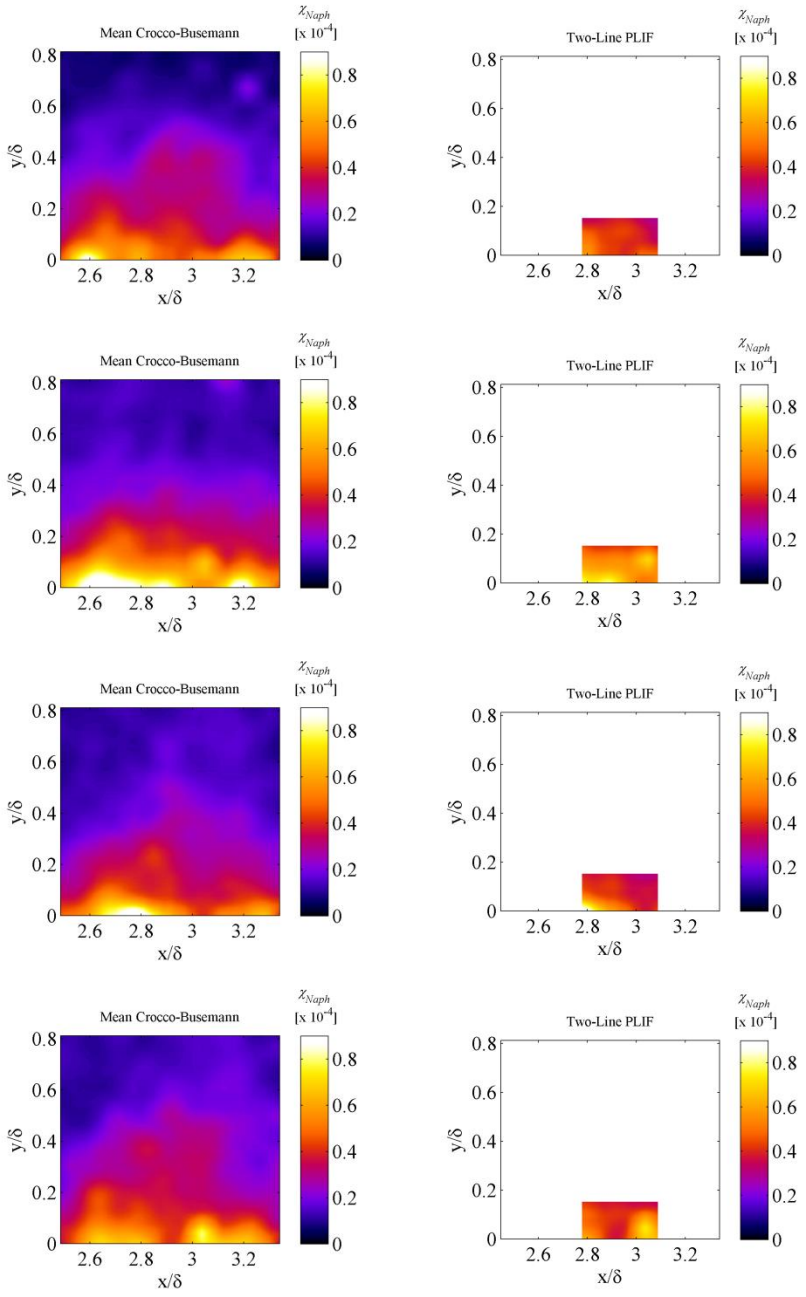

Figure A.8: Comparison of typical instantaneous naphthalene mole fraction fields acquired using the two-line naphthalene PLIF thermometry and the Crocco-Busemann temperature correction schemes.

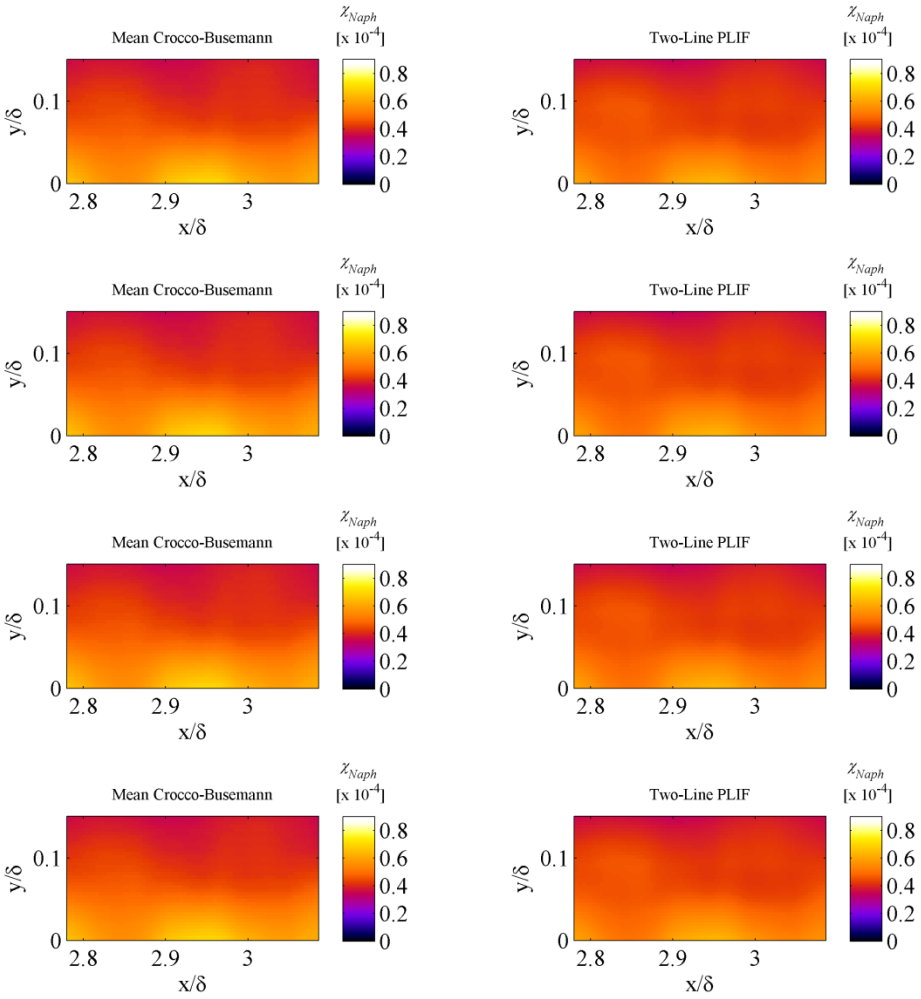

Figure A.9: Comparison of typical instantaneous naphthalene mole fraction fields acquired using the two-line naphthalene PLIF thermometry, instantaneous Crocco-Busemann, and the mean Crocco-Busemann temperature correction schemes. The images shown are the same as those presented in Figure A.8.

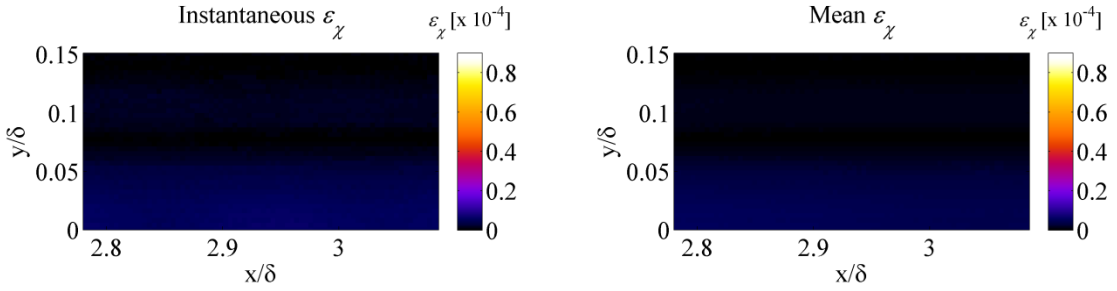

Figure A.10: Comparison of the resulting discrepancy in naphthalene mole fraction between the two different temperature correction techniques employed. A typical plot of the instantaneous discrepancy is shown on the left, while a plot of the mean discrepancy between the two calculated mole fraction fields is shown on the right.

A.4 - CONCLUSION

The largest source of error in the naphthalene PLIF measurements results from the uncertainty in the instantaneous temperature field. The mean Crocco-Busemann approximation is innaccurate, so it was desired to develop a non-intrusive temperature diagnostic based on the temperature sensitivity of naphthalene fluorescence demonstrated in Chapter 2. This technique employs 266 nm and 283 nm excitation that nearly simultaneously excites the naphthalene vapor in the flow. The fluorescence resulting from each excitation source was then imaged and the subsequent fluorescence ratio was used to calculate temperature, using the relationship illustrated in Figure 2.20.

Due to poor SNR in the images, only a mean temperature profile is presented, which showed that the measured temperatures varied primarily between 150-300 K. The temperature profile generally agreed with the mean Crocco-Busemann approximation within 12% and demonstrated the expected shape for a boundary layer temperature profile (highest value at the wall decaying to lower values away from the wall) from $0 < y/\delta < 0.15$. However, the profiles exhibited unrealistic behavior for $y/\delta > 0.2$, as the

temperature was observed to begin to increase with increasing wall distance. This is most likely the result of insufficient naphthalene PLIF signal for wall distances greater than 0.2δ and thus the technique was limited to regions with a local naphthalene mole fraction greater than 4×10^{-5}.

Mole fraction fields were then calculated using the two temperature calculation techniques and compared. It was shown that the mole fraction fields calculated using the different methods generally agreed within 10%. Furthermore, the magnitude of the mole fraction calculated from the PI-Max images was in general agreement with measurements from the Apogee camera, with χ_{Naph} calculated as approximately 1×10^{-4} in the boundary layer structures below 0.2δ. The consistency in the measurements between cameras and over multiple runs provides confidence in the robustness of the naphthalene PLIF technique.

Overall, it was demonstrated that it is possible to make temperature measurements using a two-line naphthalene PLIF thermometry technique. However, the process of making these measurements is complex, time consuming, and adds an extra degree of computational complexity to the experiment. The uncertainty in the current measurements is estimated to be ± 65% which is greater than the estimated uncertainty in the mean Crocco-Busemann method (± 20%). Additionally, due to the low power of the 283 nm laser sheet and the relatively small scale of wall distances for which naphthalene vapor was present, the application of the technique was limited to a very small field of view of approximately 0.2δ × 0.2δ. In light of these conclusions, the two-line PLIF thermometry technique provided little to no advantage over the mean and instantaneous Crocco-Busemann temperature approximation schemes in its current state. It is possible,

though, that this technique would be more advantageous if applied to a more complex flow for which a reasonable estimate of the temperature field was not readily available.

A.5 - SUGGESTED FUTURE WORK

At this point in time, the two-line naphthalene PLIF thermometry technique is still in its infancy and is definitely still a work in progress. The intent of this appendix was to demonstrate a simple application of the technique, document current progress, and verify the validity of the measurements to a certain degree through comparisons to established benchmarks.

There is much room for improvement of this diagnostic. As discussed in Section 2.5, the second excitation wavelength employed here (283 nm) was not truly optimized. It is probable that a more thorough study of the dependence on the naphthalene fluorescence temperature response to excitation wavelength will reveal a more suitable second laser line. Once this excitation wavelength is determined, a more suitable laser dye should be found, as access to 283 nm required that the dye laser be operated at the edge of the Rhodamine 590 fluorescence band. Considering the wide range of dyes commercially available, an excitation scheme with higher efficiency should be possible. A more powerful excitation source would also permit a larger imaging field of view.

Another significant hindrance to the application of the technique in the current work was the sparse selection of gated CCD cameras for image acquisition. The PI-Max camera employed in this appendix has a quantum efficiency of under 10% in the UV (compared to 57% for the Apogee camera and approximately 20% for the PixelVision camera). The most obvious solution would be the purchase of a gated camera with a higher UV quantum efficiency. However, this is easier said than done as such cameras

are extremely expensive. Another solution would be to employ colored glass filters to separate the fluorescence from two laser excitation sources. This could be achieved if the fluorescence spectra were better understood or if test cell measurements were conducted with these filters in place. Along the same lines, the temperature technique could be modified to only require excitation from 266 nm light—similar to the application by Kaiser and Long (2005)—by acquiring images of two different portions of the fluorescence band with two UV cameras and two different sets of colored glass filters. The drawback of this method is that 50% of the fluorescence signal is inherently omitted from each image. Kaiser and Long (2005) reported signal to noise ratios of just 5 for instantaneous images acquired using this technique.

Finally, it would be interesting to see this technique applied to a more complex flowfield. As alluded to earlier in this appendix, part of the reason the two-line naphthalene PLIF thermometry did not yield a noticeable improvement to the current mole fraction measurement is that there are simpler ways to approximate the boundary layer temperature field in the current work. The technique could be applied to a more complex temperature field about which little was known with no added complexity to the experimental setup or data processing procedure. In this case, a significant amount could be learned about the temperature field of the flow.

Appendix B: Uncertainty Analysis

B.1 - Quantitative PLIF Uncertainty Analysis

To quantify the uncertainty in the quantitative PLIF naphthalene mole fraction measurements, an uncertainty analysis was conducted. This analysis considered quantifiable uncertainties in the fluorescence lifetime measurements, integrated fluorescence signal measurements, PLIF signal intensity, wind tunnel test conditions, reference image conditions, laser energy, and the calculated error in the application of an estimated mean temperature profile to the instantaneous images.

The most significant source of error in the mole fraction calculation was in the use of a mean Crocco-Busemann temperature profile. This profile was based on the established velocity profile measured using a pitot probe scan by McClure (1992) and later confirmed by Beresh (1999) using the equation from White (1991):

$$T = T_{aw} - r\frac{U^2}{2c_p}, \qquad \text{B.1}$$

where T_{aw} is the adiabatic wall temperature of the air, $r = \sqrt[3]{Pr}$ is the recovery factor, Pr is the Prandtl number, U is the streamwise component of velocity, and c_p is the heat capacity of air at constant pressure. Equation B.1 assumes steady flow, adiabatic flow, zero pressure gradient, and that the transverse and cross-stream components of the velocity are negligible compared to the streamwise component. It was also assumed that c_p was a constant 1.005 kJ/kg-K.

To gain an idea of the error involved in using mean temperature profiles to correct instantaneous PLIF images, we first estimate the magnitude of the temperature fluctuations. Gross and McKenzie (1985) made temperature measurements in a Mach 2

turbulent adiabatic boundary layer and reported $\sqrt{\overline{T'^2}}/\bar{T}$ no higher than 6%. Furthermore, Smith and Smits (1993) show that the instantaneous temperature fluctuation scales as

$$\frac{T'}{\bar{T}} = -(\gamma - 1)M^2 \frac{u'}{\bar{U}} \qquad \text{B.2}$$

Evaluating this equation—based on the measured u_{rms} in the boundary layer (presented in Chapter 4), the estimated temperature profile derived from the Crocco-Busemann relationship, and the measured velocity profile—yields an estimated $\sqrt{\overline{T'^2}}/\bar{T}$ of 20% for the current work. This translates into an uncertainty of 28% in the absorption cross section calculation, a 6.1% uncertainty in the fluorescence yield calculation, and an overall uncertainty of 15% in the calculated naphthalene mole fraction. Note that the approximately 8% uncertainty in the PIV measurements (see Section B.2) corresponds to an uncertainty of 80% in temperature according to Eq. B.2, while the uncertainty in the two-line PLIF temperature measurements was approximately 65% (see Section B.3)—indicating that the mean Crocco-Busemann approximation actually results in the smallest uncertainty in mole fraction of the three temperature approximation methods available. All uncertainties were calculated using the sequential perturbation method—unless noted otherwise—as illustrated in Eq. B.3:

$$|\varepsilon_Y| = \langle abs\{Y(x) - Y(x + \varepsilon_x)\}, abs\{Y(x) - Y(x - \varepsilon_x)\}\rangle \qquad \text{B.3}$$

where ε_Y represents the uncertainty in some variable, Y, x is the variable to be perturbed, ε_x represents the known uncertainty in variable x, and the $\langle \quad \rangle$ operator represents a mean.

Another source of error related to temperature was the uncertainty in the measured wind tunnel stagnation temperature. This temperature was monitored during

each run by a thermocouple in the plenum of the facility that was connected to a digital readout at the wind tunnel control station. The readout was visually monitored during the run and a single, mean value was recorded in the run log book. A conservative estimate of the uncertainty in this measurement was determined to be ± 5 K. However, this large uncertainty in stagnation temperature only results in a 0.74% uncertainty in the final mole fraction calculation.

The wind tunnel static pressure was also not precisely measured simultaneously with each image acquisition during a run. The stagnation pressure was monitored by a pressure transducer in the plenum and this measurement was output on a digital display at the wind tunnel control station. As with the stagnation temperature measurement, this value was visually monitored during each run and a single, mean value was recorded in the run log book. The uncertainty in this measurement is estimated to be ± 17 kPa which translates to an uncertainty of just ± 32 Pa in the calculated static pressure. This uncertainty resulted in an error < 0.01% in the calculated naphthalene mole fraction. This uncertainty analysis did not consider instantaneous fluctuations in the pressure field, but considering the small uncertainty resulting from the measurement of stagnation pressure, it is likely that the impact of these fluctuations is minimal.

The uncertainty in the reference test cell temperature was also considered. A measurement of the temperature in the cell was not made and the cell was always assumed to be at a temperature of 295 K. An uncertainty of ± 2 K was estimated for this assumption, which results in a 0.21% uncertainty in the final mole fraction calculation. Similarly, the error in the pressure measurement in the reference test cell was ± 0.05 torr (± 6.7 Pa) which translated to an error < 0.01% in the calculated naphthalene mole

fraction. For this reason uncertainty in the temperature and pressure measurements in the flowing test cell experiments were considered negligibly small in this analysis.

A third component of the uncertainty stemming from the test cell measurements was the uncertainty in the estimated naphthalene mole fraction. This value was assumed to be the mole fraction of naphthalene at the saturation condition for the test cell temperature and pressure ($\chi_{sat}(T) = P_{sat}(T)/P$). The saturation pressure of naphthalene was calculated using the work of De Kruif et al. (1981). In their work, De Kruif et al. (1981) quote a maximum uncertainty of ± 6%, so that value is adopted here. This results in a direct 6% contribution to the error in calculated mole fraction, and is therefore one of the larger components of the total error.

Two other significant contributions to the total uncertainty arose from the uncertainty in the flowing test cell measurements presented in Chapter 2. These measurements were necessary to compute the absorption cross section and fluorescence yield of naphthalene with respect to varying pressure and temperature—required inputs in Eq. 1.10 which was used to calculate naphthalene mole fraction. Absorption cross section was calculated using measurements of integrated fluorescence signal in the flowing test cell. An uncertainty of 9.3% was calculated for these measurements, which was twice the mean standard deviation of measurements recorded at the same temperature. This 9.3% uncertainty directly translates to a 9.3% uncertainty in the mole fraction calculation. Fluorescence yield was calculated using measurements of naphthalene fluorescence lifetime in the flowing test cell experiments. These measurements had an uncertainty of ± 0.5 ns, or approximately 4%. This again directly results in a 4% uncertainty in the calculation of naphthalene mole fraction.

Measurements of laser energy were collected prior to each run to aid in the correction of the fluorescence signal. This enabled a correction to the overall signal intensity in Eq. 1.10 if the laser energy during a run was different than the energy when the reference cell measurement was made. Measurements were made with a power meter, and due to random fluctuations in laser energy an uncertainty of ± 1.5 mJ/pulse is estimated. Considering that the laser energy was approximately 42 mJ/pulse for most runs and calibration measurements, this results in an error of 3.6% in the naphthalene mole fraction calculation. This uncertainty was considered twice as a laser power measurement was made for both the reference cell images and the wind tunnel images.

The final factor considered in this error analysis was the uncertainty in the value of any given pixel in an image resulting from camera noise. This was measured by calculating the standard deviation of a uniform region of naphthalene PLIF signal in a sample image from a boundary layer experiment. The mean background subtracted signal level was 159 counts, with a standard deviation of 3.67 counts. For a 95% confidence interval, twice this standard deviation results in an error of 4.6%. This uncertainty was also considered twice to account for both the reference cell images and the wind tunnel images.

Upon calculating the contributions of each component of the uncertainty in the naphthalene PLIF mole fraction calculation, the various components were summed using a Euclidean norm, defined in Eq. B.4:

$$|\varepsilon_{total}| = \sum_{i=1}^{n} \sqrt{\varepsilon_1^2 + \varepsilon_2^2 + \cdots + \varepsilon_n^2} \qquad \text{B.4}$$

where ε_{total} is the cumulative uncertainty and ε_i represent the individual constituents of the uncertainty. Using this method, a total uncertainty in the naphthalene mole fraction calculation is estimated to be 20.5%.

The various sources of uncertainty discussed in this section are summarized in Table B.1 below, where $\varepsilon_{\chi_{naph},i}$ represents the contribution of each component to the naphthalene mole fraction uncertainty.

Table B.1**:** Summary of uncertainty analysis for the naphthalene PLIF mole fraction calculation.

Uncertainty Component	Experimental ε	$\varepsilon_{\chi_{naph},i}$
Wind Tunnel Static Temperature Fluctuations	20%	14.5%
Wind Tunnel Stagnation Temperature	1.4%	0.74%
Wind Tunnel Stagnation Pressure	0.70%	< 0.01%
Reference Cell Temperature	0.68%	0.21%
Reference Cell Pressure	< 0.01%	< 0.01%
Reference Cell Naphthalene Mole Fraction	6.0%	6.0%
Absorption Cross Section Measurement	9.3%	9.3%
Fluorescence Yield Measurement	4.0%	4.0%
Laser Energy*	3.6%	3.6%
Camera Noise*	4.6%	4.6%
Total Uncertainty		**20.5%**

* Counted twice in the Euclidean norm to account for both reference cell and wind tunnel measurements

B.2 - PIV UNCERTAINTY ANALYSIS

The precise quantification of uncertainty for a given PIV system can be elusive and the topic of PIV uncertainty in general is poorly understood. Most analyses of this type generally focus on the quantification of several components that contribute to the total uncertainty in the form of uncertainties in the measurement of particle displacement, Δx, and the known temporal delay between laser pulses, Δt. Potential sources of uncertainty in Δx include particle lag, image calibration errors, insufficient sample size for the convergence of statistics, and peak or pixel locking. Uncertainty in Δt is generally the result of jitter in the timing electronics or voltage fluctuations in the laser.

Particle lag was addressed in Section 4.2.3 but the discussion is repeated here. The assessment of particle lag is based on measurements presented in a Ph.D. dissertation by Hou (2003), who studied particle seeding in the wind tunnel used for the present work. Hou (2003) measured the nominal TiO_2 particle diameter to be approximately 0.26 μm and calculated the particle response time to be 2.9 μs. This results in a conservative estimate of the particle Stokes number of 0.11 for the Mach 5 boundary layer conditions, satisfying the guideline established by Samimy and Lele (1991) of a particle Stokes number < 0.5 for reliable flow tracking. For this reason, uncertainty due to particle lag is considered negligible for the current work.

Potential errors in the calibration of the acquired images from pixels to mm was discussed in detail by Beresh (1999). The task of converting the field of view of the images to some meaningful length scale was completed by imaging a ruler in the wind tunnel test section. Uncertainty arising from factors such as the shot-to-shot variation of the image field of view, misalignment of the ruler with the imaging plane, and the uncertainty in the pixel selection corresponding with a given ruler marking were summed

using a Euclidean norm to yield a conservative estimate of the uncertainty in the determination of the imaging field of view of 1.05%.

Convergence errors were measured using two different methods. First, the convergence of the mean and r.m.s. streamwise velocity components was investigated by computing the standard deviation, σ, of the mean and r.m.s. profiles computed during the eleven PIV runs conducted during the current work. This plot is presented in Figure B.1. As seen in the figure, the standard deviation of both the mean and r.m.s. peaks near the wall, similar to what was observed in a convergence analysis performed by Beresh (1999). The peak standard deviation of the mean velocity is approximately 7% of the mean velocity in the boundary layer at the wall, while the standard deviation of the r.m.s. is slightly lower. This is likely the result of the large errors near the wall as previously discussed (insufficient resolution near the wall, laser scatter, low particle seeding near the wall, and the averaging of particle displacements over a finite correlation window). Away from the wall, however, the standard deviation of the mean velocity appears to level off below 20 m/s while the standard deviation of the r.m.s. drops to around 5 m/s. This mean velocity standard deviation correlates to an uncertainty in the PIV measurements of roughly 7% for a 95% confidence interval. With an increased number of wind tunnel runs to include in the ensemble average this number would likely decrease, as illustrated by Beresh (1999).

Convergence was also investigated by calculating the residual of the mean and r.m.s. velocity profiles with respect to increasing sample size, N. Data were provided by a single wind tunnel run in which 270 PIV image pairs were collected. This was the largest number of image pairs that was acquired during a wind tunnel run with the PIV cameras operating at their maximum frame rate of 5 Hz. Images were not generally acquired at

this high frame rate so that the image pairs could be synced with the PLIF cameras. The residuals, R, plotted in Figure B.2 were calculated using the following formula:

$$R_{x,i} = \frac{\overline{x_i - x_{i-1}}}{\overline{x_{i,\infty}}} \qquad \text{B.5}$$

As seen in Figure B.2, convergence is noisy but also fairly rapid. By the end of the run (N = 270) the mean and r.m.s. appear to have converged within 0.1%. However, the majority of the PIV results presented were collected during runs where 30-50 image pairs were acquired owing to the relatively slow frame rate of the PLIF cameras. In Figure B.2 it seems that the mean and r.m.s. of the streamwise velocity have both converged within 1% by N = 30.

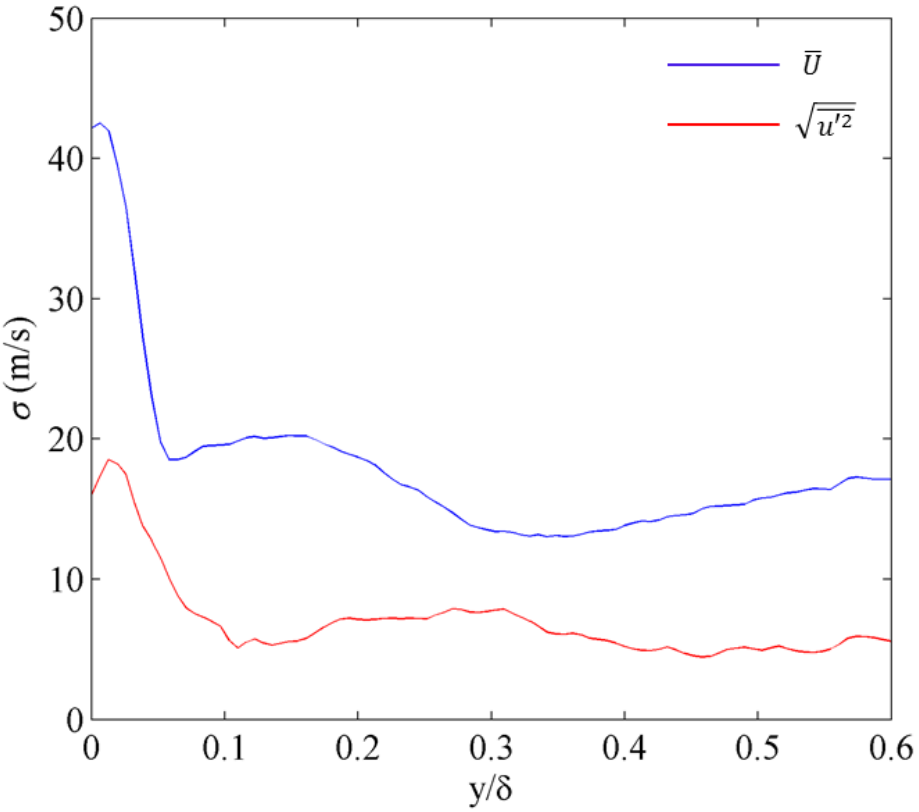

Figure B.1: Standard deviation of the streamwise velocity and r.m.s. profiles for the eleven PIV runs conducted in the current work with respect to wall-normal distance.

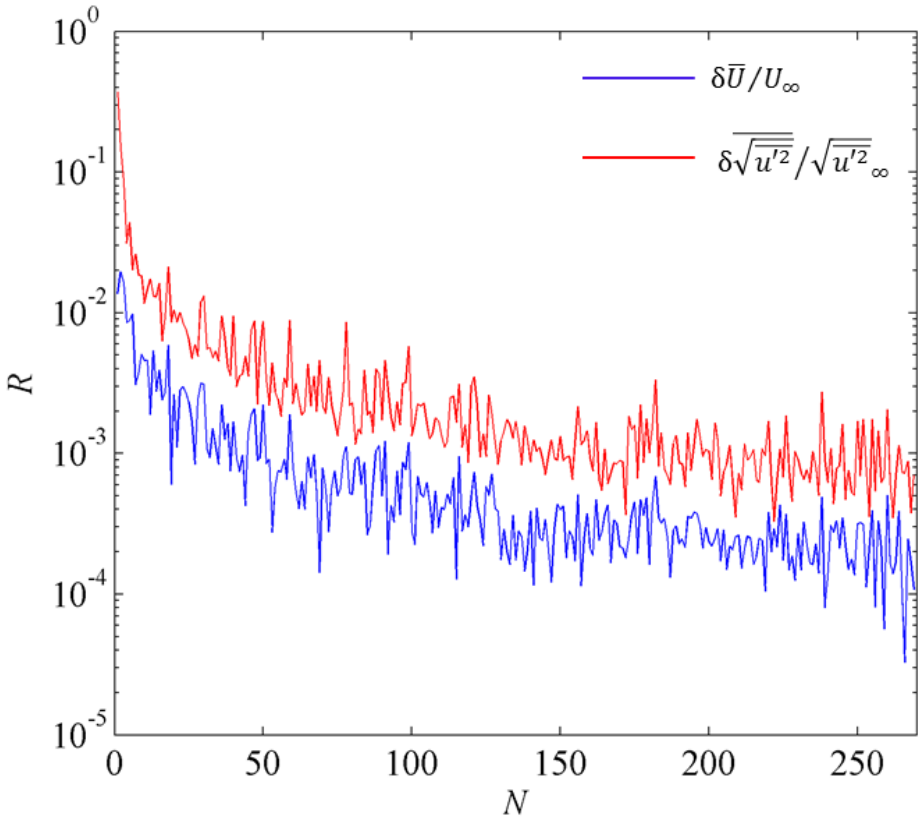

Figure B.2: Convergence of the mean streamwise velocity and r.m.s. profiles from PIV in the current work with respect to the number of image pairs employed in the ensemble average.

The presence of peak locking was investigated by plotting the probability density function of the PIV image pixel displacements calculated by DaVis, presented in Figure B.3. The resolution of the PDF is approximately 0.02 pixels. Observing the figure, there does not appear to be any preferential grouping of calculated pixel displacements around integer pixel values and the curve is effectively smooth. Therefore, this potential contribution to the PIV uncertainty has been deemed negligibly small in the current analysis.

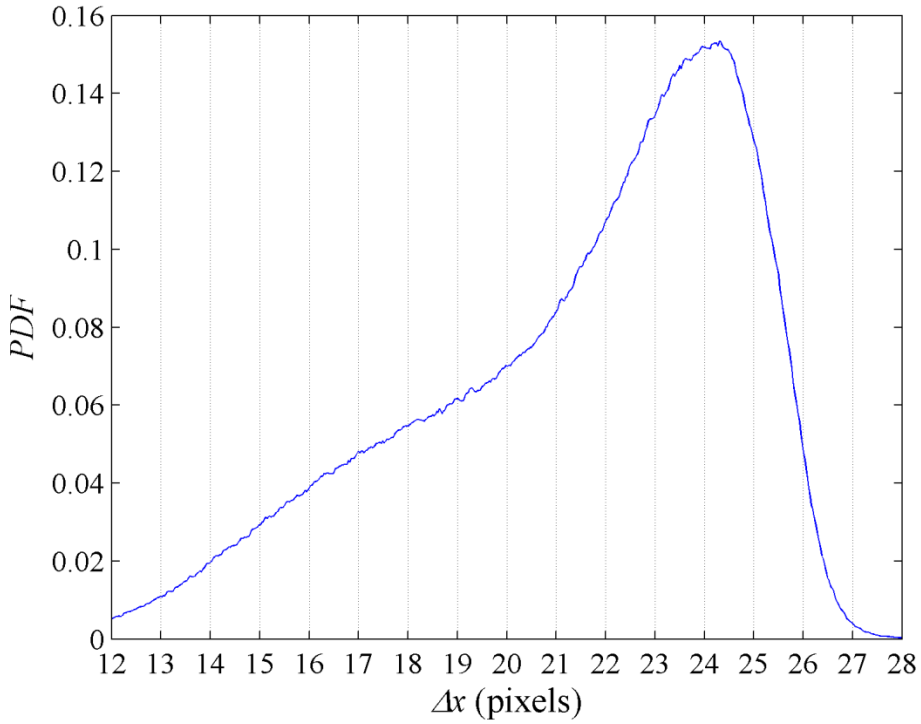

Figure B.3: PDF plot of the streamwise PIV pixel displacements.

The sum of the uncertainties in the calculation of Δx was determined using a Euclidean norm and was determined to be 7.15%.

Lastly, the uncertainty in the temporal shift between the two laser pulses was measured using a photodiode and an oscilloscope. The oscilloscope monitored the output of the photodiode, which was oriented in a way to capture the diffuse reflection of the PIV laser pulses off of a solid surface. The measurement of the displacement between the peaks of the two pulses was recorded by the oscilloscope and was observed to vary by ± 5 ns. The main source of this uncertainty was the irregular temporal behavior of the two nearly-simultaneous pulses from the PIV-400 laser. Both pulses were needed to achieve the maximum possible energy from the dye laser and the delay between the pulses was set to 0.0 ns. However, the temporal modes exhibited by the resulting pair of laser pulses

were sometimes erratic, which resulted in a ± 10 ns variation in the delay between the peak PIV-400 power and the GCR-150 pulse. Upon considering the pulse separation of 300 ns, this results in an uncertainty of 3.33%.

Upon computing all of the discussed component uncertainties, the total uncertainty, δu_{total}, was assumed to propagate with respect to the estimated uncertainties in Δx and Δt by the following formulation:

$$|\delta u_{total}| = \sqrt{\left(\frac{\delta x}{\Delta t}\right)^2 + \left(\frac{\delta t\, \Delta x}{\Delta t^2}\right)^2} \qquad \text{B.6}$$

where δx and δt represent the estimated uncertainties in Δx and Δt, respectively. From Eq. B.6, the total uncertainty in calculated streamwise velocity from PIV in the current work is estimated to be 51 m/s or 7.9% of the mean velocity measured in the boundary layer. The results of this uncertainty analysis are summarized in Table B.2.

Table B.2**:** Summary of uncertainty analysis for the PIV measurements.

Uncertainty Component	δ
Field of View Calibration	1.05%
Particle Lag	< 0.1%
Convergence Over Multiple Runs	7.15%
Single Run Sample Size Convergence	1.0%
Peak Locking	< 0.1%
Temporal Delay Between Laser Pulses	3.33%
Total Uncertainty	**7.89%**

B.3 - TWO-LINE NAPHTHALENE PLIF THERMOMETRY UNCERTAINTY ANALYSIS

An uncertainty analysis was also conducted to quantify the uncertainty in the two-line naphthalene PLIF thermometry technique. This analysis considered quantifiable uncertainties in the fluorescence signal ratio measurements, PLIF signal noise, reference image noise, and the uncertainty in the instantaneous laser energy.

Unlike the analysis of the mole fraction uncertainty, factors such as wind tunnel and reference cell temperature, pressure, and naphthalene mole fraction were not factors in the two-line PLIF thermometry uncertainty since these terms cancel out of Eq. 1.11.

The first contributor to the total uncertainty that was considered was the uncertainty in the flowing test cell measurements presented in Chapter 2—specifically the data presented in Figure 2.20. An uncertainty of 9.2% was calculated for these measurements, which was twice the mean standard deviation of measurements recorded at the same temperature. This 9.2% uncertainty translates to a 17% uncertainty in the temperature calculation. As in Section B.1, all uncertainties were calculated using the sequential perturbation method (Eq. B.3).

Measurements of laser energy were collected prior to each run to aid in the correction of the fluorescence signal. This enabled a correction to the overall signal intensity that manifested as adjustments to the calibration factors in Eqs. A.8 and A.9. The uncertainty of the laser energy in the 266 nm beam was the same as quoted in Section B.1: ± 1.5 mJ/pulse or 3.6%. The 283 nm beam was quite erratic with large fluctuations in laser energy relative to the magnitude of the pulse energy. These fluctuations were estimated to be ± 0.5 mJ/pulse or 29% of the average 1.7 mJ/pulse of 283 nm excitation available for each run. The behavior of the 283 nm laser was a direct result of damage to the second harmonic generation crystal in the PIV-400 laser that

resulted in extreme fluctuations in the dye laser pumping power. The uncertainty in the instantaneous laser energy from 266 nm and 283 nm excitation corresponded to uncertainties of 3.1% and 24%, respectively. This uncertainty was considered twice to account for both the reference cell images and the wind tunnel images.

A significant factor in this error analysis was the uncertainty in the value of any given pixel in an image resulting from camera noise. This was measured by calculating the standard deviation of a uniform region of naphthalene PLIF signal in a sample image from a boundary layer experiment and was repeated for both the PI-Max and Apogee cameras. The mean background subtracted signal level due to 266 nm excitation for the Apogee camera was 136 counts, with a standard deviation of 4.1 counts. For a 95% confidence interval, twice this standard deviation results in an uncertainty of 6.0%. The mean background subtracted signal level due to 283 nm excitation for the Apogee camera was 38 counts, with a standard deviation of 1.0 counts, which results in an uncertainty of 5.1%. Furthermore, the mean background subtracted signal level due to 266 nm excitation for the PI-Max camera was 656 counts, with a standard deviation of 46 counts, which results in an uncertainty of 14%. These measurements result in uncertainty in the calibration images and in the actual boundary layer images. Noise in the Apogee camera 266 nm test cell image, 283 nm test cell image, and boundary layer images resulted in uncertainties of 15%, 4.5%, and 13% to the final temperature calculation, respectively. Noise in the PI-Max camera 266 nm test cell image and boundary layer images both resulted in uncertainties of 33% to the final temperature calculation.

Upon calculating the contributions of each component of the uncertainty in the two-line naphthalene PLIF temperature calculation, the various components were summed using a Euclidean norm, defined in Eq. B.4. Using this method, a total

uncertainty in the two-line naphthalene PLIF temperature calculation is estimated to be 64.6%.

The various sources of uncertainty discussed in this section are summarized in Table B.3 below, where $\varepsilon_{T,i}$ represents the contribution of each component to the two-line naphthalene PLIF temperature uncertainty.

Table B.3**:** Summary of uncertainty analysis for the two-line naphthalene PLIF temperature calculation.

Uncertainty Component	Experimental ε	$\varepsilon_{T,i}$
Fluorescence Signal Ratio Measurement	9.2%	17.6%
266 nm Laser Energy*	3.6%	3.1%
283 nm Laser Energy*	29%	24%
Apogee Camera Noise - 266 nm Test Cell	6.0%	15%
Apogee Camera Noise - 283 nm Test Cell	5.1%	4.5%
Apogee Camera Noise - Boundary Layer	5.5%	13%
PI-Max Camera Noise - 266 nm Test Cell	14%	33%
PI-Max Camera Noise - Boundary Layer	14%	33%
Total Uncertainty		**64.6%**

* Counted twice in the Euclidean norm to account for both reference cell and wind tunnel measurements

It is clear from Table B.3 that the most significant sources of uncertainty are the result of noise in the PI-Max camera, uncertainty in the 283 nm laser energy, and the uncertainty in the fluorescence signal ratio measurement. It should be possible to significantly reduce the 64.6% uncertainty in the two-line naphthalene PLIF thermometry technique with some of the changes addressed in Section 5.5. For example, using a better

suited camera than the PI-Max could conceivable decrease the noise in the image to a range comparable to the Apogee camera, say 6%. Furthermore, improvements to the 283 nm excitation source so that its uncertainty is comparable to the 266 nm laser should be possible. Lastly, a more rigorous study of the fluorescence of naphthalene with respect to excitation wavelength could conceivably decrease the uncertainty in the fluorescence signal ratio to approximately 5% (on par with the fluorescence lifetime measurements). With these improvements, the technique could yield a much more serviceable 29% uncertainty. This would still not serve as an improvement to the 20% estimated uncertainty from employing a mean Crocco-Busemann temperature correction to the mole fraction calculation, however, a technique that can non-intrusively measure temperature with 29% uncertainty may be useful in more complicated flows where a sound estimate of the temperature field is not readily available.

Appendix C: Naphthalene Models

C.1 - Naphthalene

Crystalline/powder-form 99% naphthalene was purchased from Acros Organics for use in the current work. Naphthalene has a relatively low melting point at 353 K and this low melting point allows naphthalene crystals to be easily melted down and used for making molds of various shapes and sizes. The vapor pressure of naphthalene is approximately 12 Pa at 300 K, but increases by over two orders of magnitude to 1.4 kPa at 360 K (De Kruif et al., 1981). When working with naphthalene, naphthalene vapor will always be present in the laboratory environment and the material safety data sheet (MSDS) for naphthalene recommends wearing gloves, goggles, a dust respirator, and a lab coat. Although naphthalene is stable (given a zero out of four on the reactivity criterion) it is flammable and can ignite when moderately heated.

As discussed in Section 1.1.4, naphthalene possesses a wide and essentially continuous band of electronic energy levels in the UV, absorbing electromagnetic radiation from the vacuum UV to approximately 310 nm (Du et al., 1998). Excitation of naphthalene with a UV light source results in broadband fluorescence between 300 and 400 nm (Du et al., 1998). This property of naphthalene makes it a candidate for PLIF imaging, as high-intensity light sources such as frequency-quadrupled Nd:YAG lasers, KrF lasers, and various dye laser configurations can be used to excite the molecule.

C.2 - Boundary Layer Naphthalene Floor Insert

In the Mach 5 boundary layer experiments, the naphthalene vapor was introduced into the flow by allowing a solid block of naphthalene to sublimate. This is the same naphthalene insert geometry employed by both Lochman (2010) and Buxton et al. (2012) and a dimensional schematic of the model from Lochman (2010) is given in Figure C.1

below. The insert, which was mounted flush with the floor of the test section, had dimensions of 105 mm in the streamwise direction and 57 mm in the spanwise direction. The model also had a 6.35 mm lip at the bottom of the mold cavity to secure the naphthalene insert and prevent the model from being sucked into the wind tunnel during runs. A fused silica window was also integrated into the model assembly to pass the 266 nm laser sheet and reduce reflections off of the wind tunnel floor. The fused silica window had dimensions of 264.8 mm in the streamwise direction and 57 mm in the spanwise direction. The window was located 23.5 mm downstream of the trailing edge of the naphthalene insert, thus limiting optical access to distances 1.22δ downstream of the naphthalene source in the boundary layer. There was also a capability to install up to 15 thermocouples in an equally spaced 5 by 3 array inside the naphthalene insert. However, given that this work was focused on the development of the quantitative PLIF imaging technique, the heat transfer through the naphthalene insert was not investigated.

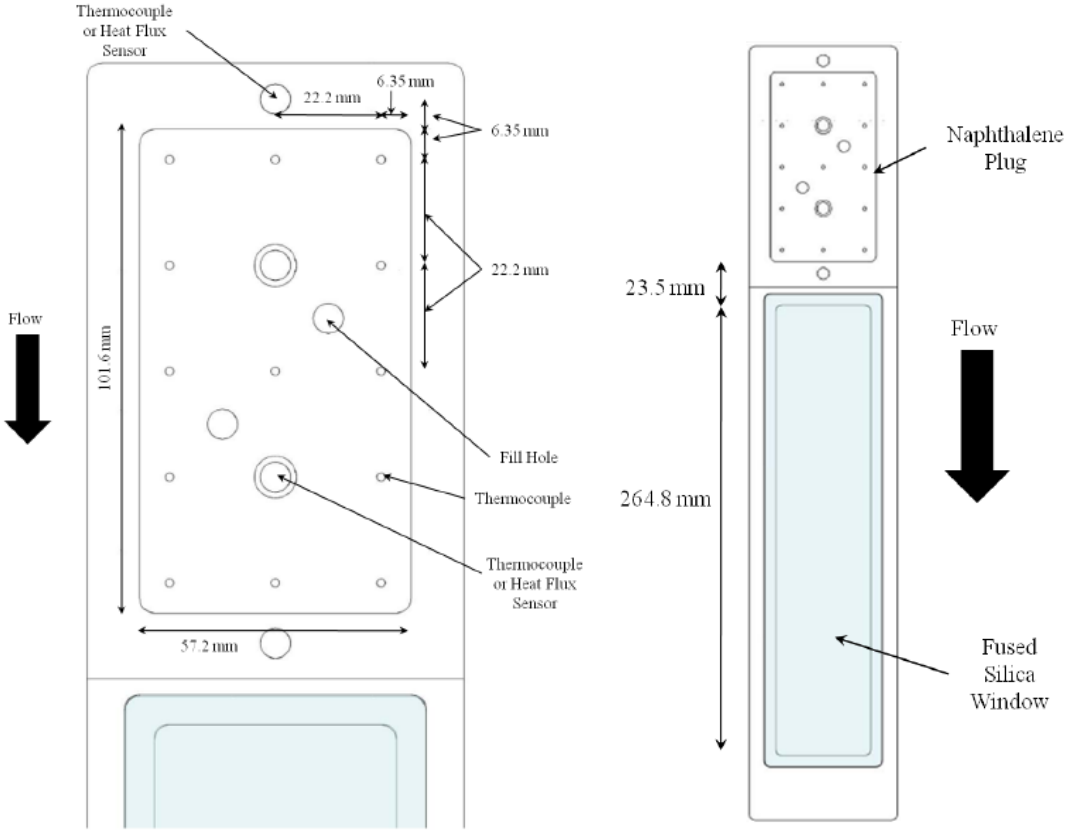

Figure C.1: Dimensions of the naphthalene floor insert (Lochman, 2010).

The solid block of naphthalene was formed by pouring liquid naphthalene into the insert through one of the two "fill holes" in the bottom of the mold, as indicated in Figure C.1. As the fused silica window was integrated into the mold assembly, it was important to first remove the fused silica window from the assembly before beginning the molding process to prevent damage to the window. Next, any naphthalene still remaining in the mold was carefully removed. An aluminum molding plate was then bolted to the top of the mold assembly to close the mold cavity and provide a smooth, flat surface on the top of the naphthalene insert. It was then necessary to flip over the naphthalene mold geometry so that the fill holes (exterior side) were facing up and the interior (test section)

side of the assembly was facing down. Wearing proper protective equipment, approximately 250 mL of naphthalene crystals were then placed in a beaker under a fume hood. This beaker would then be heated on a hot plate until the naphthalene had been completely melted. A funnel was then placed in the fill hole and the naphthalene was poured through the funnel and into the mold. To ensure that the mold was full, naphthalene was poured until the liquid was overflowing out of the top of the mold. The mold assembly would then be allowed to cool at room temperature for approximately three hours to allow the naphthalene to solidify. Next, the aluminum molding plate covering the top of the mold was detached and any excess naphthalene was carefully removed to ensure a smooth, flat test section surface. It was also verified that no air pockets were formed in the naphthalene insert during the molding process. After reinstalling the fused silica window in the assembly, the model was ready for testing and was mounted in the floor of the Mach 5 wind tunnel test section. A completed naphthalene insert model can be seen mounted in the Mach 5 test section in Figure C.2.

The sublimation rate of naphthalene at standard conditions is slow and no noticeable mass was lost if the insert was left in the test section for hours without flow. Only a small amount of ablation (a fraction of a millimeter) was observed over the course of a one minute wind tunnel run. Additionally, the placement of the naphthalene insert permitted optical access to the test section just downstream of the trailing edge of the insert.

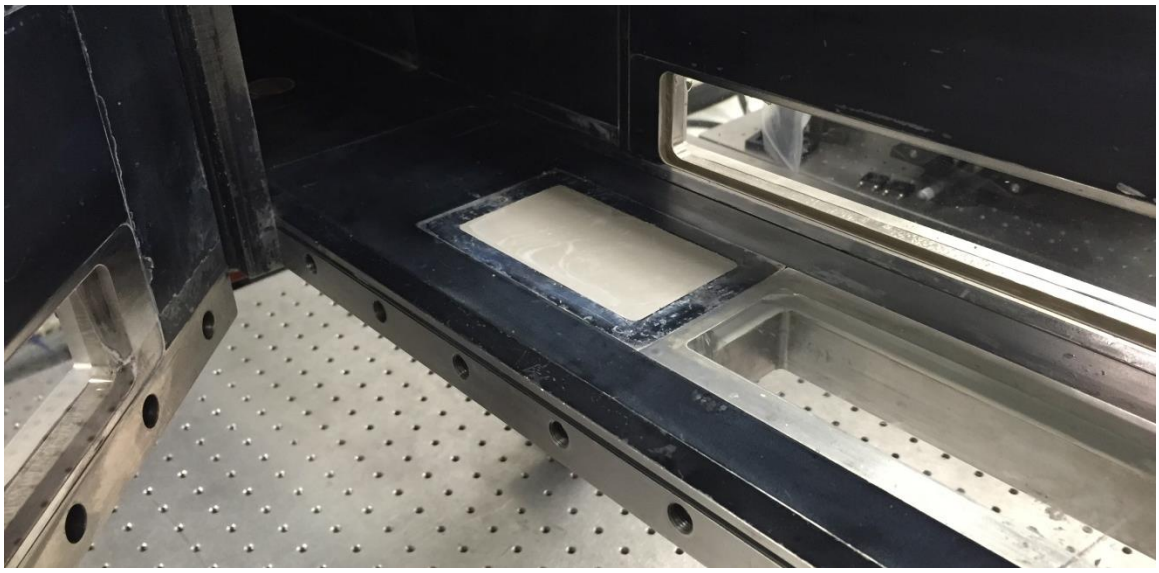

Figure C.2: Photograph of the naphthalene floor insert installed in the Mach 5 test section.

C.3 - NASA ORION MULTI-PURPOSE CREW VEHICLE MODEL

The Orion Multi-Purpose Crew Vehicle (MPCV) will carry a crew of four to and from space with missions to asteroids, Lagrange points, the moon, and Mars under consideration (NASA, 2005). An artist's conception of the Orion MPCV can be seen in Figure C.3. The model geometry for the capsule flowfield investigated in Chapter 5 consisted of a scaled Orion MPCV capsule model with smooth outer mold lines. The dimensions of the model were based on previous NASA research (Buck et al., 2008). The outer mold lines of the capsule model and the corresponding dimensions selected for the current work are given in Figure C.4 and Table C.1, respectively, with a comparison to the dimensions used in the work by Buck et al. (2008).

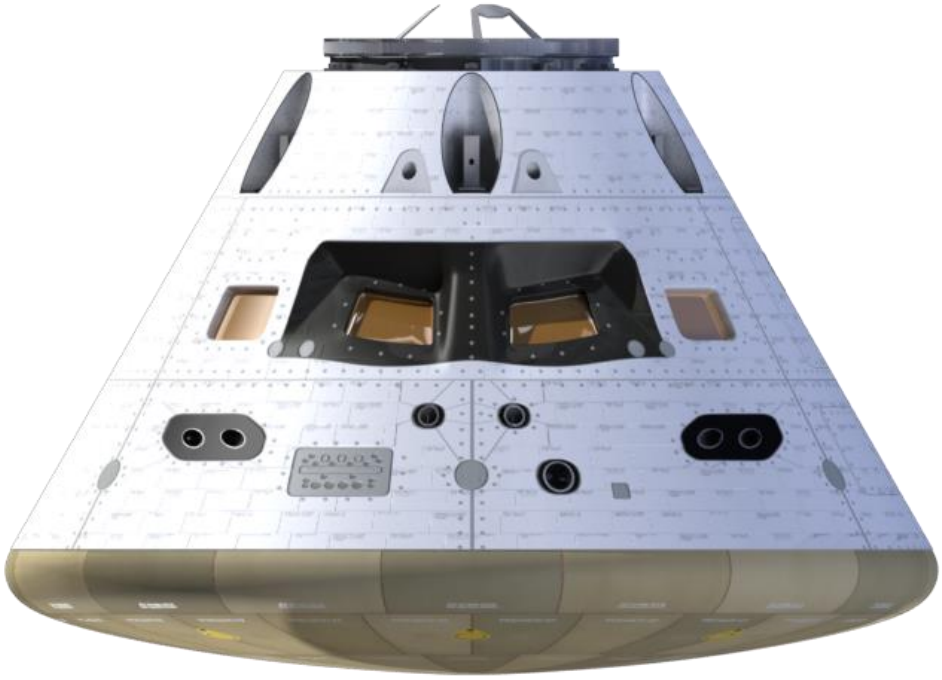

Figure C.3: Artist's conception of the Orion MPCV capsule (NASA, 2015).

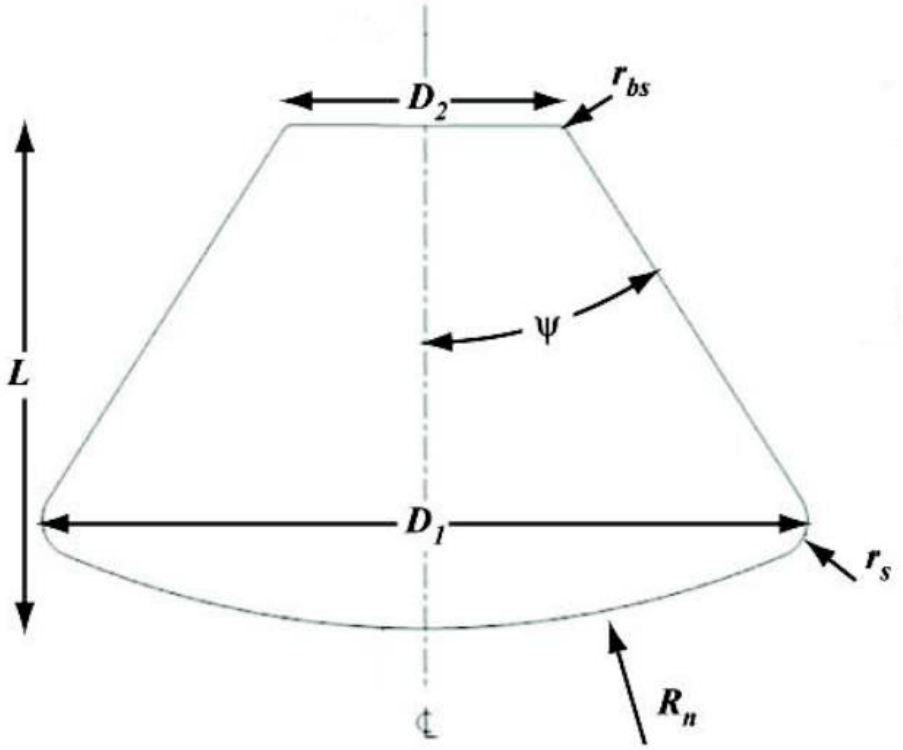

Figure C.4: Orion MPCV capsule model outer mold lines.

Table C.1**:** Outer mold line dimensions of Orion MPCV capsule model in current work compared to the work of Buck et al. (2008). Nomenclature is identified in Figure C.4.

Study	D_1 (mm)	D_2 (mm)	R_n (mm)	r_s (mm)	r_{bs} (mm)	L (mm)	Ψ (deg)
Buck et al. (2008)	127	45.9	152	6.35	6.35	83.5	32.5
Current Work	50.8	18.3	61.0	2.54	2.54	33.4	32.5

The model consisted of an aluminum capsule backshell, a separate heat shield piece, and a wire "mesh" to give the solid naphthalene heat shield structural integrity (Figure C.5(a)). The mesh was mounted to sixteen 6-32 screws that protruded approximately 4 mm from the aluminum surface. The heads of the screws were at least

2 mm below the surface of the heat shield. Thin-gauge wire was then wrapped around the bolts, creating a mesh. Without this mesh, the naphthalene heat shield would not adhere to the aluminum model and would not remain attached during wind tunnel runs. However, even with the mesh, naphthalene would still break apart from the model during wind tunnel startup for some tests. Images from these wind tunnel runs are not presented here, but for this technique to be successful it is important to have a relatively quick wind tunnel startup or to place a protective covering on the model until the freestream flow has been fully established. The aluminum model was scaled to have a 50 mm maximum heat shield diameter and was attached to a 12.7 mm diameter stainless steel sting. The sting was mounted to a strut that was fixed to the wind tunnel floor. Four different strut configurations were used in this experimental campaign, allowing four different angles of attack (0°, 12°, 24°, and 52°) to be tested. Schlieren imaging was conducted in a different experimental campaign than the PLIF and used a solid aluminum heat shield rather than a naphthalene one.

The process for creating the naphthalene heat shield involved placing the capsule model in a mold and pouring heated liquid naphthalene through a hole in the aftbody or apex of the model. The cylindrical aluminum mold had two parts, shown in Figure C.5(b). The bottom portion was a 200 mm diameter, 50 mm tall cylinder with a hemispherical bowl having dimensions of a scaled heat shield geometry machined into its top surface and eight tapped bolt holes in a circular pattern for securing the two halves of the mold. It was imperative that the mold be extremely smooth prior to pouring. Over time, scratches and chips accumulated on the surface of the mold, causing naphthalene to stick to the mold rather than the model. For this reason, the mold would occasionally be polished to remove any imperfections. The top portion of the mold was a 200 mm

diameter, 25 mm tall cylinder with a centered cutout contoured to fit the backshell model and eight thru-holes for bolts. To prepare the mold, the model was rested on top of the bottom half of the mold. The top half of the mold was then placed over the model and the two halves of the mold were secured with bolts. The complete mold assembly can be seen in Figure C.5(c). This assembly allowed the aft portion of the MPCV model to protrude from the top of the mold, exposing the hole drilled through the center of the aluminum model to be used for pouring liquid naphthalene into the mold. Wearing proper protective equipment, approximately 150 mL of naphthalene crystals were then placed in a beaker under a fume hood. This beaker would then be heated on a hot plate until the naphthalene had been completely melted. A funnel was then placed in the hole for pouring liquid naphthalene and the naphthalene was poured into the mold. To ensure that the mold was full, naphthalene was poured until the liquid was overflowing out of the top of the mold. The mold assembly would then be allowed to cool at room temperature for approximately three hours to allow the naphthalene to solidify. Next, the mold would be disassembled and any excess naphthalene on the capsule backshell would be carefully removed to ensure that the naphthalene-aluminum junction was smooth. It was also verified that no air pockets were formed in the naphthalene during the molding process. At this point the model was ready for testing and was mounted in the Mach 5 wind tunnel test section. During wind tunnel shutdown, the remaining naphthalene on the model was destroyed, preventing images of the model from being captured post-run. A new heat shield was molded before each wind tunnel run and a completed model is shown in Figure C.6 below.

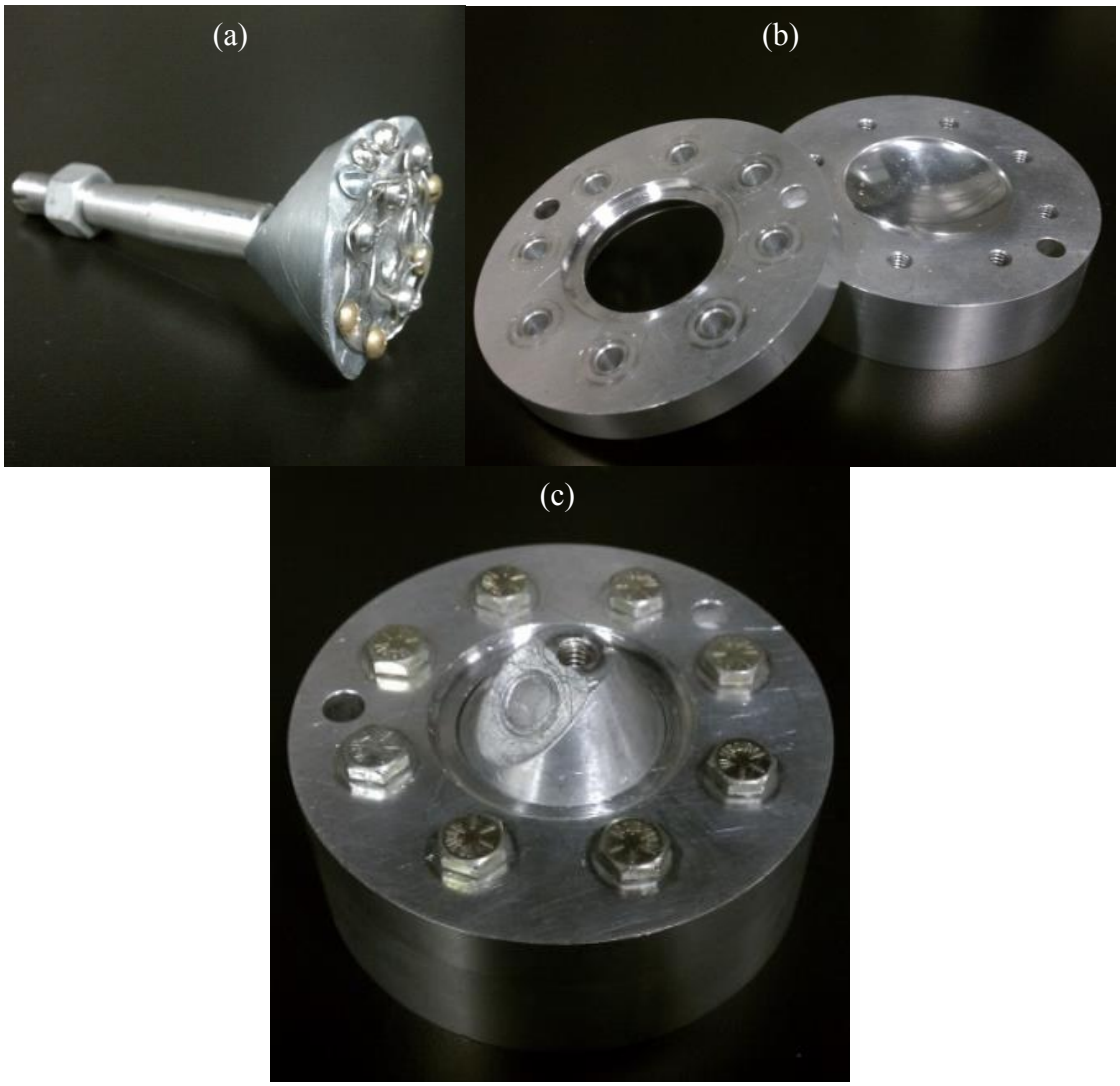

Figure C.5: (a) Orion MPCV model and sting without naphthalene heat shield, (b) top and bottom halves of mold assembly for creating naphthalene heat shield, and (c) fully-assembled mold with capsule model installed, ready for liquid naphthalene.

Figure C.6: Orion MPCV model at 52° angle of attack configuration with naphthalene heat shield installed in the Mach 5 wind tunnel facility at The University of Texas at Austin.

References

Adrian, R. J. and J. Westerweel. Particle Image Velocimetry. Cambridge University Press, New York, USA, 2011.

Alderfer, D. W., P. M. Danehy, J. A. Wilkes Inman, K. T. Berger, G. M. Buck, and R. J. Schwartz, "Fluorescence Visualization of Hypersonic Flow Over Rapid Prototype Wind-Tunnel Models" AIAA Paper 2007-1063, 45th AIAA Aerospace Sciences Meeting and Exhibit, Reno, Nevada, Jan. 8-11, 2007.

Ashpole, C. W., S. J. Formosinho, and G. Porter, "Pressure dependence of intersystem crossing in aromatic vapours," Proceedings of the Royal Society of London. A. Mathematical and Physical Sciences, Vol. 323, No. 1552, 1971, pp. 11-28.

Autodesk 3ds Max Product Information, Autodesk Inc., http://usa.autodesk.com/adsk/servlet/index?id=5659302&siteID=123112, viewed Jan 2, 2006.

Auvity, B., M. R. Etz, and A. J. Smits, "Effects of transverse helium injection on hypersonic boundary layers," Physics of Fluids, Vol. 13, No. 10, 2001, pp. 3025-3032.

Avouris, P., W. M. Gelbart, and M. A. El-Sayed, "Nonradiative electronic relaxation under collision-free conditions," Chemical Reviews, Vol. 77, No. 6, 1977, pp. 793-833.

Balakumar, B. J., G. C. Orlicz, C. D. Tomkins, and K. P. Prestridge, "Simultaneous particle-image velocimetry–planar laser-induced fluorescence measurements of Richtmyer–Meshkov instability growth in a gas curtain with and without reshock," Physics of Fluids, Vol. 20, No. 12, 2008, 124103.

Beck, S. M., D. E. Powers, J. B. Hopkins, and R. E. Smalley, "Jet-cooled naphthalene. I. Absorption spectra and line profiles," The Journal of Chemical Physics, Vol. 73, No. 5, 1980, p. 2019.

Beck, S. M., J. B. Hopkins, D. E. Powers, and R. E. Smalley, "Jet-cooled naphthalene. II. Single vibronic level fluorescence spectra," The Journal of Chemical Physics, Vol. 74, 1981, p. 43.

Beddard, G. S., S. J. Formosinho, and G. Porter, "Pressure effects on the fluorescence from naphthalene vapour," Chemical Physics Letters, Vol. 22, No. 2, 1973, pp. 235-238.

Behlen, F. M. and S. A. Rice, "Intersystem crossing in cold isolated molecules of naphthalene," The Journal of Chemical Physics, Vol. 75, 1981, p. 5672.

Beresh, S. J. 1999. The effect of the incoming turbulent boundary layer on a shock-induced separated flow using particle image velocimetry. Ph.D. Dissertation, The University of Texas at Austin.

Beresh, S. J., N. T. Clemens, and D. S. Dolling, "Relationship between upstream turbulent boundary-layer velocity fluctuations and separation shock unsteadiness," AIAA Journal, Vol. 40, No. 12, 2002, pp. 2412-2422.

Bertin, J. J., "The effect of protuberances, cavities, and angle of attack on the wind-tunnel pressure and heat-transfer distribution for the Apollo command module," NASA Technical Memorandum NASA-TM-X-1243, 1966.

Braman, K., H. Koo, V. Raman, R. Upadhyay, and O. Ezekoye, "RANS models for scalar transport in ablating compressible boundary layers," AIAA Paper 2011-207, 49th AIAA Aerospace Sciences Meeting, Orlando, Florida, Jan. 4-7, 2011.

Braman, K. and V. Raman, "A posteriori comparison of RANS scalar flux models in ablating compressible boundary layers," AIAA Paper 2011-3042, 20th AIAA Computation Fluid Dynamics Conference, Honolulu, Hawaii, June 27-30, 2011.

Borg, A., J. Bolinder, and L. Fuchs, "Simultaneous velocity and concentration measurements in the near field of a turbulent low-pressure jet by digital particle image velocimetry–planar laser-induced fluorescence," Experiments in fluids, Vol. 31, No. 2, 2001, pp. 140-152.

Buck, G. M., A. N. Watkins, P. M. Danehy, J. A. Inman, D. W. Aldefer, and A. A. Dyakonov, "Experimental Measurement of RCS Jet Interaction Effects on a Capsule Entry Vehicle," AIAA Paper 2008-1229, 46th AIAA Aerospace Sciences Meeting and Exhibit, Reno, Nevada, Jan. 7-10, 2008.

Burns, R. A. 2014. Development of scalar and velocity imaging diagnostics for supersonic hypermixing strut injector flowfields. Ph.D. Dissertation, The University of Texas at Austin.

Buxton, O. R. H., B. J. Lochman, M. Sharma, and N. T. Clemens, "Simultaneous PIV and PLIF Imaging of Low-Temperature Ablation in a Mach 5 Turbulent Boundary Layer," AIAA Paper 2012-0440, 50th AIAA Aerospace Sciences Meeting and Exhibit, Nashville, Tennessee, Jan. 9-12, 2012.

Callaway, D. W., M. F. Reeder, R. B. Greendyke, and R. Gosse, "Photogrammetric Measurement of Recession Rates of Low Temperature Ablators in Supersonic Flow," AIAA Paper 2010-1216, 48th AIAA Aerospace Sciences Meeting, Orlando, Florida, January, 2010.

Carvin, C., J. F. Debieve, and A. J. Smits, "The Near-Wall Temperature Profile of Turbulent Boundary Layers," AIAA Paper 88-0136, 26th AIAA Aerospace Sciences Meeting, Reno, Nevada, January 11-14, 1988.

Charwat, A. F., "Exploratory studies on the sublimation of slender camphor and naphthalene models in a supersonic wind-tunnel," 1968.

Chen, Y. K. and F. S. Milos, "Two-Dimensional Implicit Thermal Response and Ablation Program for Charring Materials," Journal of Spacecraft and Rockets, Vol. 38, No. 4, 2001, pp. 473-481.

Chen, Y. K. and F. S. Milos, "Finite-Rate Ablation Boundary Conditions for a Carbon-Phenolic Heat-Shield," AIAA Paper 2004-2270, 37th AIAA Thermophysics Conference, Portland, Oregon, June, 2004.

Christian, W. J. and S. P. Kezios, "Sublimation from sharp-edged cylinders in axisymmetric flow, including influence of surface curvature," AIChE Journal, Vol. 5, No. 1, 1959, pp. 61-68.

Clemens, N. T. and P. H. Paul, "Scalar measurements in compressible axisymmetric mixing layers," Physics of Fluids, Vol. 7, No. 5, 1995, pp. 1071-1081.

Combs, C. S., N. T. Clemens, P. M. Danehy, B. Bathel, R. Parker, T. Wadhams, M. Holden, and B. Kirk, "Fluorescence Imaging of Reaction Control Jets and Backshell Aeroheating of Orion Capsule" Journal of Spacecraft and Rockets, Vol. 52, No. 1, 2015, pp. 243-252.

Covington, M. A., J. M. Heinemann, H. E. Goldstein, Y. K. Chen, I. Terrazas-Salinas, J. A. Balboni, J. Olejniczak, and E. R. Martinez, "Performance of a Low Density Ablative Heat Shield Material," Journal of Spacecraft and Rockets, Vol. 45, No. 2, 2008, pp. 237-247.

Craig, D. P., J. M. Hollas, M. F. Redies, and S. C. Wait, "Analysis of the Naphthalene Vapour Absorption Bands at 3200 angstrom I. Naphthalene h-8," Philosophical Transactions of the Royal Society of London. Series A, Mathematical and Physical Sciences, Vol. 253, No. 1035, 1961, pp. 543-568.

Crimaldi, J. P. and J. R. Koseff, "High-resolution measurements of the spatial and temporal scalar structure of a turbulent plume," Experiments in Fluids, Vol. 31, No. 1, 2001, pp. 90-102.

Crimaldi, J. P., M. B. Wiley, and J. R. Koseff, "The relationship between mean and instantaneous structure in turbulent passive scalar plumes," Journal of Turbulence, Vol. 3, No. 14, 2002, pp. 1-24.

Danehy, P. M., J. A. Wilkes, D. W. Alderfer, S. B. Jones, A. W. Robbins, D. P. Patry and R. J. Schwartz, "Planar laser-induced fluorescence (PLIF) investigation of hypersonic flowfields in a Mach 10 wind tunnel," AIAA Paper 2006-3442, AIAA AMT-GT Technology Conference, San Francisco, June, 2006.

Danehy, P. M., A. P. Garcia, S. Borg, A. A. Dyakonov, S. A. Berry, J. A. Wilkes Inman, D. W. Alderfer, "Fluorescence visualization of hypersonic flow past triangular and rectangular boundary-layer trips," AIAA Paper 2007-0536, 45th AIAA Aerospace Sciences Meeting, Reno, Nevada, January 8-11, 2007.

Danehy, P. M., J. A. Inman, G. J. Brauckmann, D. W. Alderfer, S. B. Jones, and D. P. Patry, "Visualization of a Capsule Entry Vehicle Reaction-Control System (RCS) Thruster," Journal of Spacecraft and Rockets, Vol. 46, No. 1, Jan.–Feb. 2009, pp. 93–102.

Davies, C. B. and C. Park, "Trajectories of Solid Particles Spalled from a Carbonaceous Heat Shield," AIAA Paper 82-0200, 20th AIAA Aerospace Sciences Meeting, Orlando, Florida, Jan. 11-14, 1982.

De Kruif, C. G., T. Kuipers, J. C. van Miltenburg, R. C. F. Schaake, and G. Stevens, "The vapour pressure of solid and liquid naphthalene," Journal of Chemical Thermodynamics, Vol. 13, No. 11, 1981, pp. 1081-1086.

Du, H., R. A. Fuh, J. Li, Corkan, A., and Lindsey, J. S., "PhotochemCAD: A computer-aided design and research tool in photochemistry," Photochemistry and Photobiology, Vol. 68, 1998, pp. 141-142.

Eckbreth, A. C. Laser diagnostics for combustion temperature and species. Vol. 3. CRC Press, London, UK, 1996.

Elena, M. and J. P. Lacharme, "Experimental study of a supersonic turbulent boundary layer using a laser doppler anemometer," Journal de Mecanique theorique et appliquee (Journal of Theoretical and Applied Mechanics), Vol. 7. No. 2, 1988, pp.175-190.

Elsinga, G. E., R. J. Adrian, B. W. Van Oudheusden, and F. Scarano, "Three-dimensional vortex organization in a high-Reynolds-number supersonic turbulent boundary layer," Journal of Fluid Mechanics, Vol. 644, 2010, pp. 35-60.

Fajardo, C. M., J. D. Smith, and V. Sick, "Sustained simultaneous high-speed imaging of scalar and velocity fields using a single laser," Applied Physics B, Vol. 85, No. 1, 2006, pp. 25 30.

Faust, S., G. Tea, T. Dreier, and C. Schulz, "Temperature, pressure, and bath gas composition dependence of fluorescence spectra and fluorescence lifetimes of toluene and naphthalene," Applied Physics B, Vol. 110, No. 1, 2013, pp. 81-93.

Ferguson, J., L. W. Reeves, and W. G. Schneider, "Vapor absorption spectra and oscillator strengths of naphthalene, anthracene, and pyrene," Canadian Journal of Chemistry, Vol. 35, No. 10, 1957, pp. 1117-1136.

Fletcher, D. G., and R. L. McKenzie, "Single-pulse measurements of density and temperature in a turbulent, supersonic flow using UV laser spectroscopy," Optics Letters, Vol. 17, No. 22, 1992, pp. 1614-1616.

Frank, J. H., K. M. Lyons, and M. B. Long, "Simultaneous scaler/velocity field measurements in turbulent gas-phase flows," Combustion and Flame, Vol. 107, No. 1, 1996, pp. 1-12.

Gamba, M., Mungal, M. G., Hanson, R. K., "OH PLIF Imaging of the Reaction Zone in Combusting Transverse Jets in Supersonic Crossflow," 16th Int'l Symp. on Applications of Laser Techniques to Fluid Mechanics, Lisbon, Portugal, July 9-12, 2012.

Ganapathisubramani, B., N. T. Clemens, and D. S. Dolling, "Large-scale motions in a supersonic turbulent boundary layer," Journal of Fluid Mechanics, Vol. 556, 2006, pp. 271-282.

Garcia, M, "Partnerships Make Missions Possible," NASA, July 16, 2013, Web, www.nasa.gov/content/partnerships-make-missions-possible/, viewed July 17, 2013.

Goldstein, R. J. and J. R. Taylor, "Mass transfer in the neighborhood of jets entering a crossflow," Journal of Heat Transfer, Vol. 104, No. 4, 1982, pp. 715-721.

Goldstein, R. J. and H. H. Cho, "A review of mass transfer measurements using naphthalene sublimation," Experimental Thermal and Fluid Science, Vol. 10, 1995, pp. 416-434.

Gould, R. D. The Evaporation of Liquid Droplets in Highly Turbulent Gas Streams. North Carolina State University Department of Mechanical and Aerospace Engineering Technical Report No. DAAH04-95-1-0231, 1998.

Gray, W. E., "A Chemical Method of Indicating Transition in the Boundary Layer," Royal Aircraft Establishment TN Aero 1466, June, 1944.

Griffith, B. J., E. E. Edenfield, and W. T. Strike, "Wind-Tunnel Simulation of Ablation," Journal of Spacecraft and Rockets, Vol. 14, No. 10, 1977, pp. 593-599.

Grimes, J. H. and J. Casey, "Influence of ablation on the dynamics of slender re-entry configurations," Journal of Spacecraft and Rockets, Vol. 2, No. 1, 1965, pp. 106-108.

Gross, K. P. and R. L. McKenzie, "Measurements of Fluctuating Temperatures in a Supersonic Turbulent Flow Using Laser-Induced Fluorescence," AIAA Journal, Vol. 23, No. 12, 1985, pp. 1932-1936.

Hanson, R. K., J. M. Seitzman, and P. H. Paul, "Planar Laser-Fluorescence Imaging of Combustion Gases," Applied Physics B, Vol. 50, 1990, pp. 441-454.

Hishida, K. and J. Sakakibara, "Combined Planar laser-induced fluorescence–particle image velocimetry technique for velocity and temperature fields," Experiments in Fluids, Vol 29, No. 1, 2000, pp. 129-140.

Hjertager, L. K., B. H. Hjertager, N. G. Deen, and T. Solberg, "Measurement of turbulent mixing in a confined wake flow using combined PIV and PLIF," The Canadian Journal of Chemical Engineering, Vol. 81, No. 6, 2003, pp. 1149-1158.

Ho, D. W. K., J. H. Koo, M. C. Bruns, and O. A. Ezekoye, "A Review of Numerical and Experimental Characterization of Thermal Protection Materials – Part I. Numerical Modeling," AIAA Paper 2006-4936, 42nd AIAA/ASME/SAE/ASEE Joint Propulsion Conference & Exhibit, Sacramento, California, July, 2006.

Ho Ho, D. W. K., J. H. Koo, M. C. Bruns, and O. A. Ezekoye, "A Review of Numerical and Experimental Characterization of Thermal Protection Materials – Part III. Experimental Testing," AIAA Paper 2007-5773, 43rd AIAA/ASME/SAE/ASEE Joint Propulsion Conference & Exhibit, Cincinnati, Ohio, 2007.

Hou, Y. X., N. T. Clemens, and D. S. Dolling, "Wide-field PIV study of shock-induced turbulent boundary layer separation," AIAA Paper 2003-441, 41st AIAA Aerospace Sciences Meeting and Exhibit, Reno, Nevada, January 6-9, 2003.

Hou, Y. X. 2003. Particle image velocimetry study of shock-induced turbulent boundary layer separation. Ph.D. Dissertation, The University of Texas at Austin.

Humble, R. A., G. E. Elsinga, F. Scarano, and B. W. Van Oudheusden, "Three-dimensional instantaneous structure of a shock wave/turbulent boundary layer interaction," Journal of Fluid Mechanics, Vol. 622, 2009, pp. 33-62.

Humphreys, W. M., S. M. Bartram, and J. L. Blackshire, "A survey of particle image velocimetry applications in Langley aerospace facilities," AIAA Paper 93-0411, 31st AIAA Aerospace Sciences Meeting and Exhibit, Reno, Nevada, Jan. 11-14, 1993.

Inman, J. A., P. M. Danehy, D. W. Alderfer, and G. M. Buck, A. McCrea, and R. J. Schwartz, "PLIF Imaging of Capsule RCS Jets and Simulated Forebody Ablation," AIAA Paper 2008-0248, 46th AIAA Aerospace Sciences Meeting and Exhibit, Reno, Nevada, Jan. 7-10, 2008.

Jensen, R., "Multi-colored layers for visualizing aerodynamic flow effects (Patent)," Patent Number US 5035509, 1991.

Johnston, C. O., P. A. Gnoffo, and A. Mazaheri, "A Study of Ablation-Flowfield Coupling Relevant to the Orion Heatshield," AIAA 2009-4318, 41st AIAA Thermophysics Conference, San Antonio, Texas, June, 2009.

Johnston, C. O., P. A. Gnoffo, and A. Mazaheri, "Influence of Coupled Radiation and Ablation on the Aerothermodynamic Environment of Planetary Entry Vehicles," Radiation and Gas-Surface Interaction Phenomena in High Speed Re-Entry, Brussels, May, 2013.

Jones, P. F. and S. Siegel, "Quenching of naphthalene luminescence by oxygen and nitric oxide," The Journal of Chemical Physics, Vol. 54, 1971, p. 3360.

Kader, B. A., "Temperature and concentration profiles in fully turbulent boundary layers," International Journal of Heat and Mass Transfer, Vol. 24, No. 9, 1981, pp. 1541-1544.

Kaiser, S. A. and M. B. Long, "Quantitative planar laser-induced fluorescence of naphthalene as fuel tracers," Proceedings of the Combustion Institute, Vol. 30, 2005, pp. 1555-1563.

Kasagi, N., Y. Tomita, and A. Kuroda, "Direct numerical simulation of passive scalar field in a turbulent channel flow," Journal of Heat Transfer, Vol. 114, 1992, pp. 598-606.

Kim J. and P. Moin, "Transport of passive scalars in a turbulent channel flow," Turbulent Shear Flows, Vol. 6, 1989, pp. 85-96.

Koban, W., J. D. Koch, R. K. Hanson, and C. Schulz, "Oxygen quenching of toluene fluorescence at elevated temperatures," Applied Physics B, Vol. 80, No. 6, 2005, pp. 777-784.

Kohlman, D. L. and Richardson, R. W., "Experiments on the use of dry ice ablating wind-tunnel models," Journal of Spacecraft and Rockets, Vol. 6, No. 9, 1969, pp. 1061-1063.

Koochesfahani, M., R. Cohn, and C. MacKinnon, "Simultaneous whole-field measurements of velocity and concentration fields using a combination of MTV and LIF," Measurement science and technology, Vol. 11, No. 9, 2000, p. 1289.

Lachney, E. R., and N. T. Clemens, "PLIF imaging of mean temperature and pressure in a supersonic bluff wake," Experiments in Fluids, Vol. 24, No. 4, 1998, pp. 354-363.

Laor, U., and P. K. Ludwig, "Fluorescence Lifetimes of Vibronic States of Naphthalene Vapor in the Region of Excitation from 3080–2150 Å," The Journal of Chemical Physics, Vol. 54, 1971, p. 1054.

Lemoine, F., M. Wolff, and M. Lebouche, "Simultaneous concentration and velocity measurements using combined laser-induced fluorescence and laser Doppler velocimetry: Application to turbulent transport," Experiments in Fluids, Vol. 20, No. 5, 1996, pp. 319-327.

Li, F. C., D. Z. Wang, Y. Kawaguchi, and K. Hishida, "Simultaneous measurements of velocity and temperature fluctuations in thermal boundary layer in a drag-reducing surfactant solution flow," Experiments in Fluids, Vol. 36, 2004, pp. 131-140.

Li, Q., P. Schlatter, L. Brandt, and D. S. Henningson, "DNS of a spatially developing turbulent boundary layer with passive scalar transport," International Journal of Heat and Fluid Flow, Vol. 30, 2009, pp. 916-929.

Lin, H., Y. Shi-He, T. Li-Feng, C. Zhi, and Z. Yang-Zhu, "Simultaneous density and velocity measurements in a supersonic turbulent boundary layer," Chinese Physics B, Vol. 22, No. 2, 2013.

Lipfert, F. and Genovese, J., "An experimental study of the boundary layers on low-temperature subliming ablators," AIAA Journal, Vol. 9, No. 7, 1971, pp. 1330-1337.

Lochman, B., Z. R. Murphree, V. Narayanaswamy, and N. T. Clemens, "PLIF imaging of naphthalene-ablation products in a Mach 5 turbulent boundary layer," AIAA Paper 2010-4346, 27th AIAA Aerodynamic Measurement Technology and Ground Testing Conference, June, 2010.

Lochman, B. 2010. Technique for Imaging Ablation-Products Transported in High-Speed Boundary Layers by using Naphthalene Planar Laser-Induced Fluorescence. Master's Thesis, The University of Texas at Austin.

Lozano, A., B. Yip, and R. K. Hanson, "Acetone: a tracer for concentration measurements in gaseous flows by planar laser-induced fluorescence," Experiments in Fluids, Vol. 13, 1992, pp. 369-376.

Mahzari, M., R. D. Braun, T. R. White, and D. Bose, "Preliminary Analysis of the Mars Science Laboratory's Entry Aerothermodynamic Environment and Thermal Protection System Performance," AIAA Paper 2013-0185, 51st AIAA Aerospace Sciences Meeting, Grapevine, Texas, Jan. 7-10, 2013.

Martin, A., S. C. C. Bailey, F. Panerai, R. S. C. Davuluri, A. R. Vazsonyi, H. Zhang, Z. S. Lippay et al., "Preliminary numerical and experimental analysis of the spallation phenomenon," 8th European Symposium on Aerothermodynamics for Space Vehicles, March, 2015.

Martinez, M., H. Harder, X. Ren, R. L. Lesher, and W. H. Brune, "Measuring atmospheric naphthalene with laser-induced fluorescence," Atmospheric Chemistry and Physics, Vol. 4, No. 2, 2004, pp. 563-569.

McClure, W. B. 1992. An experimental study of the driving mechanism and control of the unsteady shock induced turbulent separation in a Mach 5 compression corner flow. Ph.D. Dissertation, The University of Texas at Austin.

McDevitt, J. B., "An exploratory study of the roll behavior of ablating cones," Journal of Spacecraft and Rockets, Vol. 8, No. 2, 1971, pp. 161-169.

Messersmith, N. L. and J. C. Dutton, "Laser-induced fluorescence measurements of scalar transport in compressible mixing layers," AIAA Paper 92-3547, AIAA 28th Joint Propulsion Conference and Exhibit, Nashville, Tennessee, July 6-8, 1992.

Morkovin, M. V., "Effects of Compressibility on Turbulent Flows," Mechanique de la Turbulence, Ed. A., Favre, 1962. pp. 367-380.

Murman, S. M., R. E. Childs, and J. A. Garcia, "Simulation of Atmospheric-Entry Capsules in the Subsonic Regime," AIAA Paper 2015-1930, 53rd AIAA Aerospace Sciences Meeting and Exhibit, Kissimmee, Florida, Jan. 5-9, 2015.

"NASA's Exploration Systems Architecture Study: Final Report," NASA TM-2005-214062, Nov., 2005.

Ni, T. and L. A. Melton, "Two-dimensional gas-phase temperature measurements using fluorescence lifetime imaging," Applied spectroscopy, Vol. 50, No. 9, 1996, pp. 1112-1116.

Obara, C. J., "Sublimating Chemical Technique for Boundary-Layer Flow Visualization in Flight Testing," Journal of Aircraft, Vol. 25, No. 6, 1988, pp. 493-498.

Orain, M., P. Baranger, B. Rossow, and F. Grisch, "Fluorescence spectroscopy of naphthalene at high temperatures and pressures: implications for fuel-concentration measurements," Applied Physics B, Vol. 102, No. 1 2011, pp. 163-172.

"Orion's First Flight," NASA, http://www.nasa.gov/externalflash/orionfirstflight/ (accessed August 1, 2015).

Ossler, F., T. Metz, and M. Aldén, "Picosecond laser-induced fluorescence from gas-phase polycyclic aromatic hydrocarbons at elevated temperatures. I. Cell measurements," Applied Physics B, Vol. 72, No. 4, 2001, pp. 465-478.

Palma, P. C., S. G. Mallinson, S. B. O'Byrne, P. M. Danehy, and R. Hillier, "Temperature measurements in a hypersonic boundary layer using planar laser-induced fluorescence," AIAA Journal, Vol. 38, No. 9, 2000, pp. 1769-1772.

Paschal, K. B., D. H. Neuhart, G. B. Beeler, and B. G. Allan, "Circulation Control Model Experimental Database for CFD Validation," AIAA 2012-0705, 50th AIAA Aerospace Sciences Meeting and Exhibit, Nashville, Tennessee, Jan. 9-12, 2012.

Piponniau, S., J. P. Dussauge, J. F. Debiève, and P. Dupont, "A simple model for low-frequency unsteadiness in shock-induced separation," Journal of Fluid Mechanics, Vol. 629, 2009, pp. 87-108.

Poreh, M. and J. E. Cermak, "Study of diffusion from a line source in a turbulent boundary layer," Int. J. Heat Mass Transfer, Vol. 7, 1964, pp. 1083-1095.

Radeztsky, R. H., M. S. Reibert, and W. S. Saric, "Effect of isolated micron-sized roughness on transition in swept-wing flows," AIAA Journal, Vol. 37, No. 11, 1999, pp. 1370-1377.

Reda, D. C., M. C. Wilder, D. W. Bogdanoff, and J. Olejniczak, "Aerothermodynamic Testing of Ablative Reentry Vehicle Nosetip Materials in Hypersonic Ballistic-Range Environments," AIAA Paper 2004-6829, USAF Developmental Test and Evaluation Summit, Woodland Hills, California, Nov. 16-18, 2004.

Regert, T., Y. Babou, O. Marxen, M. A. Camarinha, and O. Chazot, "Investigation of flat plate transitional boundary layer in hypersonic flow by means of naphthalene based PLIF," Personal Communication, June 4, 2013.

Robinson, S. K., "Coherent motions in the turbulent boundary layer," Annual Review of Fluid Mechanics, Vol. 23, 1991, pp. 601-639.

Rossmann, T., M. G. Mungal, and R. K. Hanson, "Laser-based diagnostics and scalar imaging in high compressibility shear layers," 11th Int'l Symp. on the Applications of Laser Techniques to Fluid Mechanics, Lisbon, Portugal, pp. 8-11, 2002.

Sarathi, P., R. Gurka, G. A. Kopp, and P. J. Sullivan, "A calibration scheme for quantitative concentration measurements using simultaneous PIV and PLIF," Experiments in Fluids, Vol. 52, No. 1, 2012, pp. 247-259.

Scarano, F. and B. W. Van Oudheusden, "Planar velocity measurements of a two-dimensional compressible wake," Experiments in Fluids, Vol. 34, No. 3, 2003, pp. 430-441.

Scarano, F, "Overview of PIV in Supersonic Flows," Topics in Applied Physics, Vol. 112, 2008, pp. 445-463.

Schaefer, J. W., D. T. Flood, J. J. Reese Jr., and J. C. Kimble, "Experimental and analytical evaluation of the Apollo thermal protection system under simulated reentry conditions Parts I & II," NASA Technical Report NACA-TM-557, 1967.

Schlag, E. W., S. Schneider, and D. W. Chandler, "Fluorescence lifetimes of vibronic levels of naphthalene vapour," Chemical Physics Letters, Vol. 11, No. 4, 1971, pp. 474-477.

Schrijer, F. F. J., F. Scarano, and B. W. Van Oudheusden, "Application of PIV in a Mach 7 double-ramp flow," Experiments in Fluids, Vol. 41, No. 2, 2006, pp. 353-363.

Schwartz, R. J., "ViDI: Virtual Diagnostics Interface Volume 1-The Future of Wind Tunnel Testing," Contractor Report NASA/CR-2003-212667, Dec., 2003.

Sietzen Jr., F, “From Mercury to CEV: Space Capsules Reemerge,” Aerospace America, Feb., 2005, pp. 26-33.

Silton, S. I. and D. B. Goldstein, “Ablation Onset in Unsteady Hypersonic Flow About Nose Tip with Cavity,” Journal of Thermophysics and Heat Transfer, Vol. 14, No. 3, 2000, pp. 421-434.

Smits, A. J. and J.-P. Dussauge. Turbulent shear layers in supersonic flow. Springer Science & Business Media, 2006.

Smits, A. J., M. P. Martin, and S. Girimaji, “Current status of basic research in hypersonic turbulence,” AIAA Paper 2009-151, 47th AIAA Aerospace Sciences Meeting and Exhibit, Orlando, Florida, 2009.

Soep, B., C. Michel, A. Tramer, and L. Lindqvist, “Study of intersystem crossing in naphthalene and 1-methylnaphthalene in collision-free conditions and pressure effects,” Chemical Physics, Vol. 2, No. 3, 1973, pp. 293-303.

Somandepalli, V. S. R., Y. X. Hou, and M. G. Mungal, “Concentration flux measurements in a polymer drag-reduced turbulent boundary layer,” Journal of Fluid Mechanics, Vol. 644, 2010, pp. 281-319.

Souza Mendes, P. R., “The naphthalene sublimation technique,” Experimental Thermal and Fluid Science, Vol. 4, No. 5, 1991, pp. 510-523.

Sparrow, E. M., and R. F. Prieto, “Heat Transfer Coefficients and Patterns of Fluid Flow for Contacting Spheres at Various Angles of Attack,” Journal of Heat Transfer, Vol. 105, No. 1, 1983, p. 48-55.

Spina, E. F., A. J. Smits, and S. K. Robinson, “The physics of supersonic turbulent boundary layers,”Annual Review of Fluid Mechanics, Vol. 26, 1994, pp. 287-319.

Steg, L. and H. Lew, “Hypersonic Ablation,” AGARD Hypersonic Conference TCEA, Geneva, April 3-6, 1962.

Stevens, B., “The Photoluminescence And Associated Processes of Complex Organic Molecules In The Vapor Phase,” Chemical Reviews, Vol. 57, No. 3, 1957, pp. 439-477.

Stock, H. W. and J. J. Ginoux, “Experimental Results on Crosshatched Ablation Patterns,” AIAA Journal, Vol. 9, No. 5, 1971, pp. 971-973.

Stockburger, M., H. Gattermann, and W. Klusmann, “Spectroscopic studies on naphthalene in the vapor phase. I. Fluorescence spectra from single vibronic levels,” The Journal of Chemical Physics, Vol. 63, 1975a, pp. 4519.

Stockburger, M., H. Gattermann, and W. Klusmann, "Spectroscopic studies on naphthalene in the vapor phase. II. Fluorescence quantum yields from single vibronic levels in the first excited singlet state—behavior of higher excited singlet states," The Journal of Chemical Physics, Vol. 63, 1975b, p. 4529.

Su, L. K. and N. T. Clemens, "Planar measurements of the full three-dimensional scalar dissipation rate in gas-phase turbulent flows," Experiments in Fluids, Vol. 27, No. 6, 1999, pp. 507-521.

Su, L. K. and M. G. Mungal, "Simultaneous measurements of scalar and velocity field evolution in turbulent crossflowing jets," Journal of Fluid Mechanics, Vol. 513, 2004, pp. 1-45.

Suto, M., X. Wang, J. Shan, and L. C. Lee, "Quantitative photoabsorption and fluorescence spectroscopy of benzene, naphthalene, and some derivatives at 106–295 nm," Journal of Quantitative Spectroscopy and Radiative Transfer, Vol. 48, No. 1, 1992, pp. 79-89.

Suzuki, T., K. Sawada, T. Yamada, and Y. Inatani, "Experimental and Numerical Study of Pyrolysis Gas Pressure in Ablating Test Piece," Journal of Thermophysics and Heat Transfer, Vol. 19, No. 3, 2005, pp. 266-272.

Thurber, M. C., F. Grisch, B. J. Kirby, M. Votsmeier, and R. K. Hanson, "Measurements and modeling of acetone laser-induced fluorescence with implications for temperature-imaging diagnostics," Applied Optics, Vol. 37, No. 21, 1998, pp. 4963-4978.

Unalmis, O. H., Y. X. Hou, P. C. Bueno, N. T. Clemens, and D. S. Dolling, "PIV investigation of role of boundary layer velocity fluctuations in unsteady shock-induced separation," AIAA Paper 2000-2450, 21st AIAA Aerodynamic Measurement Technology and Ground Testing Conference, Denver, Colorado, June 19-22, 2000.

Unalmis, O. H. 1995. Structure of the supersonic turbulent boundary layer and its influence on unsteady separation. Ph.D. Dissertation, The University of Texas at Austin.

Urban, W. D., S. Watanabe, and M. G. Mungal, "Velocity field of the planar shear layer: compressibility effects," AIAA Paper 1998-0697, 1998.

Urban, W. D. and M. G. Mungal, "Planar velocity measurements in compressible mixing layers," Journal of Fluid Mechanics, Vol. 431, 2001, pp. 189-222.

Wagner, C., S. Kuhn, and P. R. von Rohr, "Scalar transport from a point source in flows over wavy walls," Experiments in Fluids, Vol. 43, No. 2-3, 2007, pp. 261-271.

Wagner, J. L., K. B. Yuceil, and N. T. Clemens, "PIV measurements of unstart of an inlet-isolator model in a Mach 5 flow," AIAA Paper 2009-4209, 39th AIAA Fluid Dynamics Conference and Exhibit, San Antonio, Texas, June 22-25, 2009.

Wang, H. P., R. J. Goldstein, and S. J. Olson, "Effect of high free-stream turbulence with large length scale on blade heat/mass transfer," Journal of Turbomachinery, Vol. 121, No. 2, 1999, pp. 217-224.

Watts, R. J. and S. J. Strickler, "Fluorescence and Internal Conversion in Naphthalene Vapor," The Journal of Chemical Physics, Vol. 44, 1966, p. 2423.

White, E. B. and W. S. Saric, "Application of Variable Leading-Edge Roughness for Transition Control on Swept Wings," AIAA Paper 2000-0283, 38th AIAA Aerospace Sciences Meeting and Exhibit, Reno, Nevada, Jan. 10-13, 2000.

White, F. M. Viscous Fluid Flow. McGraw Hill, New York, NY, USA, 2006.

Wright, M. J., and J. H. Grinstead, "A Risk-Based Approach for Aerothermal/TPS Analysis and Testing," NATO Conference, July, 2007.

Vita

Christopher Combs was born in Lexington, Kentucky in 1988. He is the son of Mr. Craig Combs and Dr. Dorothy Combs, and is married to Casen Combs. Christopher completed high school at Model Laboratory School in Richmond, Kentucky in May of 2006. In August of 2006 he enrolled at the University of Evansville in Evansville, Indiana, where he graduated Magna Cum Laude and received his Bachelor of Science degree in Mechanical Engineering in May of 2010. In August of 2010 he enrolled at The University of Texas at Austin and began working towards a Ph.D.

Permanent email address: ccombs0022@gmail.com

This dissertation was typed by Christopher Stanley Combs.